DEPARTMENT OF MECHANICAL AND MANUFACTURING ENGINEERING

Pulsed laser deposition as a single deposition method for the fabrication of Cu(In,Ga)Se2-based solar cells: growth and characterization of the constituent layers

DOCTOR OF PHILOSOPHY DISSERTATION

CHRISTIANA NICOLAOU

2022

CHRISTIANA NICOLAOU

DEPARTMENT OF MECHANICAL AND MANUFACTURING ENGINEERING

Application of pulsed laser deposition as a single deposition method for the fabrication of Cu(In,Ga)Se2-based solar cells: growth and characterization of the constituent layers

DOCTOR OF PHILOSOPHY DISSERTATION

CHRISTIANA NICOLAOU

A Dissertation Submitted to the University of Cyprus in Partial Fulfillment of the Requirements for the Degree of Doctor of Philosophy

October 2022

CHRISTIANA NICOLAOU

CHRISTIANA NICOLAOU

©Christiana Nicolaou, 2022

VALIDATION PAGE

Doctoral Candidate: Christiana Nicolaou

Doctoral Thesis Title: Application of pulsed laser deposition as a single deposition method for the fabrication of Cu(In,Ga)Se2-based solar cells: growth and characterization of the constituent layers

The present Doctoral Dissertation was submitted in partial fulfillment of the requirements for the Degree of Doctor of Philosophy at the Department of Mechanical and Manufacturing Engineering and was approved on the 7th of October 2022 by the members of examination Committee.

Examination Committee:

Research Supervisor: Professor Ioannis Giapintzakis

Committee Member: Professor Theodora Kyratsi

Committee Member: Associate Professor Theodora Krasia-Christoforou

Committee Member: Dr Stela Canulescu

Committee Member: Dr Dimitrios Hariskos

CHRISTIANA NICOLAOU

DECLARATION OF DOCTORAL CANDIDATE

The present doctoral dissertation was submitted in partial fulfillment of the requirements for the degree of Doctor of Philosophy of the University of Cyprus. It is a product of original work of my own, unless otherwise mentioned through references, notes, or any other statements.

Christiana Nicolaou

……………………………

CHRISTIANA NICOLAOU

Περίληψη

Η ανάγκη για φιλικές προς το περιβάλλον πηγές ενέργειας είναι επιτακτική καθώς η περιορισμένη διαθεσιμότητα ορυκτών καυσίμων και οι επιβλαβείς επιπτώσεις των αερίων του θερμοκηπίου στο περιβάλλον είναι πλέον εμφανείς. Η άμεση μετατροπή της ηλιακής ακτινοβολίας σε ηλεκτρική με τη χρήση φωτοβολταϊκής (PV) τεχνολογίας αναδεικνύεται ως η κύρια υποψήφιος για την παραγωγή πράσινης ενέργειας. Τις τελευταίες δύο δεκαετίες, έχει γίνει σημαντική προσπάθεια για την προώθηση της φωτοβολταϊκής τεχνολογίας λεπτών ημενίων (thin film photovoltaics) «δεύτερης γενιάς», η οποία δεν απαιτεί τη χρήση χοντρών, άκαμπτων και ακριβών κρυσταλλικών υποστρωμάτων πυριτίου (Si). Τα ηλιακά κύτταρα λεπτών υμενίων έχουν προσελκύσει σημαντικό ενδιαφέρον λόγω των υψηλών δυνατοτήτων στην απόδοση, της υψηλής αντοχής στην ακτινοβολία, της μείωσης βάρους και της εξοικονόμησης χώρου. Συγκεκριμένα, τα ηλιακά κύτταρα λεπτών υμενίων που βασίζονται στη χημική ένωση χαλκοπυρίτη Cu(In,Ga)Se2 (CIGS) έχουν παρουσιάσει αυξημένες αποδόσεις, ειδικότερα μετά το 2014. Αποδόσεις ρεκόρ που φτάνουν έως και το 23,35% έχουν αναφερθεί από τη Solar Frontier το 2019 [1].

Το ηλιακό κύτταρο CIGS αποτελείται από πολλά στρώματα διαφορετικών υλικών και η απόδοση του κυττάρου επηρεάζεται σε μεγάλο βαθμό από το κάθε στρώμα, καθώς και την αλληλεπίδραση μεταξύ τους. Ένα τυπικό ηλιακό κύτταρο CIGS με εργαστηριακή απόδοση πάνω από 20% έχει την ακόλουθη διαμόρφωση: γυαλί ανθρακικού ασβεστίου (soda-lime glass) ως υπόστρωμα, υμένιο μολυβδενίου (Mo) ως πίσω μεταλλική επαφή εναποτιθέμενο με ιοντοβολή, φωτοαπορροφητικό στρώμα CIGS τύπου p εναποτιθέμενο με θερμική εξάχνωση πολλαπλών σταδίων, ενδιάμεσο στρώμα CdS τύπου n εναποτιθέμενο με χημικό λουτρό, διαφανές αγώγιμο παράθυρο τύπου n από ενδογενές ZnO και ντοπαρισμένο ZnO με αλουμίνιο (i-ZnO/ZnO:Al) εναποτιθέμενα με ιοντοβολή, μεταλλικό πλέγμα νικελίου/αλουμινίου (Ni/Al) και αντιανακλαστική επίστρωση MgF_2 εναποτιθέμενα με θερμική εξάχνωση [2].

Επί του παρόντος, οι πολλαπλές τεχνικές εναπόθεσης (θερμική εξάχνωση, ιοντοβολή, χημικό λουτρό, σεληνισμός) και υψηλές θερμοκρασίες επεξεργασίας (πάνω από 500°C για τα υμένια CIGS υψηλής απόδοσης) που χρησιμοποιούνται για την ανάπτυξη των διαφορετικών στρωμάτων του ηλιακού κυττάρου καθιστούν τη διαδικασία κατασκευής χρονοβόρα και ακριβή. Ως εκ τούτου, ο εντοπισμός μιας ενιαίας μεθόδου εναπόθεσης για την κατασκευή του λειτουργικού τμήματος του ηλιακού κυττάρου CIGS, που θα μειώσει τον χρόνο και το κόστος κατασκευής, είναι ιδιαίτερα επιθυμητός. Αυτή η διδακτορική διατριβή καταδεικνύει τη χρήση της μεθόδου εναπόθεσης με παλμικό λέιζερ (pulsed laser deposition, PLD) σε μια νέα διαδοχική διαδικασία για την κατασκευή της πολυστρωματικής δομής που περιγράφηκε παραπάνω. Σε αυτή την εργασία, η προετοιμασία του λειτουργικού μέρους του ηλιακού κυττάρου CIGS (CIGS/CdS/i-ZnO/ZnO:Al) πραγματοποιήθηκε με χρήση PLD σε μία συνεχόμενη ακολουθία ανάπτυξης και σε θερμοκρασίες που δεν ξεπερνούν τους 300 °C. Ηλιακά κύτταρα CIGS με ψηλές αποδόσεις στην περιοχή 14-22%

CHRISTIANA NICOLAOU

έχουν αναπτυχθεί με την χρήση πολλών διαφορετικών τεχνικών εναπόθεσης για το κάθε στρώμα, και μέχρι σήμερα δεν υπάρχει δημοσιευμένη αναφορά για την κατασκευή του ηλιακού κυττάρου CIGS στο σύνολό του με PLD. Έτσι, αυτή η διπλωματική εργασία αποτελεί μια καινοτόμο εφαρμογή του PLD στην κατασκευή ηλιακών κυττάρων CIGS λεπτών υμενίων.

Σε αυτή τη διδακτορική εργασία, έχει πραγματοποιηθεί μια συστηματική διερεύνηση των επιμέρους στρωμάτων και των διεπαφών μεταξύ τους για τη βελτιστοποίηση των ιδιοτήτων της πολυστρωματικής δομής. Κάθε κεφάλαιο είναι αφιερωμένο στη βελτιστοποίηση ενός στρώματος, ξεκινώντας από την εναπόθεση του στρώματος σε υποστρώματα SLG για την κατανόηση της επίδρασης των παραμέτρων εναπόθεσης PLD στις ιδιότητες του στρώματος. Στη συνέχεια, η βελτιστοποίηση του στρώματος με τα παρακείμενά στρώματα πραγματοποιείται μέσω μιας παραμετρικής διερεύνησης της θερμοκρασίας εναπόθεσης του αντίστοιχου στρώματος στην πολυστρωματική δομή που πραγματεύεται το κάθε κεφάλαιο. Οι ιδιότητες των επιμέρους στρωμάτων και οι διεπαφές τους εξετάστηκαν και χαρακτηρίστηκαν χρησιμοποιώντας μια ευρεία τεχνικών για να εξασφαλιστεί η ολοκληρωμένη αξιολόγηση του κάθε στρώματος.

Στο Κεφάλαιο 1 παρουσιάζεται μια επισκόπηση της τεχνολογίας ηλιακών κυττάρων CIGS, μαζί με τα κίνητρα και τους στόχους αυτής της διδακτορικής διατριβής. Στο κεφάλαιο 2 παρουσιάζεται η θεωρία του φωτοβολταϊκού φαινομένου. Στο Κεφάλαιο 3 περιγράφονται οι τεχνικές που χρησιμοποιήθηκαν για την ανάπτυξη και χαρακτηρισμό των στρωμάτων και των ηλιακών κυττάρων. Το Κεφάλαιο 4 ασχολείται με τη βελτιστοποίηση του στρώματος CIGS και της πολυστρωματικής δομής CIGS/Mo/SLG. Τα κύρια ευρήματα του Κεφαλαίου 4 έχουν δημοσιευθεί σε επιστημονικό άρθρο [3]. Το Κεφάλαιο 5 είναι αφιερωμένο στη βελτιστοποίηση του στρώματος CdS και της δομής CdS/CIGS/Mo/SLG. Τα κύρια αποτελέσματα του Κεφαλαίου 5 έχουν δημοσιευθεί σε επιστημονικό άρθρο [4]. Το Κεφάλαιο 6 περιλαμβάνει τη βελτιστοποίηση των στρωμάτων ZnO και ZnO:Al και των πολυστρωματικών δομών ZnO/CdS/CIGS/Mo/SLG και ZnO:Al/ZnO/CdS/CIGS/Mo/SLG. Οι βέλτιστες παράμετροι εναπόθεσης, που έχουν προκύψει από κάθε κεφάλαιο, έχουν χρησιμοποιηθεί για την κατασκευή των ηλιακών κυττάρων CIGS με PLD σε μια συνεχόμενη και διαδοχική εναπόθεση των CIGS, CdS, ZnO και ZnO:Al σε υποστρώματα SLG επικαλυμμένα με Mo. Το Κεφάλαιο 7 ασχολείται με την κατασκευή και τη βελτιστοποίηση αυτών των ηλιακών κυττάρων CIGS με PLD. Στο Κεφάλαιο 8 παρουσιάζεται μια σύνοψή των κύριων αποτελεσμάτων του κάθε κεφαλαίου και τέλος, το Κεφάλαιο 9 αναφέρει τις μελλοντικές δράσεις για τη βελτιστοποίηση της απόδοσης των ηλιακών κυττάρων CIGS.

CHRISTIANA NICOLAOU

Abstract

The need for environmentally friendly energy sources seems to be imperative as the limited availability of fossil fuels and the detrimental effects of greenhouse gases on the environment are becoming apparent. Harvesting solar energy by direct conversion of sunlight to electricity using the photovoltaic (PV) technology is emerging as a leading contender for next-generation green power production. Over the past two decades, there has been considerable effort in advancing thin film, "second-generation" technologies that do not require the use of thick, rigid, and expensive crystalline Si wafer substrates. Thin-film solar cells have attracted considerable interest due to high potential conversion efficiencies, high radiation resistance, weight reduction, and space savings. In particular, thin-film solar cells based on the chalcopyrite compound $Cu(In,Ga)Se_2$ (CIGS) have shown increased efficiencies, with a steeper increase since 2014. Record efficiencies reaching up to 23.35% have been reported by Solar Frontier in 2019 [1].

The CIGS cell consists of several layers of different materials and the cell efficiency is highly affected by each layer, as well as the interaction between them. A typical CIGS solar cell with laboratory efficiency over 20% has the following configuration: soda-lime glass as substrate, sputtered Mo as back contact, multi-stage co-evaporated CIGS as p-type absorber, chemical-bath-deposited CdS as n-type buffer layer, sputtered i-ZnO/ZnO:Al bilayer as transparent window, evaporated Ni/Al grid, and evaporated antireflective MgF_2 coating [2].

Currently, multiple deposition techniques (thermal evaporation, sputtering, chemical bath deposition, selenization) and high processing temperatures (higher than 500°C for the highest efficiency CIGS films) are being used to grow the different layers in the stack, which makes the fabrication process time consuming and expensive. Therefore, identifying a single growth method for the fabrication of the functional part of the CIGS cell, which will reduce the fabrication time and cost, is highly desirable. This PhD thesis demonstrates the utilization of pulsed laser deposition in a novel sequential process for the fabrication of the multi-layer structure described above. In this work, the preparation of the functional part of the CIGS solar cell (CIGS/CdS/i-ZnO/ZnO:Al) was carried out by using PLD in one growth sequence and at temperatures lower than 300 °C. While several different growth procedures have been exploited for each constituent layer in developing CIGS solar cells with efficiencies in the range of 14-22%, up to now, no published report exists of using PLD for fabricating a CIGS cell in its entirety. Thus, this work constitutes an innovative application of PLD to the fabrication of thin-film CIGS solar cells.

In this work, a systematic investigation of the individual layers and the interfaces between the dissimilar materials has been carried out to optimize the properties of the multi-layer structure. Each of the chapters 4,5 and 6 is dedicated to the optimization of each layer of the stack, starting from depositing each layer on bare SLG substrates to understand the impact of the PLD deposition parameters on the properties of the layer. The optimization of each layer with its adjacent layers is

CHRISTIANA NICOLAOU

then performed through a parametric investigation of the deposition temperature of the corresponding layer on the multi-layer structure that each chapter deals with. The properties of the individual layers and their interfaces were examined in detail using a variety of techniques to ensure the comprehensive assessment of each layer.

An overview of CIGS solar cell technology is presented in Chapter 1, along with the motivation and objectives of this PhD thesis. Chapter 2 presents the theory of the photovoltaic effect. Chapter 3 describes the techniques used to grow and characterize the layers and solar cells. Chapter 4 deals with the optimization of the CIGS layer and the CIGS/Mo/SLG multi-layer structure. The main findings of Chapter 4 are reported in a scientific publication [3]. Chapter 5 is dedicated to the optimization of the CdS layer and the CdS/CIGS/Mo/SLG stack. The results of Chapter 5 are reported in a scientific publication [4]. Chapter 6 involves the optimization of the ZnO and ZnO:Al layers and the ZnO/CdS/CIGS/Mo/SLG and ZnO:Al/ZnO/CdS/CIGS/Mo/SLG multi-layer structures. The optimum deposition parameters, which have been derived from the work reported in each chapter, have been used to fabricate the PLD-grown CIGS solar cells in a sequential deposition of CIGS, CdS, ZnO and ZnO:Al on Mo-coated SLG substrates. Chapter 7 deals with the fabrication and optimization of the PLD-grown CIGS solar cells. In Chapter 8, a summary of the main results of each chapter is presented and finally, Chapter 9 refers to the future actions for the optimization of the performance of CIGS solar cells.

CHRISTIANA NICOLAOU

Acknowledgements

First, I would like to express my deepest appreciation to my supervisor Professor Ioannis Giapintzakis for his invaluable advice, continuous support and for sharing his knowledge during the course of my PhD degree. My sincere gratitude extends to Dr Stela Canulescu, Dr Dimitrios Hariskos, Professor Theodora Kyratsi, and Associate Professor Theodora Krasia-Christoforou for finding time in their busy schedule to serve as members of my doctoral examination committee.

This PhD thesis, as part of the Excellence Hubs project “SolaCe” (EXCELLENCE/1216/0232), would not have been possible without the financial support of the Cyprus Research Promotion Foundation.

I am also grateful to Dr Elli Symeou for the training on almost all the laboratory equipment I used, Dr Maria Pervolaraki for the training on pulsed laser deposition technique, Dr Cristian Mihailescu for the training on pulsed laser deposition and X-ray diffraction techniques and Mr Kypros Stylianou for the technical support.

Many thanks to the research team of “SolaCe” project; Dr Anna Zacharia for the optical measurements and analysis, Dr Andreas Delimitis for the TEM studies and Dr Vasiliki Paraskeva for the device characterization. Special thanks to my colleagues Dr Evripides Kyriakides and Dr Panagiotis Ioannou for continuing the project and taking it forward when it seemed impossible.

I would like to thank my friends and lab mates for a cherished time spent together in the lab. The countless conversations and endless laughs on the bench made this journey memorable and unique.

I’m deeply thankful to my family and especially my parents for always being there for me and providing me with the opportunities to become who I am today. Throughout my life, you've been a constant source of support and love for me.

I’m mostly grateful to my partner, Andreas, for constantly listening to me and always believing in me. This thesis would not have been possible without your love and understanding. Thank you for always supporting me to pursuit my dreams, no matter how crazy they seemed.

Lastly, I would also like to thank my dogs, Mina and Paco, for all the entertainment and emotional support and for being my special teachers in life.

CHRISTIANA NICOLAOU

Dedicated to my parents Eleni and Georgios,

For their support at every step of my life.

CHRISTIANA NICOLAOU

List of publications

1. **E. Kyriakides, P. S. Ioannou, C. Nicolaou, V. Paraskeva, M. Hadjipanayi, P. Papagiorgis, G. E. Georghiou, G. Itskos, and J. Giapintzakis, "Investigation of the aptness of pulsed laser deposition for the sequential fabrication of Cu(In,Ga)Se$_2$-based thin-film solar cells," Solar Energy Materials and Solar Cells, *under review*.**

2. E. Symeou, M. Karyou, A. Delimitis, M. Constantinou, G. Constantinides, C. Nicolaou, I. Giapintzakis, and T. Kyratsi, "Preparation of highly efficient thermoelectric Bi-doped Mg2Si0. 55-xSn0. 4Gex (x= 0 and 0.05) materials with a scalable mechanical alloying method," Journal of Physics and Chemistry of Solids, vol. 161, pp. 110472, 2022. https://doi.org/10.1016/j.jpcs.2021.110472.

3. **C. Nicolaou, A. Zacharia, A. Delimitis, G. Itskos, and J. Giapintzakis, "Single-step growth of high quality CIGS/CdS heterojunctions using pulsed laser deposition," Applied Surface Science, vol. 511, pp. 145547, 2020. https://doi.org/10.1016/j.apsusc.2020.145547.**

4. **A. Zacharia, C. Nicolaou, J. Giapintzakis, and G. Itskos, "Luminescence properties of pulsed laser deposited CuInxGa1− xSe2 films," Journal of Physics Communications, vol. 4, no. 4, pp. 045001, 2020. https://doi.org/10.1088/2399-6528/ab8267.**

5. E. Symeou, C. Nicolaou, T. Kyratsi, and J. Giapintzakis, "Enhanced thermoelectric properties in vacuum-annealed Bi0. 5Sb1. 5Te3 thin films fabricated using pulsed laser deposition," Journal of Applied Physics, vol. 125, no. 21, pp. 215308, 2019. https://doi.org/10.1063/1.5082995.

6. G. Mesaritis, E. Symeou, A. Delimitis, S. Oikonomidis, M. Jaegle, K. Tarantik, C. Nicolaou, and T. Kyratsi, "Recycling Si-kerf from photovoltaics: A very promising route to thermoelectrics," Journal of Alloys and Compounds, vol. 775, pp. 1036-1043, 2019. https://doi.org/10.1016/j.jallcom.2018.10.050.

7. E. Symeou, C. Nicolaou, A. Delimitis, J. Androulakis, T. Kyratsi, and J. Giapintzakis, "High thermoelectric performance of Bi2-xSbxTe3 bulk alloys prepared from non-nanostructured starting powders," Journal of Solid State Chemistry, vol. 270, pp. 388-397, 2019. https://doi.org/10.1016/j.jssc.2018.11.037.

8. C. M. Orfanidou, P. S. Ioannou, E. Kyriakides, C. Nicolaou, C. N. Mihailescu, V. S. Nguyen, V. H. Mai, O. Schneegans, and J. Giapintzakis, "Stoichiometry and volume dependent transport in lithium ion memristive devices," AIP Advances, vol. 8, no. 11, pp. 115211, 2018. https://doi.org/10.1063/1.5051568.

CHRISTIANA NICOLAOU

9. **C. Nicolaou, A. Zacharia, G. Itskos, and J. Giapintzakis, "Influence of process parameters on the properties of pulsed laser deposited CuIn0. 7Ga0. 3Se2 thin films," Solar Energy, vol. 174, pp. 793-802, 2018. https://doi.org/10.1016/j.solener.2018.09.027.**

(Publications in bold represent the main findings of this PhD thesis)

CHRISTIANA NICOLAOU

List of conference presentations

1. European Materials Research Society (EMRS), Spring meeting, May 2019, Nice, France – Oral presentation: “Pulsed laser deposition of $CdS/CuIn_{0.7}Ga_{0.3}Se_2/Mo$ multi-layer structure for thin film solar cells”.

2. XXXIII Panhellenic Conference on Solid State Physics and Materials Science, September 2018, Nicosia, Cyprus – Poster Presentation: “Investigation of the growth of $CdS/CuIn_{0.7}Ga_{0.3}Se_2/Mo$ multi-layer structure on solar-lime glass using Pulsed Lased Deposition”.

3. International Conference on Modern Materials and Technologies (CIMTEC), 8th Forum on New Materials, June 2018, Perugia, Italy – Oral Presentation: “Optimization of pulsed laser deposition parameters for the growth of high-quality $CuIn_{1-x}Ga_xSe_2$ thin films”.

4. European Materials Research Society (EMRS), Fall meeting, September 2017, Warsaw, Poland – Oral presentation: “$Cu(In,Ga)Se_2$ thin films grown on soda-lime glass substrates by pulsed laser deposition”.

5. European Materials Research Society (EMRS), Spring meeting, May 2017, Strasbourg, France – Poster presentation: “Characterization of $Cu(In,Ga)Se_2$ thin films grown on soda-lime glass substrates by pulsed laser deposition”.

CHRISTIANA NICOLAOU

Table of contents

Validation page i

Declaration of Doctoral Candidate ii

Περίληψη iii

Abstract v

Acknowledgements vii

Dedication viii

List of publications ix

List of conference presentations xi

Table of contents xii

List of figures xvi

List of tables xxv

Chapter 1 - Introduction 1

1.1 The energy problem and the role of photovoltaics 1

1.2 CIGS thin film solar cells 2

1.2.1 Introduction 2

1.2.2 State of the art 3

1.3 Motivation, objectives and thesis overview 5

Chapter 2 – Theoretical background 9

2.1 Introduction 9

2.2 The photovoltaic effect 9

2.2.1 pn-junction at equilibrium 10

2.2.2 Forward and reverse biased junctions 12

2.3 pn-junction under illumination 17

2.4 Solar cell in an electrical circuit 20

2.5 Losses in a solar cell 23

2.6 Heterojunction solar cells 29

Chapter 3 – Experimental methods 32

3.1 Deposition methods 32

3.1.1 Pulsed Laser Deposition (PLD) 32

3.1.2 Magnetron Sputtering 35

3.1.3 Thermal Evaporation 37

3.2 Film characterization 38

3.2.1 X-ray Diffraction (XRD) 38

3.2.2 Scanning Electron Microscopy (SEM) 40

3.2.3 Energy Dispersive Spectroscopy (EDS) 41

3.2.4 Atomic Force Microscopy (AFM) 42

CHRISTIANA NICOLAOU

3.2.5 Adhesion test 43
3.3 Electrical measurements 44
3.3.1 Van der Pauw (VDP) method 44
3.3.2 Hall effect measurement 45
3.3.3 Dark current-voltage (IV) measurement 47
3.4 Experimental methods provided by our collaborators 48
3.4.1 Transmission electron microscope (TEM) 48
3.4.2 Optical characterization 49
3.4.3 Device performance 52
Chapter 4 – Optimization of the CIGS layer 54
4.1 CIGS on SLG 56
4.1.1. Materials and experimental methods 56
4.1.2. Results and discussion 57
4.1.2.1 Impact of Laser Fluence 57
4.1.2.2 Impact of Background pressure 61
4.1.2.3 Impact of Substrate Temperature 64
4.1.2.4 Impact of other deposition parameters 73
4.1.3 Conclusions 76
4.2 CIGS on Mo/SLG 77
4.2.1. Materials and experimental methods 77
4.2.2 Results and discussion 78
4.2.2.1 Impact of CIGS deposition temperature 78
4.2.3 Conclusions 84
Chapter 5 – Optimization of the CdS layer 86
5.1 CdS on SLG 87
5.1.1 Materials and experimental methods 87
5.1.2 Results and Discussion 89
5.1.2.1 Impact of laser fluence 89
5.1.2.2. Impact of deposition temperature 92
5.1.3 Conclusions 96
5.2 CdS on CIGS/Mo/SLG 97
5.2.1 Materials and experimental methods 97
5.2.2 Results and discussion 98
5.2.2.1 Impact of CdS deposition temperature 98
5.2.3 Conclusions 105
Chapter 6 – Optimization of the ZnO and ZnO:Al layers 106
6.1 ZnO on SLG 108
6.1.1 Materials and experimental methods 108

CHRISTIANA NICOLAOU

6.1.2 Results and discussion 108
6.1.2.1 Impact of laser fluence 108
6.1.2.2 Impact of deposition temperature 110
6.1.3 Conclusions 112
6.2 ZnO on CdS/CIGS/Mo/SLG 112
6.2.1 Materials and experimental methods 112
6.2.2 Results and discussion 113
6.2.2.1 Impact of ZnO deposition temperature 113
6.2.3 Conclusions 116
6.3 ZnO:Al on SLG 117
6.3.1 Materials and experimental methods 117
6.3.2 Results and discussion 118
6.3.3 Conclusions 120
6.4 ZnO:Al on ZnO/CdS/CIGS/Mo/SLG 120
6.4.1 Materials and experimental methods 120
6.4.2 Results and discussion 121
6.4.2.1 Impact of ZnO:Al deposition temperature 121
6.4.3 Conclusions 129
Chapter 7 – Fabrication of CIGS-based solar cells using PLD 131
7.1 One-step PLD-grown CIGS solar cells 132
7.1.1 Materials and experimental methods 132
7.1.2 Results and discussion 134
7.2 Elimination of particulates on the CIGS layer 139
7.2.1 Materials and experimental methods 141
7.2.2 Results and discussion 142
7.3 One-step SMPLD-grown CIGS solar cells 150
7.3.1 Materials and experimental methods 150
7.3.2. Results and discussion 150
7.4 Conclusions 155
Chapter 8 – Conclusions 156
8.1 Optimization of the CIGS layer on SLG 156
8.2 Optimization of the CIGS/Mo/SLG multi-layer structure 157
8.3 Optimization of the CdS layer on SLG 158
8.4 Optimization of the CdS/CIGS/Mo/SLG multi-layer structure 158
8.5 Optimization of the ZnO layer on SLG 159
8.6 Optimization of the ZnO/CdS/CIGS/Mo/SLG multi-layer structure 160
8.7 Optimization of the ZnO:Al layer on SLG 160

CHRISTIANA NICOLAOU

8.8 Optimization of the ZnO:Al/ZnO/CdS/CIGS/Mo/SLG multi-layer structure 161
8.9 Fabrication and optimization of CIGS-based solar cells 162
Chapter 9 – Future work **164**
Bibliography **166**
Appendix A - Optimization of the pattern of the Al grid **191**
Appendix B – Investigation of the geometrical parameters of the cone-shaped shadow masks **196**

CHRISTIANA NICOLAOU

List of figures

Figure 1.1 Schematic representation of the multi-layer structure of CIGS solar cell. 3

Figure 2.1 (a) simplified geometry of a pn-junction and (b) doping profiles of p and n regions of an ideal pn-junction. 10

Figure 2.2 (a) The space charge region, the electric field and the forces acting on the carriers and (b) particle and current flow at the junction. 11

Figure 2.3 (a) electric potential through the space charge region and (b) energy band diagram of the pn-junction in thermal equilibrium. 12

Figure 2.4 The electric potential barrier of a pn-junction (a) at equilibrium, (b) under reverse bias and (c) under forward bias. 13

Figure 2.5 pn-junction (a) at equilibrium, (b) under forward and (c) under reverse bias; effects on depletion region width, electric field, and energy band diagram. 14

Figure 2.6 Particle and current flow at the pn-junction (a) in equilibrium, (b) under reverse bias and (c) under forward bias. 15

Figure 2.7 IV characteristic curve of an ideal pn-junction. 17

Figure 2.8 Illumination of a pn-junction in an electrical circuit. 17

Figure 2.9 IV characteristic curve of an illuminated junction. 18

Figure 2.10 Energy band diagrams of a junction (a) at equilibrium and (b) under illumination in an open circuit. 19

Figure 2.11 Solar cell in a simple electrical circuit; solar energy converts to electrical energy at the load resistance. 20

Figure 2.12 Photon flux density for the air mass 1.5 spectrum (black curve), external quantum efficiency of a CdTe solar cell (red curve), and the short-circuit current density (area under blue curve). 22

Figure 2.13 IV characteristic (green) and output power (blue) curves of an illuminated solar cell. 22

Figure 2.14 Power conversion efficiency as a function of semiconductor band gap. Asterisks show the best confirmed solar cell efficiencies under AM 1.5 illumination. 24

Figure 2.15 Solar cell efficiency as function of temperature for various semiconductors. 25

Figure 2.16 Carrier mobility of n-type silicon doped at two different donor concentrations as function of the operation temperature. 26

Figure 2.17 Carrier concentration as function of temperature for silicon doped with 10^{15} donors/cm^3. 27

Figure 2.18 Equivalent electrical circuit of a solar cell with parasitic resistances. 28

Figure 2.19 Effect of (a) increasing series resistance and (b) decreasing shunt resistance in the IV curve of a solar cell. The area of the maximum power rectangle is reduced 28

CHRISTIANA NICOLAOU

compared to Isc x Voc. In each case, the outer curve corresponds to (a) Rs = 0 and (b) Rsh = ∞.
Figure 2.20 The energy band diagram of a pn heterojunction in thermal equilibrium. 29
Figure 2.21 The structure of a typical CIGS solar cell taken by SEM in a cross-section configuration. 30
Figure 2.22 The energy band diagram of a CIGS solar cell. 31
Figure 3.1 Schematic diagram of a pulsed laser deposition system. 32
Figure 3.2 Picture of our PLD system. 35
Figure 3.3 Schematic representation of the sputtering process. 36
Figure 3.4 Schematic of a typical thermal evaporation system. 37
Figure 3.5 Bragg's law. 39
Figure 3.6 Principal geometry of (a) θ/2θ and (b) grazing incidence XRD measurements. 39
Figure 3.7 Schematic diagram of SEM apparatus. 41
Figure 3.8 Schematic diagram of an AFM apparatus. 43
Figure 3.9 The four-probe electrical configuration of van der Pauw measurement for an arbitrarily shaped sample of uniform thickness. 44
Figure 3.10 (a) Schematic demonstration of the Hall effect of a material with negative charge carriers and (b) Electrical configuration of the Hall effect measurement. 46
Figure 3.11 Dark IV setup with two-probe configuration. 47
Figure 3.12 Schematic diagram of a typical TEM apparatus. 48
Figure 3.13 Schematic diagram of a typical experimental to measure optical density. 50
Figure 3.14 Schematic diagram of a photoluminescence experimental setup. 51
Figure 3.15 Electric circuit of the illuminated IV measurement of a solar cell. 52
Figure 4.1 Compositional ratios of CIGS thin films deposited on SLG substrates at different fluences ranging from 0.4 to 1.4 J/cm^2. Dashed lines indicate the ratios of a stoichiometric film, being CGI=Cu/(Ga+In)=1, GGI=Ga/(Ga+In)=0.3, IGI=In/(Ga+In)=0.7 and Se/M=Se/(Cu+Ga+In)=1. Stoichiometric films are obtained using fluence of 0.8J/cm^2 and higher. 59
Figure 4.2 XRD patterns of CIGS thin films deposited on SLG substrates at (a) 0.4, (b) 0.6, (c) 0.8, (d) 1.0, (e) 1.2 and (f) 1.4 J/cm^2. The bottom plot shows the XRD pattern of $CuIn_{0.7}Ga_{0.3}Se_2$ according to JCPDS 35-1102. A minor secondary phase of $Cu_{2-x}Se$, indicated by the arrows, appears in films grown at fluences higher than 0.6 J/cm^2. 59
Figure 4.3 (a) Surface roughness of CIGS thin films deposited on SLG substrates at different fluences ranging from 0.4 to 1.4 J/cm^2. (b), (c), (d) SEM images of CIGS thin films deposited on SLG substrates at fluence of 0.4, 1.0 and 1.4 J/cm^2, respectively. The surface roughness of the films increases linearly as the fluence becomes higher, due to the increasing density and size of particulates on the film surface. 60

CHRISTIANA NICOLAOU

Figure 4.4 Compositional ratios of CIGS thin films deposited on SLG substrates at different Ar pressures. Dashed lines indicate the ratios of a stoichiometric film, being CGI=Cu/(Ga+In)=1, GGI=Ga/(Ga+In)=0.3, IGI=In/(Ga+In)=0.7 and Se/M=Se/(Cu+Ga+In)=1. Stoichiometric films are obtained using Ar pressure of 0.01mbar and higher. 62

Figure 4.5 XRD patterns of CIGS thin films deposited on SLG substrates at various Ar pressures. The bottom plot shows the XRD pattern of $CuIn_{0.7}Ga_{0.3}Se_2$ according to JCPDS 35-1102. A minor secondary phase of $Cu_{2-x}Se$, indicated by the arrows, appears in all films. 63

Figure 4.6 (a) Surface roughness of CIGS thin films deposited on SLG substrates at various Ar pressures. (b), (c), (d) SEM images of CIGS thin films deposited on SLG substrates at Ar pressure of $7x10^{-4}$, $1x10^{-1}$ and $5x10^{-2}$ mbar, respectively. The arrows in (b) indicate regions with pinholes on the film's surface. The surface roughness of the films increases abruptly as the Ar pressure becomes higher, due to the increasing areal density and size of particulates on the film surface. 64

Figure 4.7 Compositional ratios of CIGS thin films deposited on SLG substrates at various substrate temperatures. Dashed lines indicate the ratios of a stoichiometric film, being CGI=Cu/(Ga+In)=1, GGI=Ga/(Ga+In)=0.3, IGI=In/(Ga+In)=0.7 and Se/M=Se/(Cu+Ga+In)=1. All films are stoichiometric in respect to the target stoichiometry. 65

Figure 4.8 XRD patterns, 10° - 90° and 20° - 30° (inset), of CIGS thin films deposited on SLG substrates at different substrate temperatures. The bottom plot shows the XRD pattern of $CuIn_{0.7}Ga_{0.3}Se_2$ (JCPDS 35-1102). The secondary phase of $Cu_{2-x}Se$ is indicated by the arrows. The $Cu_{2-x}Se$ peak gradually fades as the deposition temperature increases. The (112) peak shifts towards the stoichiometric bulk value of chalcopyrite CIGS. 66

Figure 4.9 (a) Room temperature electrical resistivity and carrier concentration and (b) Hall mobility and FWHM of (112) peak of CIGS films as function of substrate temperature. As the substrate temperature increases, resistivity increases, carrier concentration decreases, crystallinity of the films is improved, and mobility is enhanced. 68

Figure 4.10 Spectral variation of the absorption coefficient of CIGS films grown at various substrate temperatures. The first derivative of the absorbance and the estimated energy gap for each film is also shown. 69

Figure 4.11 Variation of the optical band gap energy versus substrate temperature. A systematic blue shift of the band gap energy with deposition temperature is observed. 70

Figure 4.12 (a) Comparative PL spectra of films deposited at various temperatures in the range of 100 to 500 ^{0}C, (b) Normalized PL spectra of the same film series, (c) 71

CHRISTIANA NICOLAOU

Integrated PL intensity versus deposition temperature, and (d) PL linewidth (FWHM) and Stokes shift as a function of substrate temperature.

Figure 4.13 PL decays (bottom graph) measured at the three spectral regions I, II and III within the broadband luminescence (upper graph) from a CIGS film deposited at 500 ^{0}C. The multi-exponential fits (dotted lines) and calculated average PL lifetimes are also displayed. 73

Figure 4.14 Schematic diagram of two probe IV measurement of CIGS/Mo/SLG structure. 78

Figure 4.15 Compositional ratios of CIGS thin films deposited on Mo/SLG substrates at various substrate temperatures. Dashed lines indicate the ratios of a stoichiometric film, being CGI=Cu/(Ga+In)=1, GGI=Ga/(Ga+In)=0.3, IGI=In/(Ga+In)=0.7 and Se/M=Se/(Cu+Ga+In)=1. CIGS films are stoichiometric in respect to the target stoichiometry. 79

Figure 4.16 XRD patterns of CIGS thin films deposited on Mo/SLG substrates at different substrate temperatures. The bottom plots show the XRD pattern of $CuIn_{0.7}Ga_{0.3}Se_2$ (JCPDS 35-1102) and Mo (PDF 9008543). The secondary phase of $Cu_{2-x}Se$ is indicated by the arrows. 80

Figure 4.17 (a) HRTEM image and (b) SAD pattern from the Mo/CIGS interfacial region. 82

Figure 4.18 (a) HRTEM image and (b) EDS point analysis spectrum from the CIGS layer. 83

Figure 4.19 Distinct $Cu_{2-x}Se$ crystals along with CIGS ones at the CIGS layer. 83

Figure 4.20 Two probe IV curve of CIGS(300°C)/Mo/SLG structure at room temperature. 84

Figure 5.1 Schematic deposition structures: (a) CdS on SLG and (b) sequential deposition of CIGS and CdS on Mo-coated SLG. 88

Figure 5.2 Compositional ratio of CdS thin films deposited on SLG substrates at different fluences, ranging from 0.9 to 1.6 J/cm^2. Dashed line indicates the ratio of a stoichiometric film, being S/Cd=1. Films change from sulfur-rich to sulfur-poor films, as fluence increases. At 1.1 J/cm^2 the films are almost stoichiometric. 90

Figure 5.3 XRD patterns of CdS thin films deposited on SLG substrates from 0.9 to 1.6 J/cm^2. The bottom plot shows the linear XRD pattern of CdS hexagonal phase according to JCPDS 96-900-8863. Polycrystalline films with no secondary phase and preferred orientation along (002) and (103) planes are obtained. 91

Figure 5.4 Crystallite size of CdS thin films deposited on SLG substrates as function of laser fluence and S/Cd compositional ratio. The crystallinity of the films increases as fluence increases. Sulfur-rich films have lower crystallite sizes while sulfur-poor films exhibit higher crystallite sizes. 91

CHRISTIANA NICOLAOU

Figure 5.5 Compositional ratio of CdS thin films deposited on SLG substrates at deposition temperatures, from room temperature up to 400ºC. Dashed line indicates the ratio of a stoichiometric film, being S/Cd=1. Films change from sulfur-poor to nearly stoichiometric films as the deposition temperature increases. 92

Figure 5.6 XRD patterns of CdS thin films deposited on SLG substrates at different substrate temperatures ranging from room temperature up to 400ºC. The bottom plot shows the XRD pattern of CdS hexagonal phase according to JCPDS 96-900-8863. Polycrystalline films with no secondary phase and preferred orientation along (002) and (103) planes are obtained. 93

Figure 5.7 Crystallite size of CdS thin films deposited on SLG substrates as function of deposition temperature and S/Cd compositional ratio. The crystallinity of the films increases as deposition temperature increases. Sulfur-poor films have lower crystallite sizes while stoichiometric films exhibit higher crystallite sizes. 94

Figure 5.8 (a) Variation of the optical band gap energy versus deposition temperature (b) The steady-state absorption for the CdS films grown at various deposition temperatures. The first derivative of the absorbance and the estimated energy gap for each film is also shown. 95

Figure 5.9 (a) Comparative PL spectra of films deposited at various temperatures in the range of 100 – 400 °C, (b) Integrated PL intensity versus deposition temperature, (c) PL decays measured at the band-edge PL peak from CdS films deposited at various temperatures and (d) Average PL Lifetime versus deposition temperature. 96

Figure 5.10 (a) Backscattered electron SEM image of CdS/CIGS/Mo/SLG multi-layer structure, (b) & (c) EDS point analysis spectra from the CIGS and CdS layers, respectively. The CdS layer is predominately distinguished by its Cd L peak (blue coloured), located at 3.13 keV. 98

Figure 5.11 Compositional ratio of CdS thin films deposited CIGS/Mo/SLG at various CdS deposition temperatures, from room temperature up to 400ºC. Dashed line indicates the ratio of a stoichiometric CdS film, being S/Cd=1. The CdS layer is stoichiometric at CdS deposition temperature of 300ºC. 99

Figure 5.12 XRD patterns of CdS/CIGS/Mo/SLG multi-layer structures as function of CdS deposition temperature, from room temperature up to 400ºC. The bottom plots show the XRD pattern of CdS hexagonal phase (JCPDS 96-900-8863), $CuIn_{0.7}Ga_{0.3}Se_2$ (JCPDS 35-1102), Mo (PDF 9008543) and secondary phases of $CuInS_2$ (JCPDS 65-1572) and Cu_2Se (JCPDS 04-001-9933). 100

Figure 5.13 (a) Dark IV curves for the CdS/CIGS/Mo structures grown at various CdS deposition temperature, from room temperature up to 400ºC. The knee voltage at forward bias decreases as CdS deposition temperature increases (b) Energy band 101

CHRISTIANA NICOLAOU

diagram of Mo/CIGS/CdS structure indicating the conduction band offset at CIGS/CdS interface.

Figure 5.14 (a) Ideality factor, (b) leakage current, (c) shunt and (d) series resistance of the CdS/CIGS/Mo structures as function of CdS deposition temperature, from room temperature up to 400ºC. The CdS/CIGS/Mo structures grown at CdS deposition temperature of 200 and 300ºC exhibit low values of ideality factor and leakage current, low series and high shunt resistances. 103

Figure 6.1 Schematic deposition structures: (a) ZnO on SLG and (b) ZnO/CdS/CIGS/Mo/SLG structure fabricated by the sequential deposition of CIGS, CdS and ZnO on Mo-coated SLG. 108

Figure 6.2 (a) XRD patterns and (b) FWHM and crystallite size of ZnO thin films deposited on SLG substrates at fluence of 1.0 to 1.6 J/cm^2. The bottom plot of (a) shows the linear XRD pattern of ZnO hexagonal phase according to PDF card 9004178. 109

Figure 6.3 (a) Thickness and (b) surface roughness of ZnO thin films deposited on SLG substrates as function of fluence from 1.0 to 1.6 J/cm^2. 110

Figure 6.4 (a) XRD patterns, (b) crystallite size and (c) FWHM of ZnO thin films deposited on SLG substrates as function of deposition temperature. The bottom plot of (a) shows the linear XRD pattern of ZnO hexagonal phase according to PDF card 9004178. 111

Figure 6.5 Spectral variation of the (a) absorption coefficient and (b) transmissivity of ZnO films grown at various substrate temperatures. (c)-(f) Tauc plots of the undoped ZnO films and (g) the doped ZnO:Al film. The estimated energy gap for each film is also shown. 111

Figure 6.6 XRD patterns of ZnO/CdS/CIGS/Mo/SLG multi-layer structures with different ZnO deposition temperatures. The bottom plots show the XRD pattern of ZnO hexagonal phase (PDF 9004178), CdS hexagonal phase (JCPDS 96-900-8863), $CuIn_{0.7}Ga_{0.3}Se_2$ (JCPDS 35-1102) and Mo (PDF 9008543). Secondary phase of $Cu_{2-x}Se$ (JCPDS 37-1187) is present in CIGS layer. 113

Figure 6.7 IV curves of ZnO/CdS/CIGS/Mo/SLG structures measured by the 2-probe configuration for different deposition temperatures of ZnO layer. CIGS and CdS layers have been deposited at 300ºC and ZnO at (a) 300ºC, (b) 200ºC, (c) 100ºC and (d) 50ºC. 115

Figure 6.8 Schematic deposition structures: (a) ZnO:Al on SLG and (b) ZnO:Al/ZnO/CdS/CIGS/Mo/SLG structure fabricated by the sequential deposition of CIGS, CdS, ZnO and ZnO:Al on Mo-coated SLG. 117

Figure 6.9 XRD patterns of ZnO:Al and ZnO thin films deposited on SLG substrates at fluence of 1.2 J/cm^2 and at room temperature. The bottom plot shows the XRD pattern of ZnO hexagonal phase according to PDF card 9004178. 119

CHRISTIANA NICOLAOU

Figure 6.10 XRD pattern of ZnO:Al/ZnO/CdS/CIGS/Mo/SLG multi-layer structure with the ZnO:Al layer deposited at 40°C. The bottom plots show the XRD pattern of ZnO hexagonal phase (PDF 9004178), CdS hexagonal phase (JCPDS 96-900-8863), $CuIn_{0.7}Ga_{0.3}Se_2$ (JCPDS 35-1102) and Mo (PDF 9008543). Secondary phase of Cu_2Se (JCPDS 04-001-9933) is present in CIGS layer. 122

Figure 6.11 XRD pattern of ZnO:Al/ZnO/CdS/CIGS/Mo/SLG multi-layer structure with the ZnO:Al layer deposited at 300°C. The bottom plots show the XRD pattern of ZnO hexagonal phase (PDF 9004178), CdS hexagonal phase (JCPDS 96-900-8863), $CuIn_{0.7}Ga_{0.3}Se_2$ (JCPDS 35-1102) and Mo (PDF 9008543) and secondary phases of $CuInS_2$ (JCPDS 65-1572) and Cu_2Se (JCPDS 04-001-9933). 123

Figure 6.12 IV curves of ZnO:Al/ZnO/CdS/CIGS/Mo/SLG structures measured by the 2-probe configuration for different deposition temperatures of ZnO:Al layer. CIGS and CdS layers have been deposited at 300°C, ZnO has been deposited at 40°C and ZnO:Al at (a) 300°C, (b) 200°C, (c) 100°C and (d) 40°C. 124

Figure 6.13 Conventional TEM image of the CIGS/CdS and CdS/ZnO interfaces 127

Figure 6.14 (a) HRTEM image of the CIGS/CdS and CdS/ZnO interfaces and (b) common SAED pattern of the CIGS/CdS interfacial area. 127

Figure 6.15 EDS linescans of the CIGS/CdS/ZnO/ZnO:Al layers and their interfacial regions: (a) with cross-section SEM image at the background and (b) without cross-section SEM image at the background. 128

Figure 6.16 The upper area of the ZnO:Al – intrinsic ZnO layer. 129

Figure 7.1 The complete multi-layer structure of the CIGS solar cell along with the metallic grid. 133

Figure 7.2 XRD pattern of CdS-300 solar cell. The bottom plots show the XRD pattern of ZnO hexagonal phase (PDF 9004178), CdS hexagonal phase (JCPDS 96-900-8863), $CuIn_{0.7}Ga_{0.3}Se_2$ (JCPDS 35-1102) and Mo (PDF 9008543). Secondary phase of Cu_2Se (JCPDS 37-1187) is present in CIGS layer. 135

Figure 7.3 SEM image of (a) the upper surface of the CdS-300 solar cell with the arrows indicating the three components of the Al metal grid and (b) the upper surface of the CdS-300 solar cell in higher magnification**.** 136

Figure 7.4 2-probe dark IV curves of the CdS-100, CdS-200 and CdS-300 devices based on the SLG/Mo/CIGS/CdS/ZnO/ZnO:Al structure. 137

Figure 7.5 Illuminated JV curve and major electrical parameters of a CdS-300 solar cell. 138

Figure 7.6 (a) Schematic representation of the shadow masked PLD used for the deposition of CIGS layer and (b) Photo image of the PLD chamber during the deposition of CIGS layer with the cone shaped mask. 140

CHRISTIANA NICOLAOU

Figure 7.7 (a) Number of particulates as function of particulate area at various lateral distances along a line through the center of the SMPLD-CIGS sample and at the center of the PLD-CIGS, (b) SEM images of SMPLD-CIGS sample at various lateral distances. The number and size of particulates increases along the lateral distance away from the center of SMPLD-CIGS film. The particulates of SMPLD-CIGS film are substantially reduced in number and size compared to the particulates of PLD-CIGS film. 143

Figure 7.8 Compositional ratios of PLD-CIGS and SMPLD-CIGS film obtained at various lateral distances along a line through the deposition center. Dashed lines indicate the ratios of a stoichiometric film, being CGI=Cu/(Ga+In)=1, GGI=Ga/(Ga+In)=0.3, IGI=In/(Ga+In)=0.7 and Se/M=Se/(Cu+Ga+In)=1. The SMPLD-CIGS film is significantly Cu-deficient and Se-rich across the surface. 144

Figure 7.9 Compositional ratios of SMPLD-CIGS films with different number of pulses and PLD-CIGS film with 15000 pulses. Dashed lines indicate the ratios of a stoichiometric film, being CGI=Cu/(Ga+In)=1, GGI=Ga/(Ga+In)=0.3, IGI=In/(Ga+In)=0.7 and Se/M=Se/(Cu+Ga+In)=1. 145

Figure 7.10 XRD patterns of SMPLD-CIGS films deposited on SLG substrates at different pulses and PLD-CIGS deposited at 15000 pulses. The bottom plot shows the XRD pattern of CuIn0.7Ga0.3Se2 according to JCPDS 35-1102. A minor secondary phase of Cu_2Se appears in all films. 146

Figure 7.11 (a) Surface roughness of SMPLD-CIGS thin films deposited on SLG substrates with different number of pulses and a PLD-CIGS film with 15000 pulses, (b) 3-D images of PLD-CIGS surface of 15000 pulses and SMPLD-CIGS surface of 90000 pulses. SMPLD-CIGS films have a surface roughness that is one order of magnitude lower than that of PLD-CIGS. 147

Figure 7.12 Compositional ratios of SMPLD-CIGS film deposited at 90000 pulses obtained at various positions from the center to the corner of the film. Dashed lines indicate the ratios of a stoichiometric film, being CGI=Cu/(Ga+In)=1, GGI=Ga/(Ga+In)=0.3, IGI=In/(Ga+In)=0.7 and Se/M=Se/(Cu+Ga+In)=1. 148

Figure 7.13 (a) Surface roughness of SMPLD-CIGS thin film deposited at 90000 pulses at various lateral distances from the deposition center. Surface roughness increases as the distance from the center increases. This tendency is also illustrated by the 2-D AFM images. 149

Figure 7.14 SEM image of (a) the upper surface of SMPLD-CIGS/CdS-300 solar cell with the arrows indicating components of the Al metal grid and (b) the upper surface of SMPLD-CIGS/CdS-300 solar cell in higher magnification. 151

Figure 7.15 XRD pattern of SMPLD-CIGS/CdS-300 solar cell. The bottom plots show the XRD pattern of ZnO hexagonal phase (PDF 9004178), CdS hexagonal phase 152

CHRISTIANA NICOLAOU

(JCPDS 96-900-8863), CuIn0.7Ga0.3Se2 (JCPDS 35-1102) and Mo (PDF 9008543). Secondary phase of Cu2Se (JCPDS 37-1187) is present in CIGS layer.
Figure 7.16 Light JV curves of SMPLD-CIGS solar cells with different CdS pulses (SMPLD-CIGS/CdS-300, SMPLD-CIGS/CdS-600, SMPLD-CIGS/CdS-800) and PLD-CIGS solar cell. 153
Figure A.1 Schematic representation of the design of the metallic grid illustrating the three components (central pad, central busbar, and fingers) and the parameters A, B, S, W_F and W_B. 191
Figure B.1 Geometrical parameters and schematic representation of the various conical shadow masks used during the deposition of SMPLD-CIGS films. 196
Figure B.2 Surface roughness of SMPLD-CIGS films with different number of pulses using different SMPLD setups. 196

CHRISTIANA NICOLAOU

List of tables

Table 4.1 Summary of the main results obtained from the investigation of laser fluence. 60

Table 4.2 Summary of the main results obtained from the investigation of Ar pressure. 64

Table 4.3 Electrical properties, FWHM and crystallite size of CIGS films deposited on SLG substrates at different substrate temperatures. 68

Table 4.4 Summary of the main results obtained from the investigation of substrate temperature. 72

Table 4.5 Main results of the impact of secondary PLD deposition parameters on the properties of CIGS films. 74-5

Table 4.6 Properties of purchased Mo films deposited on SLG substrates. 78

Table 4.7 Pictures of Mo/SLG and CIGS/Mo/SLG samples prior and afterwards the application of the scotch tape test for various CIGS deposition temperatures. 80-81

Table 6.1 Diode characteristics of the best performing ZnO/CdS/CIGS/Mo and CdS/CIGS/Mo structures: ideality factor, leakage current, shunt and series resistance. 116

Table 6.2 PLD deposition parameters, thickness, roughness and energy gap of ZnO and ZnO:Al films deposited on SLG substrates. 119

Table 6.3 Planar electrical resistivity, carrier concentration and Hall mobility of ZnO:Al film deposited at 25°C on SLG substrate. 120

Table 6.4 Diode characteristics of the ZnO:Al/ZnO/CdS/CIGS/Mo/SLG device and reported values in the literature calculated by dark IV measurements. 125

Table 6.5 Pictures taken prior and afterwards the application of the scotch tape test for the ZnO:Al/ZnO/CdS/CIGS/Mo/SLG device with CIGS and CdS layers deposited at 300°C and ZnO and ZnO:Al layers deposited at 40°C. 126

Table 7.1 PLD deposition parameters for CIGS, CdS, ZnO and ZnO:Al layers for the fabrication of the solar cells. 133

Table 7.2 Deposition parameters of CIGS films prepared by the conventional (PLD-CIGS) and shadow masked (SMPLD-CIGS) PLD method. 141

Table 7.3 Main properties of the SMPLD-CIGS film deposited at 90000 pulses. 149

Table 7.4 PLD deposition parameters for SMPLD-CIGS, CdS, ZnO and ZnO:Al layers for the fabrication of the SMPLD-CIGS solar cells. 150

Table 7.5 Electrical parameters of SMPLD-CIGS solar cells with different CdS pulses (SMPLD-CIGS/CdS-300, SMPLD-CIGS/CdS-600, SMPLD-CIGS/CdS-800) and PLD-CIGS solar cell. 153

Table A.1 Values of the parameters used in the equations for the calculation of the optimum grid features and the optimum calculated features of the unit cell for finger width of 10 μm and 20 μm. 194-5

CHRISTIANA NICOLAOU

Table A.2 The optimum features of the designs used for the fabrication of the shadow masks. 195

CHRISTIANA NICOLAOU

Chapter 1 - Introduction

1.1 The energy problem and the role of photovoltaics

With the universal acknowledgement of the limited availability of fossil fuels and the detrimental effects of greenhouse gases on the environment, the need for environmentally friendly energy sources seems to be imperative. More specifically, the European Commission has initiated the Renewable Energy Directive, which establishes an overall policy for the production and promotion of energy from renewable sources in the European Union (EU). The directive has set a common target – currently set at 32% and recently proposed to be increased to 45% – for the amount of renewable energy in the EU's overall energy consumption by 2030 [5]. On a global level, international treaties on climate change, such as the Kyoto protocol and more recently the Paris agreement, commit their parties to significantly reduce their greenhouse gas emissions [6, 7]. These driving forces have steered the scientific community, in recent years, to direct its efforts towards renewable energy sources and, especially, solar energy.

Harvesting solar energy by direct conversion of sunlight to electricity using photovoltaic (PV) technology is emerging as a leading contender for next-generation green power production. Solar power is now being increasingly recognized by leading policy makers as the preferred technical solution to fight climate change, as well as a stable-priced energy source. PV cells are small, require much less maintenance and are more reliable in comparison with other alternative energy sources, like wind turbines, which are more disruptive and more prone to noise pollution. Also, some of the major solar thermal energy projects in the globe have been converted into solar PV installations due to the high cost of such projects. The installation of solar thermal plants is usually implemented in deserts because of the necessity for large areas. Having moving parts and massive arrays of mirrors raises concerns about the impact on the desert wildlife. In addition, the usage of large quantities of water in the desert is a significant problem.

Converting solar energy directly into electricity using semiconducting materials has become the current trend for green power production and PV modules based on crystalline silicon (including both large-grain polycrystalline and single-crystalline materials) represent 94% of the market [8]. These Si wafer-based "first-generation" single junction cells have a maximum theoretical conversion efficiency of ~31% under direct AM1.5 solar spectrum (limited by thermodynamic considerations - Shockley and Queisser limit [9]); however, they also have a high cost especially in the case of high-efficiency cells based on single-crystalline Si. Hence, the development of new PV technologies based on "second" and "third generation" cells is important in making the electricity production cost of solar cells commercially competitive by reducing the cell fabrication costs and elevating the efficiencies approaching the Shockley and Queisser limit.

CHRISTIANA NICOLAOU

1.2 CIGS thin film solar cells

1.2.1 Introduction

Over the past two decades, there has been devoted effort in advancing thin-film, "second-generation" technologies that do not require the use of thick, rigid, and expensive crystalline Si wafer substrates. Thin-film solar cells have attracted considerable interest due to high potential conversion efficiencies, high radiation resistance, weight reduction, and space savings. In particular, thin-film solar cells based on the chalcopyrite compound $Cu(In,Ga)Se_2$ (CIGS) have shown promising laboratory efficiencies. A tremendous enhancement in the efficiency of CIGS solar cells has been reported through the years with a steeper increase since 2014, reaching record efficiencies of 23.35% achieved by SolarFrontier in 2019 [10] and 22.6% by Jackson et al. in laboratory conditions in 2016 [11], exceeding that of multi-crystalline Si-based cells. The recent improvement in cell efficiency paves the way for progress in module efficiencies up to 18% over the next few years [12]. The total world-wide CIGS production capacity is about 2 GWp/a with production costs of 0.048 EUR/kWh which are already comparable to that of crystalline Si (0.051 EUR/kWh) [12]. Improved productivity by next-generation equipment and new infrastructure, combined with enhanced module efficiency - up to 18% - and reduced material costs, hold the potential of yielding a total cost of 0.25 USD/Wp at production capacities of 1000 MWp/a [12]. Fulfilling this potential is contingent on the ability to perform deposition and processing on larger substrates and accelerated production lines.

A typical CIGS solar cell (Figure 1.1) with laboratory efficiency over 20% has the following configuration: soda-lime glass (SLG) as substrate, sputtered Mo as back contact, multi-stage co-evaporated CIGS as p-type absorber, chemical-bath-deposited CdS as n-type buffer layer, sputtered i-ZnO/ZnO:Al bilayer as transparent window, Ni/Al grid, and antireflective MgF_2 coating [2]. The key feature of CIGS solar cells is their remarkable stability [13-16]. Outdoor tests at elevated temperatures have established that no light-induced degradation occurs for periods up to eight years [17]. The stability of CIGS solar cells sets CIGS technology in an advantageous position in comparison with other PV technologies, like perovskites [18, 19]. Furthermore, CIGS solar cells are considered to be the most suitable candidate for space applications due their superior radiation hardness [20, 21].

CHRISTIANA NICOLAOU

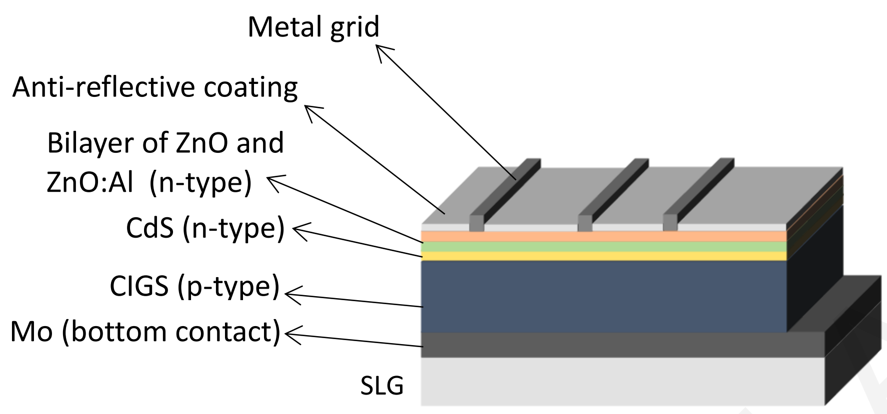

Figure 1.1 Schematic representation of the multi-layer structure of CIGS solar cell.

The CIGS cell consists of several layers of different materials and the cell efficiency is highly affected by each layer, as well as the interaction between them. A variety of methods has been used to prepare each layer of CIGS solar cells, with the most common being thermal evaporation, sputtering, chemical bath deposition (CBD), and selenization. Despite significant improvements in CIGS solar cell efficiency, several factors related to both device fabrication and cell efficiency hamper their development. The industry norm of using multiple deposition techniques and high processing temperatures (higher than 500°C for the highest efficiency CIGS films) for different layers in the stack adds time and cost to the fabrication process. The deposition methods used for each layer and the challenges of CIGS solar cells are thoroughly presented in the next section.

1.2.2 State of the art

Remarkably high efficiencies have been obtained throughout the efforts of the research community in advancing thin-film solar cells based on Cu(In,Ga)Se2 (CIGS). Currently, the record value of 22.6%. is achieved by Jackson et al. by applying a post-deposition alkali treatment on CIGS layer. This record efficiency exceeds the best-performing multi-crystalline Si-based solar cells up to this day [11]. Moreover, record efficiency of up to 16.5 % on 1.09 m^2 fully integrated CIGS thin film solar modules on glass substrate have been achieved by TSMC solar [22]. Although, the highest efficiency (22.6%) reported for CIGS solar cells has been attained on glass substrates, the use of flexible substrates offers new possibilities for the application of solar cells on flexible and uneven surfaces. Chirila et al. have developed the most efficient (18.7%) CIGS solar cell to date on flexible polymer surfaces by adjusting the band gap grading of the CIGS absorber. This breakthrough was found to be of crucial importance for reducing recombination losses and ensuring highly efficient charge carrier collection [23, 24].

CHRISTIANA NICOLAOU

A literature review of CIGS solar cells reveals various aspects that deem further investigation. Therefore, issues concerning the different parts of the CIGS solar cell structure are being addressed and hereby presented, starting with the Mo back contact and proceeding up the stack.

Focusing on the back contact, several metals, such as W, Cr, Ta, Nb, Pt, Au, Ag, Cu and Mo, have been investigated [25-27]. A Mo layer, 0.5-1 μm thick and usually deposited by magnetron sputtering [28, 29], is typically chosen for the back contact for multiple reasons. Primarily, the Mo back contact enables the diffusion of Na^+ ions from the SLG substrate into the absorber CIGS layer resulting in an improvement of the photovoltaic properties [30, 31]. Also, it has been reported that the formation of the $MoSe_2$ layer at the interface of CIGS/Mo provides a nearly ideal ohmic contact between Mo and CIGS [32-34]. On the other hand, delamination issues are typically correlated with the interface between the Mo back contact layer and the absorber CIGS layer, and specifically, with the orientation and thickness of the $MoSe_2$ interfacial layer [35, 36].

A variety of methods have been employed to deposit CIGS films. These methods belong to two general approaches. The first approach is a single-step growth process. In this process, all the constituent elements (Cu, In, Ga, Se) are being co-evaporated and deposited on a substrate heated at 400-600°C, with four different sequences (with variation in fluxes and substrate temperature over time) resulting in a cell efficiency greater than 16% [37, 38]. The second approach is a two-step process. In this process, the metals are deposited at low temperatures and then the resulting film is annealed in H_2Se atmosphere [39] or in Se vapor [40] in the range of 400-600°C. The grain microstructure of CIGS films is dictated by the deposition method used, with large grain sizes resulting in more efficient devices [41].

N-type CdS is widely used as buffer layer in CIGS solar cells because it has continuously yielded high efficiency cells, with the highest efficiency values obtained when CdS layers are grown by chemical bath deposition (CBD) [42, 43]. However, CBD is incompatible with in-line vacuum-based fabrication. The CdS contact layer also functions as a window for solar radiation. Because CdS absorbs in the blue wavelength range, it is important that this layer be thin. When the layer is too thin, however, pinholes between the transparent conducting oxide (TCO) contact, that is ZnO:Al, and the absorber CIGS layer create short circuits. In recent years, the research community has directed its efforts towards Cd-free cells in order to avoid the toxicity of Cd. The substitution of CdS buffer layer with non-toxic materials will make the production environment safer, while also making module recycling feasible. Zn-based compounds are the current promising candidates as alternatives to CdS [44-46].

The functional part of the solar cell is completed by the front contact. This layer should exhibit sufficient optical transparency and high electrical conductivity. Based on these requirements, TCOs are the most suitable candidates for use as front contacts. Today, Sn-doped In_2O_3 (ITO) and aluminum-doped ZnO (ZnO:Al) deposited by RF-sputtering are the most widely used TCOs [47, 48].

CHRISTIANA NICOLAOU

The inclusion of a thin layer between the TCO and the CdS, such as a highly-resistive transparent oxide, that is intrinsic ZnO (i-ZnO), improves the efficiency [49, 50]. The exact role of this additional layer, whether it just introduces resistance into short circuits and/or changes the interfacial energetics, is not well understood. The optimization of this interface is, therefore, a critical need [51].

The films discussed above are the necessary layers for a CIGS solar cell to operate but are not adequate to obtain high-efficiency devices. An antireflective (AR) coating is required to reduce reflection losses and thus improve the efficiency of the device. The most widely used material as AR coating in CIGS solar cells is magnesium fluoride (MgF_2). MgF_2 has two important characteristics: low refractive index and the ability of forming high quality films. The thickness of the AR coating is the key feature that must be optimized to optically enhance the performance of the device. Modeling together with experimental results can be jointly used to investigate the effect of the AR coating thickness to the performance of the cell, as Rajan et al. have realized, reporting an increase of 5% in device efficiency [52].

Finally, the goal of fabricating a solar cell is for it to be incorporated into an external circuit so that the generated current can flow through a load. Collecting the current accumulating on the transparent conductive contact in an effective way is a challenge that researchers still face. A highly conductive metal grid deposited at the front contact is a good solution to reduce the high resistive losses along the front contact. The design of the metal grid has a variety of parameters, such as grid finger height, grid finger width and grid finger spacing, which must be optimized to present a significant gain to the efficiency. The effects of the metal grid parameters have been studied through modeling and simulations and a quantitative analysis have been reported for CIGS solar cells [53] and modules [54, 55].

As discussed herein, remarkable progress has been made over the past years in the development of high efficiency CIGS solar cells, but there is potential for more improvement. The thin-film solar cell industry needs to design its own unique process equipment, integrating simplified deposition methods in an in-line sequential process with low deposition temperatures (<450 °C) to reduce manufacturing time and cost. In light of the above, a promising technique for the deposition of CIGS absorber films has to be defined in order to achieve a single-step, low-cost and high-deposition-rate growth with thickness uniformity and stoichiometry over large areas. In this study, the overarching goal is to demonstrate the suitability of PLD as a growth method to fabricate the functional part of the complicated multilayer structure of the CIGS solar cell, at temperatures lower than 450 °C. A systematic investigation has been carried out for further understanding, controlling, and optimizing the layers and interfaces between the dissimilar materials.

1.3 Motivation, objectives and thesis overview

Currently, multiple deposition techniques and high processing temperatures are being used to grow the different layers in the stack which makes the fabrication process time consuming and

CHRISTIANA NICOLAOU

expensive. Therefore, identifying a single growth method for the fabrication of the functional part of the CIGS cell, which will reduce the fabrication time and cost, is highly desirable. This PhD thesis demonstrates the utilization of pulsed laser deposition (PLD) in a novel sequential process for the fabrication of the multi-layer structure described above. **In this work, the preparation of the functional part of the CIGS solar cell (CIGS/CdS/i-ZnO/ZnO:Al) was carried out by using PLD in one growth sequence and at temperatures lower than 450 °C**. While several different growth procedures have been exploited for each constituent layer in developing CIGS solar cells with efficiencies in the range of 14-22%, up to now, no published report exists of using PLD for fabricating a CIGS cell in its entirety. Thus, this work constitutes an innovative application of PLD to the fabrication of thin-film CIGS solar cells.

PLD is considered to be an excellent lab-scale research tool, because it can produce multi-layered structures of thin films from different bulk targets without interrupting the fabrication procedure. In addition, PLD is a suitable method to fabricate small-area (1 cm^2) CIGS solar cells because of the stoichiometric transfer of materials from the target to the film [56], the lower deposition temperature (non-equilibrium process), the high deposition rates, and the reduction in pin holes in very thin layers (highly compact films). With these features, PLD offers a variety of advantages over other methods of physical vapor deposition (PVD). Moreover, PLD has recently reached the potential of large-area deposition with thickness uniformity. State-of-the-art PLD systems, that are now commercially available, enable for the deposition of high-quality thin films on various substrates, up to wafer sizes of 200 mm [57]. The thickness uniformity is achieved by the rotation of the substrate along with laser beam scanning across the target surface. The recent development on the scalability of PLD systems will enable the utilization of PLD in the fabrication of CIGS mini modules.

More specific, the high deposition rate and the stoichiometric transfer of complex materials that occurs using PLD is ideal for depositing the "thick" absorber layer of CIGS; CIGS layer thickness of ~2μm is essential for sufficient absorption. Also, high quality polycrystalline CIGS films can be obtained by PLD due to the precise control of deposition parameters which define the growth process. In regard to CdS layer, it has been recently reported that CdS films deposited by PLD are more compact and uniform than those grown by CBD and sputtering [58]. Thus, PLD may allow the realization of high quality and possibly thinner CdS layers without the creation of short circuit pinholes between the TCO and the absorber layer [8]. Concerning the ZnO layers, it is also well known that PLD is the most suitable method to grow high quality oxide thin films [59].

The primary objectives of this PhD thesis for implementing the concept described above are the following:

Objective 1: Optimization of individual layers of the CIGS solar cell and their adjacent interfaces

CHRISTIANA NICOLAOU

- Systematic investigation of PLD growth parameters of each individual layer (CIGS, CdS, intrinsic ZnO and Al-doped ZnO) along with the exploration of multi-layer stacks (CIGS/Mo, CdS/CIGS/Mo, ZnO/CdS/CIGS/Mo, ZnO:Al/ZnO/CdS/CIGS/Mo).

- Identification of the optimum PLD growth parameters for each layer through an overall assessment of crystal structure, morphology, chemical composition, electrical and optical properties and interface characterization.

Objective 2: Fabrication of the CIGS solar cell and optimization of the fabrication process

- Fabrication of PLD-grown CIGS solar cells through the sequential deposition of CIGS, CdS, ZnO and ZnO:Al layers using the optimum growth conditions of each layer. The structure of the PLD-grown CIGS solar cells was based on the state-of-the-art CIGS solar cells derived from bibliography, which is SLG/Mo/CIGS/CdS/ZnO/ZnO:Al and Ni/Al grid on the top.
- A systematic investigation of the effect of CdS layer on the efficiency of the PLD-grown CIGS solar cells .
- The evalutation of PLD-grown CIGS solar cells through material characterization, electrical measurements and efficiency tests and optimization of the fabrication process using the shadow masked PLD method.

The thesis overview is given below with a short description of the following chapters:

Chapter 2 introduces the fundamental physics and theoretical background of a pn-junction, which constitutes the main functional part of a solar cell, where the photovoltaic effect takes place. The governing equations of the pn-junction in equilibrium, biased and under illumination conditions are being extracted. Furthermore, the key characteristics that define the quality of a solar cell are being discussed in this chapter.

Chapter 3 discusses the experimental methods and laboratory equipment used to carry out this study. The deposition techniques, material characterization, electrical and optical measurements of the films along with characterization and evaluation of the solar cells are described in this chapter.

Chapter 4 concerns the optimization of the PLD growth parameters of the CIGS layer. A systematic investigation of the effect of PLD growth parameters on the properties of $CuIn_{0.7}Ga_{0.3}Se_2$ thin films deposited on SLG (CIGS/SLG) and on Mo-coated SLG (CIGS/Mo/SLG) substrates is presented. The optimum PLD parameters for the deposition of the CIGS layer are being derived from an overall assesment of crystal structure, morphology, chemical composition, electrical and optical properties and interface characterization.

Chapter 5 deals with the optimization of the PLD growth parameters of the CdS layer. The deposition of CdS thin films on SLG substrates (CdS/SLG) in order to investigate the influence of

CHRISTIANA NICOLAOU

the PLD growth parameters on the properties of CdS thin films is initially discussed. The optimum PLD growth conditions of CdS layer are derived through a complete structural, compositional, morphological and optical characterization. Moreover, the sequential deposition of CIGS and CdS layers on Mo-coated SLG (CdS/CIGS/Mo/SLG) using PLD without interrupting the deposition process is examined. In addtion, the evaluation of the quality of CdS/CIGS junction based on electrical measurements and calculations is presented in this chapter.

Chapter 6 involves the optimization of the PLD growth parameters of the ZnO and ZnO:Al layers. The investigation of PLD parameters of the deposition of ZnO thin films on SLG substrates (ZnO/SLG) is initially discussed. A thorough structural, morphological and optical characterization of ZnO films is examined for the identification of the optimum PLD growth conditions of ZnO layer. Moreover, the sequential deposition of CIGS, CdS and ZnO layers on Mo-coated SLG (ZnO/CdS/CIGS/Mo/SLG) using PLD without interrupting the deposition process is discussed, along with the evaluation of ZnO/CdS/CIGS junction based on electrical measurements and calculations. Similar methodology and investigation is presented for ZnO:Al on glass and ZnO:Al/ZnO/CdS/CIGS/Mo/glass structure in this chapter.

In **Chapter 7** the fabrication of the PLD-grown CIGS solar cells with sequential deposition of CIGS, CdS, ZnO and ZnO:Al layers on Mo-coated SLG substrates is presented. The efficiency and characterization of the PLD-grown CIGS solar cells with varying CdS thickness are examined in this chapter. Moreover, the optimization of the fabrication process has been explored to improve the performance of the PLD-grown CIGS solar cells through the elimination of particulates on the CIGS layer using the shadow masked PLD method.

Chapter 8 summarises the main findings of this study concerning the deposition of the individual layers and multi-layer structures and the fabrication of the CIGS solar cells using PLD.

Chapter 9 presents suggestions for future work regarding the enhancement of the performance of the PLD-grown CIGS solar cells. With further improvement of the multi-layer structure and optimization of the fabrication process, a greater efficiency of the PLD-grown CIGS solar cells will be achieved.

CHRISTIANA NICOLAOU

Chapter 2 – Theoretical background

2.1 Introduction

The photovoltaic effect is the direct conversion of light into usable electrical energy, through photovoltaic devices or solar cells. The first report of this effect is attributed to Edmund Bequerel in 1839 [60], who observed the generation of an electric current when a silver coated platinum electrode immersed in electrolyte was exposed to light. The experimental efforts continued from the research community, but the results were not well received, until the introduction of quantum mechanics. However, the efficiency of the solar cells in the 1930's was too low (1%) to be considered as a practical power source. Further research on photovoltaics along with the beginning of silicon in microchip technology in the 1950's, led to the increase of the efficiency to 15% on silicon based solar cells. When the space race began, the need for non-expendable and lightweight power sources for satellites brought the interest of the researchers on photovoltaic technology back. Nowadays, silicon solar cell industry dominates the market of photovoltaics with a wide range of applications, including integrated terrestrial and space systems [61].

The need for photovoltaic devices with high power-to-weight ratio for space applications steered the development of thin-film solar cells in the 1970s. Today, the driving force for development of thin-film solar cells are mainly their potential high efficiency, the reduced manufacturing cost and material utilization. The earliest thin-film cells were based on Cu_2S/CdS and suffered from poor stability due to the high diffusivity of Cu. Amorphous hydrogenated silicon (a-Si:H) cells entered the PV market in the 1980s, but today are increasingly challenged by CdTe and Cu(In,Ga)Se_2 based cells due to their remarkable stability [17]. The stability of Cu(In,Ga)Se 2 solar cells is also superior to other thin-film PV technologies, such as perovskite solar cells [18, 19]. However, the thin-film materials used in CdTe and Cu(In,Ga)Se_2 based cells are not used elsewhere in the electronics industry, therefore, there is comparatively little expertise about them [62].

2.2 The photovoltaic effect

Solar energy is converted into electrical energy when light is absorbed by a photovoltaic device. The absorption of photons by a photovoltaic device excites electrons into higher energy states, which are quickly separated by a built-in electric field before they can relax. The result from this process is the generation of a potential difference at the ends of the solar cell that drives the electrons through a load in an external circuit. This chapter deals with the fundamental physics of a pn-junction which constitutes the main functional part of a photovoltaic cell where the phenomenon described above takes place.

CHRISTIANA NICOLAOU

2.2.1 pn-junction at equilibrium

A pn-junction consists of two separate regions of p- and n-type semiconductors that are joined together to form a junction (Figure 2.1). This is not the experimental way of fabricating the junction, but it happens through various processes that spatially change the doping concentration from n-type to p-type [63]. The n-type semiconductor has a large concentration of electrons coming from the impurity atoms (donors, N_d) that have one additional valence electron, which contribute to the carrier concentration of the material. The p-type semiconductor has a large concentration of holes coming from the impurity atoms (acceptors, N_a) that have one less valence electron, which can accept a neighboring electron creating a hole that contributes to the carrier concentration of the material. The *majority carriers* of the n-type and p-type material are electrons and holes, respectively. A thorough discussion on the nature of p- and n-type semiconductors, can be found in Streetman and Banerjee [63].

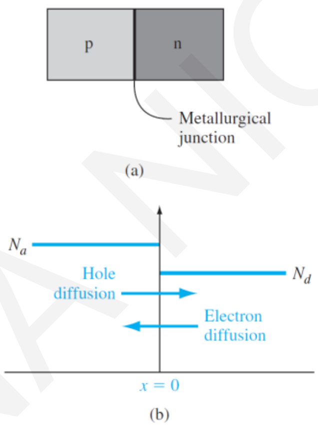

Figure 2.1 (a) simplified geometry of a pn-junction and (b) doping profiles of p and n regions of an ideal pn-junction [64].

When the two regions are in contact, diffusion of the majority carriers takes place in each side because of the large concentration gradients at the junction. Electrons diffuse from n side to p side, where they recombine with holes, leaving behind uncompensated donors (N_d) in the n material near the junction. Conversely, holes diffuse from p to n side, where they recombine with electrons, leaving behind uncompensated acceptors (N_a) in the p material near the junction (Figure 2.2a).

CHRISTIANA NICOLAOU

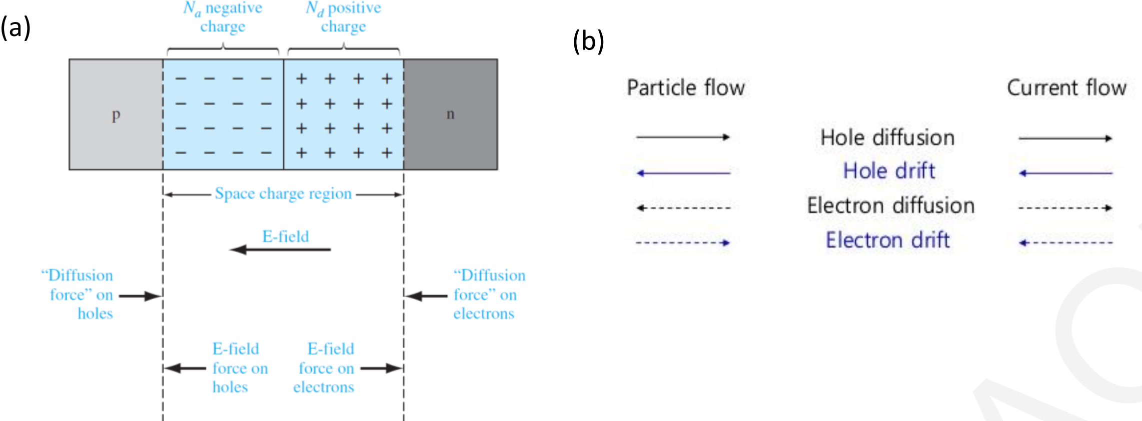

Figure 2.2 (a) The space charge region, the electric field and the forces acting on the carriers [64] and (b) particle and current flow at the junction [63].

The diffusion of the carriers results in the development of a depleted region of positive charge in the n region and negative charge in the p region near the junction. This region is known as *depletion/transition region* and is also called as *space charge region* because it contains only uncompensated charged ions and no free carriers. The ions in the depletion region create an electric field with direction from n side to p side. The density gradient produces a "diffusion force" that acts on the majority carriers at the edges of the space charge region, as shown in the Figure 2.2a. The electric field in the space charge region produces another force on the electrons and holes, which is in the opposite direction to the diffusion force for each type of particle. Therefore, the electric field generates a drift component of current that opposes the diffusion current (Figure 2.2b). As the diffusion current increases, more ions remain uncovered and the depletion region gets wider, thus the electric field is enhanced and consequently the drift current increases. These two competing currents cancel each out when equilibrium is reached (the diffusion force and the E-field force exactly balance each other), thus the depletion region limits to a certain size.

According to the relation $E(x) = -\frac{dV(x)}{dx}$, a gradient in electrostatic potential is established in the space charge region ($-x_p < x < x_n$), when equilibrium is reached. Assuming that the electric field is zero in the neutral regions, the electric potential in the p and n neutral regions must be constant but not equal. The potential difference at the edges of depletion region is called *contact or built-in potential*, V_{bi}, as shown in Figure 2.3a. The built-in potential maintains equilibrium between majority carrier electrons in the n region and minority carrier electrons in the p region, and between majority carrier holes in the p region and minority carrier holes in the n region. This potential difference across the junction cannot be measured with a voltmeter because new potential barriers will be formed between the probes and the semiconductor that will cancel V_{bi}. The potential V_{bi} maintains equilibrium, so no current is produced by this voltage.

CHRISTIANA NICOLAOU

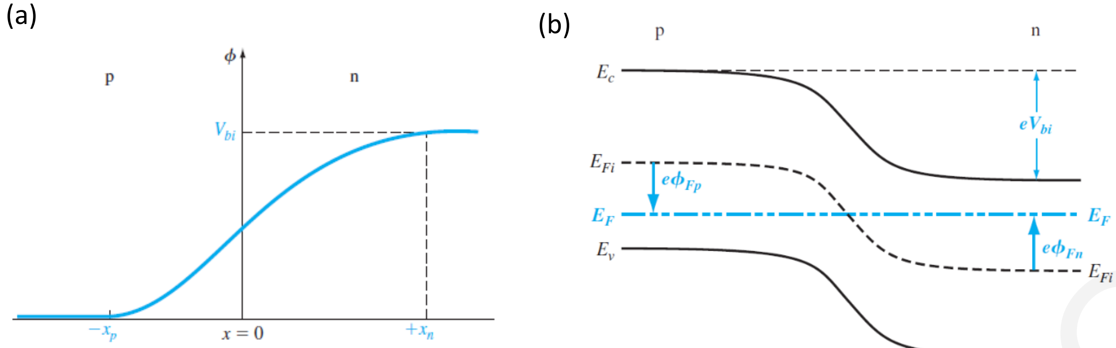

Figure 2.3 (a) electric potential through the space charge region and (b) energy band diagram of the pn-junction in thermal equilibrium [64].

The energy band diagram of the pn-junction in thermal equilibrium is shown in Figure 2.3b. At equilibrium, the Fermi level must be constant throughout the device (no spatial variation); as a result, the valence and conduction bands on the p side are separated from the n side by an amount of energy equal to eV_{bi}. Electrons in the conduction band of the n region must overcome the built-in potential barrier eV_{bi} to move into the conduction band of the p region. The built-in potential V_{bi} can be determined as the difference between the intrinsic Fermi levels in the p and n regions, $V_{bi} = |\varphi_{Fp}| + |\varphi_{Fn}|$, leading to the equation 2.1

$$V_{bi} = \frac{kT}{q} ln \frac{N_a N_d}{n_i^2}, \qquad \text{Equation 2.1}$$

where, N_d and N_a denote the net donor and acceptor concentrations in the individual n and p regions, respectively.

2.2.2 Forward and reverse biased junctions

In this section, a qualitative examination of the important features of a junction like the built-in potential, electric field and components of current is presented in the presence of an applied bias at the pn-junction. In addition, the diode equation and the *I-V* characteristic of a pn-junction are derived.

In the case of an external voltage being applied at the pn-junction with the positive terminal on the p side relative to the n side, then the junction is forward biased and the applied voltage *V* is considered to be positive. The vice versa applies for the reverse bias. The voltage drop in the neutral regions is small due to the small resistance (large carrier concentration and the length of each region is small compared to its area) of these regions and can be neglected. Therefore, it is valid to assume that the external applied voltage appears intact across the depletion region [63].

The impact of biasing on the potential barrier of the pn-junction is shown in Figure 2.4. The *electrostatic potential barrier* on a forward biased junction is lowered from the equilibrium built-in potential to the value V_{bi}-V_a, where V_a is the forward applied voltage. This lowering of the barrier

CHRISTIANA NICOLAOU

occurs because a forward bias raises the potential on p side and lowers the potential on n side. On a reverse biased junction (-V_R) the potential on p side is lowered relative to the n side and the potential barrier at the junction becomes larger, equal to $V_{bi}+V_R$.

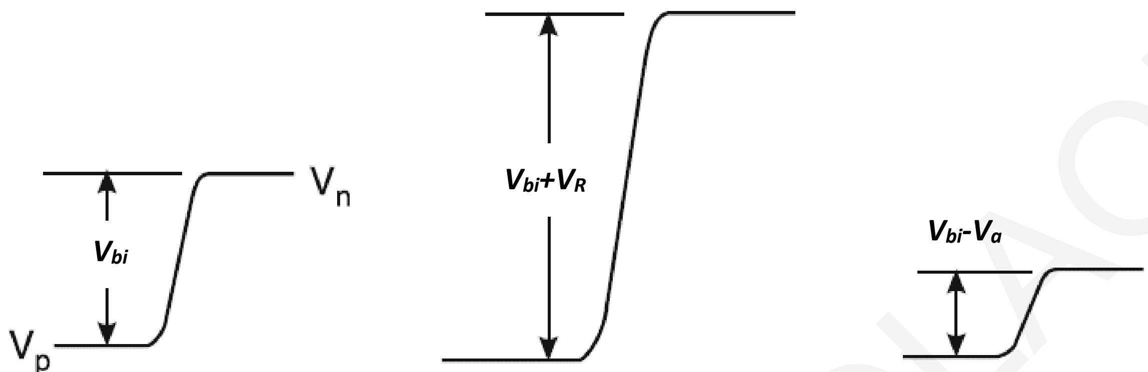

Figure 2.4 The electric potential barrier of a pn-junction (a) at equilibrium, (b) under reverse bias and (c) under forward bias [65].

Figure 2.5 illustrates the changes that occur on the electric field, the width of the depletion region and the energy band diagram under bias in relation to the junction in thermal equilibrium. The *electric field* within the depletion region decreases at forward bias since the applied electric field opposes to the equilibrium field. At reverse bias, the opposite occurs; the electric field increases because the applied field is at the same direction as the equilibrium field. Another way to deduct the electric field is from the slope of the potential barrier through the relation $E(x) = -\frac{dV(x)}{dx}$, which agrees with the above description.

The *width of the depletion region W* changes since it depends on the electric field at the junction. Under forward bias, the electric field is smaller, thus fewer ions are being uncompensated therefore the width W becomes smaller. The same reasoning facilitates that the width of the depletion region becomes larger under reverse bias.

The *separation of the energy bands* also changes since it depends on the potential barrier at the junction. Thus, the separation of the band becomes narrower under forward bias related to the separation at equilibrium, at an energy amount of $q(V_{bi}\text{-}V_a)$. Under reverse bias, the separation becomes wider at an energy amount of $q(V_{bi}+V_R)$. The Fermi level deep inside each neutral region must be at the equilibrium level, therefore the shift of the energy bands implies a discontinuity of the Fermi level within the depletion region. The Fermi levels in the two neutral regions differ by an energy amount equal to the applied voltage times the charge of electron q. Thus, the energy difference is $E_{Fp} - E_{Fn} = qV_R$ under reverse bias and $E_{Fn} - E_{Fp} = qV_a$ under forward bias.

CHRISTIANA NICOLAOU

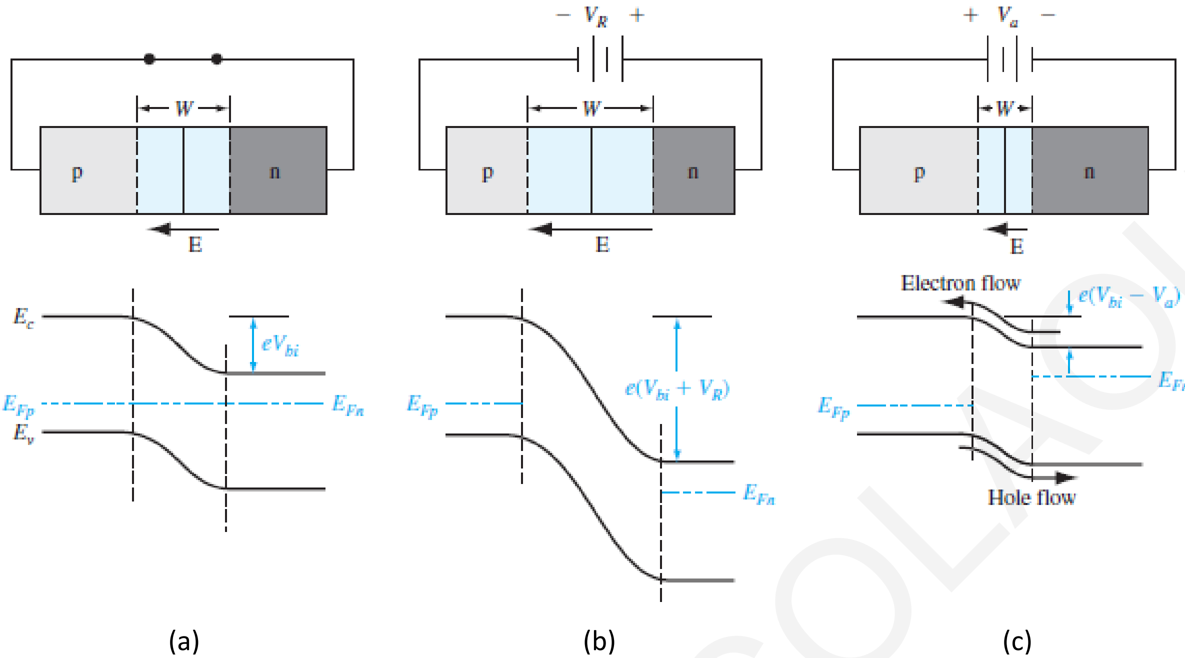

Figure 2.5 pn-junction (a) at equilibrium, (b) under forward and (c) under reverse bias; effects on depletion region width, electric field, and energy band diagram.

The particle and current flows are presented in Figure 2.6 for the pn-junction in equilibrium and under bias. The *diffusion current* is attributed to the flow of *majority* carriers on each side that surpass the potential energy barrier to diffuse to the other side of the junction. Some electrons on the conduction band of the n side have enough energy to overcome the barrier and diffuse from n to p at equilibrium. However, under forward bias, the potential barrier is lowered (V_{bi}-V_a) and the population of electrons in the n side conduction band which have sufficient energy to pass the barrier increases, thus electron diffusion current can be quite large. Similarly, more holes in the p side valence band can diffuse to n side due to lowering of the barrier, thus the diffusion current increases under forward bias. Under reverse bias, the potential barrier becomes larger (V_{bi}+V_R) and is too high for electrons in the conduction band of the n side to surpass and diffuse to the p side. Therefore, very few or no electrons and holes have enough energy to overcome the barrier and diffuse on either side, thus the diffusion current is negligible at reverse bias.

The *drift current* is attributed to the flow of minority carriers which have wandered near or into the depletion region and swept down the barrier by the electric field. The drift current is relatively independent to the height of the potential barrier (and therefore the applied voltage), because the limitations of drift current are related on how often the carriers are swept down the barrier and not on how fast. In other words, every electron on p side which has wandered into the depletion region will be swept down the potential barrier, whether the height is large or small. For example, the electron drift current, which arises from the minority electrons on p side that have been drifted to the n side by the electric field, does not depend on how fast electrons are swept from p to n, but rather on how many electrons are swept per second. Similarly, the same reasoning applies to the hole drift

CHRISTIANA NICOLAOU

current that drives the holes from n to p side of the junction. This implication leads to the approximation that the electron and hole drift currents are independent of the applied voltage.

The drift current, as discussed above, mainly depends on the concentration of minority carriers near or into the depletion region. Therefore, the drift current is low in both cases of bias, because of the low concentration of minority carriers that give rise to the current. The minority carriers on each side are generated by thermal excitation of electron-hole pairs (EHPs). If an EHP is generated within a diffusion length L_n near the depletion region on the p side, this electron can reach the depletion region by diffusion and be swept by the electric field to the n side. This generation of EHPs near the junction can be greatly enhanced by optical excitation, as occurs in a solar cell. The drift current is also called the *generation current* since its magnitude depends on the rate of generation of EHPS.

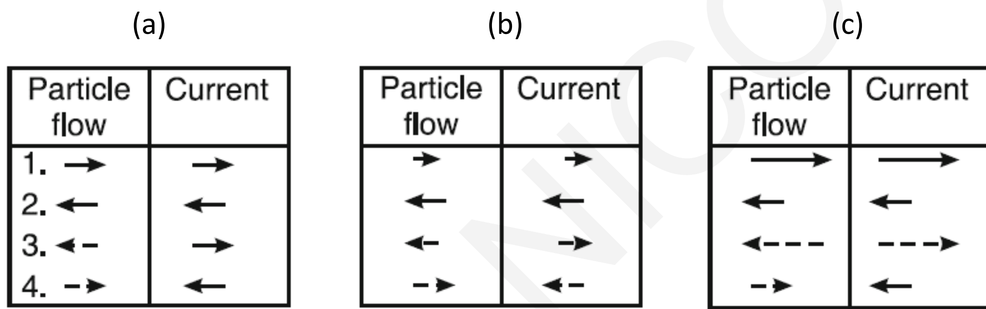

1. Hole diffusion 2. Hole drift 3. Electron diffusion 4. Electron drift

Figure 2.6 Particle and current flow at the pn-junction (a) in equilibrium, (b) under reverse bias and (c) under forward bias.

The total current passing through the junction is derived from the sum of diffusion and drift current. The diffusion current of both types of carriers is directed from p to n side and the drift current is directed from n to p side. At equilibrium (*V=0*), the net current through the junction is zero, since the drift and diffusion currents cancel for each type of carrier:

$$I = I(diff.) - |I(gen.)| = 0 \quad for\ V = 0, \qquad \text{Equation 2.2}$$

It is noted that the positive direction of the current is taken from p to n and the applied voltage is positive when the positive terminal is attached to p material. Under forward bias (*V>0*), the diffusion current increases due to the low potential barrier and the generation current remains constant and relatively small. The applied forward bias, $V=V_a$, increases the probability of a carrier to diffuse across the junction by a factor of $e^{(qV_a/kT)}$. Thus, the diffusion current under forward bias is given by its equilibrium value multiplied by $e^{(qV_a/kT)}$. Since the equilibrium diffusion current is equal to the absolute value of generation current, the diffusion current at forward bias is written as shown in equation 2.3. Therefore, the total current under forward bias is equal to the diffusion current minus the absolute value of the generation current (Equation 2.4).

CHRISTIANA NICOLAOU

$$I(diff.) = |I(gen)|e^{\left(\frac{qV_a}{kT}\right)} \; for\, V > 0, \qquad \text{Equation 2.3}$$

$$I = |I(gen)| \left[e^{\left(\frac{qV_a}{kT}\right)} - 1\right] \; for\, V > 0, \qquad \text{Equation 2.4}$$

Under reverse bias (*V<0*), the reverse bias, $V=V_R$, reduces the probability of the diffusion by the factor of $e^{(-qV_R/kT)}$ and the diffusion current for both types of carriers is negligible due to the large potential barrier at the junction. The diffusion current under reverse bias is shown in equation 2.5. Thus, the only current passing through the junction is the relatively small (and voltage independent) generation current from n to p (Equation 2.6). The negative generation current on reverse bias is also called the *reverse saturation or leakage current.*

$$I(diff.) = |I(gen)|e^{\left(-\frac{qV_r}{kT}\right)} \approx 0 \;\; for\, V < 0, \qquad \text{Equation 2.5}$$

$$I \approx -|I(gen.)| \quad for\, V < 0, \qquad \text{Equation 2.6}$$

The equation 2.4 can be revised to a more general expression that is applicable for both forward and reverse bias:

$$I = I_0\left(e^{(qV/kT)} - 1\right), \qquad \text{Equation 2.7}$$

The IV characteristic of a pn-junction that derives from equation 2.7 summarizes the alteration of the total current crossing the junction under forward or reverse bias and is illustrated in Figure 2.7. The significant feature emerging from the IV curve is the nonlinear dependence of the current as function of the applied voltage. In forward bias the current flows relatively freely, conversely to reverse bias in which there is almost no current flow.

When *V* is positive (forward bias) and significantly greater than *kT/q*, the exponential term becomes much greater than the unity and the total current increases exponentially with *V*. When *V* is negative (reverse bias), the exponential term approaches zero and the total current is equal to leakage current, $-I_o$. The leakage current is voltage-independent until a critical reverse bias is reached (*breakdown voltage*), for which the reverse current sharply increases. This phenomenon is called the *reverse breakdown*, where a small increase in the reverse voltage can drive large currents to flow through the device. In this case, the junction can be damaged by the excessive reverse current that overheats the device. Reverse breakdown can occur by two mechanisms: *Zener effect* that occurs at low voltages and *avalanche breakdown* that occurs at higher voltages.

CHRISTIANA NICOLAOU

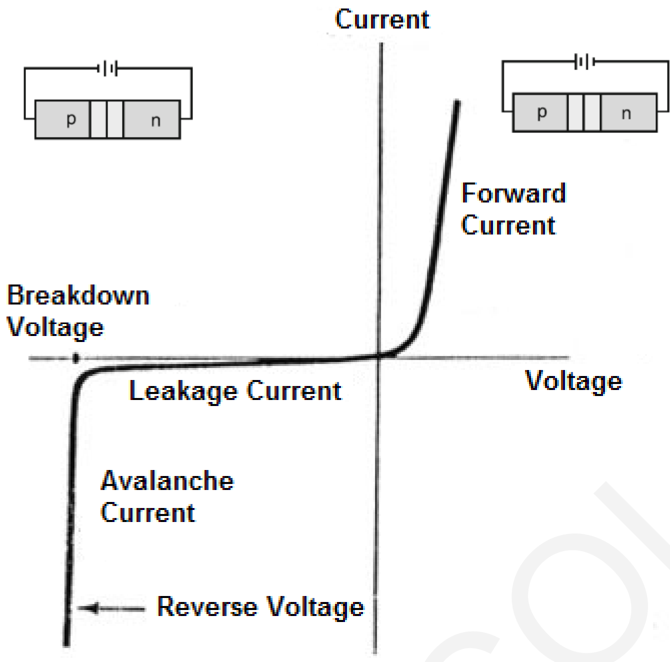

Figure 2.7 IV characteristic curve of an ideal pn-junction.

By calculating the diffusion currents at the edges of the depletion region through the excess minority carrier distributions, equation 2.7 can be written as

$$I = qA\left(\frac{D_p}{L_p}p_n + \frac{D_n}{L_n}n_p\right)\left(e^{(qV/kT)} - 1\right) = I_0\left(e^{(qV/kT)} - 1\right), \qquad \text{Equation 2.8.}$$

Equation 2.8 is called the *diode equation* and describes the total current through the diode for either forward or reverse bias, at every position x in the device (the derivation of the diode equation can be found in [63].

2.3 pn-junction under illumination

In this section, the operation of a pn-junction as a solar cell will be discussed. When a pn-junction is exposed to light, the generation of EHPs is enhanced by the absorption of photons and as a result, a potential difference appears at the ends of the solar cell (Figure 2.8). In this case, the pn-junction operates as a photovoltaic device that converts optical energy into electrical energy.

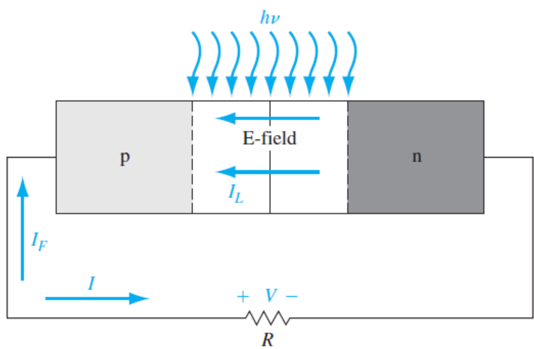

Figure 2.8 Illumination of a pn-junction in an electrical circuit [64].

CHRISTIANA NICOLAOU

The illumination of a pn-junction results to an additional generation rate of EHPs, g_{op} *[EHP/cm^3-s]*, that participates in the drift current of minority carriers across the junction. Thus, if the junction is uniformly exposed to light with photon energy $hv>E_g$, the minority carriers can be generated via thermal or optical excitation. The minority carriers which are generated within a diffusion length at each side of the junction, can diffuse to the depletion region and drift to other side by the electric field. The number of holes created per second within a diffusion length L_p on the n side is AL_pg_{op} and similarly, the number of electrons created per second within a diffusion length L_n on the p side is AL_ng_{op}. In addition, the number of carriers AWg_{op} which are generated within the depletion region W contribute to the current, thus, the current that arises from the collection of these optically generated carriers by the junction can be written as:

$$I_L = qAg_{op}\left(L_p + L_n + W\right),$$ Equation 2.9 [63].

Since I_L is directed from n to p, the *total reverse current* of an illuminated diode is the sum of the current described by the diode equation and the current due to optical generation, as shown in equation 2.10.

$$I = I_F - I_L = I_o\left(e^{(qV/kT)} - 1\right) - I_L = A\left(\frac{D_p}{L_P}p_n + \frac{D_n}{L_n}n_p\right)\left(e^{(qV/kT)} - 1\right) - qAg_{op}\left(L_p + L_n + W\right),$$

Equation 2.10

Therefore, the IV characteristic curve shifts to lower values of current, as shown in Figure 2.9. The amount of the shift is proportional to the generation rate g_{op} which is proportional to the intensity of light (number of photons per unit time) [63].

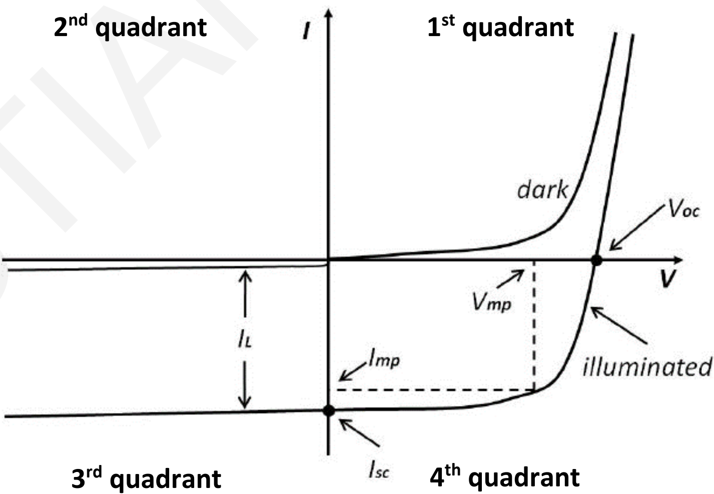

Figure 2.9 IV characteristic curve of an illuminated junction [66].

In the case of a short circuit (*V=0*), the only current flowing through the device is $-I_L$ with direction from n to p, which is called the *short circuit current*, I_{sc}. The short circuit current is proportional to the optical generation of EHPs, therefore the short circuit current is proportional to the intensity of light. Thus, solar cells that absorb photons with energies lying on the high intensity

CHRISTIANA NICOLAOU

region of the solar spectrum can yield higher efficiencies, because of the larger absolute values of short circuit current that can be obtained [63].

In the case of the device being in an open circuit ($I=0$), the potential difference that appears at the ends of the device is called the *open circuit voltage*, V_{oc}. The open circuit voltage can be obtained by setting the total current equal to zero and $D_{p/n} = L^2_{p/n}/\tau_{p/n}$ in equation 2.10:

$$V_{oc} = \frac{kT}{q}\ln\left[\frac{I_L}{I_o}+1\right] = \frac{kT}{q}\ln\left[\frac{L_p+L_n+W}{(L_p/\tau_p)p_n+(L_n/\tau_n)n_p}g_{op}+1\right], \qquad \text{Equation 2.11}$$

where $\tau_{p/n}$ is the lifetime of an EHP before recombination occurs.

The V_{oc} has an upper limit value that is equal to the equilibrium built-in potential V_o, since the built-in potential is the maximum forward bias that can appear across a junction. One can say that increasing the generation rate g_{op}, the V_{oc} can increase to infinity, but as the minority carrier concentration is increased by the optical generation of EHPs, the lifetime $\tau_{p/n}$ becomes shorter and the V_{oc} confines to a maximum value [63].

The energy band diagram of a junction at equilibrium and of an illuminated junction in an open circuit is shown in the Figure 2.10a and 2.10b, respectively. At thermal equilibrium, the Fermi level is constant through the device and the separation of the conduction bands is equal to qV_{bi}. When the device is illuminated, the appearance of a forward voltage across the junction causes a discontinuity to the Fermi levels. The Fermi levels in the two neutral regions differ by an energy equal to $E_{Fn} - E_{Fp} = qV_{oc}$, as it happens to the forward biased junction discussed in the previous section [63].

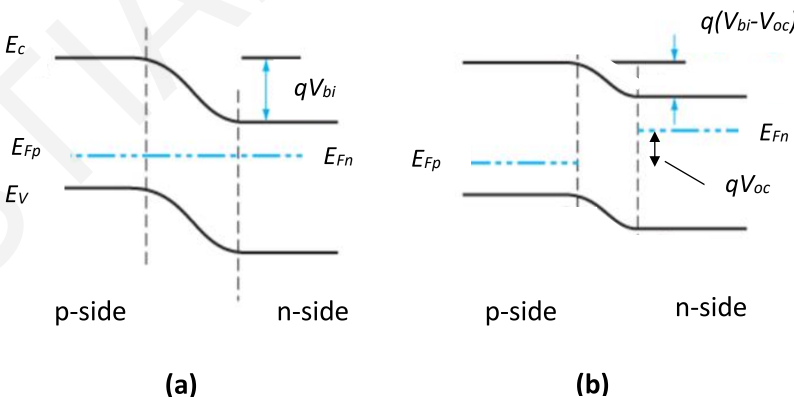

Figure 2.10 Energy band diagrams of a junction (a) at equilibrium and (b) under illumination in an open circuit [63].

The *IV* curve of the illuminated junction can be divided into four quadrants as shown in Figure 2.9. Regarding to the intended application, the device can operate in the third or fourth quadrant. Considering the power equation, $P=I.V$, when the current and the applied voltage are both

CHRISTIANA NICOLAOU

positive or negative, the power is positive (*P>0*). First and third quadrant belong to the case of *P>0* in which power is delivered to the device from the external circuit. The operation in the third quadrant corresponds in applications which the device is used as a photodetector. In the fourth quadrant, the current is negative, and the internal junction voltage is positive, thus the power is negative (*P<0*). In this case, the power is delivered from the device to the external circuit and the device operates as a solar cell. The junction's operation in the fourth quadrant can be considered as of a battery because the current flows from the negative terminal to the positive terminal of the junction. The appearance of a forward voltage across an illuminated junction results in a reverse current that can flow through a load in an external circuit, thus power is given to the load from the device and electrical work is done. In other words, solar energy is converted into electrical energy and this is known as the photovoltaic effect [63].

2.4 Solar cell in an electrical circuit

Integrating a solar cell into a simple electrical circuit can result in the production of usable power, as shown in Figure 2.11. When the solar cell is exposed to light, a voltage drop appears across the front and back contact and current flows through a given load resistance. A voltmeter and ammeter can be used to measure the voltage drop and current, respectively.

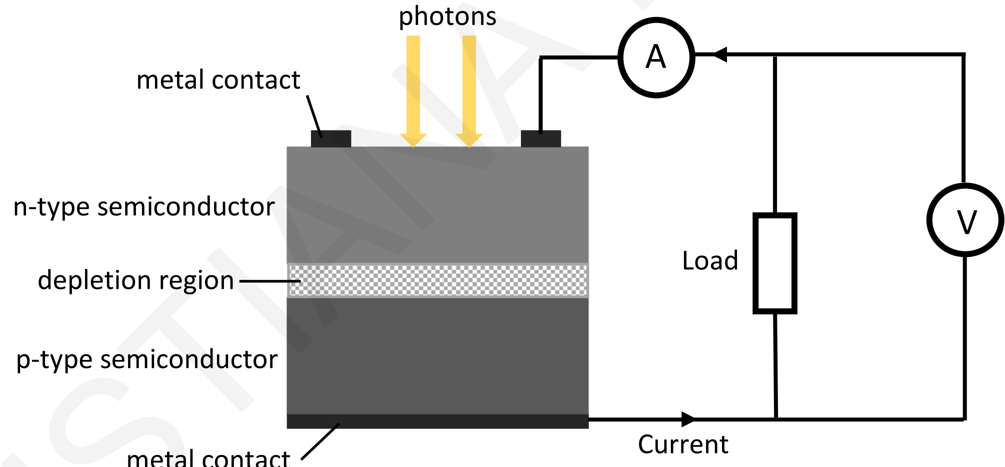

Figure 2.11 Solar cell in a simple electrical circuit; solar energy converts to electrical energy at the load resistance.

The potential difference, which develops between the terminals of the cell when a load is present in a circuit, generates a current flowing in the opposite direction of the photocurrent I_L. This current is called the *dark current* and is equal to the current which flows across the device under an applied voltage *V* in the dark [67]. For an ideal diode, the net current of an illuminated diode is given by the equation 2.12:

CHRISTIANA NICOLAOU

$$I = I_{dark} - I_L = I_o\left(e^{\frac{qV}{kT}} - 1\right) - I_L, \qquad \text{Equation 2.12}$$

Having the intensity of the incoming light is fixed, T_L, the current depends only on the load resistance. With the load varying, the values of the current and voltage change in such a way that the relation $R=V/I$ is always true. The two extreme conditions are the open circuit and the short circuit condition.

In the open circuit condition, the resistance is infinite, and the current is zero. The voltage difference created by the separation of the photon generated EHPs by the internal electric field on either side of the cell is called open circuit voltage, V_{oc}. For a given intensity of light, the open circuit voltage remains constant with time, even though photons are continually absorbed. The reason of V_{oc} remaining constant is the recombination of EHPs that occurs at a certain rate. Based on the latter, V_{oc} can be considered as a quality measure of a solar cell because it indicates how efficient is a cell in converting photons into electrical energy [67].

In the short circuit condition, the resistance is zero and the voltage drop is also zero. Under a given intensity of light, the current generated by the solar cell will be at its maximum value and is known as the short circuit current, I_{sc}. The short circuit current is proportional to the intensity of light (as discussed in the previous section), but is limited by the recombination rate of the material, thus it is considered to be a quality measure of a solar cell, as V_{oc} [67].

A close look to the short circuit current dependence with incident light gives rise to the quantity known as *quantum efficiency*, *QE*. Quantum efficiency is defined as the probability of an incident photon of energy *E* to deliver one electron to the external circuit. The relation of the density of short circuit current, J_{sc}, with the quantum efficiency is shown in the following equation:

$$J_{sc} = q \int b_s(E)\, QE(E)\, dE, \qquad \text{Equation 2.13}$$

where b_s is the incident spectral photon flux density (number of photons of energy in the interval (E, $E+dE$) per unit incident area in unit time) and q is the electronic charge. J_{sc} is obtained by integrating the product of the photon flux density and quantum efficiency over photon energy of the solar spectrum. High values of J_{sc} can arise by having high *QE* at wavelengths where solar flux density is high (Figure 2.12). *QE* depends on the absorption coefficient of the solar cell material, the efficiency of the charge separation and the efficiency of the charge collection in the device. It is independent on the incident spectrum; thus, it can be considered as a key quantity in describing solar cell performance under different conditions of the incident light [67].

CHRISTIANA NICOLAOU

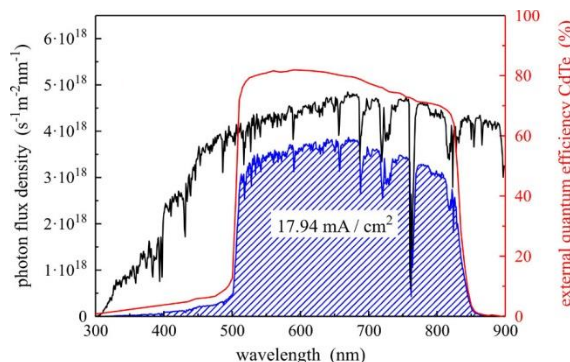

Figure 2.12 Photon flux density for the air mass 1.5 spectrum (black curve), external quantum efficiency of a CdTe solar cell (red curve), and the short-circuit current density (area under blue curve) [68].

Between the two extreme conditions (open circuit and short circuit), the resistance has a finite value and the current and voltage drop exhibit values less than their maximum values. Figure 2.13 represents the fourth quadrant of a solar cell characteristic curve with the current plotted upward for convenience of illustration. The voltage drop and the current in the circuit vary as the load resistance changes for a given amount of intensity of light, as shown in Figure 2.13. The power that is supplied to the load is the product of current and voltage ($P=I.V$). The curve of the output power shown in blue color indicates that there is a maximum power point that corresponds to a specific load resistance. The maximum power point corresponds to a certain value of current, I_{mp}, and voltage, V_{mp}. Therefore, the optimum load resistance is the one that maximize the output power ($P_m= I_{mp}.V_{mp}$) in a solar cell circuit and it is selected during the design of the circuit [67].

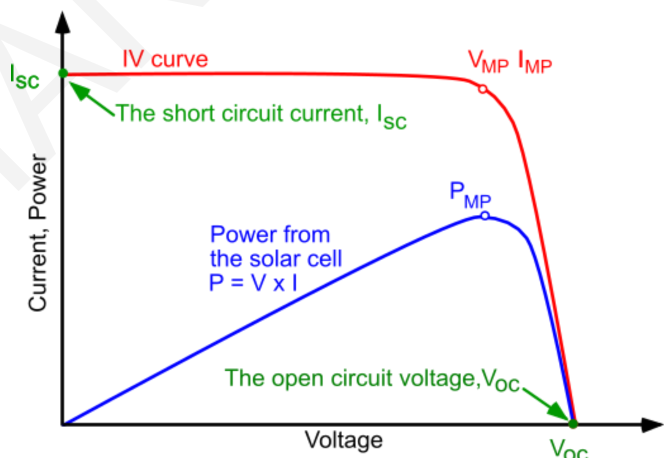

Figure 2.13 IV characteristic (green) and output power (blue) curves of an illuminated solar cell [69].

A variable known as the *fill factor* is a useful measurand to characterize the squareness of the *IV* curve. Fill factor is defined as the ratio of the maximum output power to the product of the open circuit voltage and the short circuit current:

CHRISTIANA NICOLAOU

$$FF = \frac{V_{mp} I_{mp}}{V_{oc} I_{sc}}, \qquad \text{Equation 2.14.}$$

As the fill factor approaches the unity, the maximum output power increases [67].

The *efficiency* of the solar cell is defined as the ratio of the maximum electrical output power to the power of the incident light:

$$\eta = \frac{V_{mp} I_{mp}}{T_L A}, \qquad \text{Equation 2.15}$$

where T_L is the intensity of light in $\left[\frac{mW}{cm^2}\right]$ and A is the solar cell area in $[cm^2]$.

Efficiency is also related to *FF, Voc, Isc,* as shown in the equation 2.16. Thus, the four quantities *FF, Voc, Isc* and η are the key features characterizing a solar cell under specific illumination conditions.

$$\eta = \frac{FF V_{oc} I_{sc}}{T_l A}, \qquad \text{Equation 2.16 [67]}$$

The *IV* curve of the solar cell can be obtained by measurements of a circuit consisting with a voltage source, an ammeter and a solar cell. Varying the voltage and measuring the current is the equivalent of varying the load resistance from zero to infinity. The goal is to maximize the efficiency of a solar cell as this leads to the enhancement of the output power for a given intensity of light.

2.5 Losses in a solar cell

The maximum theoretical limit of the efficiency of a solar cell is close to 30%, however even the most efficient cells that currently exist have lower efficiencies. This fact indicates that part of the energy of light that reaches the cell is lost before it can be converted into electricity. The cell efficiency is limited by several physical processes, some of these are inherent and cannot be avoided and the rest can be improved by proper design. This section addresses the major phenomena which are responsible for the losses that limit the efficiency of a solar cell.

Reflection from the cell's surface: The solar cell surface reflects part of the incident sunlight during the illumination. For example, untreated silicon reflects about 36% of the sunlight that impinges on the surface. This could have a detrimental effect on the efficiency, but fortunately there are several ways of treating the surface to decrease reflection. The most widely method is the deposition of an antireflective coating on the surface of the cell. An antireflective coating can decrease the surface reflection down to 5% [70].

Energy of photons: The sunlight that reaches the earth surface is characterized by the large fluctuations of intensity at a broad spectrum of wavelengths. Losses associated with the energy of light results from the interaction of light with the material of a solar cell at different wavelengths. When the light enters a solar cell, it can be absorbed or transmitted. In the case of absorption, if the energy of photons is lower than the cell's energy gap ($h\nu<E_g$), the absorbed energy generates heat in

CHRISTIANA NICOLAOU

the form of atomic vibrations. The generation of an EHP can be achieved only when the energy of photons is equal or larger than the cell's energy gap. When a photon with energy $hv>E_g$ is absorbed, an EHP is created and the electron is excited into the empty states of the conduction band. The excess of energy which the excited electron initially carries is delivered to the lattice as heat via scattering events, until it reaches the bottom of the conduction band. The perfect mechanism of transforming light energy into electricity is the generation of an EHP by optical absorption of photon with energy $hv=E_g$ since no heat is produced. Figure 2.14 represents the efficiency of a solar cell as function of the semiconductor band gap under AM1.5. A band gap energy lying around 1.5 eV under AM 1.5 is the optimum for producing maximum output [70].

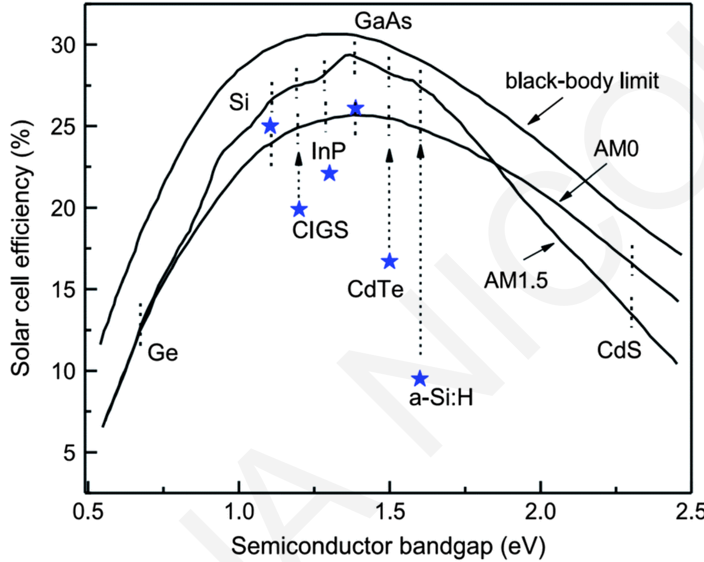

Figure 2.14 Power conversion efficiency as a function of semiconductor band gap. Asterisks show the best confirmed solar cell efficiencies under AM 1.5 illumination [71].

Recombination of electron-hole pairs: The recombination of optical generated EHPs before they separated by the electric field, is an inadvertent loss mechanism but can be eliminated by proper design. There are two types of recombination depending on the way is taking place, the direct and indirect recombination.

Direct recombination is defined as the event in which an electron randomly encounters a hole and the energy is given as photon. Thus, an electron in the conduction band spontaneously falls to an empty state (hole) in the valence band and a photon is emitted. Direct recombination is relatively rare, and the radiation is very weak. It usually takes place before the separation of EHPs by the electric field. When an EHP is generated on the p side, the electron must quickly sweep to the n side by the junction's electric field to avoid recombination with holes at the p side. Therefore, solar cells must be designed to minimize the time that electrons spend on the p side before they move to the n side [70].

CHRISTIANA NICOLAOU

Indirect recombination is defined as the event in which an electron encounters a hole through several actions and the energy lost by the recombination is given up to the lattice as heat. Experiments have shown that indirect recombination occurs in about a hundredth of a second while calculations have shown that direct recombination can occur in about one second. Thus, indirect recombination is the dominant recombination mechanism, causing a hundredfold increase in the recombination rate and a detrimental consequence to the efficiency of a solar cell. This kind of recombination occurs via recombination levels within the bandgap coming from impurity or lattice defects, which are capable in receiving electrons and holes. The surface of a solar cell is a region where indirect recombination is prevalent. Small paths on the cell's surface provide to the carriers an effective way to avoid junction's electric field. In addition, the increased scattering of carriers and the existence of dangling bonds at the surface make the carriers more prone to recombine. Regions where scattering is more pronounced can result to carriers having low mobility and therefore the probability to recombine is increased [70].

Self-shading: The electrical grid is composed from narrow contact lines of conductive material that is usually opaque. The metallic lines are spreading over the front surface of the cell and shade part of the cell's active surface where the light is hindered to enter the cell. The losses of self-shading are ranging from 3% up to 20%, with a typical shading loss percentage of 8% [70].

Operation temperature: The efficiency of a solar cell is altered with the operation temperature. In Figure 2.15, the decrease in solar cell's efficiency with increasing temperature is shown for various materials. A performance degradation also occurs at low temperatures for each material, although is not displayed in Figure 2.15. There is an optimum operation temperature which depends on the material properties of the cell and results in maximum efficiency. The choice of the material is based on the intended application and operation temperature. For example, solar cells that orbit around earth operate at low temperatures while solar cells for terrestrial use operate at moderate temperatures. High temperatures occur on applications that utilize concentrated solar cells [70].

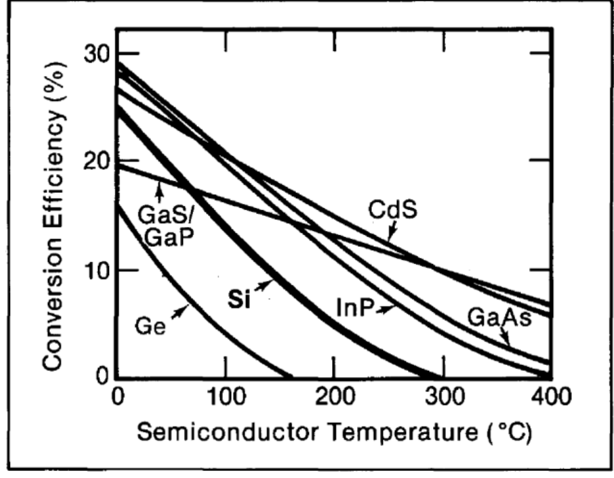

Figure 2.15 Solar cell efficiency as function of temperature for various semiconductors [72].

CHRISTIANA NICOLAOU

High temperature losses: The performance degradation of solar cells at high temperatures is attributed to two predominate effects. As the temperature increases, the lattice vibrations become more intense and the mean free path of the carriers decreases and therefore their mobility decreases [70] as shown in Figure 2.16.

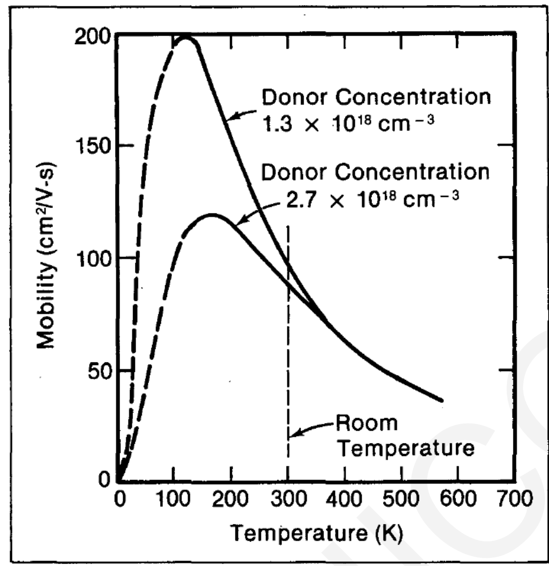

Figure 2.16 Carrier mobility of n-type silicon doped at two different donor concentrations as function of the operation temperature [72].

At the same time, the junction diminishes, and the electric field has no longer the ability to separate the optically generated EHPs. A close look to the temperature dependence of electron concentration of an n-type semiconductor presented in Figure 2.17 can explain this effect. At very low temperatures, all donor electrons are bound to their donor atoms and negligible intrinsic EHPs exist. As the temperature increases, the donor electrons gain energy and become loosely bonded, donating to the conduction of the material (*freeze-out region*). When all donor atoms are ionized, every available extrinsic electron has been transferred to the conduction band ($n_o \approx N_d$), thus the electron carrier concentration becomes constant with temperature (*extrinsic region*) [63]. Further increase of the temperature results to an increase of intrinsic EHPs that contribute to the overall carrier concentration. The concentration of intrinsic EHPs n_i becomes comparable to that of the extrinsic carriers and the carrier concentration is no longer constant.

CHRISTIANA NICOLAOU

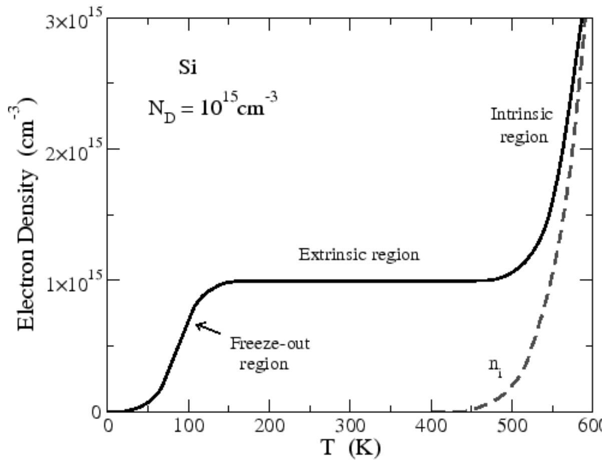

Figure 2.17 Carrier concentration as function of temperature for silicon doped with 10^{15} donors/cm^3 [73].

At high temperatures, the concentration of intrinsic carriers originates from the thermally generated EHPs become much greater than the concentration of donor electrons, $n_i >> N_d$, and the intrinsic carrier concentration is dominant ($n_o \approx n_i$). Therefore, the n-type nature of the semiconductor is lost (*intrinsic region*). A solar cell operating at high temperatures exhibits the effect described above; the p-type and n-type character of each side of the junction diminish and the junction does no longer exist resulting to the drop of the efficiency nearly to zero [70].

Low temperature losses: These losses are important mainly for deep-space applications and are more complex and less understood. However, the two effects described below can be responsible for the performance degradation of a solar cell. First, at very low temperatures, electrons and holes are strongly bounded to their donor and acceptor atoms respectively, and the thermally generated EHPs are negligible, thus the carrier concentration on each side of the junction is very low (Figure 2.17). Since the n and p materials no longer exhibit their doped character, the junction disappears. Second, the ionized atoms are not screened by the clouds of the charge carriers, since the carrier concentration is low, thus the scattering of the carriers with the atoms is increased. As a result, the mobility of the carriers decreases rapidly at very low temperatures (Figure 2.16) [70].

Parasitic resistances: The collection of the carriers at the edges of a solar cell by an external circuit is hindered by various resistances that appear at their flow. The equivalent electrical circuit of a solar cell with parasitic resistances is illustrated in Figure 2.18 with two parasitic resistances, one in series (R_s) and one in parallel (R_{sh}) with the cell [67].

CHRISTIANA NICOLAOU

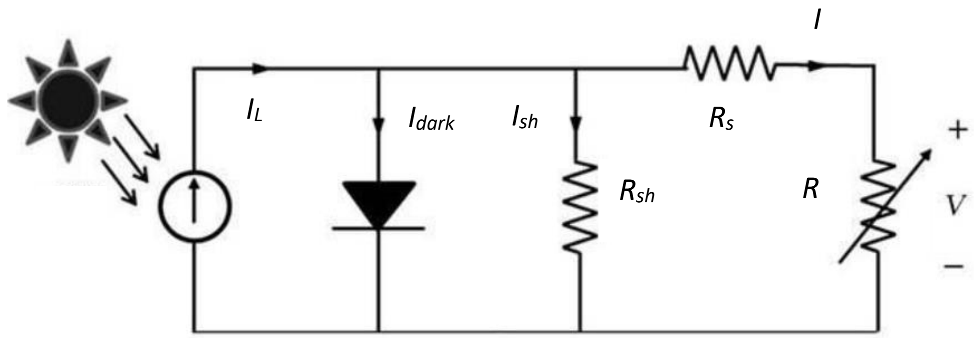

Figure 2.18 Equivalent electrical circuit of a solar cell with parasitic resistances [74].

The series resistance represents the resistance of the bulk material of the cell, the resistance of the front and back surfaces to the metal contacts, the resistance at the interfaces and the resistance of the metal contacts. The parallel or also called shunt resistance represents the leakage current that returns across the junction, around the edges of the device and between the contacts of different polarity. These parasitic resistances reduce the fill factor and affect the rectangular shape of the IV curve [67], as shown in Figure 2.19.

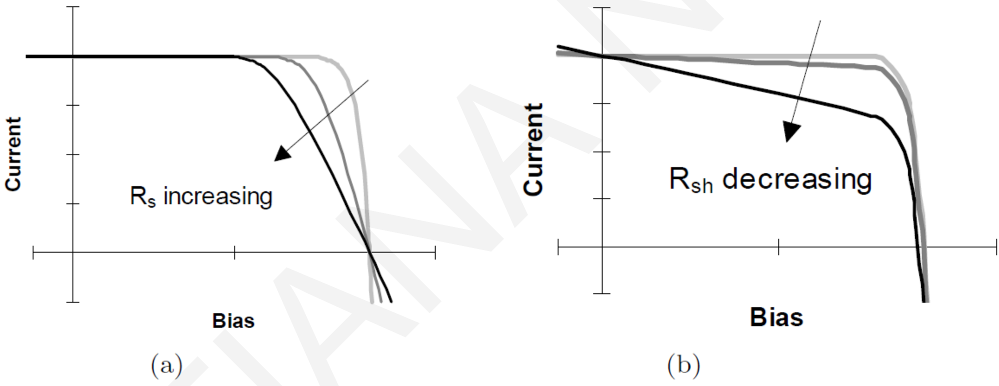

Figure 2.19 Effect of (a) increasing series resistance and (b) decreasing shunt resistance in the IV curve of a solar cell. The area of the maximum power rectangle is reduced compared to I_{sc} x V_{oc}. In each case, the outer curve corresponds to (a) $R_s = 0$ and (b) $R_{sh} = \infty$ [67].

For an ideal diode, shunt resistance must be infinite (no current could return across the junction) and series resistance must be zero (no resistance to current flow). Taking into consideration the parasitic resistances, the equation of the total current of a solar cell under illumination becomes:

$$I = I_o\left(e^{\frac{qV+IR_s}{nkT}} - 1\right) + \frac{V+IR_s}{R_{sh}} - I_L, \qquad \text{Equation 2.17}$$

where n is the ideality factor [67].

Design: The proper design of a solar cell in multiple extends can result to the enhancement of the efficiency. However, many compromises must be made for the design of a solar cell to achieve the best performance due to the interdependence of the solar cell properties. First, the voltage

CHRISTIANA NICOLAOU

difference at the edges of a cell is restricted to values less than the built-in potential, which in turn cannot be greater that the bandgap voltage E_g/q. In order to have large photovoltage, large built-in potential is required. Therefore, heavy doping can result in increasing the built-in potential, but at the same time the lifetime of the carriers is shorten due to higher recombination and the open circuit voltage is reduced. Photocurrent on the other hand depends on the illuminated area, thus large area junction must be located near the surface of the device. In addition, the thickness of the n type material should be less than L_p to allow holes generated near the surface to diffuse to the junction before they recombine. Similarly, the thickness of p type material should benefit as many as possible electrons to reach the junction, and at the same time as many as possible photons to be absorbed. Therefore, the thickness of the p material can be optimized by taking into account the electron diffusion length L_n and the mean optical penetration depth $1/\alpha$ (α is the absorption coefficient of the material). Finally, the metallic grid of the cell requires careful design in order to reduce the series resistance and shading but maintain the performance of the cell. Small contact fingers must be distributed over the surface of the cell in such a way that the maximum collection of carriers can be achieved without considerably interfering with the incoming light [67].

2.6 Heterojunction solar cells

A heterojunction is formed between two semiconductors with different bandgap energies. A typical energy-band diagram of a heterojunction in thermal equilibrium is shown in Figure 2.20 with the n-type semiconductor as the wide-bandgap material (Eg_N) and the p-type semiconductor as the narrow-bandgap material (Eg_P). Assume that photons are incident on the wide-bandgap material. Photons with energy between Eg_P and Eg_N will pass through the wide-bandgap material and will be absorbed in the narrow bandgap material. The EHPs created in the depletion region and within a diffusion length near the junction will be separated by the electric field of the junction and will contribute to the photocurrent. Photons with an energy greater than Eg_N will be absorbed in the wide-bandgap material, and EHPs generated within one diffusion length near the junction will be collected.

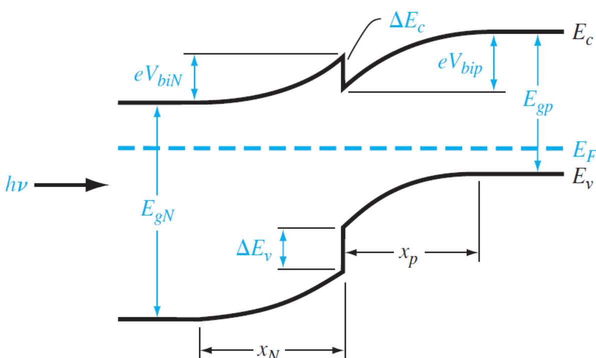

Figure 2.20 The energy band diagram of a pn heterojunction in thermal equilibrium [64].

CHRISTIANA NICOLAOU

The operation of the CIGS solar cells is based on the heterojunctions that are formed in accordance with their structure. The SEM cross-section of a typical CIGS-based solar cell is shown in Figure 2.21. The solar cell is built on a soda-lime glass substrate. The substrate is coated with a layer of Mo of about 1 μm thickness which serves as the back contact of the solar cell. On top of the Mo layer, the p-type CIGS absorber layer of about 1.6 μm thickness is deposited. The CdS buffer layer is placed on top of the CIGS layer with a thickness of only 50 nm. After the buffer layer, a bilayer of intrinsic and Al-doped ZnO is located with a thickness of approximately 1 μm [75]

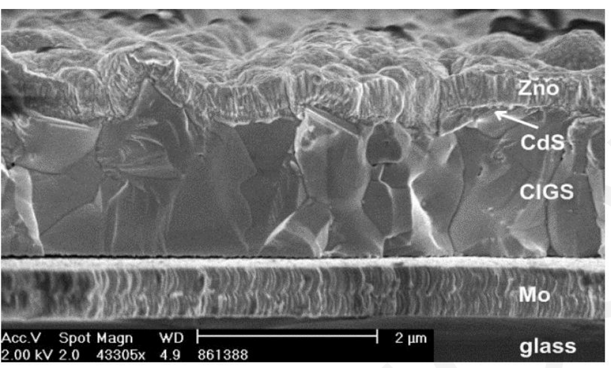

Figure 2.21 The structure of a typical CIGS solar cell taken by SEM in a cross-section configuration [75].

The energy band diagram of the heterojunction ZnO/CdS/CIGS solar cell is presented in Figure 2.22. A conduction band offset (CBO) of about 0.4 eV is located in the conduction band close to the interface of i-ZnO/CdS [75]. In addition, a difference between the conduction band minima of CdS and CIGS exists, giving rise to a conduction band offset at the CdS/CIGS interface. The E_c of CdS is higher than that of CIGS and an energy barrier is formed at the interface. The discontinuity in the conduction band in the CdS/CIGS interface varies from -0.4eV for $CuInSe_2$ to +0.3eV for $CuGaSe_2$ depending on the concentration of Ga [76]. The conduction electrons in the CIGS region must overcome the energy barrier at the CdS/CIGS interface to move towards the CdS region. The optimum CBO value is in the range of 0.3 - 0.4 eV [77] for which the open-circuit voltage (V_{oc}) of the CIGS solar cell is enhanced [77, 78]. However, the short-circuit current (J_{sc}) can be reduced by the CBO in the CdS/CIGS interface. Therefore, a thin CdS layer is introduced in the solar cell and its thickness is precisely controlled to maximize the fill factor [79, 80].

CHRISTIANA NICOLAOU

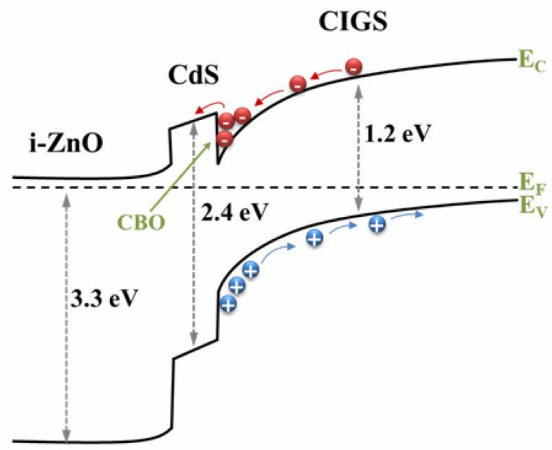

Figure 2.22 The energy band diagram of a CIGS solar cell [77].

CHRISTIANA NICOLAOU

Chapter 3 – Experimental methods

3.1 Deposition methods

3.1.1 Pulsed Laser Deposition (PLD)

PLD is a deposition technique that is widely used for thin-film growth. This idea has been known practically from the early days of the first ruby laser in the 1960s. However, PLD has been extensively used to produce thin films since 1980, after the growth of superconducting thin films with superior properties using the PLD method [81].

In a PLD system, the surface of a target material is irradiated by an intense pulsed laser beam. When the high-energy laser is focused on a rotating target, the ejection of material from the target takes place through various processes, leading to the formation of a visible "plume". The plume consisting of high energy species (electrons, atoms, diatomic species, and/or aggregates), expands in the direction perpendicular to the target [81]. Species from the plume adsorb onto a substrate placed in the direction of the plume expansion. The species then diffuse on the surface of the substrate and nucleate in islands. A continuous film is created as the islands grow and merge by the continuous arrival of the plume species. Substrates are usually heated to enhance the sticking and diffusion of the species on the substrate surface [82]. Figure 3.1 shows a schematic diagram of a pulsed laser deposition system. Prior the deposition, high vacuum is required to reduce impurities from being incorporated in the film. The deposition can be conducted in either high vacuum or in the presence of a high purity background gas (usually oxygen, nitrogen or argon), depending on the application and the desired stoichiometry of the film [82].

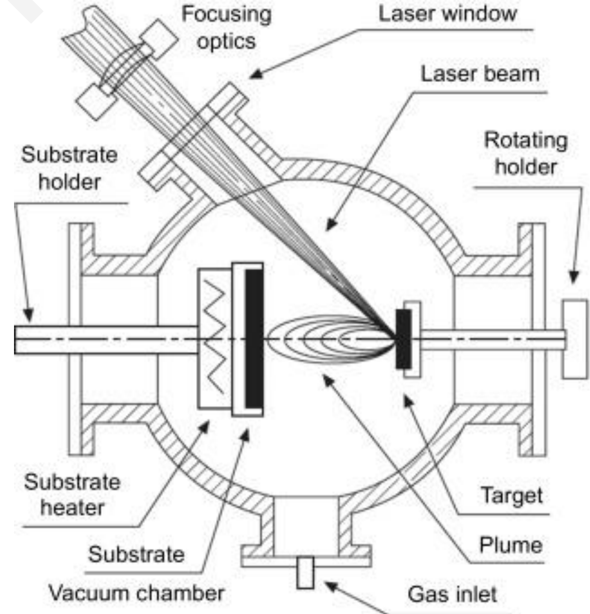

CHRISTIANA NICOLAOU

Figure 3.1 Schematic diagram of a pulsed laser deposition system [81].

The deposition process of a PLD-grown film can be described in five stages [83-85]. The first stage involves the absorption of the photons from the pulsed laser in the target material. Several mechanisms take place by the interaction of the laser light and the target, such as thermal, electronic, exfoliation and hydrodynamic sputtering [86]. At this stage, the strong energy of the laser absorbed in the solid leads to high temperature electron and atoms in the solid. An explosive evaporation of ions, electrons and neutral atoms follows, and the ablation process starts. For a typical PLD process many layers are ablated during one pulse [83, 87]. The ablation yield of the elements in a target is determined by the cohesive energy which is the energy required to release an atom from a solid [56]. The material ejected will have the same chemical composition as that in the target if the intensity of laser beam over the beam spot is uniform and the fluence is essentially high for ablating the target material without evaporation taking place [88]. Moreover, particulates, also called droplets, are generated in some cases. Their sizes, chemistry, and microstructure depend upon the processing conditions and the target material [81].

The second stage involves the generation of the initial state of the plume which is formed very close to the target surface. At this point, the laser light interacts with both the plume species and the solid behind the plume. Within the duration of a laser pulse, the plume plasma continues to absorb light and the ionization of the plasma occurs which results to the formation of a partly ionized plasma plume. The composition of the plume plasma does not deviate much from the original one. and the plume is strongly luminescent from excited neutrals and ions [84, 89-92]. During the laser irradiation, the plume expansion of the ablated material takes place with the plume front propagating 30–100 μm after the termination of the laser pulse [56]. The initial conditions of the plume are the high temperature (T = 10,000 K) and the high pressure (more than 5-10 bars) [93, 94] which drives the expansion into the vacuum or the background gas.

At the third stage, the expansion of the plume changes from the initial one-dimensional to the three-dimensional expansion. The high pressure of the initial plume is strongly directing the plume expansion in forward motion [83, 84, 95-97]. In the case of the expansion taking place in vacuum, the plume expands adiabatically in a forward direction. Eventually the plume particles will perform a free motion with constant velocity and the propagation of the plume species is mass dependent. In stage three, the flow is largely stoichiometric at fluences typical for PLD [56].

The fourth stage involves the expansion of the plume in the presence of a background gas. The initial high pressure of the plume provides the ablated atoms with sufficient kinetic energy to move away from the target in a free expansion towards the background gas. Eventually, the pressure of the plume is significantly decreased, and the plume is slowed down by the background gas [56]. The plume is moving into the background gas with a confined structure [90-92] and stops within tens of microsecond. Then, the plume atoms diffuse out of the confinement while mixing with the

CHRISTIANA NICOLAOU

background gas and migrate to the substrate [98-101]. The propagation dynamics and the angular distribution of the plume is influenced by the total mass of the plume, as well as the mass density of the background gas [97, 99, 102, 103]. Moreover, experimental studies have demonstrated that a large number of collisions between the plume species and the background gas occurs while the plume expands in the presence of a background gas. These collisions reduce both the ion fraction of the plume and the kinetic energy of the species [104]. In addition, a preferential propagation of the heavy atoms along the normal has been found [105]. Nevertheless, the flow of the plume species diffusing towards the substrate, once the plume has stopped, behaves strongly non-stoichiometric [56].

Stage five concerns the collection of the ablated atoms on a substrate and the subsequent film growth [56]. The growth of a film on a substrate surface is a very complicated process [106] and different growth modes can occur, depending on the energetics of the atoms and aggregates on the surface, as well as their arrival energy [107]. The arriving atoms or aggregates typically possess sufficient kinetic energy to diffuse on the substrate's surface until they form stable and energetically favor bonds with the other atoms of the film [56]. The nucleation and growth of the film on the substrate involve several mechanisms in which the atoms/ions undergo once they arrive at the surface of the substrate. These mechanisms include the diffusion of atoms over the substrate or cluster surface, encounter of between mobile film atoms to form mobile or stationary clusters, attachment to preexisting film-atom clusters, re-evaporation from the substrate or from a cluster and dissociation from a cluster [108].

The detailed description of the mechanisms involved in the PLD process is beyond the scope of this chapter. A thorough presentation of the PLD method, the mechanisms involved in each stage of the process and many other information can be found in [108] and in published works that summarize the fundamental mechanisms of PLD [56, 87, 109-112].

PLD offers a variety of deposition parameters which can be investigated and adjusted in a way that a desired film is obtained. The experimental parameters can be categorized into two groups: the parameters regarding the laser source and the parameters regarding the deposition chamber. The laser source parameters include the laser fluence, pulse duration, wavelength and repetition rate and the chamber parameters include the background gas and pressure, substrate temperature and target-to-substrate distance. These main deposition parameters have a major impact on the film's growth and can be exploited and optimized in order to obtain the desired film properties. In this thesis, the deposition of $CuIn_{0.7}Ga_{0.3}Se_2$, CdS, ZnO and ZnO:Al films was carried out using the PLD method. A systematic investigation of the effect of PLD growth parameters on the properties of the films had led to the optimization of the PLD growth parameters for each layer and their interfaces.

The PLD system used for the depositions of this thesis consisted of a Krypton Fluoride (KrF) excimer laser, a vacuum chamber and an arrangement of optics, as shown in Figure 3.2. A *Coherent COMPexPro 201* KrF laser with wavelength of 248 nm, maximum pulse energy of 700mJ, pulse

CHRISTIANA NICOLAOU

duration of 25 ns and repetition rate range of 1-10 Hz was used as the laser source for the PLD depositions of this study. The vacuum chamber was purchased from *SURFACE systems + technology GmbH + Co KG* included a heating station for the substrate with maximum temperature of 1000°C, a rotating/rastering four-target carrousel, two different inlets for background gas and three turbo pumps with base pressure of 6.10^{-8} Torr. The laser beam was directed into the deposition chamber through an arrangement of mirrors and focused on the target surface by a focus lens and a window glass. The substrate was mounted on a sample holder with the use of mechanical pins. A thermal conductive silver paint was applied between the sample holder and the substrate to ensure the uniform conduction of heating across the surface of the substrate.

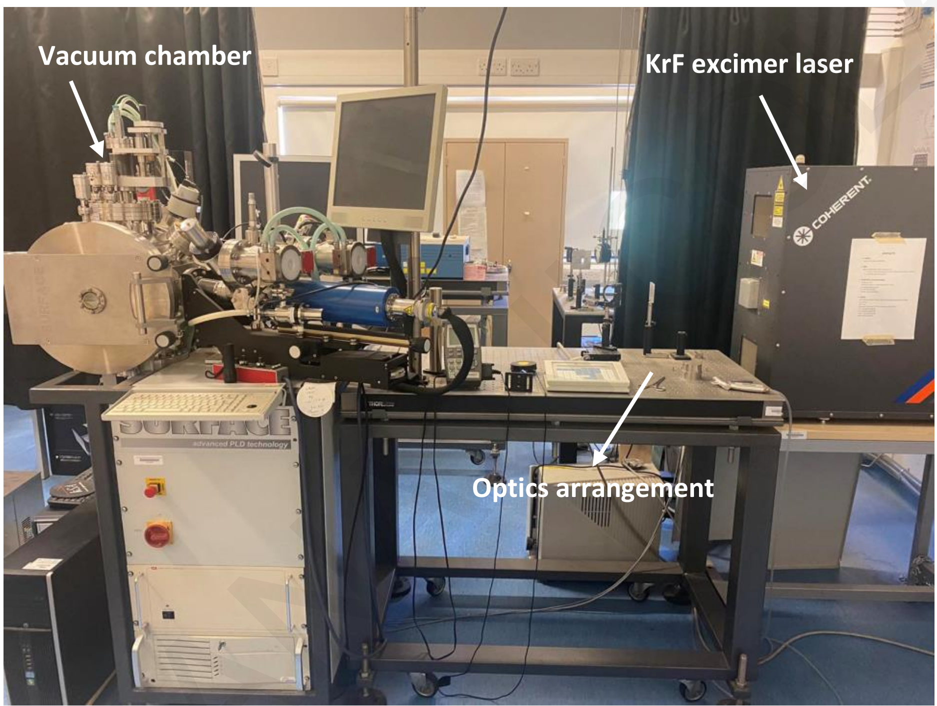

Figure 3.2 Picture of our PLD system.

3.1.2 Magnetron Sputtering

Magnetron sputtering is a physical vapor deposition (PVD) vacuum coating technique that allows the deposition of a thin film onto a substrate. A wide variety of target materials and substrates can be used in the sputtering process. DC power is used for depositing pure metals and either RF power or pulsed DC is required for the deposition of semiconductors and isolators. The sputtering process requires also the presence of a background gas, either non-reactive (inert gas only) or reactive (inert and reactive gas) [113, 114].

The sputtering process involves the bombardment of a target's surface by high-energy particles that results to the ejection of atoms or molecules from the target, as shown in Figure 3.3. The working principle is based on the supply of electrical power to the magnetron system with a negative voltage (typically -300V or more) applied to the target. The positive ions of the background gas which are present in the vacuum chamber are attracted by the negative voltage of the target and

CHRISTIANA AOU

accelerate towards the target. By the time the positive ions reach the surface of the target, they possess a large kinetic energy. Collisions between the positive ions and the atoms of the target's surface occurs and the kinetic energy of the ions is transferred to the atoms. If the energy transferred on a direction normal to the surface is larger than about three times the surface binding energy (approximately equal to the heat of sublimation), then sputtering occurs and the atoms are liberated from the target [113, 114]. The atoms can be ejected from the target by binary collisions either with the positive ion (direct knock-on) or with other target atoms that receive their kinetic energy through a sequence of collisions (collision cascade) originating from the positive ion [115].

Except from the sputtering process, ion bombardment of the target results to the emission of secondary electrons from the target surface. In magnetron sputtering, a magnetic field is used to confine these electrons close to the sputtered target resulting to a sustained glow discharge close to the target surface [116]. The sputtered atoms from the target material travel through the vacuum chamber and deposit onto a substrate to form a thin film.

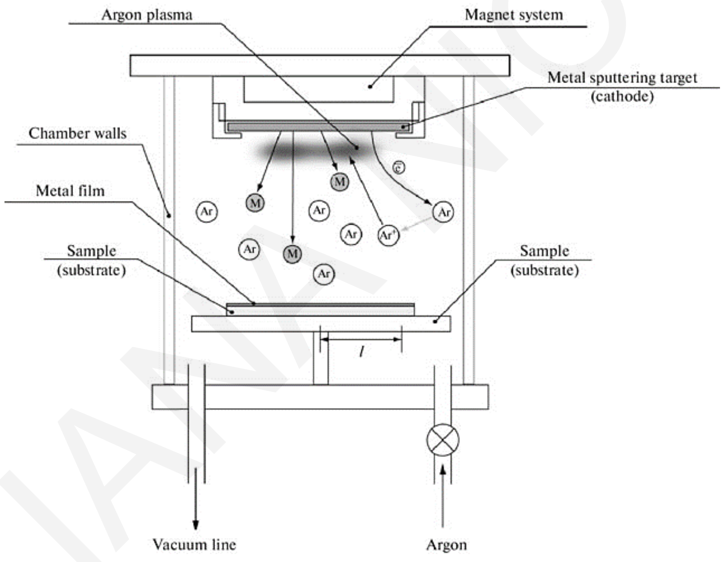

Figure 3.3 Schematic representation of the sputtering process [117].

In this thesis, the sputtering process was used to deposit a 100nm Ni patterned film on the surface of ZnO:Al layer of the ZnO:Al/ZnO/CdS/CIGS/Mo/SLG multi-layer structure. The Ni layer constitutes the first layer of the Ni/Al metallic grid which serves as a front contact for the collection of the photo-generated electrons of the PV device. A stainless-steel patterned shadow mask was fixed on the top of the multi-layer structure in order to obtain the desirable pattern of the metallic grid. More details about the Ni/Al metallic grid and the design of the pattern can be found in Chapter 7. A DC magnetron system was used for the deposition of Ni film. The setup is a commercial system from BAL-TEC equipped with a vacuum chamber, a quartz thickness monitor and a turbo pump with base pressure of 10^{-6} Torr.

CHRISTIANA NICOLAOU

3.1.3 Thermal Evaporation

Thermal evaporation is a simple physical vapor deposition technique which is widely used for the deposition of metals such as aluminum, silver, nickel and many other metals. During the process, a bulk material (target) is placed in a resistive boat or filament which is heated using Joule effect by passing current through it. When the source material is heated to an appropriate temperature at which there is an appreciable vapor pressure, atoms and molecules are removed in the form of a vapor flux [118]. The vaporized molecules then travel from the target to the substrate where they nucleate together and form a continuous thin film. Figure 3.4 presents a schematic representation of an evaporation system.

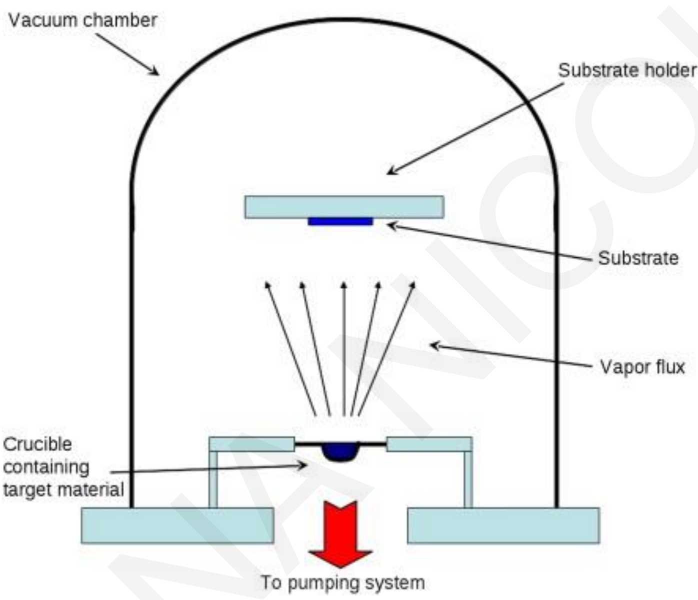

Figure 3.4 Schematic of a typical thermal evaporation system [118].

The evaporation process takes place in a high-vacuum chamber to avoid both the contamination of the growing film with residual background gas and the collisions of the vapor molecules with the gas molecules. Typically, the resistive heated container is made from refractory elements such as carbon, molybdenum, tantalum, and tungsten [119] and comes in many configurations including basket, boat, crucible and filament. The rate of material evaporation is achieved by adjusting the current supply passing through the resistive container [120]. Thermal evaporation is not suitable for depositing multicomponent thin films, since the components of the target can have different melting points and vapor pressures.

In this thesis, the thermal evaporation process was used to deposit ~1 μm Al patterned on top of the Ni patterned film which was deposited on the surface of ZnO:Al layer of the ZnO:Al/ZnO/CdS/CIGS/Mo/SLG multi-layer structure. The Al layer constitutes the second layer of the Ni/Al metallic grid and therefore the deposition of Al film took place immediately after the deposition of Ni film, without moving the stainless-steel patterned shadow mask that was fixed on the top of the multi-layer structure for obtaining the desirable pattern of the metallic grid. More

CHRISTIANA NICOLAOU

details about the Ni/Al metallic grid and the design of the pattern can be found in Chapter 7. The deposition of Al patterned film was carried out using a thermal evaporation commercial system from BAL-TEC equipped with a vacuum chamber, a quartz thickness monitor and a turbo pump with base pressure of 10^{-6} Torr.

3.2 Film characterization

3.2.1 X-ray Diffraction (XRD)

XRD one of the primary characterizations used for crystalline materials such as powders, thin films and bulk materials. The structural properties like crystal structure, crystallite size, lattice parameters and strain can be determined from the XRD characterization of a material. In addition, XRD offer a qualitative and quantitative identification of multi-phase materials.

X-ray diffraction is based on the constructive interference between the reflected waves produced from the interaction of the incident monochromatic X-rays waves with a crystalline sample. Consider a set of crystallographic lattice planes with distances d_{hkl} and a monochromatic X-ray plane wave impinging on the lattice planes at an angle θ, as shown in Figure 3.5. The X-ray wave is reflected from the lattice planes at an equal angle θ and a path difference between two plane waves is created due to the difference in the travelling distance. Constructive interference for the reflected waves, however, can only be achieved when the path difference which is equal to 2dsinθ is a multiple of the wavelength. Therefore, 2dsinθ = nλ, which is called the Bragg's law, is the condition that must be satisfied for diffraction to occur where a maximum intensity of the transmitted waves is obtained [121]. More specific, the Bragg law is written as:

$$2d_{hkl}sin\theta_B = n\lambda, \text{ Equation 3.1}$$

where d_{hkl} is the interplanar spacing of the *hkl* planes, θ_B is the incident angle of the X-rays on the sample surface, *n* is the order of reflection and *λ* is the wavelength of the X-rays.

XRD measurement involves the generation of X-rays in a cathode tube, the monochromatization, collimation and direction of the X-rays at the sample, and the collection of the diffracted rays from a detector. X-rays are generated in a cathode ray tube by the bombardment of a target material with electrons that are produced by heating a filament and accelerated towards the target by applying a voltage. A continuous X-ray spectrum is produced when the electrons transfer their energy by collisions with the atoms of the target via multiple events. Characteristic wavelengths are present in the continuous spectrum and their wavelength depends on the target material (Cu, Fe, Mo, Cr). Copper is the most common target material for single-crystal diffraction, with CuKα radiation equals to 1.5418Å. Crystal monochromators and filters are required to isolate the characteristic wavelength and produce monochromatic X-rays needed for diffraction. The monochromatic X-rays are then collimated through various slits and collimators and directed toward the sample. As the sample and detector are rotated (or the generator and the detector are rotated), the

CHRISTIANA NICOLAOU

intensity of the reflected X-rays is recorded from the detector. When the geometry between the incident and the reflected X-rays satisfies the Bragg law, constructive interference occurs, and the intensity is maximized. A detector records and converts this X-ray signal to a count rate which is then presented as an X-ray diffraction pattern [122].

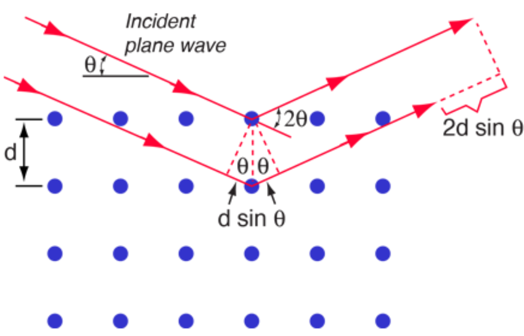

Figure 3.5 Bragg's law [123].

The conventional geometry of an X-ray diffractometer is such that the sample or the X-ray generator rotates at an angle θ while the arm of the X-ray detector rotates at an angle of 2θ, as shown in Figure 3.6a. This type of measurement is called θ/2θ scan and it is typically used for powders. However, the θ/2θ scanning method is not generally used for the X-ray diffraction measurements of thin films (1-1000 nm) as it produces a week signal from the film and an intense signal from the substrate, if the substrate is a crystalline material. The intense signal from the substrate can be avoided by performing a 2θ scan in which the X-ray generator and the sample are fixed through the measurement and the detector rotates at an angle of 2θ, while the angle of the incident X-rays is small and fixed. This type of measurement is popularly known as grazing incidence XRD (GIXRD) (Figure 3.6b). This geometry provides a strong signal from the film and avoids the intense signal from the substrate as the penetration depth of the X-rays is limited at the film's surface. The fixed angle is generally chosen to be slightly above the critical angle for total reflection of the film material [124].

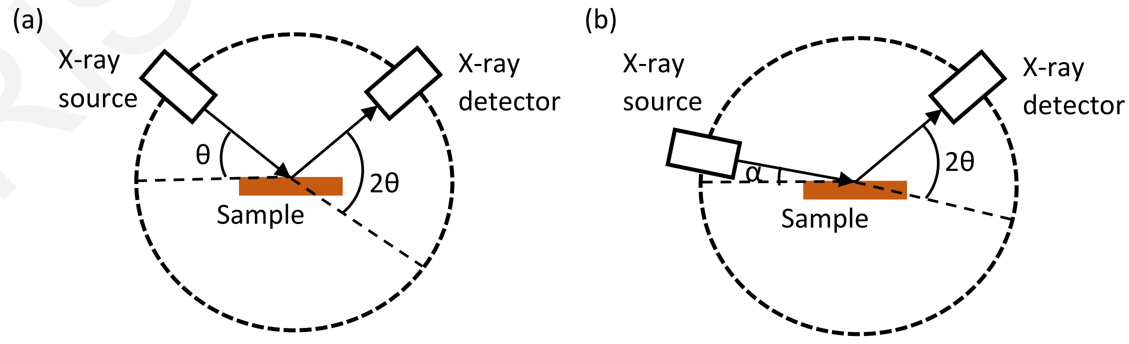

Figure 3.6 Principal geometry of (a) θ/2θ and (b) grazing incidence XRD measurements.

CHRISTIANA NICOLAOU

In this thesis, the structural characterization of the individual CIGS, CdS, ZnO and ZnO:Al layers as well as the multi-layer structures gradually fabricated up to the final device structure (ZnO:Al/ZnO/CdS/CIGS/Mo/SLG with the Ni/Al grid) has been performed using the high-resolution SmartLab Rigaku X-ray diffractometer with a 9 kW Cu rotating anode.

3.2.2 Scanning Electron Microscopy (SEM)

SEM is a multipurpose instrument used to observe the surface phenomena of the materials with high resolution. A detailed visual image of a material with high-quality and spatial resolution of 1 nm can be achieved using SEM [125, 126]. Topography, morphology, composition and crystallographic information of a specimen can be provided by SEM examination. More specific, the surface features and texture, shape, size and arrangement of the particles on the sample's surface can be examined and analyzed. In addition, the presence of secondary phases within a matrix and their relative ratios can also be provided. The arrangement of atoms in a single crystal and their degree of order can be observed with high resolution SEM [127].

The principle of SEM imaging is based on the interaction of the primary electrons released from a source (electron gun) with the specimen surface. A variety of signals due to the interaction of incoming electrons with specimen nucleus and electrons (both elastically and inelastically scattering), such as secondary electrons, backscattered electrons, X-rays and visible light (cathodoluminescence) are emitted [128, 129]. An image is then formed by the collection these secondary electrons from each point of the specimen.

Figure 3.7 shows a schematic diagram of a SEM apparatus. The primary electrons are produced from the electron gun accelerated by a high voltage. Then, the primary electron travel through magnetic field lenses and metal slits within a vacuum column to be focused and confined to a monochromatic beam. The sample surface is scanned by the confined primary electron using scanning coils [127, 128]. The impinging electrons accelerated towards the sample surface interact with the atoms of the sample and several signals are generated through multiple mechanisms [130]. The electron detectors receive the signals and the required image is formed after the process of the signals. Two different images can be provided about the sample, according to the detected signal (secondary electrons or backscattered electrons) [127]. Secondary electrons are used to build the visual image of the sample surface providing insights about the surface morphology and topography. Backscattered electrons are used to demonstrate the contrast between the phases of a multiphase sample.

CHRISTIANA NICOLAOU

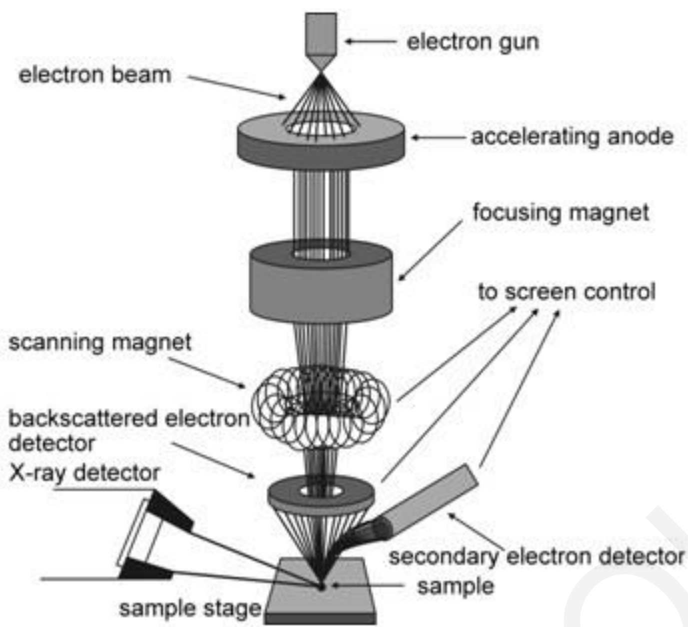

Figure 3.7 Schematic diagram of SEM apparatus [131].

The operation of SEM is performed under vacuum to avoid interaction of the emitted electrons with the gas molecules. The basic requirement of SEM process to obtain high quality images is that the samples must be electrically conductive to avoid overcharging on the surface. Thus, non-conductive samples are usually sputter coated [127] with a thin layer of carbon [128] or metal to provide a conductive surface for electrons [127, 129].

In this thesis, the surface of the individual CIGS, CdS, ZnO and ZnO:Al layers, as well as the surface of the multi-layer solar cells (ZnO:Al/ZnO/CdS/CIGS/Mo/SLG with the Ni/Al grid) have been investigated through SEM characterization, using the SEM *Tescan Vega LSU* scanning electron microscope.

3.2.3 Energy Dispersive Spectroscopy (EDS)

EDS analysis, also known as energy dispersive X-ray (EDX) analysis, it is a quantitative technique used for the elemental analysis and chemical composition of a sample. EDS is applicable for a variety of materials such as bulk materials, thin films and powders.

EDS is incorporated in the SEM chamber and is basically the addition of an X-ray detector, as shown in Figure 3.7. EDS functions along with SEM and enables the compositional analysis of an area which is being scanned and visualized by SEM. The working principle of EDS relies on the ionization of atoms in the specimen by the ejection of an inner shell electron (secondary electron) by the incident electron beam (primary electrons produced from the electron gun), as discussed in 3.2.2 regarding the SEM description. One of the ways that the ionized atom can relax is through the transition of an outer shell electron to the lower energy level of the ejected electron. The transition is accompanied with the emission of an X-ray photon with an energy equal to the difference between the energy levels of the ejected and outer shell electrons involved. Each element has a unique X-ray

CHRISTIANA NICOLAOU

emission spectrum due to a unique atomic structure; thus, the chemical analysis of a specimen can be determined [132].

Qualitative analysis involves the identification of the elements that are present in a sample by analyzing the position of the X-rays peaks in the spectrum. Quantitative analysis involves the determination of the concentrations of the elements present and therefore the stoichiometry of a sample. Quantitative analysis is carried out by measuring the intensities of the peaks for each element in the sample and comparing them with the intensities of the same elements in calibration standards of known composition [133].

The spatial resolution depends by the penetration and spreading of the electron beam in the specimen which is a function of density. The nominal resolution is about several micrometers under typical conditions. Elements with low atomic numbers ($Z<11$) are difficult to detect due to the limitation of the detector which is unable to detect elements with atomic number below 11 [134]. EDS can be used to determine elements that are present in concentrations > 1% by mass for a 95% confidence interval, although mitigating factors such as spectral overlap can complicate such detection [132].

In this thesis, the composition of the individual CIGS and CdS layers, as well as the composition of the upper layers of CIGS/Mo/SLG and CdS/CIGS/Mo/SLG multi-layer structures have been investigated through planar EDS characterization, using the Jeol Bruker Nano 129eV SEM equipped with XFlash 5010 detector.

3.2.4 Atomic Force Microscopy (AFM)

AFM is a simple but useful technique for the characterization of surfaces. AFM can provide quantitative and qualitative information about the topography of a sample surface in atomic resolution. Properties such as surface roughness, texture, size and density of particles on the surface, spring constant of the samples and high-resolution imaging (two and three dimensional) of surfaces can be obtained by AFM. The AFM can be employed to examine a wide variety of samples (i.e., plastic, metals, glasses, semiconductors, and biological samples), in the range of nanometer dimensions, under various conditions, including ambient environment, aqueous solutions, and ultrahigh vacuum [135].

The working principle of AFM is based on the sensing of the interactions between a sharp tip (<10 nm) attached on a flexible cantilever and the surface separated at very small distances, typical in the order of 0.1–10 nm. These interactions can be broadly classified into attractive and repulsive forces which cause vertical and lateral deflections of the cantilever. Therefore, the topography of the sample can be obtained in the form of two- or three-dimensional images by observing the deflection of the cantilever due to various forces acting between the tip and the sample [135, 136].

CHRISTIANA NICOLAOU

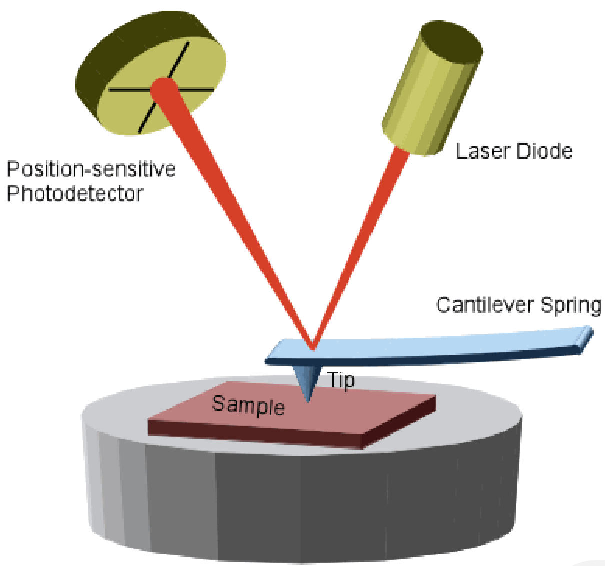

Figure 3.8 Schematic diagram of an AFM apparatus [137].

Figure 3.8 shows a schematic diagram of an AFM apparatus. The four main parts of an AFM are: a sharp tip attached on a cantilever, a laser diode and a position-sensitive detector. A piezoelectric scanner is used to drive the cantilever and therefore the scanning of the sample's surface with the tip is achieved. During the scanning of the surface, the tip interacts with the features on the surface and forces are acting that cause the bending of the cantilever. The nature of these forces, whether repulsive or attractive depends on the distance between the tip and the atoms of the surface. The laser spot, which is reflected from the top of the surface of the cantilever into the detector, strikes the detector on different positions according to the deflection of the cantilever. The detector consists of four segments and the signals obtained from the various segments indicate the angular deflection of the cantilever determined by the surface morphology. Thus, the signals of the cantilever's deflection can be converted into height information and the image of the surface is created as the tip scans over the surface [135].

In this thesis, the topography and surface roughness of the individual Mo, CIGS, CdS, ZnO and ZnO:Al layers have been investigated through AFM characterization, using the *Agilent Technologies AFM* equipment in contact mode.

3.2.5 Adhesion test

A simple and qualitative technique commonly used to measure the adhesion strength of a thin film to its substrate is the "Scotch Tape Test". The technique uses an adhesive tape which is applied to the film and subsequently pulled off. Adhesion is considered to be adequate if the film is not pulled off by the tape when it is removed [138].

Improved methods have been proposed for obtaining quantitative results using a test strip which contains several regions with adhesives of different strengths. When performing the Scotch Tape test with this test strip, different adhesive strengths are applied to the surface of the film. If an

CHRISTIANA NICOLAOU

area of the film's surface fails the adhesion test, it can be correlated to the adhesive strength of the test strip. However, the test remains a qualitative technique which is not very reproducible and applies only to a small range of adhesion strengths. Despite these weak points, the test is frequently used because of its simplicity.

In this thesis, the adhesion Mo/SLG, CIGS/Mo/SLG and ZnO:Al/ZnO/CdS/CIGS/Mo/SLG multi-layer structures have been investigated through the simple scotch tape adhesion test by applying the tape on the surface of the structures and removing the tape by applying force manually.

3.3 Electrical measurements

3.3.1 Van der Pauw (VDP) method

The VDP method is a widely used technique for measuring the electrical resistivity of thin film materials that has been developed by L. J. van der Pauw in 1958 [139]. The VDP method is based on using four-point contacts placed at arbitrary sites on the boundaries of the sample, as shown in Figure 3.9. The electrical resistivity of an arbitrary shaped sample can be accurately measured if the following conditions are met [139]:

- The contacts are placed at the circumference of the sample
- The area of the contacts is sufficiently small (compared to the distance between the contacts)
- The sample is homogeneous in thickness and composition
- The surface of the sample is singly connected (i.e., the sample do not contain any isolated holes)

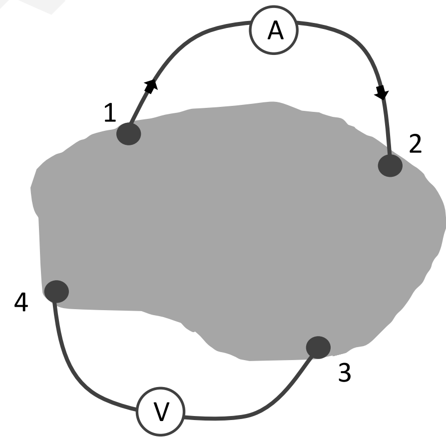

Figure 3.9 The four-probe electrical configuration of van der Pauw measurement for an arbitrarily shaped sample of uniform thickness.

Figure 3.9 presents the electrical configuration of the van der Pauw method in which four contacts, labeled with the numbers 1, 2, 3, and 4, are placed on the circumference of a square sample. When a current passes from contact 1 to contact 2 and the potential difference is measured between

CHRISTIANA NICOLAOU

contacts 4 and 3, the resistance of the sample can be written as $R_A = R_{43/12} = \frac{V_{43}}{I_{12}} = \frac{V_4 - V_3}{I_{12}}$. If the contacts of current and voltage are changed and the current passes through 1 and 4 and the voltage drop is measured between 2 and 3, the resistance is written as $R_B = R_{23/14} = \frac{V_{23}}{I_{14}} = \frac{V_2 - V_3}{I_{14}}$. A general relationship between the resistances measured when the voltage and current contacts are interchanged has been derived by Van der Pauw:

$$\exp\left(-\pi \frac{R_A}{R_S}\right) + \exp\left(-\pi \frac{R_B}{R_S}\right) = 1, \qquad \text{Equation 3.2}$$

where R_S is the sheet resistance of the film. If the two measured resistances are similar ($R_A = R_B$), Equation 3.2 can be written as:

$$R_S = \frac{\pi}{ln2} \left(\frac{R_A + R_B}{2}\right), \qquad \text{Equation 3.3}$$

and the electrical resistivity of the sample can be calculated by

$$\rho = R_S * t, \qquad \text{Equation 3.4}$$

where t is the thickness of the film. The derivation of Equation 3.2 can be found in full detail in the original paper of van der Pauw [140].

In this thesis, the electrical resistivity of Mo, CIGS and ZnO:Al layers deposited on SLG substrates have been measured using the VDP method with the four-probe configuration. Au wires were attached on the films' surface using conductive silver paste. The VDP setup used for the VDP measurements consists of a DC voltage source (Keithley 6221), a nanovoltometer (Keithley 2182A) and a switch system (Keithley 7001) for switching the voltage and current contacts. The samples were placed in the sample chamber of Physical Measurement Property System (PPMS, Quantum Design) and the measurements were conducted in vacuum, at 300K.

3.3.2 Hall effect measurement

The Hall effect was first introduced by Edwin H. Hall in 1879 [141]. Hall discovered that a transverse electric field is developed across a conductor, when the conductor carrying an electric current *I* is placed in a magnetic field *B* perpendicular to the current. The electric field is transverse to both the current flow and the magnetic field and generates a voltage difference (Hall voltage, V_H). The process indicates that the Hall voltage could have been produced only by the deflection of charge carriers (Figure 3.10a).

CHRISTIANA NICOLAOU

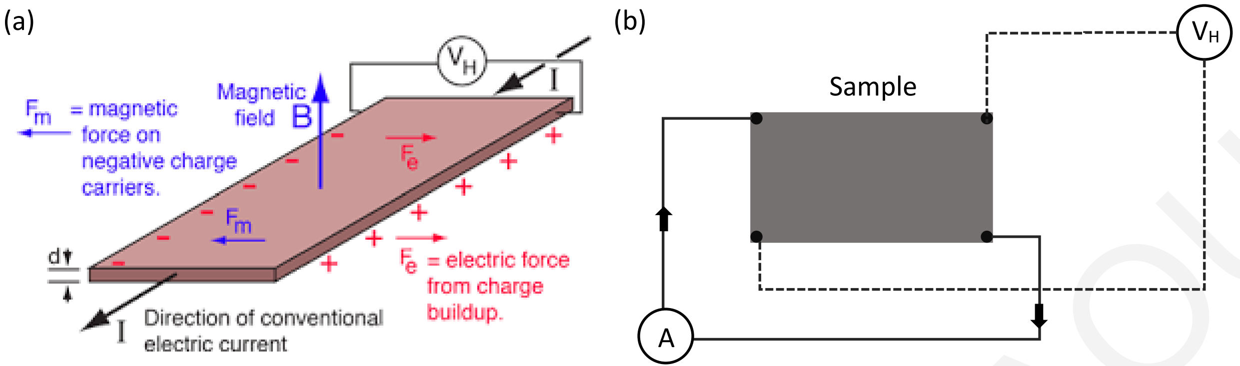

Figure 3.10 (a) Schematic demonstration of the Hall effect of a material with negative charge carriers [142] and (b) Electrical configuration of the Hall effect measurement.

During the Hall process, the paths of the carriers are deflected due to the Lorentz force, $\boldsymbol{F} = q(\boldsymbol{E} + \boldsymbol{u}\ x\ \boldsymbol{B})$, acting upon them as a result of the current flow and the magnetic field. Thus, the moving carriers accumulate on one side of the material, leaving an equal and opposite amount of static charges depleted on the other side, as shown in Figure 3.10a. An electric field is created due to the charge build up at the two sides which generates a force that opposes to the accumulation of further charge. When equilibrium is reached, a steady electric field transverse to the current flow and magnetic field, and a voltage difference across the two sides are established. The voltage difference is called the Hall voltage and its magnitude depends on *I, B* and the specimen thickness *d* as follows:

$$V_H = \frac{IB}{nqd}, \qquad \text{Equation 3.5}$$

where *n* is the carrier concentration and *q* is the electron charge.

Hall effect measurement is used for the determination of the majority charge carrier type, concentration, and mobility of a solid material. Equation 3.5 applies for materials with a single carrier, such as metals. For semiconducting materials, the determination of majority carrier type and its concentration are more complicated and will not be discussed here, however, more details can be found in [143].

In this thesis, the type of conductivity and carrier concentration of Mo, CIGS and ZnO:Al layers deposited on SLG substrates have been determined using the Hall effect measurement with the four-probe configuration, as shown in Figure 3.10b. Au wires were attached on the films' surface using conductive silver paste. The Hall effect measurement was performed using the VDP setup which consists of a DC voltage source (Keithley 6221), a nanovoltometer (Keithley 2182A) and a switch system (Keithley 7001) for switching the voltage and current contacts. The current flow was driven through the two opposite corners of the sample and the Hall voltage was measured across the other two opposite corners, as shown in Figure 3.10b. The samples were placed in the sample chamber of Physical Measurement Property System (PPMS, Quantum Design). The magnetic field

CHRISTIANA NICOLAOU

and the conditions (pressure and temperature) of the measurements were controlled by the sample chamber. The Hall effect measurements were conducted in vacuum and at 300K.

3.3.3 Dark current-voltage (IV) measurement

Dark IV measurements use inject carriers into the circuit by applying a voltage difference and measuring the current flow in a device. Dark IV measurement is a simple and effective process of determining fundamental performance parameters of a solar cell without the need of a solar simulator. Under illumination, small fluctuations in the light intensity introduces significant amounts of noise to the IV measurement and accurate readings are hard to obtain. Dark IV measurements are widely used to evaluate the electrical characteristics of a solar cell, such as series resistance, shunt resistance, diode ideality factor and diode saturation current which are key features for the performance of a solar cell [144].

In this thesis, dark IV measurements were performed on the following multi-layer structures: CIGS/Mo/SLG, CdS/CIGS/Mo/SLG, ZnO/CdS/CIGS/Mo/SLG and ZnO:Al/ZnO/CdS/CIGS/Mo/SLG. The dark IV measurements for CIGS/Mo/SLG was conducted to determine the type of contact between the CIGS/Mo interface. Regarding the CdS/CIGS/Mo/SLG, ZnO/CdS/CIGS/Mo/SLG and ZnO:Al/ZnO/CdS/CIGS/Mo/SLG structures, the dark IV measurements were conducted to evaluate the diode characteristics of each structure. The dark IV measurements were performed at room temperature, in air ambience using a two-probe setup with a voltage source/ammeter apparatus (Keithley 6487), as shown in Figure 3.11. Be-Cu tips of 20μm radius were controlled by micro-manipulators and were mechanically placed on the samples' electrode surfaces using a digital microscope. The IV measurements were carried out by applying voltage and measuring the current. A homemade LabVIEW routine (Virtual Instruments) was used to control the parameters of the measurement, such as maximum voltage, voltage step, time step and current limit.

Figure 3.11 Dark IV setup with two-probe configuration.

CHRISTIANA NICOLAOU

3.4 Experimental methods provided by our collaborators

The following experimental methods have been performed by our collaborators and in conjunction with the techniques described above, a complete characterization and study of the individual layers, multi-layer structures, as well as the entire solar cell devices was achieved.

3.4.1 Transmission electron microscope (TEM)

The TEM characterization has been performed by the Dr. Andreas Delimitis at the Department of Mechanical and Structural Engineering and Materials Science, University of Stavanger.

Transmission electron microscope (TEM) is an advanced scientific tool used for examining the structure, chemical composition, and morphological and electrical properties at the nanoscale by detailed imaging of very small features. The high-resolution image obtained by TEM provides characteristics like size, quality, crystal structure, defects, and chemical composition [145].

TEM working principle is based on the interaction between the electrons produced by an electron source and the atoms of the sample. A schematic diagram of a typical TEM apparatus is presented in Figure 3.12. An electron gun is used for producing and controlling an intense electron beam which is focused to irradiate the sample. Variable lenses are used to focus the electron beam onto the sample and to form the image. The remaining necessary components are a viewing screen and a charge-coupled device (CCD) to record the images. TEM requires vacuum environment to avoid the deflection of electrons by contaminants and gases [145].

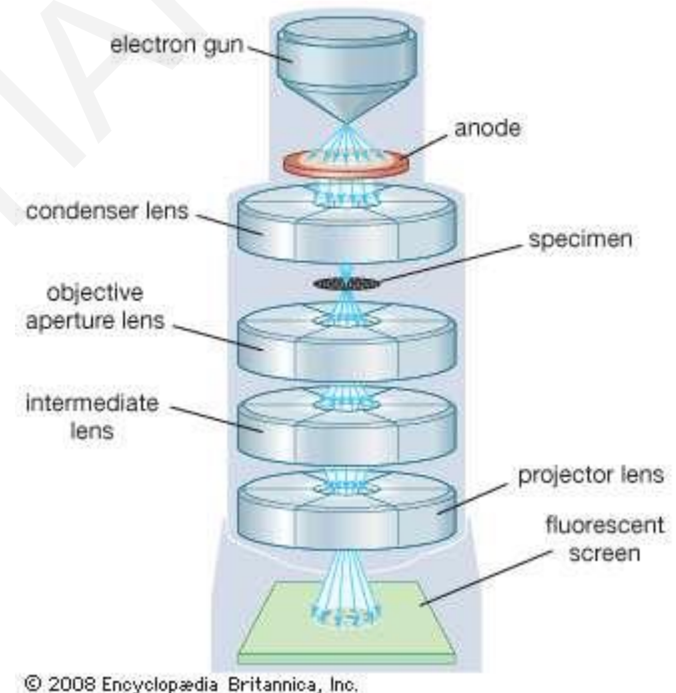

Figure 3.12 Schematic diagram of a typical TEM apparatus [146].

CHRISTIANA NICOLAOU

Contrast phenomena, arising from the interaction of the electron beam and the material, are responsible for the image formation and determine whether a characteristic will appear bright or dark in the image [147]. These contrast mechanisms can be categorized into three types, i.e., mass thickness, diffraction, and phase-contrast mechanisms. The image acquisition depends largely on the electrons that can pass through the aperture to be collected from the CCD camera. This is realized by controlling by the position of the aperture which determines the imaging mode. Bright field images are obtained when the aperture is positioned at the center which allows transmitted beam to be collected. Dark field images are obtained when the aperture is positioned at the scattered electron beam [148].

High-resolution TEM (HRTEM) is a powerful imaging technique that is used to provide micrographs of crystal surfaces at atomic resolution with 1 nm spatial resolution, providing crystal structure information and real-space imaging to local structure of thin specimens [149, 150]. In diffraction mode, both transmitted and diffracted beams can be imaged, thus the diffraction patterns of a sample can also be obtained in HRTEM, along with the high-resolution images. The diffraction patterns are very useful for structural analysis and to study of the crystal defects of a specimen. An area of the sample is selected for obtaining its diffraction pattern; thus, this method is called selected area electron diffraction (SAED).

In this thesis, the microstructure and interfacial characterization of the SLG/Mo/CIGS, SLG/Mo/CIGS/CdS, SLG/Mo/CIGS/CdS/ZnO and SLG/Mo/CIGS/CdS/ZnO/ZnO:Al multi-layer structures have been studied using conventional TEM and HRTEM imaging, along with SAED patterns and EDS analysis. Conventional TEM and HRTEM observations were carried out using a JEOL 2011 TEM operating at 200 kV with a point resolution of 0.25 nm and equipped with an EDS detector (EDAX Apollo XLT TEM-SDD). In addition, complementary morphological and elemental analysis of the CdS/CIGS/Mo/SLG structure was performed by a field emission gun Zeiss Supra 35VP SEM, equipped with an EDAX Octane Elite Plus EDS detector with a resolution of 125 eV (Mn K_α line).

3.4.2 Optical characterization

The optical characterization, investigation and data analysis have been performed by the PhD. candidate Anna Zacharia at the Experimental Condensed Matter Physics Laboratory, Department of Physics, University of Cyprus, under the supervision of Dr. Grigorios Itskos.

Absorption – Transmittance

Absorption of electromagnetic radiation is the way in which the energy of a photon is taken up by matter, typically the electrons of an atom. Thus, the electromagnetic energy is transformed into internal energy of the absorber, for example thermal energy [151]. The absorption of light by an optical medium is quantified by its absorption coefficient α.

CHRISTIANA NICOLAOU

A typical setup is presented in Figure 3.13. The light from a polychromatic light source is spectrally analyzed by a monochromator. The initial beam is separated into two beams. One beam transmits through the reference sample with intensity Io. The reference sample is a transparent substrate, identical to that of which the studied film is deposited on. The second beam transmits through the sample, typically a film deposited into a transparent substrate, with intensity $I(z)$. Both beams are measured simultaneously by photodetectors. The reference sample is used to ensure that the light scattering or absorption that may take place from the substrate of the sample are taken into account when calculating the absorption properties of the film under investigation. The spectrometer is connected to a computer from which the data are collected for processing. Absorption spectra can provide important information about the nature of energy gap (direct or indirect energy gap), exciton energy and the structure of material, the presence of defects or Urbach tail states. The absorption coefficient α of the studied film is calculated using the Beer's Law:

$$I(z) = Ioe^{-\alpha z}, \qquad \text{Equation 3.6}$$

where, z is the thickness of the studied film.

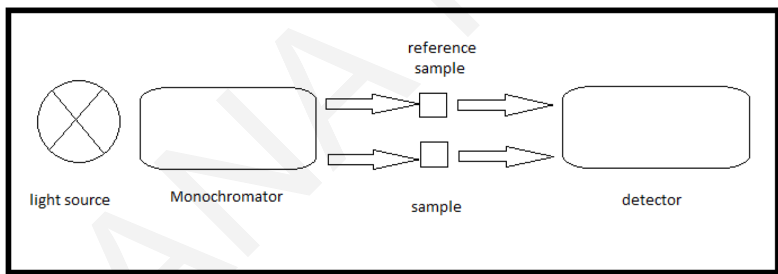

Figure 3.13 Schematic diagram of a typical experimental to measure optical density.

In this thesis, the absorption/transmittance spectra of CIGS, CdS, ZnO and ZnO:Al layers deposited on SLG substrates have been examined using the Perkin Elmer Lambda 1050 apparatus. The energy gap and absorption coefficient have been derived from the analysis of the measured spectra.

Photoluminescence (PL)

Upon absorption of a photon with energy exceeding the band gap Eg of the material, the electron is excited in the conduction band and a hole is generated in the valence band, creating an electron-hole pair. The electron-hole pair can recombine radiatively with the emission of a photon, or non-radiatively by transferring the electron's energy to impurities or defects in the material or dangling bonds at the surface [152]. The radiatively recombination of the electron-hole pair by the emission of a photon is called photoluminescence (PL).

CHRISTIANA NICOLAOU

PL experiments can provide important information about the nature of the photoexcitations and recombination channels in the material. Further information about the material can be extracted by varying experimental parameters of the PL experiments such as excitation density (excitation-dependent PL), sample temperature (temperature-dependent PL), the excitation wavelength (resonant versus non-resonant PL) and polarization state (anisotropy measurements).

The PL experiment involves the excitation of the sample by a monochromatic laser diode and the detection of the emitted photons by a detector, as shown in Figure 3.14. The sample is usually placed on a temperature controlled optical cryostat for temperature-dependent PL measurements. Between the sample and the detector, a configuration of optics such as lenses, slits and mirrors are inserted to make the beam parallel and focused. A diffraction grating analyses the beam to the different wavelengths and in different directions towards an array of photodetectors that measure the intensity of each wavelength component.

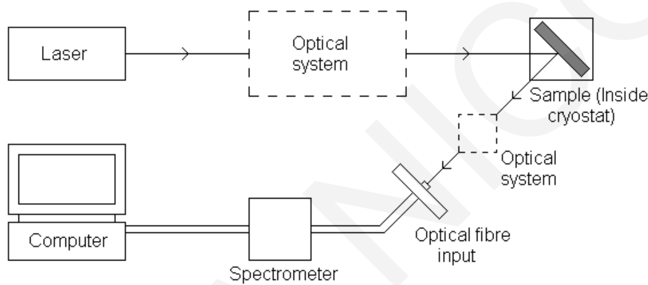

Figure 3.14 Schematic diagram of a photoluminescence experimental setup [153].

In this thesis, the PL spectra of CIGS and CdS films deposited on SLG substrates have been examined using the Princeton Acton Advanced 2750A apparatus. The lineshape, linewidth, integrated intensity and stokes shift of the measured PL spectra have been examined to provide information about the quality of the films.

Time-resolved Photoluminescence (TRPL)

In addition to steady-state PL experiments, time-resolved spectroscopy is used to assess the dynamics of the recombination mechanisms in a material. TRPL allows the study of the temporal characteristics of recombination processes and the analysis of the data provide useful information about the material, such as the exciton lifetime, Auger or trapping rates.

TRPL experiment involves the excitation of a sample with a pulsed light source and the measurement of the subsequent photoluminescence decay as a function of time. A pulsed laser with pulse width of tens of picoseconds is used, while the PL decay is detected via a photomultiplier tube. The time resolution of the TRPL measurement can be obtained via different experimental techniques. A digital counting technique called time correlated single photon counting method has been used for the TRPL measurements of this thesis. Measurements build a probability histogram relating the time between an excitation pulse and the observation of the first emitted photon [154].

CHRISTIANA NICOLAOU

In this thesis, TRPL measurements of CIGS and CdS films deposited on SLG substrates have been performed using the Horiba-Jobin Yvon FL3 apparatus with time-resolution the order of 50 ps in the visible range and 100 ps in the infrared range. The average PL lifetimes have been obtained by the time-resolved PL decays of CIGS and CdS films.

3.4.3 Device performance

The characterization of the device performance and data analysis have been performed by Dr. Vasiliki Paraskeva at the FOSS Research Centre for Sustainable Energy, Department of Electrical Engineering, University of Cyprus, under the supervision of Dr. George E. Georghiou.

Illuminated current-voltage (IV) measurement

Illuminated IV measurements involve the determination of the IV curve of a solar cell while it is illuminated under standard conditions. A solar cell is placed in a simple circuit that includes a variable resistor, a voltmeter and an ammeter (Figure 3.15). When the solar cell is exposed to light, a voltage drop appears across the terminals of the cell and is measured with a voltmeter. As a consequence, a current flow through the resistor and is measured with an ammeter. The solar cell illuminated IV curve can be obtained by altering the variable resistor and recording the voltage and current at the cell terminals. However, the most common method is to use a variable voltage source and an ammeter which is the equivalent of varying the resistor. Except from the efficiency of the cell, the basic cell parameters can be defined, such as the I_{sc}, V_{oc} and fill factor. The standard conditions for cell testing are:

- Air mass 1.5 spectrum (AM1.5) for terrestrial cells and Air Mass 0 (AM0) for space cells
- Intensity of 100 mW/cm^2 (1 kW/m^2, also known as one-sun of illumination)
- Cell temperature of 25 °C (not 300 K) [69].

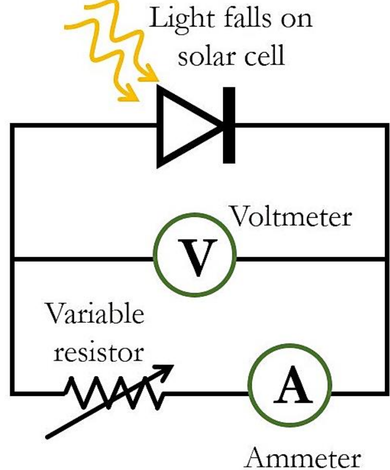

Figure 3.15 Electric circuit of the illuminated IV measurement of a solar cell [155].

CHRISTIANA NICOLAOU

In this thesis, illuminated IV measurements have been performed for the complete solar cell devices using a setup that includes a steady state solar simulator, a temperature controller, a voltage source/ammeter and a software to control the voltage rate and direction. The steady state solar simulator meets the IEC standard 60904-9 for light uniformity, light stability and conformity to the AM1.5G spectrum. The irradiance provided by the simulator is 1000W/m^2. The temperature controller keeps the temperature of the cell at 25°C. A two-probe configuration was used with the two probes mechanically placed on the front and back contacts of the cells, creating an electrical circuit. A Python dedicated software is used to conduct current-voltage measurements of the cells at different scan rates. Current-voltage curves at different scan rates are important for high capacitance solar cells presenting hysteresis effects.

CHRISTIANA NICOLAOU

Chapter 4 – Optimization of the CIGS layer

Chalcopyrite $CuIn_{1-x}Ga_xSe_2$ (CIGS) quaternary compound is a p-type, direct semiconductor used as the absorber layer in the cell's structure. The tunable energy gap of CIGS varies from 1.04 to 1.68 eV as the Ga composition ratio x changes from 0 to 1, and lies within the maximum theoretical efficiency region of AM1.5 solar irradiation [156]. The superior absorptivity of ~10^5 cm^{-1} in the visible spectrum gives the ability of effectively reducing the thickness of the absorber [21], thus reducing raw material needs and cell volume.

A variety of methods have been employed to deposit CIGS films, such as electrodeposition [157], thermal co-evaporation [158-160] and sputtering [161-163], with the latter two being the most widespread methods for obtaining high-performance solar cells. These methods often require a post-selenization treatment and precise control of the growth conditions in order to achieve the desirable composition of CIGS film. However, handling toxic Se-containing vapors raises concerns about production safety and environmental effects. Pulsed laser deposition (PLD) is well established as an efficient deposition method for multi-component films due to the stoichiometric transfer of the target material to the deposited film [56]. In the case of the quaternary $Cu(In,Ga)Se_2$ material, PLD stands out from other deposition techniques as stoichiometric films can be obtained without post-selenization. Furthermore, crystalline films can be produced at low deposition temperatures, due to the non-equilibrium process occurring during PLD growth. Along with the high deposition rates and its simplicity of use, PLD can be considered a fast, simple and low-cost method for depositing CIGS films.

Despite the advantages of PLD over other deposition techniques, few published reports exist on the growth of CIGS films using PLD [164] [165] and only a handful of those have studied the correlation between the growth parameters and the properties of PLD-grown CIGS films, towards their rational optimization in order to achieve high-quality CIGS films [166] [167] [168].

The common configuration of CIGS solar cells consist the multilayer structure Mo/CIGS/CdS/i-ZnO/ZnO:Al which implies several hetero-interfaces whose chemical, structural, and electrical properties are rather complex. These interfaces are formed in different growth conditions (temperature, pressure, background gas, etc.) and they involve many different chemical elements and compounds. The role of these interfaces is significant for the efficiency of the device. Mechanisms such as carrier recombination, trapping on interfacial states or other mechanisms affecting the charge carrier transport throughout the device are highly influenced by the interfaces [169]. Specifically, the desirable characteristics of Mo/CIGS interface for the efficient collection of the photo-generated charge carriers are the formation of an ohmic contact with a low contact resistance between the Mo and CIGS layers.

CHRISTIANA NICOLAOU

The contact between Mo and CIGS leads to a Schottky-like behavior, rectifying the current-voltage characteristic [170]. The existence of Schottky barrier at the CIGS/Mo contact results to substantial resistive losses, affecting negatively the device efficiency. Consequently, the formation of a Schottky junction at CIGS/Mo interface limits the open-circuit voltage and the fill factor of a solar cell [171]. However, it has been reported that $MoSe_2$ layer can be formed at the Mo/CIGS interface which leads to an ohmic contact [172-174]. The CIGS/Mo contact, including the MoSe2 layer, is found to be ohmic due to the small valence-band offset at the $MoSe_2$/CIGS interface which does not present an appreciable barrier to hole transfer across the interface [175].

The formation and properties of the intermediate $MoSe_2$ layer depend on the CIGS deposition method and growth conditions [176], therefore, the orientation of the $MoSe_2$ layer (c axis parallel or perpendicular to the Mo surface) vary a lot in the literature. Several works report for a layered structure of $MoSe_2$ with its layers oriented perpendicular to the Mo layer [176, 177]. In addition, it is considered that the $MoSe_2$ layer contributes to the improvement of the adhesion at the CIGS/Mo interface [172]. On the other hand, delamination issues are typically correlated with the interface between the Mo back contact layer and the absorber CIGS layer, and specifically, with the orientation of the two-dimensional $MoSe_2$ interfacial layer [176, 178, 179]. The variety of studies as well as the variety of results shows that the properties of the $MoSe_2$ interfacial layer are very sensitive to the experimental conditions.

Section 4.1 of this chapter reports on the systematic investigation of the effect of PLD growth parameters on the properties of $CuIn_{0.7}Ga_{0.3}Se_2$ thin films deposited on soda-lime glass substrates. The influence of the growth conditions of CIGS films is investigated through a comprehensive characterization of structure, composition and morphology. In addition, electrical and optical measurements of CIGS films have been performed in order to study the transport and optical properties of the films. The optimum PLD growth conditions for CIGS films are identified based on an overall assessment of film characteristics. Next, in section 4.2, the deposition temperature of CIGS on Mo-coated SLG substrates is investigated using the optimum PLD growth conditions obtained from the previous section. A thorough characterization of structure, composition and adhesion of CIGS/Mo/SLG structure, along with IV measurements, have been implemented for the identification of the optimum deposition temperature.

CHRISTIANA NICOLAOU

4.1 CIGS on SLG

4.1.1. Materials and experimental methods

CIGS films were deposited on soda-lime glass (SLG) substrates by PLD using a KrF excimer laser source (λ = 248 nm, $\tau \leq 25$ ns) in a high-vacuum chamber. The laser beam was driven through an arrangement of mirrors and focused by a focal lens on a polycrystalline $CuIn_{0.7}Ga_{0.3}Se_2$ (*Testbourne, England*) target at an incident angle of 45° inside the chamber. The target rotation during the irradiation ensured a uniform ablation of the target surface. The substrate was placed parallel to the surface target at a fixed distance of 4.5 cm. The deposition was carried out in the presence of background gas after the chamber was evacuated at a base pressure of $4x10^{-6}$ mbar. Argon (Ar) was used as background gas to confine the plume. The number of pulses and the repetition rate were kept constant at 6000 and 10 Hz respectively, for all depositions. Laser fluence, Ar background pressure and substrate temperature as the primary PLD deposition parameters were systematically investigated in order to achieve the optimum growth conditions for high quality CIGS films. Prior to deposition, the substrates were ultrasonically cleaned with a sequence of organic solvents. In addition, secondary PLD deposition parameters, such as pulses, repetition rate, distance between target and substrate and the type of substrate, were investigated and are briefly presented in the next section.

Structural properties and crystallinity of the films were studied by X-ray diffraction (*SmartLab RIGAKU, Cu Kα, λ = 1.5405 Å*). Morphology and chemical composition of the films were determined by scanning electron microscopy (*SEM Tescan Vega LSU*) and energy dispersive X-ray spectroscopy (*Jeol Bruker Nano 129eV, XFlash 5010 detector*), respectively. The electron accelerating voltage of the EDS source was adjusted at 20 kV, corresponding to a penetration depth of 1.5 μm, which was larger than the thickness of the films. The thickness of the films was measured with a stylus profilometer. Topography and surface roughness were probed via atomic force microscopy (*AFM, Agilent Technologies*) scanning a 20x20 μm^2 area within the film's surface. The electrical resistivity ρ, and carrier concentration n, of the films were measured at room temperature using the Van der Pauw method and Hall Effect measurement. Au wires were directly attached on the films' surface using conductive silver paste. A current of 20 μA and a magnetic field of 6 T were applied for the electrical measurements. Hall mobility was calculated by the following equation:

$$\mu = \frac{1}{\rho n e}. \qquad \textbf{(Equation 4.1)}$$

Optical transmission was recorded using a triple-detector spectrophotometer (*Perkin Elmer, Lamda 1050*) covering the 200-3000 nm spectral range. The measurements allow the determination of the transmissivity T of the films as the ratio of the transmitted light intensity I_T to that of the incident intensity I_0:

CHRISTIANA NICOLAOU

$$T = \frac{I_T}{I_0}. \qquad \textbf{(Equation 4.2)}$$

Reflectivity experiments were performed using the output of a 450 W Xe Arc broadband lamp spectrally filtered by a double monochromator and detected by a photolumultiplier tube.

The absorption coefficient α of the films can then be estimated [180] through the relationship:

$$T = (1 - R)^2 e^{-al}, \qquad \textbf{(Equation 4.3)}$$

where T is the transmissivity and R is the reflectivity, measured by the aforementioned optical experiments, and ℓ is the film thickness.

Steady-state photoluminescence (PL) was excited via a 785 nm laser diode module (*Coherent StingRay*) with a power density of ~50 $mW\text{-}cm^{-2}$ and detected by a high-resolution spectrometer (*0.75 m Acton750i Princeton*) equipped with a liquid-nitrogen-cooled InGaAs array detector. Time resolved PL was recorded on a FluoroLog FL3 Horiba Jobin Yvon spectrofluorimeter using a time correlated single photon counting (TCSPC) method. The PL was excited by a 785 nm pulsed laser diode (DeltaDiode-785L) with a pulse width of ~80 ps. The average PL lifetime t_{avg} of the PL decays was calculated from the relation:

$$t_{avg} = \frac{\sum_i A_i \tau_i^2}{\sum_i A_i \tau_i}, \qquad \textbf{(Equation 4.4)}$$

where τ_i are the decay times extracted from multi-exponential fits of the PL transients and A_i the corresponding decay amplitudes.

4.1.2. Results and discussion

4.1.2.1 Impact of Laser Fluence

The fluence of the irradiation was regulated by the laser energy and the spot size to obtain values from 0.4 to 1.4 J/cm^2. Figure 4.1 shows the compositional ratios of the films deposited at 300 ^oC in Ar atmosphere of 0.01 mbar obtained by EDS measurements. The compositional ratios of a stoichiometric transfer from the target to the film are denoted on Figure 4.1 with the dashed lines and are the following: CGI=Cu/(Ga+In)=1, GGI=Ga/(Ga+In)=0.3, IGI=In/(Ga+In)=0.7 and Se/M=Se/(Cu+Ga+In)=1. As the figure shows, all films are slightly In-rich and Ga-poor with respect to the target stoichiometry. The GGI ratio of the films is ~0.26, which lies within the range of high-efficiency cells [181]. Nearly stoichiometric films are obtained as the fluence increases with a lower threshold at 0.8 J/cm^2. The films grown at lower fluences (0.4 and 0.6 J/cm^2) are Se-rich and Cu-poor. The magnitude of the ablation yield is determined by the cohesive energy of an element [56] and tends to be higher for elements with low cohesive energy. In this case, Se is more readily extracted from the target as it has the lowest cohesive energy (2.46 eV/atom), while Cu having the

CHRISTIANA NICOLAOU

highest cohesive energy (3.49 eV/atom) is much less volatile. Low fluence leads to pure evaporation of the elements [56] with preferential evaporation of Se and unfavorable evaporation of Cu, resulting in Se-rich and Cu-poor films. Similar results have also been observed for Cu_2ZnSnS_4 (CZTS) absorber, which consists of earth-abundant elements [182]. Generally, the congruent ablation of the elements of a target can be achieved when the fluence is above a threshold value, which is defined by the elements in the target. In the case of CIGS, the threshold fluence of CIGS target is 0.8 J/cm^2, as shown in Fig. 1. Moreover, Cu-poor films have been grown by PED due to incongruent evaporation caused by low-energy electrons [183] [184].

Grazing incidence XRD (GIXRD) patterns of the films deposited at various values of fluence, with 2θ ranging between 10° and 90° are shown in Figure 4.2. All deposited films exhibit seven diffraction peaks identified as (112), (220)/(204), (312)/(116), (400)/(008), (332), (424), (512) planes of $CuIn_{0.7}Ga_{0.3}Se_2$ chalcopyrite phase (JCPDS 35-1102), with (112) peak being the most prominent. The XRD patterns reveal the polycrystalline nature of the films. It must be noted that the pronounced (112) peak also appears in the out-of-plane XRD patterns of all samples (not shown here), indicating the existence of preferred orientation along the (112) plane. The preferred orientation of (112) have also been observed in films grown by PED [183]. This (112) texture of CIGS films is beneficial for obtaining good lattice matching with CdS layers, which can lead to highly efficient solar cells [185]. An additional peak at ~25.6^o appears on the GIXRD patterns of films grown at fluences higher than 0.6 J/cm^2, attributed to the Cu_2Se secondary phase (JCPDS 37-1187). The appearance of the Cu_2Se phase at high laser energies has also been observed by Jo et al. [167]. It is worth mentioning that the minor peak of Cu_2Se phase can only be distinguished when the GIXRD intensity data are presented in a logarithmic scale. The appearance of the Cu_2Se secondary phase in CIGS films grown at high fluences can be attributed to the enhanced kinetic energy of the atoms upon arriving at the substrate surface. At high fluences, atoms possess sufficient kinetic energy to diffuse at greater distances on the surface, before they establish stable, energetically favorable bonds with other film atoms [56]. Since light atoms diffuse faster than heavy ones, Cu-Se bonds are formed and the Cu_2Se secondary phase appears.

CHRISTIANA NICOLAOU

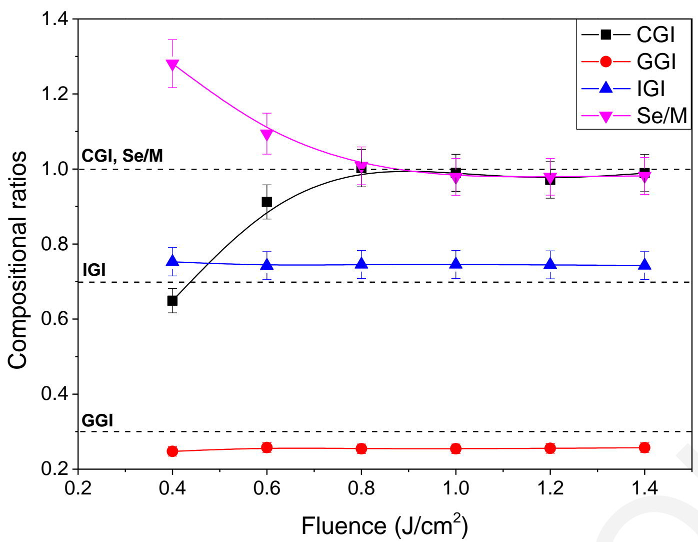

Figure 4.1 Compositional ratios of CIGS thin films deposited on SLG substrates at different fluences ranging from 0.4 to 1.4 J/cm^2. Dashed lines indicate the ratios of a stoichiometric film, being CGI=Cu/(Ga+In)=1, GGI=Ga/(Ga+In)=0.3, IGI=In/(Ga+In)=0.7 and Se/M=Se/(Cu+Ga+In)=1. Stoichiometric films are obtained using fluence of 0.8J/cm^2 and higher.

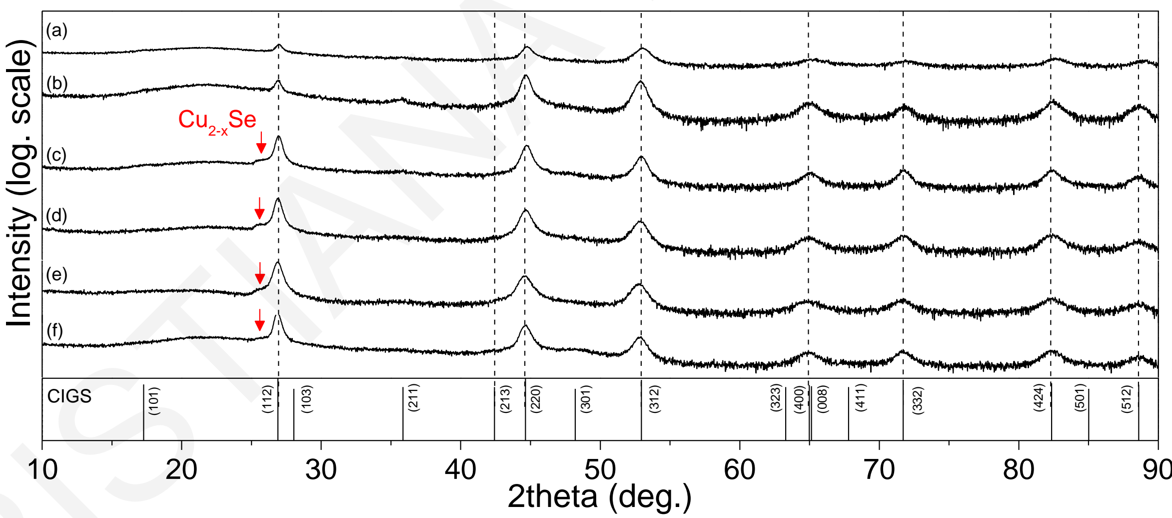

Figure 4.2 XRD patterns of CIGS thin films deposited on SLG substrates at (a) 0.4, (b) 0.6, (c) 0.8, (d) 1.0, (e) 1.2 and (f) 1.4 J/cm^2. The bottom plot shows the XRD pattern of $CuIn_{0.7}Ga_{0.3}Se_2$ according to JCPDS 35-1102. A minor secondary phase of $Cu_{2-x}Se$, indicated by the arrows, appears in films grown at fluences higher than 0.6 J/cm^2.

CHRISTIANA NICOLAOU

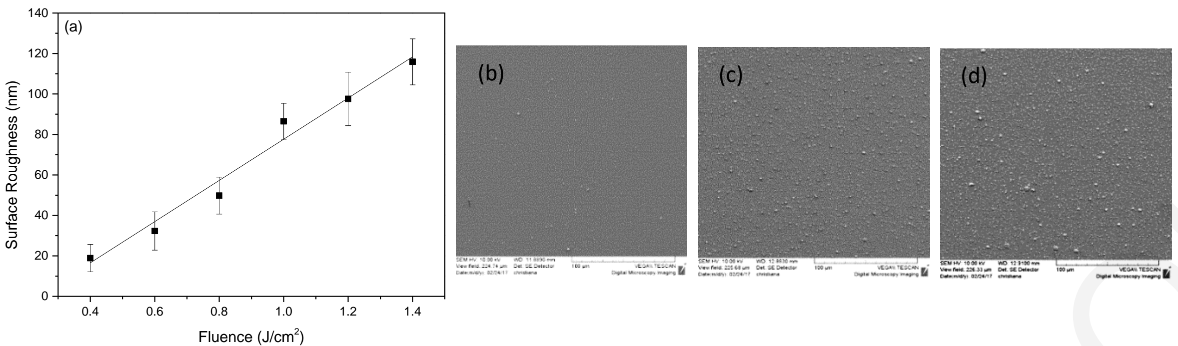

Figure 4.3 (a) Surface roughness of CIGS thin films deposited on SLG substrates at different fluences ranging from 0.4 to 1.4 J/cm^2. (b), (c), (d) SEM images of CIGS thin films deposited on SLG substrates at fluence of 0.4, 1.0 and 1.4 J/cm^2, respectively. The surface roughness of the films increases linearly as the fluence becomes higher, due to the increasing density and size of particulates on the film surface.

The surface roughness of the films as a function of fluence, measured by AFM, is presented in Figure 4.3a. Three different areas of 20x20 μm^2 were scanned for each film. The surface roughness was calculated by averaging the rms roughness of each area. The evident linear increase in the surface roughness of the films with increasing fluence is attributed to the concurrently increasing density and size of particulates on the film surface, as illustrated in the SEM images of Figure 4.3(b - d). The generation of more particulates at high fluence could be attributed to the increased number of species which are ejected from the target as a result of the repeated thermal shocks [109]. In addition, overheating of the target at high fluence leads to the formation of droplets that are expelled from the melted surface of the target directly onto the substrate [186].

Property	Low Fluence (0.4-0.6 J/cm^2)	High Fluence (0.8 – 1.4 J/cm^2)
Stoichiometry	Se-rich, Cu-poor films	Nearly stoichiometric films, $CuIn_{1-x}Ga_xSe_2$ (x~0.26)
Secondary phase	None	$Cu_{2-x}Se$ phase
Surface roughness	Increasing from ~20 nm to ~120 nm	
Particulates	Increasing density and size	

Table 4.1 Summary of the main results obtained from the investigation of laser fluence.

Table 4.1 shows the main results of the impact of laser fluence on the properties of CIGS films. The results of the systematic investigation of the fluence on the growth of CIGS thin films reveal the existence of a threshold fluence value of 0.8 J/cm^2 above which stoichiometric films $CuIn_{1-x}Ga_xSe_2$ (x~0.26) are obtained. Additionally, a minor secondary phase of Cu_2Se appears at fluences equal or higher than 0.8 J/cm^2 due to the sufficient kinetic energy and diffusion of the light Cu and

CHRISTIANA NICOLAOU

Se atoms. Hence, a fluence of 1 J/cm^2 is deduced to be the most appropriate for the growth of CIGS thin films, because stoichiometric films are obtained having an intermediate roughness of ~80 nm, while maintaining the high deposition rates of PLD. Working at 1 J/cm^2, stoichiometric CIGS films with a thickness of ~800 nm are obtained, using 6000 pulses in a deposition which lasts only 10 minutes (deposition rate ~0.13 nm/pulse). Thus, PLD can serve as a fast, single-step process, without the need of selenization, for the deposition of stoichiometric CIGS films.

4.1.2.2 Impact of Background pressure

Argon (Ar) was used as background gas for the growth of all samples. Figure 4.4 shows the EDS-determined compositional ratios of the films deposited under various background pressures at 300 ^{o}C with fluence 1 J/cm^2. As the figure indicates, all films are slightly In-rich and Ga-poor with respect to the target stoichiometry, with x~0.26. Nearly stoichiometric films are obtained as Ar pressure increases with a threshold at 0.01 mbar. The films grown at low pressure are Se- and Cu-poor. In general, the presence of an ambient gas during the PLD process results in several effects such as collisions and reactive scattering of the plume species with the gas particles, sharpening of the plume boundary and spatial confinement of the plume [187]. In the case of inert gas such as Ar, reactive scattering does not take place. The angular distribution of the plume atoms depends on their atomic mass. Light ablated atoms are scattered much more than heavy ones in the presence of a heavy background gas, such as Ar [188] [107]. In the case of the multicomponent CIGS target, the assortment from light to heavy elements is: Cu (Z=29), Ga (Z=31), Se (Z=34) and In (Z=49). Heavy atoms preferentially propagate along the normal direction (where the substrate is usually placed) during the expansion in a background gas [189], which explains the In-rich samples. Cu, Ga and Se atoms being the light elements of the plume, scatter the most and their angular distribution is broad. At low pressure, the light elements are more prone to escape from the plume and are lost through the pumping system. As the Ar pressure increases, the plume becomes more confined and the light elements cannot easily escape from the plume, thus the films become nearly stoichiometric. Indium atoms, as the heaviest species of the plume, propagate along the normal direction at the same concentration, regardless of Ar pressure. Considering that Ga content reaching the substrate increases as Ar pressure increases, the IGI ratio decreases and becomes more stoichiometric.

CHRISTIANA NICOLAOU

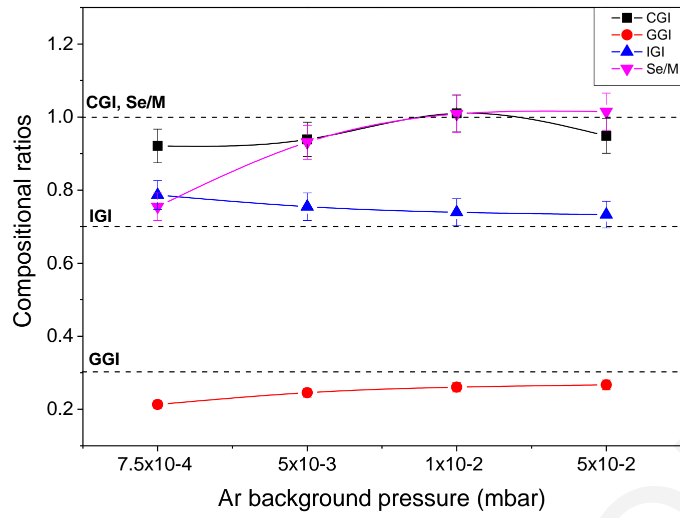

Figure 4.4 Compositional ratios of CIGS thin films deposited on SLG substrates at different Ar pressures. Dashed lines indicate the ratios of a stoichiometric film, being CGI=Cu/(Ga+In)=1, GGI=Ga/(Ga+In)=0.3, IGI=In/(Ga+In)=0.7 and Se/M=Se/(Cu+Ga+In)=1. Stoichiometric films are obtained using Ar pressure of 0.01mbar and higher.

GIXRD patterns of the films deposited at various Ar pressures ranging from 10^{-4} to 10^{-2} mbar are shown in Figure 4.5 in a logarithmic scale. All deposited films exhibit seven diffraction peaks identified as (112), (220)/(204), (312)/(116), (400)/(008), (332), (424), (512) planes of $CuIn_{0.7}Ga_{0.3}Se_2$ chalcopyrite phase (JCPDS 35-1102), with (112) peak being the most prominent. The XRD patterns indicate the polycrystalline structure of the films. An additional very-low intensity peak at ~25.6°, is attributed to the Cu_2Se secondary phase described earlier (JCPDS 37-1187). This minor peak of Cu_2Se phase becomes more distinct as Ar pressure increases in which case the plume becomes more confined and the species are restricted in a smaller volume, thus, the collisions between the species are increased. As a consequence, the formation of Cu-Se clusters in the plume, which are being transferred to the substrate as crystalline clusters, is favored.

CHRISTIANA NICOLAOU

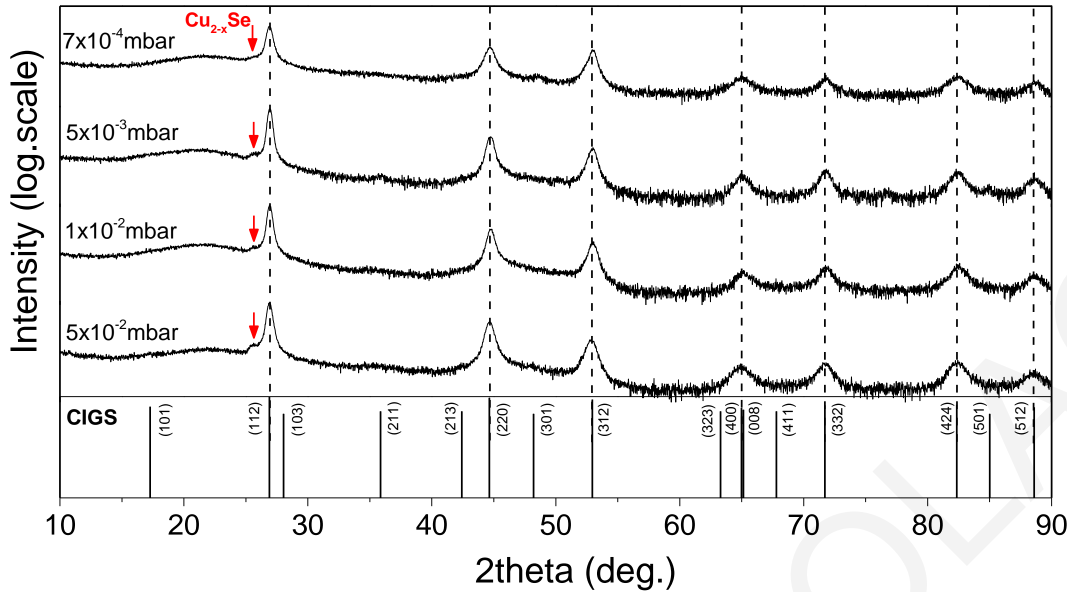

Figure 4.5 XRD patterns of CIGS thin films deposited on SLG substrates at various Ar pressures. The bottom plot shows the XRD pattern of $CuIn_{0.7}Ga_{0.3}Se_2$ according to JCPDS 35-1102. A minor secondary phase of $Cu_{2-x}Se$, indicated by the arrows, appears in all films.

The AFM-measured surface roughness of the films as a function of Ar pressure is presented in Figure 4.6a. The surface roughness was calculated by averaging the rms roughness of three different areas of 20x20 μm^2. The surface roughness increases with increasing background pressure and exhibits an abrupt increase at $5x10^{-3}$ mbar. The large roughness of the films (>80 nm) grown at high pressure is attributed to the high areal density of particulates on the film surface. SEM images (Figure 4.6b - d) indicate that the areal density and size of particulates increase with increasing Ar pressure. The collision rate of the ejected species with the ambient gas atoms increases as the ambient gas pressure increases leading to nucleation and growth of these plume species into particulates before their arrival at the substrate. The longer the time the particulate resides in the plume, the larger the particulate becomes, as in the case of high Ar pressure [190]. Pinholes are observed in the Cu-deficient film grown at the lowest Ar pressure, which are shown by the arrows in Figure 4.6b. Similar microstructure defects have also been found in Cu-deficient CIGS films deposited by one-step radio frequency sputtering [161].

CHRISTIANA NICOLAOU

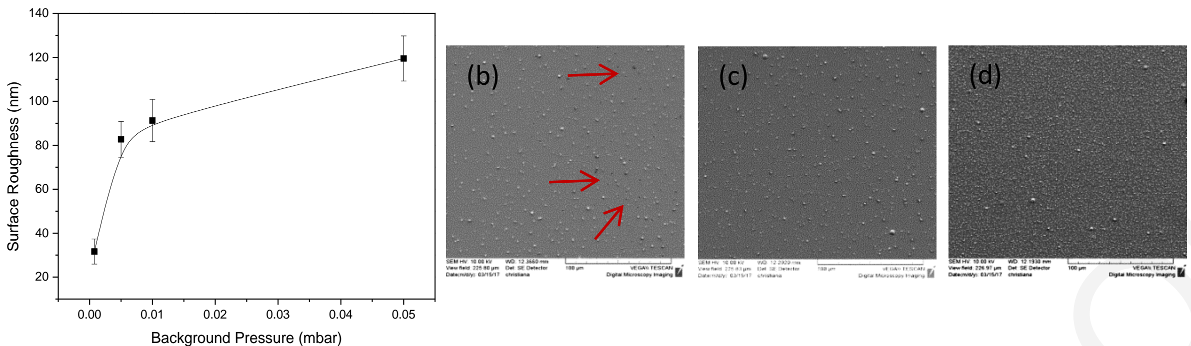

Figure 4.6 (a) Surface roughness of CIGS thin films deposited on SLG substrates at various Ar pressures. (b), (c), (d) SEM images of CIGS thin films deposited on SLG substrates at Ar pressure of $7x10^{-4}$, $1x10^{-1}$ and $5x10^{-2}$ mbar, respectively. The arrows in (b) indicate regions with pinholes on the film's surface. The surface roughness of the films increases abruptly as the Ar pressure becomes higher, due to the increasing areal density and size of particulates on the film surface.

Property	Low Ar Pressure (10^{-4} – 10^{-3} mbar)	High Ar Pressure (10^{-2} mbar)
Stoichiometry	Se- and Cu-poor films	Nearly stoichiometric films, $CuIn_{1-x}Ga_xSe_2$ (x~0.26)
Secondary phase	$Cu_{2-x}Se$ phase	
Surface roughness	Increasing from ~30 nm to ~120 nm	
Particulates	Increasing density and size	

Table 4.2 Summary of the main results obtained from the investigation of Ar pressure.

The impact of Ar pressure on the films properties is summarized in Table 4.2. The systematic investigation of the effect of background pressure on the growth of CIGS thin films reveals that there is a threshold Ar pressure, 0.01 mbar, in obtaining stoichiometric $CuIn_{1-x}Ga_xSe_2$ films (x~0.26). In addition, a minor secondary phase of Cu_2Se appears in all films. Hence, Ar pressure of 0.01 mbar is deduced as the most appropriate for the growth of CIGS thin films, because stoichiometric films can be obtained having an intermediate roughness of ~ 90 nm.

4.1.2.3 Impact of Substrate Temperature

Soda-lime glass was used as substrate for the deposition of CIGS films. Figure 4.7 shows the EDS-determined compositional ratios of the films deposited at various substrate temperatures. The assessment of the previous investigations related to fluence and background gas pressure have led to the selection of 1 J/cm^2 and 0.01 mbar, respectively. As the figure indicates, all films are nearly stoichiometric independently of the deposition temperature, with slightly In-excess and Ga-

CHRISTIANA NICOLAOU

deficiency with respect to the target stoichiometry. Specifically, the stoichiometry of the films is $CuIn_{1-x}Ga_xSe_2$, with x~0.26. It is noted that CGI ratio changes with the growth temperature in the case of PED-grown films [183].

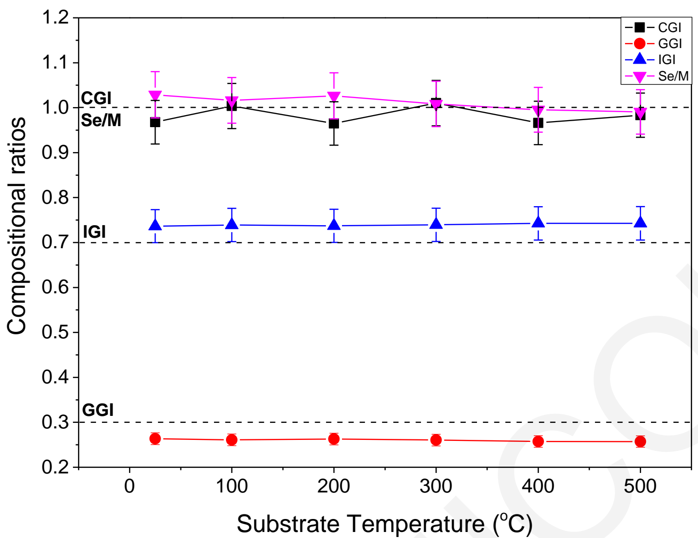

Figure 4.7 Compositional ratios of CIGS thin films deposited on SLG substrates at various substrate temperatures. Dashed lines indicate the ratios of a stoichiometric film, being CGI=Cu/(Ga+In)=1, GGI=Ga/(Ga+In)=0.3, IGI=In/(Ga+In)=0.7 and Se/M=Se/(Cu+Ga+In)=1. All films are stoichiometric in respect to the target stoichiometry.

GIXRD patterns of the films deposited at various substrate temperatures, from room temperature up to 500 °C, are shown in Figure 4.8 in a logarithmic scale. All deposited films exhibit the diffraction peaks described previously with the addition of the weak peak of Cu_2Se secondary phase (JCPDS 37-1187) on the films grown at low temperatures. The detailed XRD patterns, from 20° to 30°, are shown in the inset of Figure 4.8. The $Cu_{2-x}Se$ peak becomes less intense as the deposition temperature increases and eventually disappears on films grown at 500 °C. As the substrate temperature increases, the surface mobility of the ablated species increases, regardless of the atomic mass, and the single CIGS chalcopyrite phase is obtained. The results concerning the $Cu_{2-x}Se$ secondary phase are contradictory with those of Jo et al. [167]. No secondary phase was observed in their XRD patterns for PLD-grown CIGS films on soda-lime glass substrates even at the high deposition temperature of 500 °C. However, Raman spectra of CIGS films showed the existence of a $Cu_{2-x}Se$ phase, which becomes more discrete as the substrate temperature increases. These conflicting reported results can be attributed to the fact that the deposition of CIGS films was carried out by Jo et al. in vacuum and the plume dynamics were completely different in comparison with our deposition in Ar atmosphere. Figure 4.8 inset shows also that the position of the (112) peak shifts to higher 2θ angles as the deposition temperature increases. Specifically, the (112) peak shifts from 26.72° to 26.92° as the substrate temperature increases from room temperature to 500 °C. The shift

CHRISTIANA NICOLAOU

of the Bragg angle towards the stoichiometric bulk value of chalcopyrite CIGS (2θ=26.92°, JCPDS 35-1102) indicates the relief of strain in the film's crystal structure. This observation is reinforced by the fact that the films grown at room temperature and at 100 °C underwent delamination a few hours after deposition. Similar results have been reported previously [166, 168].

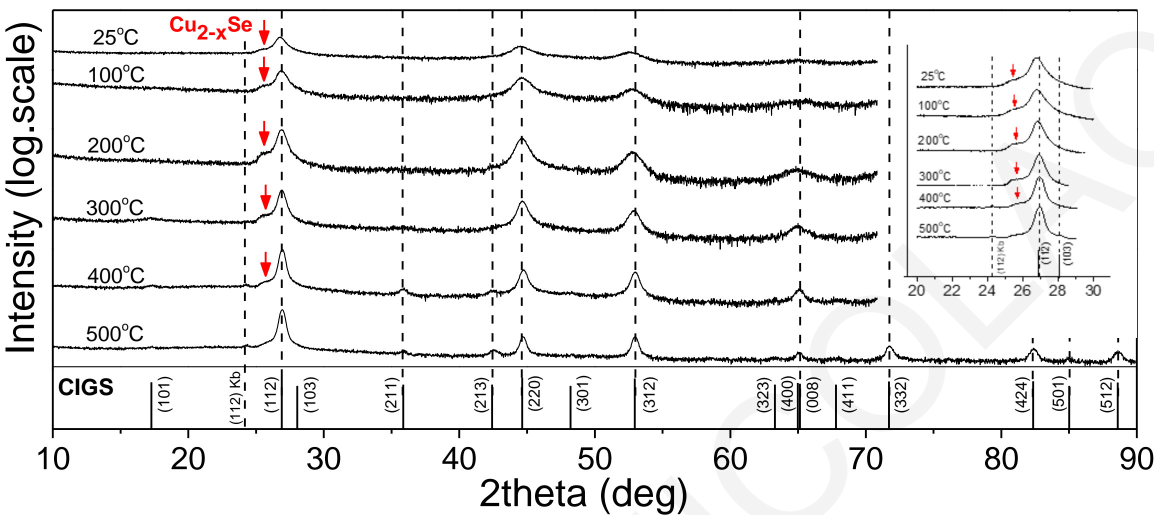

Figure 4.8 XRD patterns, 10° - 90° and 20° - 30° (inset), of CIGS thin films deposited on SLG substrates at different substrate temperatures. The bottom plot shows the XRD pattern of $CuIn_{0.7}Ga_{0.3}Se_2$ (JCPDS 35-1102). The secondary phase of $Cu_{2-x}Se$ is indicated by the arrows. The $Cu_{2-x}Se$ peak gradually fades as the deposition temperature increases. The (112) peak shifts towards the stoichiometric bulk value of chalcopyrite CIGS.

The electrical properties of the films grown at different substrate temperatures are shown in Figure 4.9a. Dark electrical resistivity ρ and carrier concentration n were measured at room temperature by the van der Pauw four-probe technique. Resistivity is in the order of 10^{-1} Ω·cm and increases as the substrate temperature increases. This resistivity increase is attributed to the increasing purity of CIGS films. As the substrate temperature increases, the highly conductive p-type Cu_2Se [191] phase gradually disappears and the single CIGS chalcopyrite phase is obtained (Figure 4.8). The hypothesis is further confirmed by Hall measurements, which indicate that all CIGS films exhibit p-type conductivity with carrier concentration decreasing by one order of magnitude, i.e. from 10^{19} to 10^{18} cm^{-3}, as the substrate temperature increases from room temperature to 500 °C. Similar values of carrier concentration were measured on PLD-grown [167] [168] and sputtered [162] [163] CIGS films. The decreasing carrier concentration with increasing substrate temperature can be attributed to the presence of p-type Cu_2Se phase in the films grown at low temperature. The Cu_2Se phase, which is characterized by a large carrier concentration [192], contributes a large number of holes, thus resulting in a high overall carrier concentration of the CIGS films. As the substrate temperature increases, the Cu_2Se phase disappears and the carrier concentration of CIGS films decreases. In addition, the presence of Cu_2Se phase in films grown at room temperature up to 400 °C may lead to the formation of Cu and Se vacancies in the CIGS lattice. Because Cu and Se atoms are

CHRISTIANA NICOLAOU

involved in both CIGS and Cu_2Se lattices and since Cu and Se compositional ratios are stoichiometric (Figure 4.7), we expect that Cu and Se atoms which take part in the formation of the Cu_2Se phase will leave vacancies in the CIGS lattice. Cu vacancies act as shallow acceptors and Se vacancies act as donors [193]. Since Cu vacancies would be twice the number of Se vacancies in the CIGS lattice, the p-type conductivity of the films is enhanced and the carrier concentration is high. The single CIGS phase obtained in the film deposited at 500 °C is nominally free of Cu and Se vacancies, thus the carrier concentration decreases. Similar results of the increase of resistivity and decrease of carrier concentration as Cu_2Se phase disappears are found in the literature for CIGS films deposited by PLD [167], by three-stage co-evaporation [160] [159], by two stage DC and MF sputtering [194] [162] and by one-stage RF sputtering [163].

Regarding the incorporation of Na into CIGS films through diffusion from SLG substrates, there have been several studies reporting the beneficial effects on cells' performance. Na diffusion increases the effective hole carrier concentration and improves the p-type conductivity, thus resulting in higher open circuit voltages V_{oc}. The proposed models for the above effect are numerous and can be found in the literature [195] [196] [197] [198]. The enhancement of (112) texture in CIGS films is also linked with Na diffusion [199] [200] [30]. In our case, all films exhibit (112) preferred orientation, which becomes more pronounced as the substrate temperature increases, indicating stronger Na diffusion. However, the hole carrier concentration decreases with the deposition temperature despite the stronger Na diffusion, leading to the conclusion that the effect of Cu_2Se phase on carrier concentration, described above, is more significant than the effect of Na diffusion into CIGS films.

The electrical properties (resistivity, Hall mobility and carrier concentration) of the samples along with the full-width half maximum (FWHM) of the (112) peak and the crystallite size, as a function of the substrate temperature, are listed in Table 4.3. Figure 4.9b shows the dependence of Hall mobility and FWHM of (112) peak on substrate temperature. The highest value of ~1.9 $cm^2V^{-1}s^{-1}$ is obtained at the deposition temperature of 500 °C, which is similar to other reported values for PLD-grown CIGS films [168]. The enhancement of carrier mobility with increasing deposition temperature is consistent with the improved crystal quality of the films. The increase in crystallite size, calculated by the Debye-Scherrer formula, indicates an improvement in the crystallinity of the films; thus, the grain boundary scattering of charge carriers decreases and the carrier mobility is expected to increase (Figure 4.9b). The high mobility of the film deposited at 500 °C is also attributed to the diminished scattering of charge carriers by ionized defects and other charge carriers due to its pure CIGS phase and its low defect and carrier concentration.

CHRISTIANA NICOLAOU

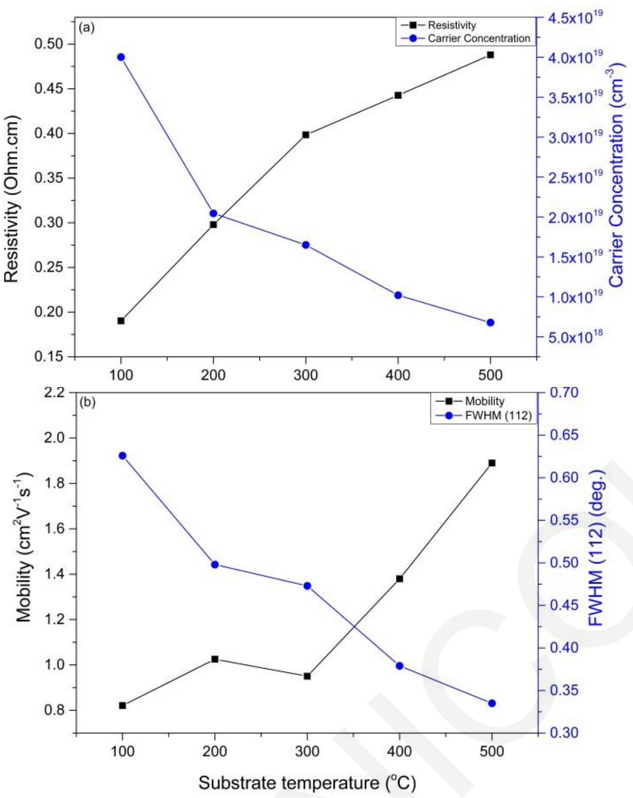

Figure 4.9 (a) Room temperature electrical resistivity and carrier concentration and (b) Hall mobility and FWHM of (112) peak of CIGS films as function of substrate temperature. As the substrate temperature increases, resistivity increases, carrier concentration decreases, crystallinity of the films is improved, and mobility is enhanced.

Substrate Temperature (^oC)	Resistivity (Ω.cm)	Carrier Concentration (cm^{-3})	Hall Mobility ($cm^2V^{-1}s^{-1}$)	FWHM of (112) (deg.)	Crystallite size (nm)
25	-	-	-	0.623	14.27
100	0.190	4.00×10^{19}	0.821	0.626	14.21
200	0.298	2.05×10^{19}	1.03	0.498	17.86
300	0.398	1.65×10^{19}	0.951	0.473	18.82
400	0.443	1.02×10^{19}	1.38	0.379	23.50
500	0.488	6.79×10^{18}	1.89	0.335	26.59

Table 4.3 Electrical properties, FWHM and crystallite size of CIGS films deposited on SLG substrates at different substrate temperatures.

The light harvesting ability of the PLD-grown CIGS films is evaluated by the magnitude and spectral variation of the absorption coefficient, which has been estimated by optical transmission and reflectivity experiments, as described in the experimental section. The absorption coefficient in the

CHRISTIANA NICOLAOU

range of 0.8 to 2 eV for CIGS films grown at various substrate temperatures is displayed in the graphs of Figure 4.10.

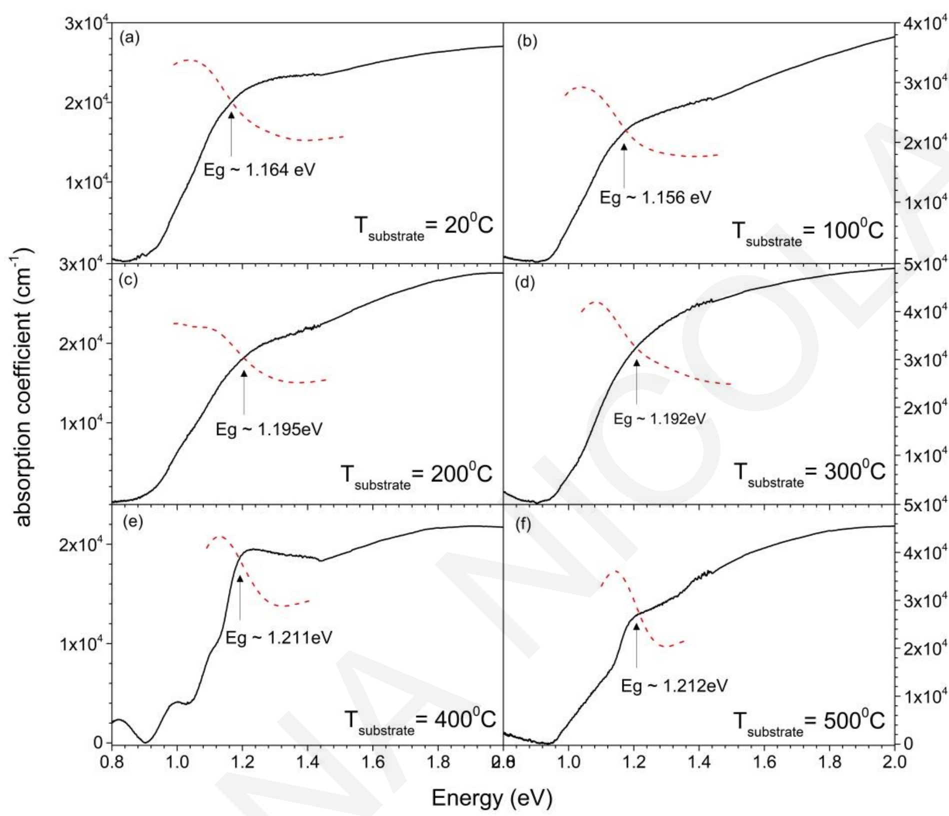

Figure 4.10 Spectral variation of the absorption coefficient of CIGS films grown at various substrate temperatures. The first derivative of the absorbance and the estimated energy gap for each film is also shown.

The films exhibit high absorption coefficients of ~2-3x10^4 cm^{-1} in the vicinity of the band-edge standing in par with coefficients of previously reported module-ready CIGS films [201] and recently demonstrated PLD-grown CIGS thin films [202] [203]. A recent publication reports on higher absorption coefficients in PLD-grown CIGS thin films, surpassing 10^5 cm^{-1} in the visible [204]; however, such values appear artificially inflated as the optical absorption measurements do not account for the significant light scattering losses at the films' surface.

In the latter report, the influence of deposition temperature on the absorption coefficient is also investigated, demonstrating a reduction of the absorption coefficient and an increase of the band gap energy (E_g) as substrate temperature increases. In our studies, we have not observed a correlation of the optical absorption strength with the substrate temperature; on the other hand, a systematic blue shift of the band gap energy with deposition temperature is indeed observed, as shown in Figure 4.11.

CHRISTIANA NICOLAOU

A systematic temperature-dependent variation of the stoichiometry has to be excluded as a possible origin of the effect based on the EDS results of Figure 4.7, revealing a negligible compositional impact of the substrate temperature. Quantum confinement effects suggested by Sima et al. [204] as a possible source of the shift are also unimportant at the micron-size scales of the deposited films. It is likely that the hypsochromic shift of the band gap energy is a result of the strain relief of the chalcopyrite crystal structure, indicated by the respective Bragg angle shifts in the XRD patterns of Figure 4.8; such band-edge shifts, induced by lattice strain, have been reported previously [205].

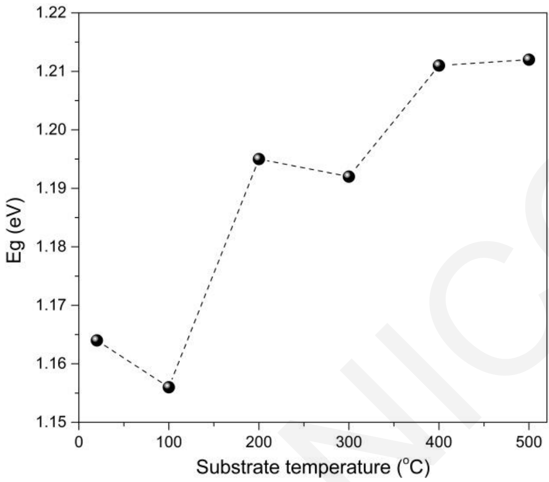

Figure 4.11 Variation of the optical band gap energy versus substrate temperature. A systematic blue shift of the band gap energy with deposition temperature is observed.

It is noted that the band gap energy of the studied films is determined from the inflection point of the first derivative of the absorbance, which is superimposed to the absorption coefficient data of Figure 4.10. Almost identical values are also obtained using the minima of the second derivative of the absorbance. Compared to the conventionally used Tauc plot method, the first-derivative method in our case provides a more reliable estimation of the CIGS band-edge, which is consistent with the photoluminescence spectra presented later in the text. This is due to the fact that the linear extrapolation process used in the former method to determine the band gap energy is affected by the presence of the $Cu_{2-x}Se$ secondary phase and the contribution of band-tail states of the complex quaternary semiconductor.

Figure 4.12 presents comparative and normalized PL spectra of the CIGS films under non-resonant excitation with a 785 nm laser at 300K. The observed broad, multi-peak lineshape is typical of the high spatial and energetic disorder of CIGS materials, as well as the presence of high energy band-edge and low energy defect-mediated recombination channels. A detailed analysis of the nature and characteristics of the carrier recombination mechanisms is beyond the scope of the present manuscript, however PL experiments reported herein strongly indicate an improvement in the material quality and uniformity with increasing substrate temperature. This is evidenced by the: (i)

CHRISTIANA NICOLAOU

monotonic increase in the integrated PL intensity, and (ii) systematic decrease of the PL linewidth and Stokes shift. The observed trends are attributed to the reduction of the band-edge potential fluctuations and the suppression of non-radiative recombination at defects related to the secondary $Cu_{2-x}Se$ phase, as well as the presence of Cu and Se vacancies elaborated previously in the manuscript, that act as shallow acceptors and donors, respectively. The effective blue-shift of the luminescence as temperature increases is also consistent with an increased contribution at high energies due to emission from electronic states at the expense of the lower energy defect-related recombination; it also supports the small band gap hypsochromic shift revealed by the optical absorption experiments.

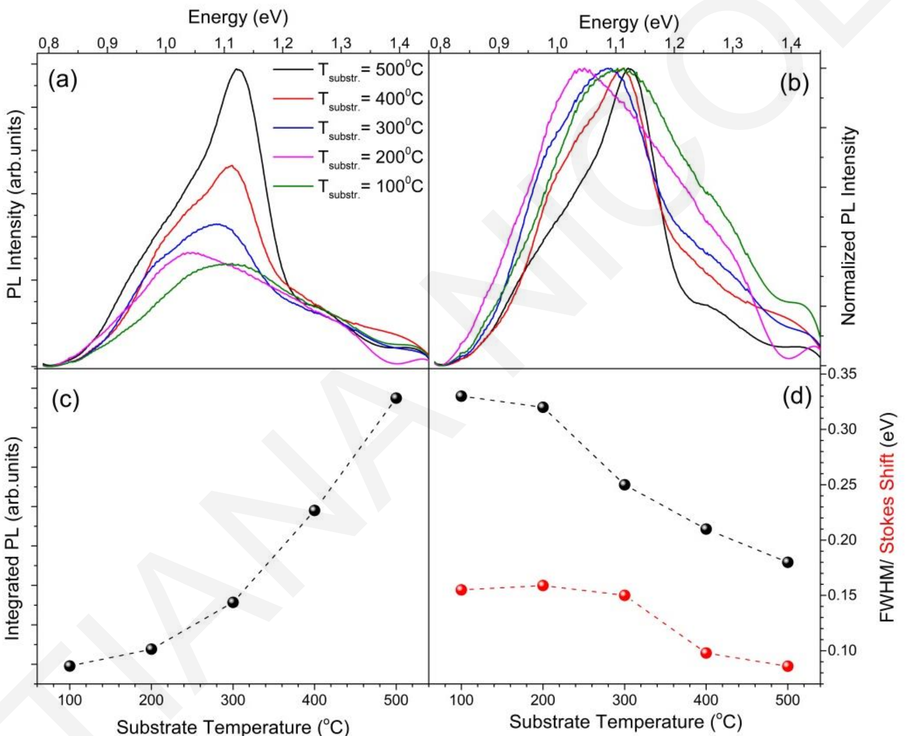

Figure 4.12 (a) Comparative PL spectra of films deposited at various temperatures in the range of 100 to 500 ^{0}C, (b) Normalized PL spectra of the same film series, (c) Integrated PL intensity versus deposition temperature, and (d) PL linewidth (FWHM) and Stokes shift as a function of substrate temperature.

The impact of substrate temperature on the films' properties is summarized in Table 4.4. The films grown at 500 ^{o}C exhibit the best properties for the application as an absorber layer in a solar cell. Single CIGS phase, increased crystallinity, higher mobility, wider bandgap, high absorption coefficient and less spatial and energetic disorder are some features indicating the high quality of the films obtained at 500 ^{o}C.

CHRISTIANA NICOLAOU

Substrate Temperature	
Property	**Low Temperature (25°C) ⟹ High Temperature (500°C)**
Stoichiometry	All films are nearly stoichiometric, $CuIn_{1-x}Ga_xSe_2$ (x~0.26)
Secondary phase	$Cu_{2-x}Se$ phase gradually fading
Electrical resistivity	Increasing from ~0.2 to ~0.5 Ohm.cm
Carrier concentration	Decreasing from ~4x10^{19} to ~7x10^{18} cm^{-3}
Mobility	Increasing from ~0.8 to ~2 cm^{2}V^{-1}s^{-1}
Energy gap	Increasing from ~1.16 to ~1.21 eV
Absorption coefficient	High absorption coefficients of ~2-3x10^4 cm^{-1}
Photoluminescence spectra	Increasing integrated PL intensity and decreasing PL linewidth and Stokes shift

Table 4.4 Summary of the main results obtained from the investigation of substrate temperature.

Time-resolved PL decays of the best performing film grown at 500 ^{0}C, sampling the radiative recombination across the broad emission spectrum at three spectral regions, named I, II, and III in descending energy order, are displayed in Figure 4.13. Modeling of the PL transients requires triple exponentials for regions I and II and double exponentials for the low energy region III. Typically the luminescence decay of evaporated or sputtered CIGS thin films is biexponential [206] [207] containing two contributions, one due to minority carrier (electron) trapping or localization at potential fluctuations and one due to band-edge recombination. The use of an additional term to describe the PL transients in regions I and II, indicates a complex competition of the aforementioned channels that depends on temperature and excitation and will be elaborated in a follow-up publication, as mentioned above. For the scope of the present discussion, we implement a phenomenological description of the PL decay based on the average PL lifetime, without referring to the individual decay terms and amplitudes.

CHRISTIANA NICOLAOU

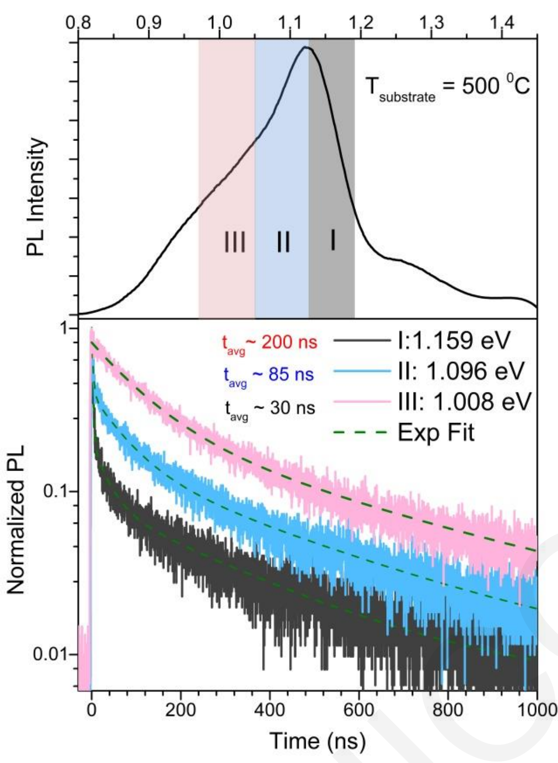

Figure 4.13 PL decays (bottom graph) measured at the three spectral regions I, II and III within the broadband luminescence (upper graph) from a CIGS film deposited at 500 ^{0}C. The multi-exponential fits (dotted lines) and calculated average PL lifetimes are also displayed.

The average PL lifetime is displayed in the bottom graph of Figure 4.13 for the three spectral regions probed. A systematic shortening of the lifetime by almost an order of magnitude, i.e., from ~200 to ~30 ns, as the detecting energy increases is attributed to the presence of recombination channels such as trapping at midgap states and charge separation and localization at potential minima that effectively quench the lifetime of the high energy, band-edge related photoexcitations. At the PL peak, a long average PL lifetime of the order of ~50 ns is obtained, comparable to the PL lifetimes measured in pristine evaporated CIGS films suitable for high efficiency solar cell devices [208], confirming the high material quality and reduced non-radiative recombination in the films produced at elevated PLD deposition temperatures.

4.1.2.4 Impact of other deposition parameters

Secondary PLD deposition parameters, such as number of pulses, repetition rate, distance between target and substrate and the type of substrate, were investigated through chemical, structural, morphological and electrical characterization. The impact of each of these deposition parameters on the properties of CIGS films is briefly presented in the Table 4.5. CIGS films were deposited at 300°C, using fluence of 1.0J/cm^2 and argon pressure of 0.01mbar. The investigation of the type of substrate (SLG and fused SiO_2), also contains a parametric investigation of the deposition temperature of CIGS at 200, 300 and 400°C, for each substrate.

CHRISTIANA NICOLAOU

PULSES, N: 3000 – 10500 (step = 1500)	
Stoichiometry (EDS)	Low N: Se-rich and Cu-poor films. High N: nearly stoichiometric films.
Structure (XRD)	CIGS chalcopyrite phase and minor secondary phase of $Cu_{2-x}Se$ for all films.
Surface roughness (AFM)	Increases from 88 nm to 190 nm as the number of pulses increases.
Morphology (SEM)	The density of the particulates on the surface increases as the number of pulses increases.
Thickness (Profilometer)	Increases almost linear from 150 nm to 900 nm as the number of pulses increases.
Resistivity (VDP)	Increases from $5x10^{-2}$ to $27x10^{-2}$ Ohm.cm as the number of pulses increases.
Carrier concentration (Hall)	Decreases from $8x10^{19}$ to $1.5x10^{19}$ cm^{-3} as the number of pulses increases.
Repetition Rate, RR (Hz): 1, 5, 10	
Stoichiometry (EDS)	Low RR: Se-rich films High RR: nearly stoichiometric films.
Structure (XRD)	CIGS chalcopyrite phase and minor secondary phase of $Cu_{2-x}Se$ for all films. Crystallite size decreases from 21 nm to 19 nm as the repetition rate increases.
Surface roughness (AFM)	Increases from 117 nm to 140 nm as the repetition rate increases.
Morphology (SEM)	The density and size of the particulates on the surface increases as the repetition rate increases.
Thickness (Profilometer)	Increases from 408 nm to 517 nm and then decreases to 479 nm increases as the repetition rate increases.
Target – Substrate distance, D (cm): 3.5 – 6.0 (step = 0.5)	
Stoichiometry (EDS)	Small D: nearly stoichiometric films. Large D: Se-rich and Cu-poor films.
Structure (XRD)	CIGS chalcopyrite phase and minor secondary phase of $Cu_{2-x}Se$ for all films. $Cu_{2-x}Se$ phase gradually fades at large D.
Surface roughness (AFM)	Decreases from 88 nm to 34 nm as the distance decreases.

CHRISTIANA NICOLAOU

Morphology (SEM)	The density of the smaller particulates on the surface decreases as the distance decreases. No change to the density of the larger particulates.
Substrate and deposition temperature: SLG and fused SiO_2 at 200, 300 and 400°C	
Stoichiometry (EDS)	Nearly stoichiometric films on both substrates and at all deposition temperatures.
Structure (XRD)	CIGS chalcopyrite phase and minor secondary phase of $Cu_{2-x}Se$ on both substrates. $Cu_{2-x}Se$ phase gradually fades as deposition temperature increases for both substrates.
Thickness (Profilometer)	SLG: Increases from 424 nm to 706 nm as the deposition temperature increases. SiO_2: Increases from 570 nm to 615 nm and then decreases to 540 nm for deposition temperature at 200, 300 and 400°C, respectively.
Resistivity (VDP)	SLG: Increases from $9x10^{-2}$ to $36x10^{-2}$ Ohm.cm as the deposition temperature increases. SiO_2: Increases from $12x10^{-2}$ to $49x10^{-2}$ Ohm.cm as the deposition temperature increases. Slightly lower resistivity for the films grown on SLG.
Carrier concentration (Hall)	SLG: Decreases from $5.9x10^{19}$ to $2.6x10^{19}$ cm^{-3} as the deposition temperature increases. SiO_2: Decreases from $4.2x10^{19}$ to $2.4x10^{19}$ cm^{-3} as the deposition temperature increases. Slightly higher carrier concentration for the films grown on SLG.

Table 4.5 Main results of the impact of secondary PLD deposition parameters on the properties of CIGS films.

The parametric investigation of the secondary PLD parameters has led to the following results:

- **Number of pulses:** CIGS layer can display superior optical absorption with absorption coefficient of as high as 10^5 cm^{-1}. Theoretically and based on this value, a CIGS layer with thickness of less than 1μm thick can absorb almost the entire incident light if the energy of photons is greater than the bandgap [21]. However, there are fundamental physics limitations, as well as practical experimental limitations, that may influence the device parameters and performance. High efficiency solar cells that exhibit efficiencies over 20% involve a CIGS layer of about 2μm [209]. Hence, the number of pulses has been selected to be more than 10500 and specifically 15000 pulses were used to obtain a thickness of ~1.5 μm. However, as the number of pulses increases in order to obtain the desirable thickness,

CHRISTIANA NICOLAOU

the films become stoichiometric but at the same time the surface roughness increases. Thus, the films obtained at 15000 pulses are stoichiometric with thickness of ~1.5 μm, though the surface roughness is high.

- **Repetition rate:** As repetition rate increases, the CIGS films become nearly stoichiometric, the crystallite size slightly decreases, and the surface roughness slightly increases. In order to achieve the deposition of CIGS layer in the shortest time, the maximum repetition rate of 10Hz has been selected. At 10Hz, the films are stoichiometric, and there is no significant change on the roughness and crystallite size compared to the films deposited at lower repetition rates.
- **Target to substrate distance:** As the distance increases, the surface of the films becomes smoother and the Cu_2Se secondary phase gradually decreases. However, the stoichiometry of the films diverges from the optimum values. At 4.5 cm, the films are stoichiometric, having a moderate surface roughness and a minor Cu_2Se phase.
- **Type of substrate:** In order to investigate the impact of Na diffusion into CIGS layer, two types of amorphous glass substrates were used regarding their Na content. Specifically, the two substrates used are the SLG which contains Na and the fused SiO_2 which is Na-free. The results of the compositional and structural characterization of CIGS films were similar for both substrates; stoichiometric CIGS films with a minor Cu_2Se secondary phase. The incorporation of Na into CIGS films through diffusion from SLG substrates has mainly affected the electrical properties of the films. The films that were deposited on SLG substrates exhibit lower values of resistivity and higher values of carrier concentration compared to the films deposited on fused SiO_2. These results indicate that the diffusion of Na from SLG substrate into CIGS layer lead to the enhancement of CIGS conductivity and carrier concentration. The increase of the effective hole carrier concentration and improvement of the p-type conductivity is also reported on several studies in the literature [195] [196] [197] [198]. Moreover, a parametric investigation of the deposition temperature of CIGS at 200, 300 and 400°C has been performed for each substrate. Electrical resistivity increases and carrier concentration decreases as the deposition temperature increases, for both subsrates. The influence of deposition temperature on the properties of CIGS films for both substrates are similar to the results that are discussed in section 4.1.2.3.

4.1.3 Conclusions

A systematic investigation of laser fluence, background gas and substrate temperature was performed to understand the influence of these process parameters on various properties of CIGS thin films grown by PLD on soda-lime glass substrates. Stoichiometric films with a minor $Cu_{2-x}Se$ secondary phase, moderate surface roughness, high absorption coefficient (>10^4 cm^{-1}) and high lifetime (~50ns) of the minority carriers are obtained at deposition temperatures 300 - 500 °C, fluence of 1 J/cm^2 and Ar pressure of 0.01 mbar. The overall assessment of electrical, optical, compositional,

CHRISTIANA NICOLAOU

structural and morphological properties of the investigated CIGS films indicates that PLD is a very promising technique for the fabrication of high-quality CIGS-based solar cells without the need for post-selenization. Although the results of this comprehensive study concern the optimization of growth parameters for CIGS deposition on bare glass substrates by PLD, they be utilized in future work depositing high-quality CIGS thin films on Mo-coated soda-lime glasses, which are usually used as the substrate and bottom electrode on CIGS solar cells.

4.2 CIGS on Mo/SLG

4.2.1. Materials and experimental methods

Mo-coated SLG substrates were purchased from a commercial vendor (*Techinstro, India*). CIGS films were deposited on Mo-coated SLG substrates by PLD using a KrF excimer laser source (λ = 248 nm, $\tau \leq$ 25 ns) in a high-vacuum chamber. Polycrystalline $CuIn_{0.7}Ga_{0.3}Se_2$ (Testbourne, England) target was used for the deposition of CIGS films. The substrate was placed at a fixed distance of 4.5 cm. The deposition was carried out in the presence of background gas after the chamber was evacuated at a base pressure of $4x10^{-6}$ mbar. Argon was used as background gas to confine the plume. The number of pulses and the repetition rate were kept constant at 6000 and 10 Hz respectively, for all depositions. The substrate temperature was systematically investigated in order to achieve the optimum growth conditions for high quality CIGS films on Mo-coated SLG substrates.

Structural properties and crystallinity of CIGS and Mo films were studied by X-ray diffraction (SmartLab RIGAKU, Cu Kα, λ = 1.5405 Å). The chemical composition of the films was determined by energy dispersive X-ray spectroscopy (Jeol Bruker Nano 129eV, XFlash 5010 detector). The surface roughness of Mo layer was probed via atomic force microscopy (*AFM, Agilent Technologies*). Angle-resolved reflectivity experiments of the Mo layer were performed in the range of 400 -1100 nm using the output of a 450 W Xe Arc broadband lamp spectrally filtered by a double monochromator and detected by CCD and InGaAs detectors. The electrical resistivity ρ of the Mo layer was measured at room temperature using the Van der Pauw method. Au wires were directly attached on the films' surface using conductive silver paste and a current of 2 mA was applied. The adhesion of CIGS and Mo layers on SLG was investigated using the scotch tape test method by attaching the tape on the surface of CIGS and detaching it by applying force manually.

The microstructure of the CIGS layer and characterization of the Mo/CIGS interfacial region have been studied using conventional TEM and HRTEM imaging, along with SAED patterns and EDS pont analysis. Conventional TEM and HRTEM observations were carried out using a JEOL 2011 TEM operating at 200 kV with a point resolution of 0.25 nm and equipped with an EDS detector (EDAX Apollo XLT TEM-SDD).

CHRISTIANA NICOLAOU

Current-Voltage (IV) measurements of CIGS/Mo/SLG structure were performed at room temperature using a two-probe configuration, as shown in Figure 4.14. The electrodes of the voltage source/ ammeter were mechanically placed on CIGS and Mo surface, creating an electrical circuit. The CIGS/Mo structure was electrically biased with an applied voltage of ±1V.

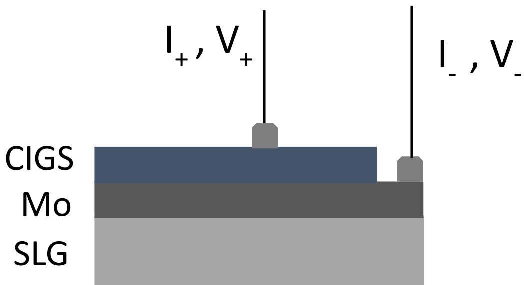

Figure 4.14 Schematic diagram of two probe IV measurement of CIGS/Mo/SLG structure.

4.2.2 Results and discussion

4.2.2.1 Impact of CIGS deposition temperature

Prior the deposition of CIGS on Mo-coated SLG substrates, the characterization of the purchased Mo films was carried out to define the quality of the films. The properties of Mo films are presented in Table 4.6. Low electrical resistivity, high reflectance and low surface roughness are the required properties of a bottom electrode [210]. The purchased Mo films have low electrical resistivity, medium reflectance, and low surface roughness (Table 4.6), rendering them as suitable back contacts for the solar cell devices.

Layer	Deposition method	Thickness (nm)	Resistivity @ 300K (Ohm.cm)	Reflectance @ 300K, 45°	Roughness (nm)
Mo	Sputtering	500	$3.48x10^{-5}$	40-60% in the range of 400-1000 nm	10.3

Table 4.6 Properties of purchased Mo films deposited on SLG substrates.

The deposition of CIGS films on Mo/SLG substrates were carried out at fluence of 1 J/cm^2 and argon pressure of 0.01 mbar, based on the assessment of the previous investigations regarding the deposition of CIGS films on SLG (section 4.1). The impact of substrate temperature was investigated by varying the deposition temperature of CIGS layer from 300 to 500°C, which were the optimum substrate temperatures obtained from the deposition of CIGS on SLG substrates, as

CHRISTIANA NICOLAOU

discussed section 4.1. Figure 4.15 shows the EDS-determined compositional ratios of CIGS films deposited 300, 400 and 500°C. As the figure indicates, all CIGS films are nearly stoichiometric independently of the deposition temperature, with slightly In-excess and Ga-deficiency with respect to the target stoichiometry. Specifically, the stoichiometry of CIGS films is $CuIn_{1-x}Ga_xSe_2$, with x~0.26.

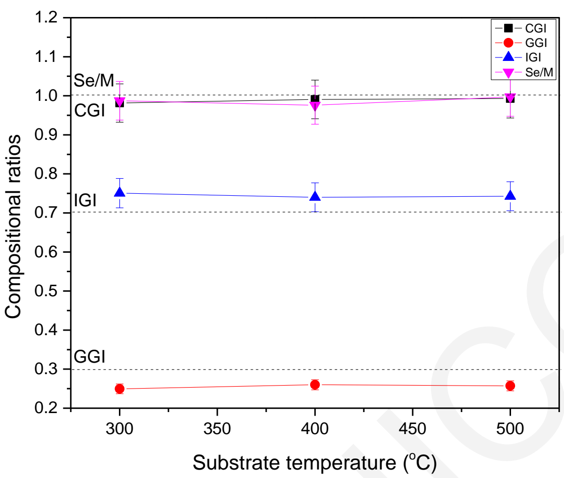

Figure 4.15 Compositional ratios of CIGS thin films deposited on Mo/SLG substrates at various substrate temperatures. Dashed lines indicate the ratios of a stoichiometric film, being CGI=Cu/(Ga+In)=1, GGI=Ga/(Ga+In)=0.3, IGI=In/(Ga+In)=0.7 and Se/M=Se/(Cu+Ga+In)=1. CIGS films are stoichiometric in respect to the target stoichiometry.

GIXRD patterns of CIGS films deposited on Mo/SLG at 300, 400 and 500°C, are shown in Figure 4.16 in a logarithmic scale. The diffraction peaks of CIGS/Mo/SLG structures are identified by CIGS chalcopyrite phase (JCPDS 35-1102) and Mo phase (PDF 9008543). In addition, a weak peak of Cu_2Se secondary phase (JCPDS 37-1187) appears in CIGS films, regardless of the deposition temperature. The results concerning the $Cu_{2-x}Se$ secondary phase contradict with the results of section 4.1 regarding the deposition of CIGS films on SLG substrates, where the $Cu_{2-x}Se$ peak becomes less intense as the deposition temperature of CIGS on SLG increases and eventually disappears on films grown at 500°C. However, the dissimilar results can be attributed to the different substrate used for the deposition of CIGS. The deposition dynamics and mechanisms that are taking place are completely different on the Mo-coated SLG substrate in comparison with the bare SLG substrate.

It is worth mentioning that there is no evidence of $MoSe_2$ phase, even at the deposition temperature of 500°C. The deposition temperature of CIGS along with the deposition method appear to have major impact on the formation of $MoSe_2$ phase at the CIGS/Mo interface. In particular, Ballif et al. could not detect any intermediate compound within the interface of sputtered Mo and physical vapor deposited CIGS [211]. Moreover, the fundamental work by Raud and Nicolet on Mo/Se, Mo/In, and Mo/Cu diffusion couples showed Se to react with Mo, forming $MoSe_2$ in very small

CHRISTIANA NICOLAOU

amounts after annealing at 600°C [32]. In addition, an investigation of the interface properties of d.c. sputtered Mo on CIS layers, deposited by co-evaporation, led to the conclusion that the $MoSe_2$ does not form below 500°C and it might be an artifact of the sputtering process [210]. Since the deposition of CIGS on Mo/SLG substrates were carried using PLD and at temperatures up to 500°C, the absence of $MoSe_2$ phase agrees with the above studies.

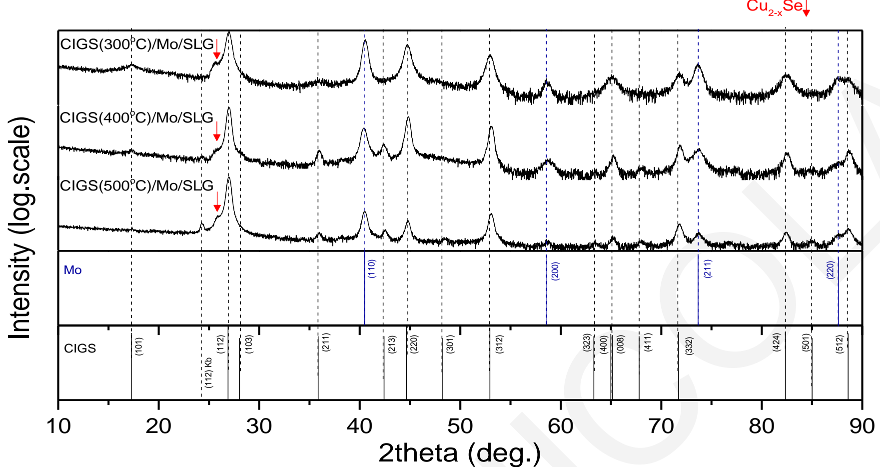

Figure 4.16 XRD patterns of CIGS thin films deposited on Mo/SLG substrates at different substrate temperatures. The bottom plots show the XRD pattern of $CuIn_{0.7}Ga_{0.3}Se_2$ (JCPDS 35-1102) and Mo (PDF 9008543). The secondary phase of $Cu_{2-x}Se$ is indicated by the arrows.

Adhesion tests of Mo/SLG and CIGS/Mo/SLG structures were performed using the scotch tape method described in 4.2.1. The adhesion of CIGS layers on Mo/SLG was investigated as function of CIGS deposition temperature. The pictures of the samples, presented in Table 4.7, were taken prior and afterwards the application of scotch tape test. The scotch tape test involved several attempts in order to thoroughly examine the quality of the adhesion between the layers.

Sample	**CIGS deposition temperature (°C)**	**Prior adhesion test**	**After adhesion test**
Mo on SLG	**-**		

CHRISTIANA NICOLAOU

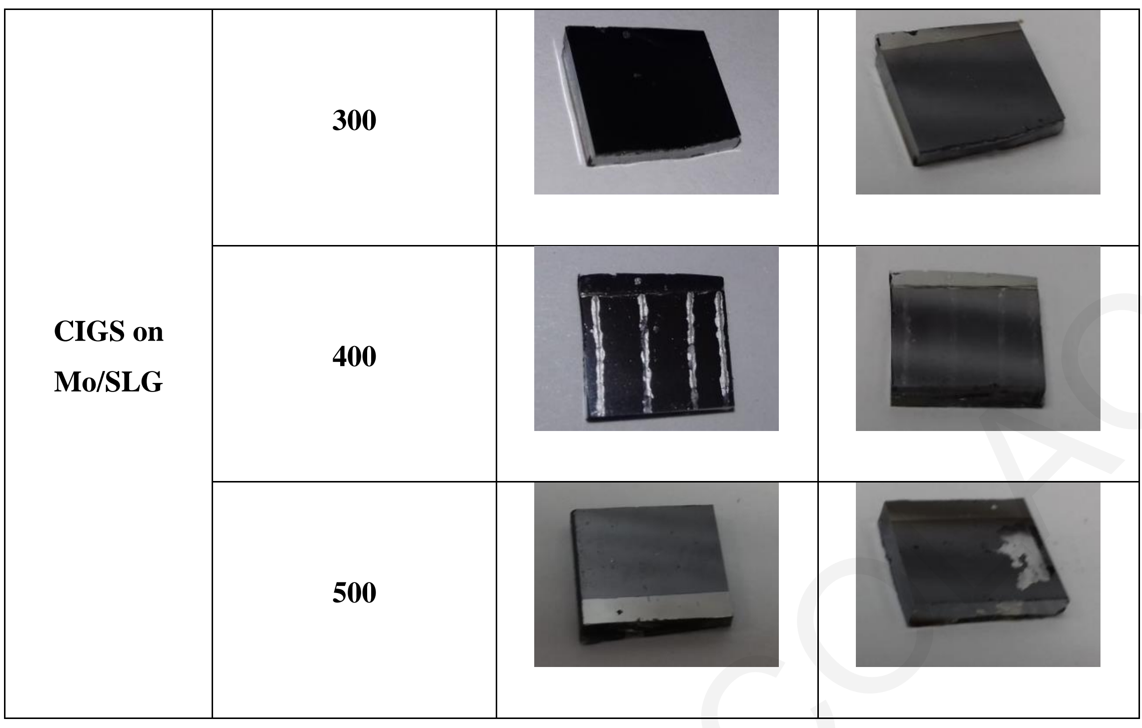

CIGS on Mo/SLG	300		
	400		
	500		

Table 4.7 Pictures of Mo/SLG and CIGS/Mo/SLG samples prior and afterwards the application of the scotch tape test for various CIGS deposition temperatures

After the application of the scotch tape adhesion test on Mo/SLG sample, the Mo layer remained intact, as shown in Table 4.7. This result indicates that the adhesion of Mo on SLG substrate is superior and the purchased Mo-coated SLG substrates are suitable for using them as back contacts in the photovoltaic device. Regarding the CIGS/Mo/SLG samples, the pictures in Table 4.7 indicate that the adhesion between CIGS, Mo layers and SLG substrate depends on the deposition of CIGS on Mo/SLG. The results of the adhesion test for CIGS/Mo/SLG structures show that the samples of which CIGS layer was deposited at 300 and 400°C were stable and the adhesion between the layers and the substrate was superior, as no delamination occurred. The sample of which CIGS was grown at 500°C presented poor adhesion between the layers and the substrate, since delamination occurred at the very first attempts of the adhesion test. The delamination of CIGS and Mo layers from the substrate can be attributed to the different thermal expansions coefficients of SLG (9 x 10^{-6}/K), Mo (4.8 - 5.9 x 10^{-6}/K) and CIGS (7 – 11 x 10^{-6}/K) [212] which lead to different expansions during the deposition of CIGS layer at 500°C. This effect is more significant at higher deposition temperatures, where the impact of the different thermal expansion of the layers at 500°C lead to deleterious adhesion due to higher induced stress. In addition, the softening point of SLG substrate is at 700°C [213] where the SLG becomes unstable. Thus, the SLG substrate is stable during the deposition of CIGS at 500°C.

CHRISTIANA NICOLAOU

The Mo and CIGS layers, as well as the CIGS/Mo interface of the CIGS/Mo/SLG structure with the CIGS layer deposited at 300ºC, were thoroughly studied using advanced electron microscopy (HRTEM imaging, SAED pattern acquisition and EDS point analysis). The results from the HRTEM characterization of the CIGS/Mo interface revealed that the interfacial region between Mo and CIGS is generally smooth, with both layers comprising of a columnar morphology of growth (Figure 4.17a). The Mo layer comprises of cubic Mo crystallites [SG Im-3m (229)], usually exhibiting (220) reflections in SAED patterns as shown in Figure 4.17b.

The HRTEM image of the CIGS layer is presented in Figure 4.18a. The CIGS layer also appears in columnar morphology, where all CIGS particles adopt the tetragonal $CuIn_xGa_{1-x}Se_2$ phase [SG I-42d (122)]. A great percentage of planar defects is present at the CIGS layer, which were identified as twins lying on (110) planes. This is also manifested by the characteristic streaking of the 110 reflection at the SAD pattern shown in the inset of Figure 4.18a.

Elemental analysis of the near interfacial region between Mo and CIGS has been studied by EDS point analysis of the CIGS layer, as shown in Figure 4.18b. A small amount of residual Mo inside the CIGS layer is identified. However, there was no indication for a $MoSe_2$ distinct phase formation in CIGS layer, as demonstrated by SAED and HRTEM analysis. The absence of $MoSe_2$ phase at the CIGS/Mo interface has also been observed by the XRD patterns in Figure 4.16.

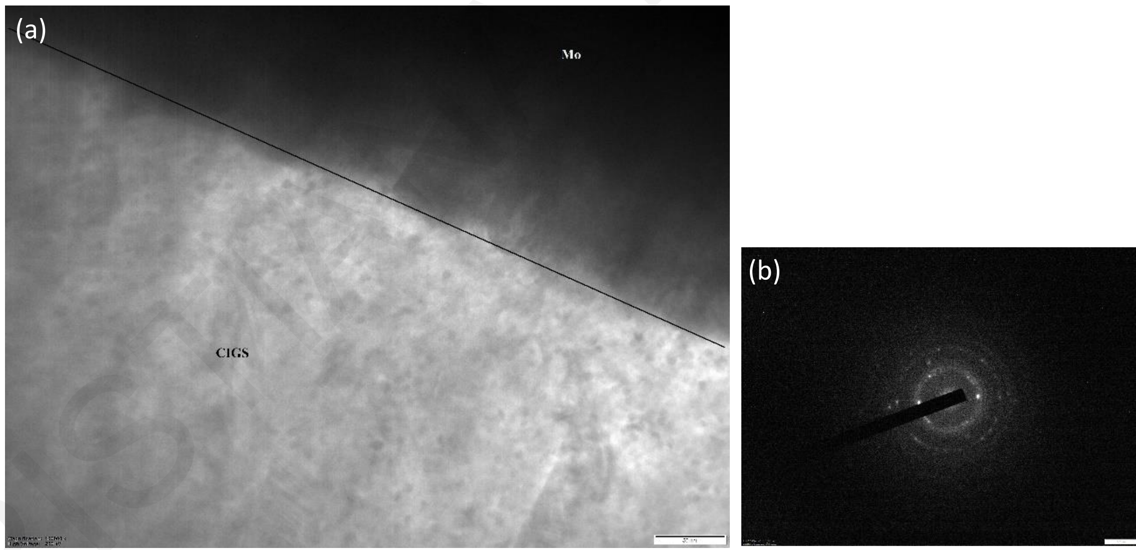

Figure 4.17 (a) HRTEM image and (b) SAD pattern from the Mo/CIGS interfacial region.

CHRISTOS NICOLAOU

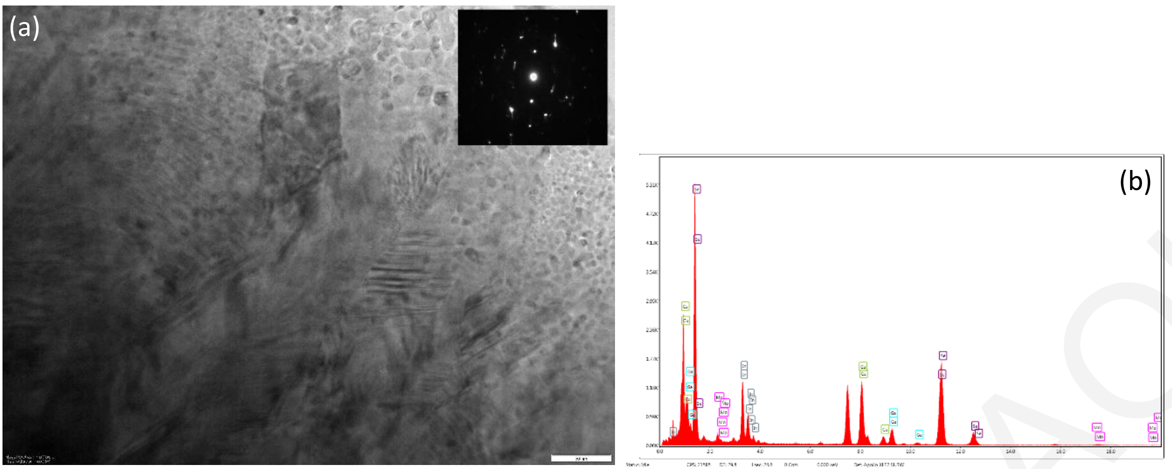

Figure 4.18 (a) HRTEM image and (b) EDS point analysis spectrum from the CIGS layer.

On the other hand, a small percentage of small $Cu_{2-x}Se$ crystallites were detected by means of HRTEM, among the CIGS ones, as outlined in Figure 4.19. The $Cu_{2-x}Se$ particles have sizes up to 12 nm with no specific shape. The presence of a weak peak of Cu_2Se secondary phase (JCPDS 37-1187) has also been observed in CIGS films by the XRD patterns in Figure 4.16.

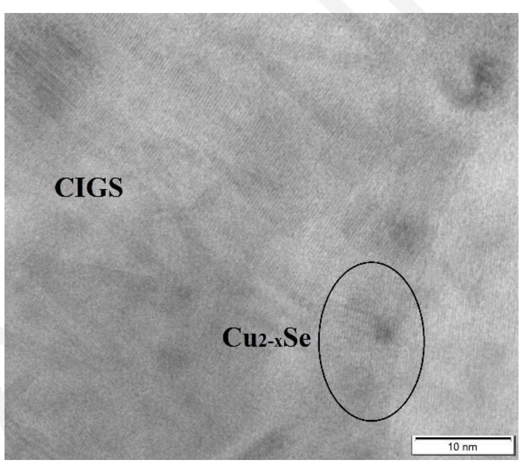

Figure 4.19 Distinct $Cu_{2-x}Se$ crystals along with CIGS ones at the CIGS layer.

The IV curve of CIGS/Mo/SLG structure with the CIGS layer deposited at 300ºC is presented in Figure 4.20. The IV measurements of the sample were performed at room temperature using a 2-probe configuration, as described in section 4.2.1. The linearity of the IV curve indicates the formation of an ohmic contact at CIGS/Mo interface, despite that there was no indication from the XRD patterns (Figure 4.16) of the existence of the MoSe2 phase at the interface. Contrary to the literature, the ohmic contact between CIGS and Mo layers is related with the presence of $MoSe_2$ phase at the interface [172, 174, 214]. Here, the observed ohmic contact of the sample concurs with the absent of $MoSe_2$ phase at the CIGS/Mo interface. These conflicting results with the literature can be attributed to the fact that the studies, reporting on formation of nearly ideal ohmic contact between Mo and CIGS via an intermediate $MoSe_2$ layer, have used a different deposition method for growing the CIGS layer on Mo, other than PLD.

CHRISTINA NICOLAOU

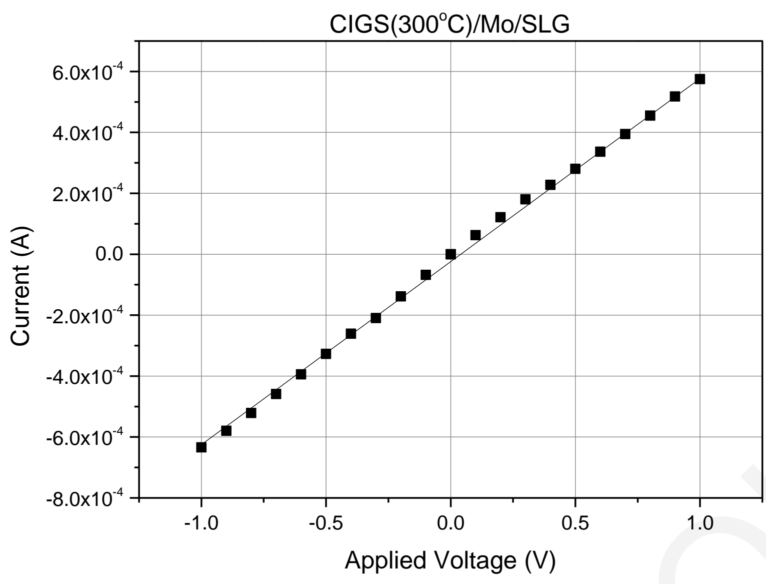

Figure 20 Two probe IV curve of CIGS(300ºC)/Mo/SLG structure at room temperature.

4.2.3 Conclusions

The impact of deposition temperature of CIGS on Mo-coated SLG substrates has been investigated by fabricating the CIGS/Mo/SLG structures at various deposition temperatures. Initially, Mo-coated SLG substrates were purchased and tested through various characterizations for their suitability as the back contact for a photovoltaic device. Low electrical resistivity of $\approx 3.5x10^{-5}$ Ohm.cm, medium reflectance of 40-60% in the range of 400-1000 nm, low surface roughness of $\approx$10 nm and superior adhesion with the SLG substrate have been found for Mo layer, which fulfill the requirements of a good back contact. Next, the CIGS/Mo/SLG structures were fabricated by depositing the CIGS layer on Mo-coated SLG substrates at 300, 400 and 500ºC. The deposition parameters of CIGS were selected based on the previous investigation of CIGS on SLG described in section 4.1.2. CIGS layers on Mo/SLG were nearly stoichiometric and independent from the deposition temperature. The XRD patterns of CIGS/Mo/SLG structures were identified by the CIGS chalcopyrite phase, the Mo phase and a weak peak of Cu_2Se secondary phase in CIGS layers. There was no evidence of $MoSe_2$ phase at the interface for none of the deposition temperatures. The adhesion tests of CIGS/Mo/SLG structures revealed that the adhesion between CIGS, Mo and SLG was superior for the samples of which CIGS was grown at 300 and 400ºC. On the contrary, delamination occurred for the samples grown at 500ºC.

HRTEM image of CIGS/Mo/SLG structure with the CIGS layer deposited at 300ºC revealed a generally smooth interfacial region between Mo and CIGS, with both layers in columnar growth. There was no indication for a $MoSe_2$ distinct phase formation in CIGS layer, as demonstrated by SAED and HRTEM analysis, even though a small amount of residual Mo inside the CIGS layer is identified. A small percentage of small $Cu_{2-x}Se$ crystallites were detected by means of HRTEM in

CHRISTIANA NICOLAOU

the CIGS layer. The results of the electron microscopy (HRTEM imaging, SAED pattern acquisition and EDS point analysis) corroborate with the results of the XRD patters. The linearity of the IV curve of CIGS/Mo/SLG structure with the CIGS layer deposited at 300°C indicates the formation of an ohmic contact at CIGS/Mo interface. The overall assessment of compositional, structural, morphological and electrical properties of the investigated CIGS films grown on Mo-coated SLG substrates indicates that the best properties of CIGS layer and the CIGS/Mo interface are obtained at the CIGS deposition temperature of 300°C.

CHRISTIANA NICOLAOU

Chapter 5 – Optimization of the CdS layer

CdS is an n-type, II-VI semiconductor with a direct band gap of 2.42 eV at room temperature [215, 216]. The incorporation of high quality CdS buffer layer, usuallu deposited by chemical bath deposition (CBD), with thickness of only tens of nanometers, between the CIGS absorber and ZnO transparent conductive oxide (TCO) holds a key role in the performance of the cell. Numerous published works discuss the impact of the CdS buffer layer on the formation of the heterojunction on CIGS solar cells [21, 45, 217]. CdS provides an optimization of the band alignment between CIGS and ZnO [210], protects CIGS absorber surface from further processing steps [75], establishes higher contact potential that allows higher open circuit voltage [210] and reduces the lattice misfit between CIGS and ZnO layers [75]. Despite the beneficial effects of the CdS layer on the properties of the cell, some disadvantages inherently emerge. CdS is not fully transparent in the visible as it absorbs in the blue spectral range. Blue photons photogenerate electron-holes pairs in CdS, which are short-lived due to efficient recombination. As a result, the external quantum efficiency (EQE) of the solar cell structure in the blue wavelength region is reduced [44]. Fabrication of thin CdS layers can minimize the light absorption losses in the blue, however for very thin layers, pinholes between the TCO contact and the absorber layer are formed, which create short circuits [8] in the device.

High efficiency cells have been reported with CdS buffer layer grown by CBD [218-220], while cells with CdS deposited by other techniques exhibit poorer efficiencies [221-223]. However, CBD is incompatible with the vacuum-based methods used for the deposition of the previous and consequent layers of CdS.

Considering the blue absorption losses, the toxicity of Cd and the incompatibility of CBD with the in-line vacuum-based production methods, one of the major challenges is the development and implementation in the production line of Cd-free alternative buffer layers. The first approach has been to omit overall the CdS layer and form a direct junction between CIGS and ZnO. However the absence of the buffer layer appears to result in lower efficiencies [224]. Alternative buffer materials, such as Zn(O,S) and (Zn,Mg)O are under consideration as they can be deposited using vacuum-based deposition methods, such as sputtering [225], molecular beam epitaxy [226] and atomic layer deposition [227, 228], while their band gap energy is larger than that of CdS so that blue absorption losses are reduced. Nevertheless, the band alignment between Zn-based compounds and CIGS absorber appears to be unfavorable due to the formation of a blocking barrier [229]. In view of the above and the absence of better alternatives for the moment, the presence of a CdS buffer layer appears necessary for the fabrication of high efficiency CIGS solar cells.

An important breakthrough that would simplify the line production process and reduce manufacturing time and cost for CIGS solar cells is the determination of a single-step growth method

CHRISTIANA NICOLAOU

for the fabrication of the device structure. This chapter reports on the utilization of pulsed laser deposition (PLD) as a novel deposition method for the preparation of the CdS and CIGS layers on Mo-coated SLG substrates in one growth sequence. In chapter 4, regarding the deposition of CIGS films using PLD, it has been demonstrated that PLD-grown CIGS films are of high quality, stoichiometric, thus the need for post-selenization is eliminated [3]. In addition, it has been recently reported that CdS films deposited by PLD are more compact and uniform than those grown by CBD and sputtering [58]. Thus, PLD may allow the realization of high quality and possibly thinner CdS layers without the creation of short circuit pinholes between the TCO and the absorber layer [8].

Section 5.1 of this chapter reports on the systematic investigation of the influence of PLD growth parameters on the properties of CdS thin films deposited on soda-lime glass substrates. A comprehensive characterization of structure, composition and morphology has been carried out to understand the impact of the deposition parameters on the properties of CdS films. In addition, optical measurements of CdS films have been performed in order to study the optical properties of the films. The optimum PLD growth conditions for CdS films are identified based on an overall assessment of film characteristics.

Section 5.2 deals with the fabrication of CdS/CIGS/Mo structure. The results of section 5.1 regarding the deposition of CdS on SLG substrates have been used to consequently grow optimized CdS films on top of CIGS/Mo/SLG structure. CIGS and CdS layers have been deposited on Mo-coated SLG using PLD without interrupting the deposition process. The growth parameters of CIGS, which have been optimized in Chapter 4, have been herein utilized for the deposition of CIGS layer [3]. The influence of CdS deposition temperature on the properties of CdS/CIGS heterojunction has been extensively studied and reported herein for the first time. Complete structural, compositional and morphological characterization, along with electrical measurements, have been performed in order to evaluate the quality of CdS/CIGS junction and identify the optimum PLD growth conditions. Few published works report on the correlation between the growth parameters and the properties of PLD-grown CdS films [230-235] and there is no published work on the electrical properties of CdS/CIGS junction, regardless of the deposition method.

5.1 CdS on SLG

5.1.1 Materials and experimental methods

CdS films were deposited on bare SLG substrates by PLD using a KrF excimer laser source (λ = 248 nm, $\tau \leq 25$ ns) in a high-vacuum chamber (Figure 5.1a). The bare SLG substrates were ultrasonically cleaned with a sequence of organic solvents. A configuration of mirrors has guided the laser beam to enter the PLD chamber. Prior entering the chamber, the beam was focused by a focal lens and was adjusted to hit on the polycrystalline target of CdS (*Testbourne, England*) at an incident angle of 45°. The rotation and toggling of the target provided a uniform ablation of the target surface

CHRISTIANA NICOLAOU

during deposition. The substrate was placed across the target surface at a fixed distance. Prior to deposition, the chamber was evacuated at a base pressure of $4x10^{-6}$ mbar. The deposition of CdS was carried out in the presence of Argon background gas at 0.01mbar. The number of pulses, repetition rate and target to substrate distance were kept constant at 300, 10 Hz and 4cm respectively, for all CdS depositions. Section 5.1 is focused on the parametric investigation of laser fluence (0.9 – 1.6 J/cm^2) and deposition temperature (25 – 400°C) of PLD-grown CdS films.

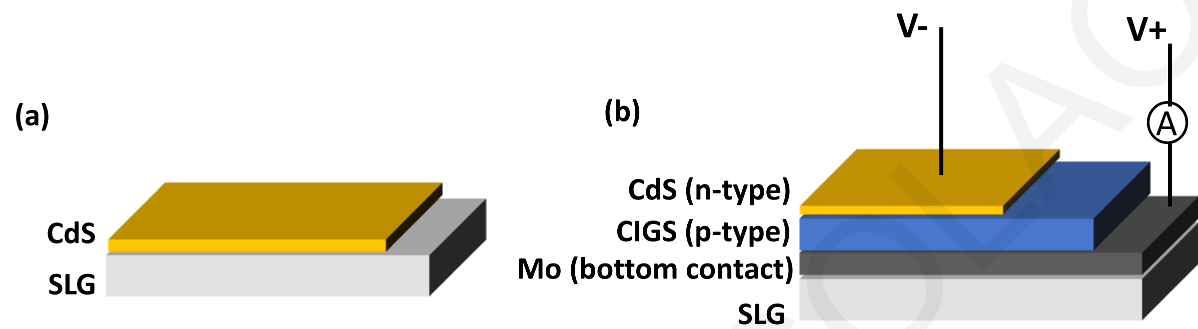

Figure 5.1 Schematic deposition structures: (a) CdS on SLG and (b) sequential deposition of CIGS and CdS on Mo-coated SLG.

An X-ray diffractiometer (XRD) (*SmartLab RIGAKU, Cu Kα, λ = 1.5405 Å*) was used to identify the crystal phases present in the films. The thickness of CdS films was measured by a stylus profilometer. The planar chemical composition of CdS films was determined by energy dispersive X-ray spectroscopy (EDS) (Jeol JSM-6610 LV, Bruker Nano 129eV, XFlash 5010 EDS detector). The electron accelerating voltage of the scanning electron microscope (SEM) was set at 10 kV for the planar EDS analysis.

Optical absorption measurements were performed using a Lamda 1050 Perkin Elmer spectrophotometer covering the 200-3000 nm spectral range. Steady-state photoluminescence (PL) was excited via a 375 nm Oxxius diode laser. The luminescence was spectrally analysed and detected using a FluoroLog FL3 Horiba Jobin Yvon spectrofluorimeter. The PL measurements were performed on a side by side geometry to allow a direct emission-intensity comparison. Furthermore, the laser fluence was normalized to the optical absorbance of each sample at the excitation wavelength used to approximately photogenerate an equal density of excitations at all films. Time-resolved photoluminescence (TR-PL) was performed on the same instrument using a time correlated single photon counting (TCSPC) method and excitation via a 375nm NanoLED pulsed laser with a pulse width of ~175 ps and excitation energy of 28 pJ/pulse. The PL dynamics were quantified by the average transient PL lifetime τ_{ave}, calculated by equation below:

$$\tau_{ave} = \frac{\sum_i A_i \tau_i^2}{\sum_i A_i \tau_i}, \quad \text{(Equation 5.1)}$$

where τ_i are the decay times extracted from triple-exponential fitting of the PL transients and A_i their corresponding decay amplitudes.

CHRISTIANA NICOLAOU

5.1.2 Results and Discussion

5.1.2.1 Impact of laser fluence

The influence of laser fluence on the growth of CdS films has been investigated by depositing CdS on SLG substrates using PLD, with laser fluence varying from 0.9 to 1.6 J/cm^2. The preliminary study on the growth of CdS films using PLD has been conducted on SLG substrates because the amorphous SLG should not promote the epitaxial growth of CdS films, similarly to what is expected in the case of CdS deposition on the polycrystalline CIGS layer. The thickness of the films monotonically increases with increasing fluence from 50 to 110 nm. Figure 5.2 shows the compositional S/Cd ratio of the films deposited at 300 ^{o}C in Ar atmosphere of 0.01 mbar, as obtained by EDS measurements. The S/Cd ratio was calculated by averaging the composition values obtained by scanning multiple areas for each sample. S/Cd ratio equal to unity corresponds to stoichiometric films and is denoted on Figure 5.2 with the dashed line. As fluence increases, from 0.9 to 1.6 J/cm^2, S/Cd ratio decreases, from ~1.03 to ~0.95 and films composition changes from sulfur-rich to sulfur-poor. At 1.1 J/cm^2 the films appear to be nearly stoichiometric. Pure evaporation of the elements occurs when the fluence is lower than a threshold value [56], which is defined by the elements of the target. In the case of CdS, S atoms are more volatile than Cd atoms, thus preferential evaporation of S takes place at low fluence and S-rich films are obtained. Stoichiometric films are obtained at 1.1J/cm^2 indicating that congruent ablation begins at 1.1J/cm^2. At higher values of fluence, S content of the films decreases, resulting in sulfur-poor films despite the congruent ablation. The S/Cd content of the ablated species is equal to unity at the early stages of the plume formation. During the flight of the ablated species to the substrate, the S/Cd ratio is changed because collisions between the species occur. At high fluence, the plume species possess higher kinetic energy and the collisions become stronger and more frequent, therefore the collisions become significantly impactful. S atoms, being the lighter of the ablated atoms, are scattered much more than the heavier Cd atoms in the presence of a high mass background gas, such as Ar [107, 188]. In addition, the heavy Cd atoms preferentially propagate along the normal direction (where the substrate is usually placed) during the expansion in a background gas [189]. Thus, Cd atoms propagate towards the substrate while S atoms are scattered and escape from the plume, therefore the S/Cd ratio reaching the substrate is less than one and the films become S-poor.

CHRISTIANA NICOLAOU

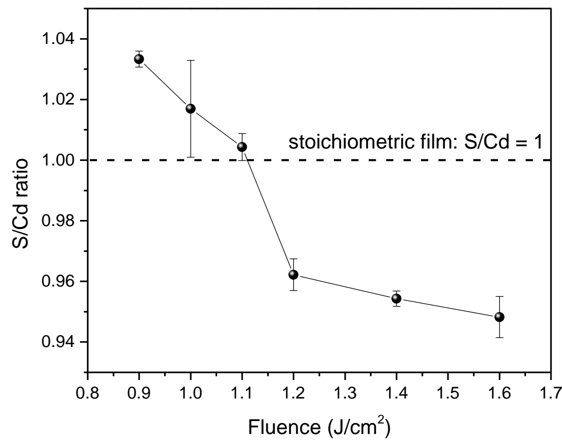

Figure 5.2 Compositional ratio of CdS thin films deposited on SLG substrates at different fluences, ranging from 0.9 to 1.6 J/cm^2. Dashed line indicates the ratio of a stoichiometric film, being S/Cd=1. Films change from sulfur-rich to sulfur-poor films, as fluence increases. At 1.1 J/cm^2 the films are almost stoichiometric.

CdS films deposited at various values of fluence have been examined by grazing incidence XRD (GIXRD) with 2θ values ranging between 10° and 90° and grazing incident angle of 0.5^o; the XRD patterns are shown in Figure 5.3. All deposited films exhibit thirteen diffraction peaks which are identified by the CdS hexagonal phase (JCPDS 96-900-8863), revealing the polycrystalline nature of the films. No secondary phase is observed in the XRD patterns indicating the pure CdS phase of the films, independently of laser fluence. It must be noted that in the out-of-plane XRD patterns (not shown here) of all samples, the (002) diffraction peak is the most intense one, indicating the existence of preferred orientation along the (002) plane. Similar preferred orientation is reported in CdS films grown by PLD [234, 235].

Crystallite size of the films has been calculated by the Debye-Scherrer formula using the (002) diffraction peak. Figure 5.4 illustrates the dependence of crystallite size with fluence and composition of CdS films. The crystallinity of the films increases with fluence. This may be due to the higher kinetic energy that atoms possess at increased fluences, resulting in increased diffusion of the atoms at the substrate surface and enhanced nucleation. Alternatively, the variation of crystallite size of the films may be associated with the fluence-dependent content of the films reported in Figure 5.2, with sulfur-poor films exhibiting higher crystallite sizes to those of sulfur-rich films. Crystallinity is enhanced at stoichiometric composition of the film occuring at fluence of 1.1 J/cm^2 with a crystallite size of about 18 nm. The trend of crystallite size of CdS films with S/Cd composition appears similar to other reported studies [236].

CHRISTIANA NICOLAOU

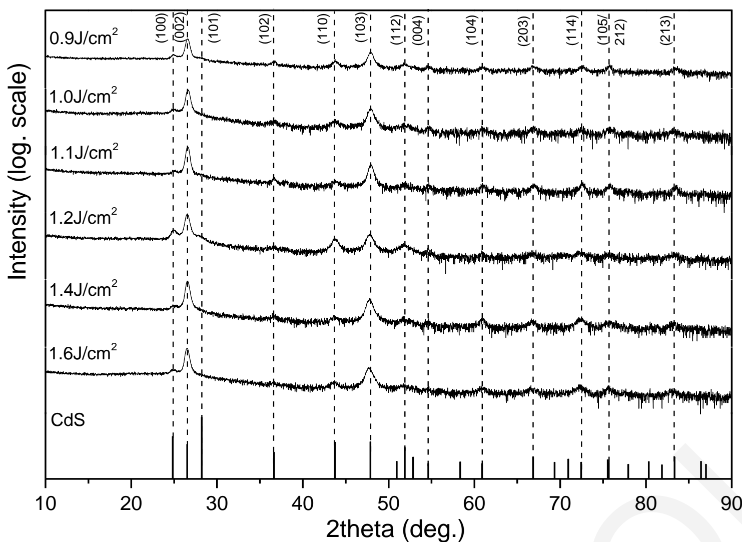

Figure 5.3 XRD patterns of CdS thin films deposited on SLG substrates from 0.9 to 1.6 J/cm^2. The bottom plot shows the linear XRD pattern of CdS hexagonal phase according to JCPDS 96-900-8863. Polycrystalline films with no secondary phase and preferred orientation along (002) and (103) planes are obtained.

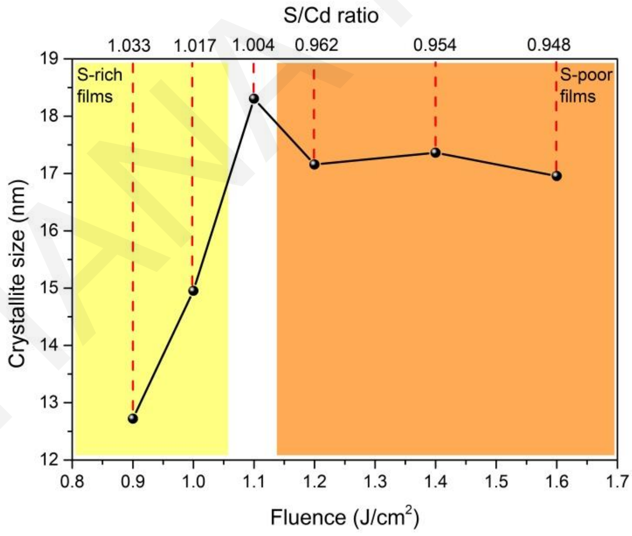

Figure 5.4 Crystallite size of CdS thin films deposited on SLG substrates as function of laser fluence and S/Cd compositional ratio. The crystallinity of the films increases as fluence increases. Sulfur-rich films have lower crystallite sizes while sulfur-poor films exhibit higher crystallite sizes.

The impact of fluence on the properties of CdS films grown by PLD has been investigated. Polycrystalline CdS films with hexagonal lattice without the presence of secondary phase are grown at all fluences. Stoichiometric CdS films with high crystallinity are obtained at fluence of 1.1 J/cm^2.

CHRISTIANA NICOLAOU

5.1.2.2 Impact of deposition temperature

The influence of deposition temperature on the growth of CdS films has been investigated by depositing CdS on SLG substrates using PLD, with deposition temperatures varying from 20 to 400°C, at optimum fluence of 1.1 J/cm^2 identified in the parametric investigation of fluence presented in section 3.1. The thickness of the films monotonically decreases with increasing deposition temperature from 130 to 55 nm. Figure 5.5 shows the EDS-determined compositional ratio S/Cd of the films deposited at various deposition temperatures. The S/Cd ratio was calculated by averaging the composition values obtained by scanning multiple areas for each sample. As the figure indicates, the films are sulfur deficient at room temperature and at 100°C with increasing S/Cd ratio. At temperature of 200°C and higher, the S/Cd ratio is almost constant, and the films are nearly stoichiometric. A plausible source for the compositional deviation described is the different sticking coefficient of S and Cd atoms during the film growth. The sticking coefficient of each element is a complex function of atomic mass, kinetic energy, incidence angle, surface energy and temperature [237]. The EDS analysis of the films presented in Figure 5.5 leads to the conclusion that the sticking coefficient of S increases (and/ or the sticking coefficient of Cd decreases) with increasing deposition temperature and the films become stoichiometric at higher temperatures. However, this is only a hypothesis as no published works exist in the literature reporting on the temperature dependence of the sticking coefficients of Cd and S atoms on SLG substrates, using PLD.

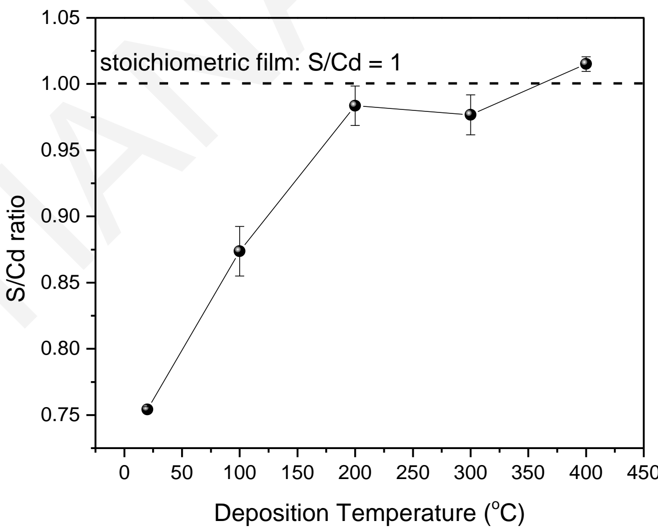

Figure 5.5 Compositional ratio of CdS thin films deposited on SLG substrates at deposition temperatures, from room temperature up to 400°C. Dashed line indicates the ratio of a stoichiometric film, being S/Cd=1. Films change from sulfur-poor to nearly stoichiometric films as the deposition temperature increases.

As shown in the GIXRD patterns (Figure 5.6) with grazing incident angle of 0.5°, the polycrystalline nature of the films is evident by the multiple diffraction peaks. All peaks are identified

CHRISTIANA NICOLAOU

by the CdS hexagonal phase (JCPDS 96-900-8863). The pure CdS phase is obtained at all deposition temperatures, as no secondary phase is observed on the XRD patterns. Preferred orientation along (002) plane is observed from the out-of-plane XRD patterns (not shown here), similarly to the investigation of fluence.

Crystallite size of the films has been calculated by the Debye-Scherrer formula using the (002) diffraction peak. Figure 5.7 illustrates the dependence of crystallite size with deposition temperature. As the deposition temperature increases, nucleation is enhanced due to the higher kinetic of the atoms, thus larger crystallites are being formed. An abrupt increase is observed at deposition temperatures higher than 200°C, with crystallite size of about 18nm. Comparing the crystallite size with S/Cd ratio, stoichiometric films with S/Cd ratio close to unity are formed by larger crystallites, while sulfur-poor films exhibit small crystallite sizes of about 3-5 nm. The results of Figures 5.4 and 5.7 can be merged in a general conclusion which relates the stoichiometry of CdS films with their crystallite size. Non-stoichiometric films (whether sulfur-poor or sulfur-rich) appear to have low crystallite sizes, while stoichiometric films with S/Cd ratio around unity grow in larger crystallites. Small crystallites have also been observed for non-stoichiometric CdS films deposited by chemical technique [238]. The observed compositional deviations of CdS films can lead to structural defects, such as S and Cd vacancies and interstitials. These point defects act as low-energy nucleation centers that limit the crystallite growth due to multiple adjacent crystallites growing next to each other [109]. Therefore, non-stoichiometric CdS films are composed of smaller crystallites compared to the stoichiometric films. Similar results have been found in other PLD-grown films [239-243].

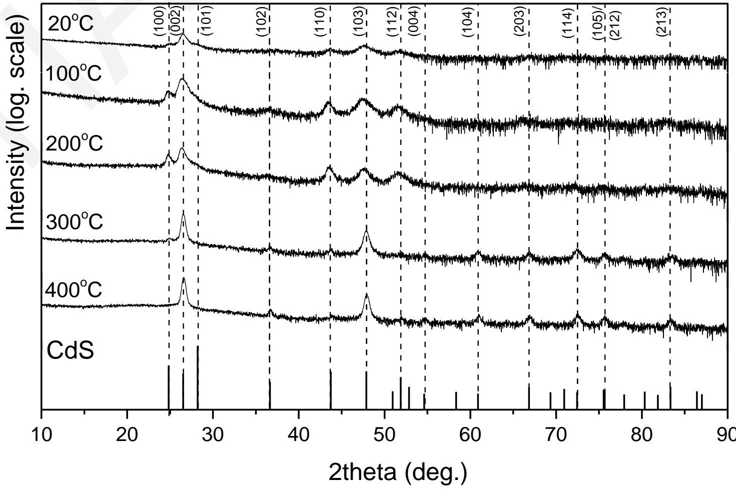

Figure 5.6 XRD patterns of CdS thin films deposited on SLG substrates at different substrate temperatures ranging from room temperature up to 400°C. The bottom plot shows the XRD pattern

CHRISTIANA NICOLAOU

of CdS hexagonal phase according to JCPDS 96-900-8863. Polycrystalline films with no secondary phase and preferred orientation along (002) and (103) planes are obtained.

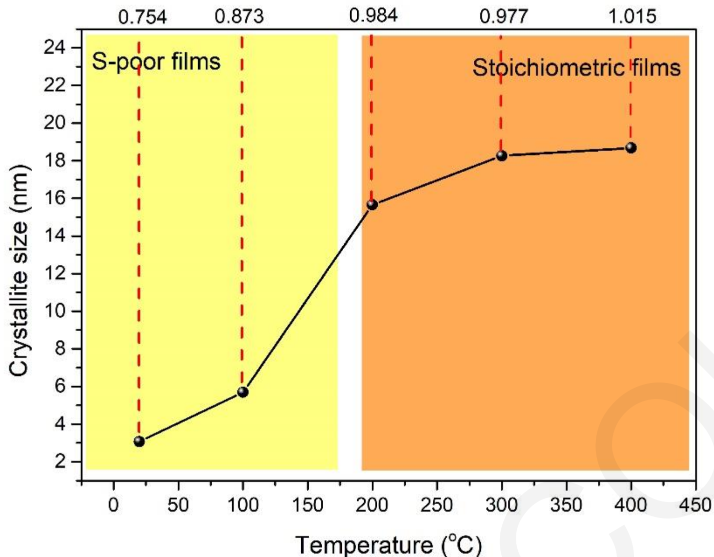

Figure 5.7 Crystallite size of CdS thin films deposited on SLG substrates as function of deposition temperature and S/Cd compositional ratio. The crystallinity of the films increases as deposition temperature increases. Sulfur-poor films have lower crystallite sizes while stoichiometric films exhibit higher crystallite sizes.

The estimated energy gaps and the respective optical absorption spectra of the CdS films grown at various substrate temperatures are shown in Figures 5.8 (a) and (b), respectively. The band gap energy is determined from the inflection point of the first derivative of the absorbance, as it has also been found in Chapter 4 [3], to provide a more reliable estimation of the energy gap of pulsed laser deposited thin films. Figure 5.8a reveals a small but systematic red shift of the band gap energy from 2.55 to 2.49 eV as the substrate temperature increases from 100 to 400°C. The estimated values are within the literature reported values of CdS [244-246]; furthermore the red shift of the gap with temperature is consistent with the respective increase of the crystallite size shown in Figure 5.7 that results in reduction of carrier quantum confinement effects [247].

CHRISTIANA NICOLAOU

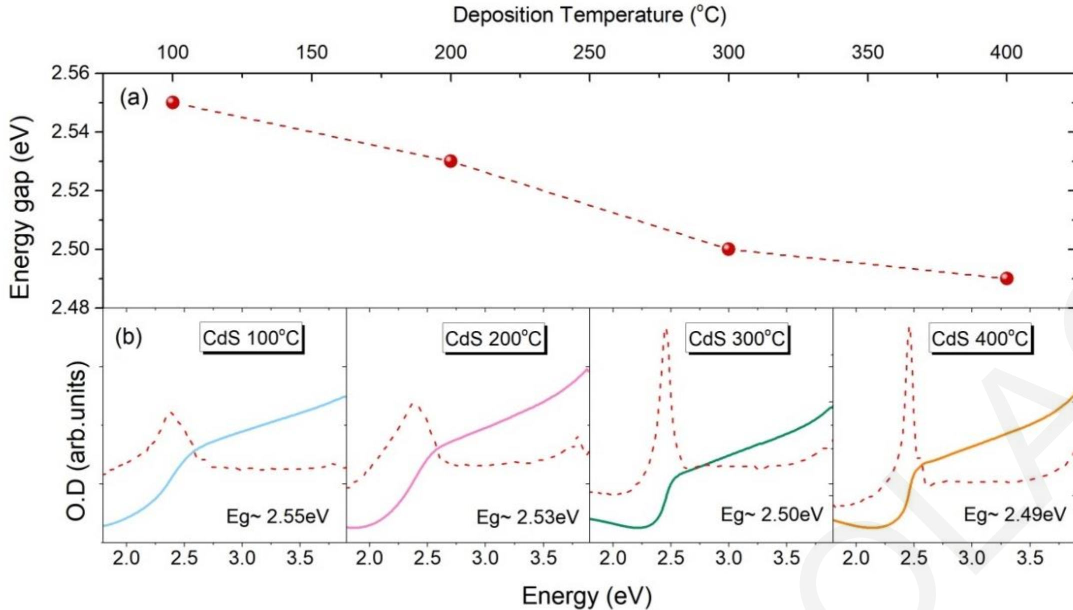

Figure 5.8 (a) Variation of the optical band gap energy versus deposition temperature (b) The steady-state absorption for the CdS films grown at various deposition temperatures. The first derivative of the absorbance and the estimated energy gap for each film is also shown.

Comparative non-resonant photoluminescence (PL) spectra at 300K of the CdS films deposited at various temperatures are displayed in Figure 5.9a. The emission is peaked at ~ 2.26 to 2.28 eV and exhibits a broad PL lineshape of 650 to 660 meV. Figure 5.9b indicates that the integrated emission increases systematically with the deposition temperature within the 100 to 400ºC range. The weaker emission from the S-poor film deposited at lower temperatures can be attributed to the presence of S vacancies that quench non-radiatively a fraction of the photogenerated excitons.

Time-resolved PL data confirm the results of the steady-state study. The PL dynamics are quantified by the average PL lifetime τ_{ave} that is found to systematically increase from ~4 to 6 ns as the growth temperature is raised from 100 to 400ºC. The measured lifetimes appear longer than the PL dynamics measured in CdS films fabricated by CBD and DC Pulse Sputtering, witnessing the high optical quality of the produced material [248].

CHRISTIANA NICOLAOU

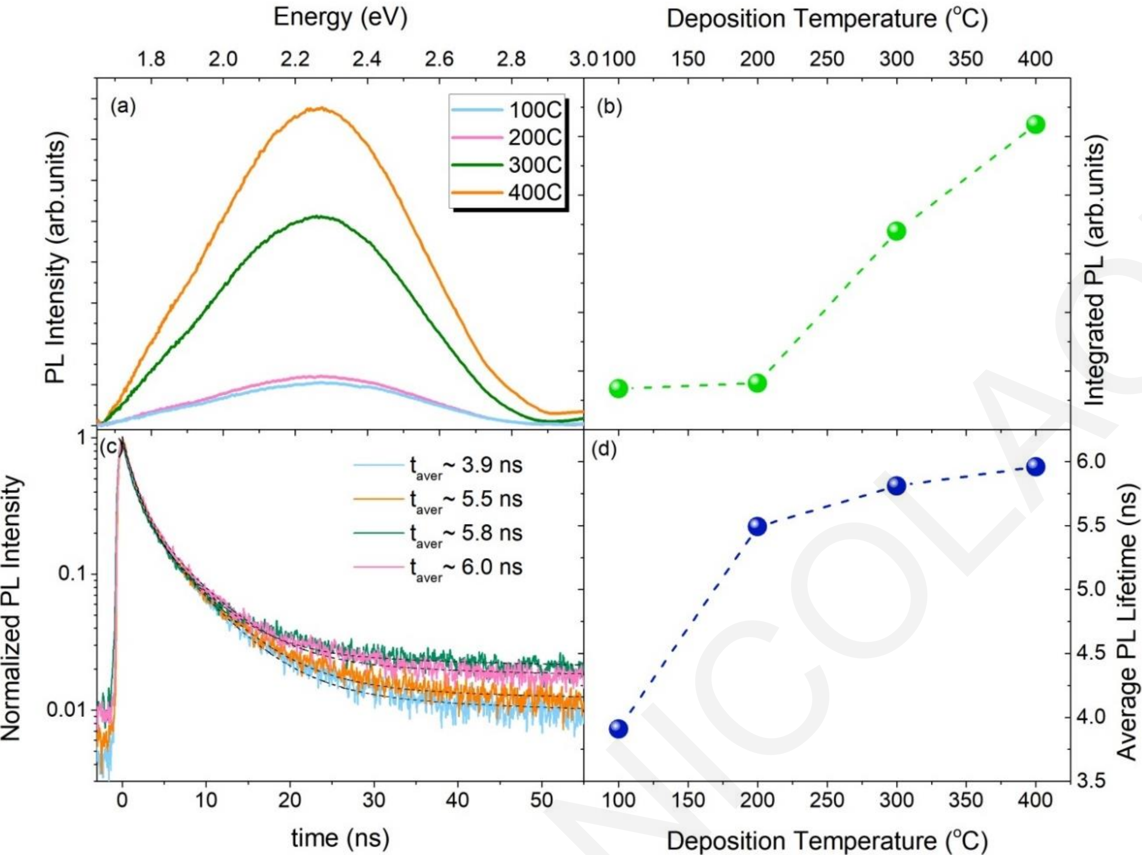

Figure 5.9 (a) Comparative PL spectra of films deposited at various temperatures in the range of 100 – 400 °C, (b) Integrated PL intensity versus deposition temperature, (c) PL decays measured at the band-edge PL peak from CdS films deposited at various temperatures and (d) Average PL Lifetime versus deposition temperature.

The impact of deposition temperature on the properties of CdS films grown by PLD has been investigated through structural, chemical and optical characterization. Polycrystalline and stoichiometric films with relatively large crystallites are obtained at deposition temperatures of 200 – 400°C. The band gap energy of the films is red shifted from 2.55 to 2.49 eV as the substrate temperature increases from 100 to 400°C. The PL lifetimes of the PLD-grown CdS films were estimated to be in the range of ~4 to 6 ns, which are longer compared to CdS films fabricated by other deposition techniques. Although the results of this comprehensive study concern the optimization of the growth parameters for CdS deposition on bare SLG substrates using PLD, they have been employed as the initial deposition conditions for the growth of CdS on the CIGS/Mo/SLG structure.

5.1.3 Conclusions

Polycrystalline CdS thin films have been deposited on bare SLG substrates using PLD under various growth conditions. A systematic investigation of laser fluence and deposition temperature

CHRISTIANA NICOLAOU

has been performed. Highly crystalline, single phase, stoichiometric CdS films are obtained at a fluence of 1.1 J/cm^2 and at deposition temperatures of 200 – 400°C.

5.2 CdS on CIGS/Mo/SLG

5.2.1 Materials and experimental methods

Sequential depositions of CIGS followed by CdS on Mo-coated SLG substrates were carried out using PLD with an KrF excimer laser source (λ = 248 nm, $\tau \leq$ 25 ns) in a high-vacuum chamber (Figure 5.1b). Commercially available Mo-coated SLG substrates were purchased (*Techinstro, India*) and used as is. The thickness of Mo films was 500 nm. The PLD chamber hosts a target carousel which can take up to four targets and the sequential deposition of CIGS and CdS was feasible. A configuration of mirrors guided the laser beam to enter the PLD chamber. Prior entering the chamber, the beam was focused by a focal lens and was adjusted to hit on the polycrystalline targets of CdS and $CuIn_{0.7}Ga_{0.3}Se_2$ (*Testbourne, England*) at an incident angle of 45°. The rotation and toggling of each target provided a uniform ablation of the target surface during deposition. Prior to deposition, the chamber was evacuated at a base pressure of 4x10^{-6} mbar. Argon gas was used for the depositions of CIGS and CdS at pressure of 0.01mbar. The deposition of CIGS on Mo/SLG has been carried out using the optimum growth conditions which are reported in Chapter 4. The number of pulses, repetition rate and target to substrate distance were kept constant at 300, 10 Hz and 4cm respectively, for all CdS depositions. This section is focused on the parametric investigation of the CdS deposition temperature (25 – 400°C) for the fabrication of the CdS/CIGS/Mo/SLG structure.

An X-ray diffractiometer (XRD) (*SmartLab RIGAKU, Cu Kα, λ = 1.5405 Å*) was used to identify the crystal phases present in the CdS/CIGS/Mo/SLG structure. The planar chemical composition of CdS films was determined by energy dispersive X-ray spectroscopy (EDS) (Jeol JSM-6610 LV, Bruker Nano 129eV, XFlash 5010 EDS detector). The electron accelerating voltage of the scanning electron microscope (SEM) was set at 10 kV for the planar EDS analysis. Therefore, the penetration depth extends down to CIGS layer in the multilayer structure. Complementary morphological and elemental analysis of the CdS/CIGS/Mo/SLG films was performed by a field emission gun Zeiss Supra 35VP SEM, operating at 25 kV. For chemical analysis, the microscope is equipped with an EDAX Octane Elite Plus EDS detector with a resolution of 125 eV (Mn K_α line). Samples suitable for SEM were prepared in cross section configurations and coated with carbon at an Emitec K250 coating unit.

Current-Voltage (IV) measurements were performed at room temperature using a two-probe configuration, as shown in Figure 5.1b. The electrodes of the voltage source/ ammeter were mechanically placed on CdS and Mo surface, creating an electrical circuit. The CIGS/CdS junction was electrically forward and reverse biased with an applied voltage of ±4V. The IV measurements have been performed at room temperature and in ambient atmosphere.

CHRISTIANA NICOLAOU

5.2.2 Results and discussion

5.2.2.1 Impact of CdS deposition temperature

CdS/CIGS heterojunctions have been grown using PLD in a sequential deposition of CIGS and CdS layers on Mo-coated SLG substrates. Even though CdS deposition temperature has been investigated on the single layer structure (section 5.1), a parametric investigation of CdS deposition temperature has been conducted also for the fabrication of CdS/CIGS heterojunctions, since the growth temperature of CdS is one of the most impactful parameters of the deposition process of the multilayer structure. Thus, different heterojunctions with CdS deposition temperature varying from 20 to 400°C have been fabricated, at optimum fluence of 1.1 J/cm^2 identified in the parametric investigation of fluence discussed in section 3.1. The only difference between the investigated samples was the deposition temperature of CdS, while all the other process parameters were kept the same for all samples. The deposition temperature of CIGS was 300°C. More details on the deposition parameters of CIGS layer are discussed in previous work [3].

A typical cross section SEM image of the CdS/CIGS/Mo/SLG structure, with CdS layer grown at 300°C is manifested in Figure 5.10a, obtained using backscattered electrons. The Mo and CIGS layers are readily observed, exhibiting sharp interfaces, while the layer of CdS is less clearly resolved. The thickness of the three layers is about 630 nm, 1470 nm and ~52 nm for the Mo, CIGS and CdS layers, respectively. EDS point analysis spectra of the *cross section* were acquired in the main body of the multi-layer (Figure 5.10b), as well as in its upper part (Figure 5.10c). The families of Cu K, In L, Ga K and Se K peaks illustrate the formation of the CIGS layer in Figure 5.10b. Some residual molybdenum was also resolved in these EDS spectra, too. Identification of the CdS layer was predominately accomplished by the Cd L and S K peaks, resolved in Figure 5.10c along with the rest ones from CIGS. However, indications of residual Mo from the CIGS layer cannot be entirely excluded due to the large (~800 nm) electron beam size of SEM, though not resolvable since the S K peak coincides with the Mo L one. This is thus denoted as a double Mo/S peak in Figure 5.10c.

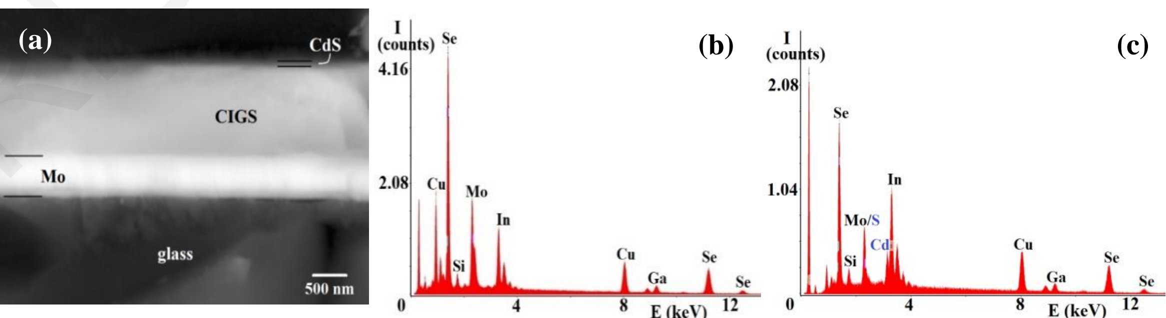

Figure 5.10 (a) Backscattered electron SEM image of CdS/CIGS/Mo/SLG multi-layer structure, (b) & (c) EDS point analysis spectra from the CIGS and CdS layers, respectively. The CdS layer is predominately distinguished by its Cd L peak (blue coloured), located at 3.13 keV.

CHRISTIANA NICOLAOU

Figure 5.11 shows the EDS-determined *planar* compositional ratio of CdS layers deposited on CIGS/Mo/SLG at various deposition temperatures. The S/Cd ratio was calculated by averaging the composition values obtained by scanning multiple areas for each sample. S/Cd ratio increases as the deposition temperature of CdS increases from room temperature up to 300ºC. The CdS films are sulfur-poor and become stoichiometric as the deposition temperature of CdS reaches at 300ºC. An abrupt decrease of S/Cd is observed at 400ºC, where the CdS films become sulfur-deficient again.

The GIXRD patterns of CdS/CIGS/Mo/SLG structure with different CdS deposition temperatures have been examined with grazing incidence angle of 1.0º and 2θ ranging from 10º to 90º (Figure 5.12). At the CdS deposition temperature of 400ºC, a secondary phase of $CuInS_{2-x}$ (JCPDS 65-1572) appears in the samples most likely due to the interdiffusion of the elements between CIGS and CdS layer. In addition, a secondary phase of $Cu_{2-x}Se$ is identified in the samples with CdS layer grown at 300 and 400ºC. However, based on the results of a previous work regarding the deposition of CIGS by PLD [3], $Cu_{2-x}Se$ phase appears in CIGS layer for deposition temperatures up to 400ºC. Thus, regardless of the sequential deposition of CdS and its deposition temperature, $Cu_{2-x}Se$ phase is expected to be present in the CIGS layer of all multilayer structures, since the CIGS layer was grown at 300ºC in all cases. The $Cu_{2-x}Se$ phase is not distinguishable in the XRD patterns of CdS/CIGS/Mo/SLG structure because the two main peaks of $Cu_{2-x}Se$ phase at ~43.4º and 26.2º, indicated in Figure 5.12, are in close proximity with CdS peaks. In addition, $CuInS_2$ phase is formed at the CdS/CIGS interface and hence, is expected to play a major role in the performance of the junction. For all these reasons, the $Cu_{2-x}Se$ phase is not taken into account in the discussion of the electrical properties of CdS/CIGS junction.

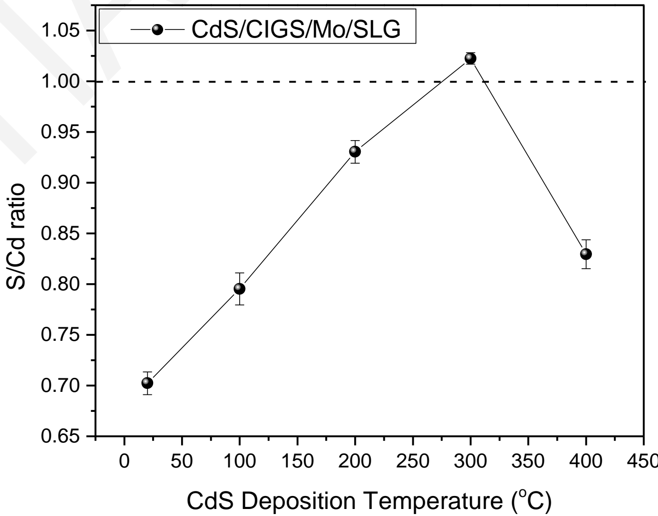

Figure 5.11 Compositional ratio of CdS thin films deposited CIGS/Mo/SLG at various CdS deposition temperatures, from room temperature up to 400ºC. Dashed line indicates the ratio of a

CHRISTIANA NICOLAOU

stoichiometric CdS film, being S/Cd=1. The CdS layer is stoichiometric at CdS deposition temperature of 300°C.

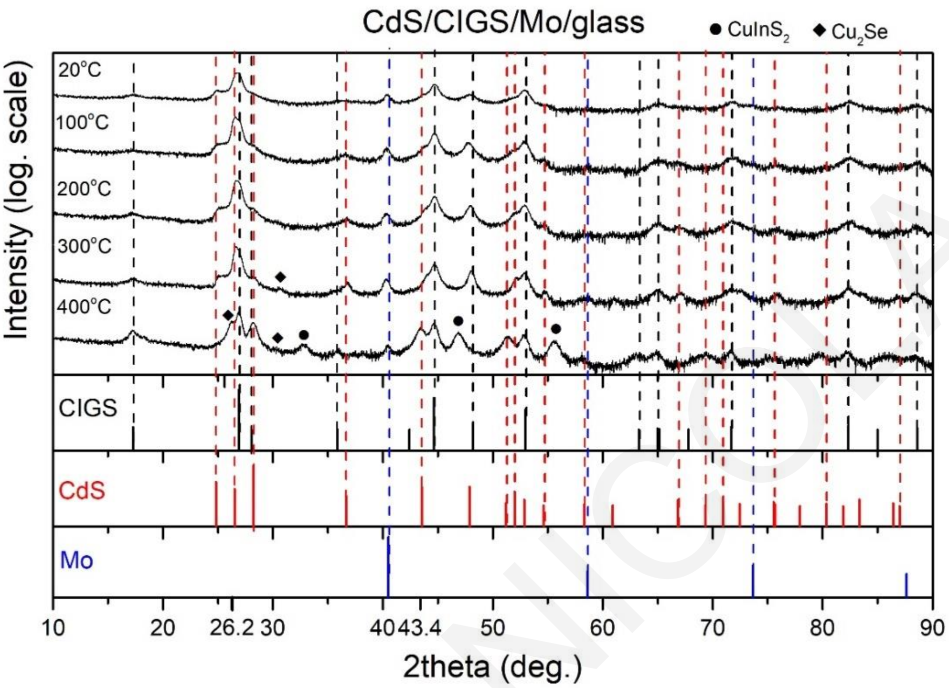

Figure 5.12 XRD patterns of CdS/CIGS/Mo/SLG multi-layer structures as function of CdS deposition temperature, from room temperature up to 400°C. The bottom plots show the XRD pattern of CdS hexagonal phase (JCPDS 96-900-8863), $CuIn_{0.7}Ga_{0.3}Se_2$ (JCPDS 35-1102), Mo (PDF 9008543) and secondary phases of $CuInS_2$ (JCPDS 65-1572) and Cu_2Se (JCPDS 04-001-9933).

The electrical properties of the CdS/CIGS heterojunctions have been investigated by performing 2-probe dark IV measurements. The configuration is shown in Figure 5.1b and the details of the measurements are reported at the experimental session. The dark IV curves for the samples grown at a CdS deposition temperature from room temperature up to 400°C reveal the diode-like behavior of the CdS/CIGS junction (Figure 5.13a). The characteristic curves of CdS/CIGS diode shift to lower voltages as CdS deposition temperature increases and as a consequence, the knee voltage at forward bias decreases. The decrease of knee voltage indicates the formation of a lower potential barrier at the interface of CdS/CIGS junction as the deposition temperature of CdS increases. The band alignment of CdS/CIGS heterojunction has two configurations regarding the conduction band offset at the interface. Specifically, the difference between the conduction band minima of CdS and CIGS induces a conduction band offset which can be positive (spike-like) or negative (cliff-like). The spike-like alignment (Figure 5.13b) is obtained in cases where the energy gap of CIGS is relatively low [249-251] and is reported to be beneficial due to the observed enhancement of the open-circuit voltage [78, 252]. Here, the stoichiometry of $CuIn_{1-x}Ga_xSe_2$ ($x \approx 0.26$) [3] layer resides at the low energy gap regime and thus, a spike-like potential at the interface of

CHRISTIANA NICOLAOU

CdS/CIGS is expected to be formed. As the deposition temperature of CdS increases from room temperature up to 400ºC, the knee voltage of the IV curve decreases (Figure 5.13a) indicating a decrease of the spike-like potential barrier at CdS/CIGS interface.

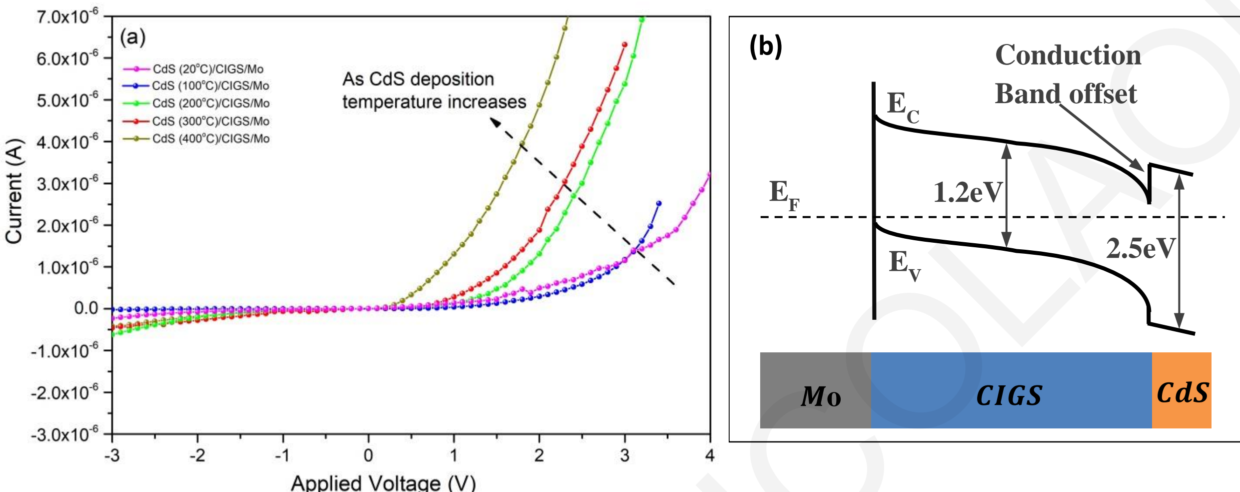

Figure 5.13 (a) Dark IV curves for the CdS/CIGS/Mo structures grown at various CdS deposition temperature, from room temperature up to 400ºC. The knee voltage at forward bias decreases as CdS deposition temperature increases (b) Energy band diagram of Mo/CIGS/CdS structure indicating the conduction band offset at CIGS/CdS interface.

The rectifying performance of a diode in the dark taking into account the single diode model and the parasitic resistances of the diode can be described by Equation 2:

$$I = I_O \left[exp\left(\frac{q(V-IR_S)}{nkT}\right) - 1\right] + \frac{V-IR_S}{R_{sh}} \quad , \qquad \text{(Equation 5.2)}$$

where I is the current through the diode, V is the applied voltage across the diode, I_o is the dark saturation current, n is the ideality factor, T is the temperature in kelvin, q is the electron charge, K is the Boltzmann constant and R_s and R_{sh} are the series resistance and shunt resistance of the diode, respectively.

Ideality factor, leakage current, shunt and series resistance were calculated by the fitting of Equation 2 on the experimental data of the IV curves, using the equivalent circuit calculator by PV Lighthouse [253].

Ideality factor and leakage current as function of CdS deposition temperature are shown in Figures 5.14a and 14b. As Figure 5.14a illustrates, ideality factor is abnormally high for the sample of which CdS layer has been grown at room temperature. As CdS deposition temperature increases, ideality factor of the diode decreases, reaching a minimum at 300ºC. Further increase in CdS deposition temperature brings about an increase in ideality factor. Such large values of ideality factor

CHRISTIANA NICOLAOU

indicate the presence of unusual recombination mechanisms taking place and have been reported in the literature for various junction devices [254]. The CdS/CIGS diode grown at CdS deposition temperature of 300ºC exhibits an ideality factor closer to 2, which indicates the domination of a Shockley-Read-Hall (SRH) recombination through defect states at the forbidden gap [255].

The ideality factor has been correlated with the compositional and structural characterization of the diodes. By comparing CdS composition (Figure 5.11) and ideality factor (Figure 5.14a) with CdS deposition temperature an interesting correlation is obtained. The quality of the junction improves as the S/Cd ratio of CdS layer is closer to unity. Non-stoichiometric CdS layers grown on CIGS/Mo give high diode ideality factors due to the enhanced recombination mechanisms caused by high degree of defects (such as interface states), barrier inhomogeneity, and non-uniform distribution of the interfacial charges. Stoichiometric CdS layers grown on CIGS/Mo result in lower ideality factors indicating the low degree of defects, decreased recombination and improved junction uniformity. In addition, the XRD patterns reveal a secondary phase of $CuInS_{2-x}$ for the CdS/CIGS diode grown at CdS deposition temperature of 400ºC which corroborates with the junction inhomogeneity and the high ideality factor.

The leakage current follows a similar trend as that of ideality factor with the increase of CdS deposition temperature (Figure 5.14b). At temperatures of 20 and 400ºC, the leakage current is large and of the order of 10^{-9} to 10^{-8} A. Low leakage current of the order of 10^{-11} A is obtained for the diodes where CdS have been deposited at 100, 200 and 300ºC with the minimum value calculated at 300ºC. Low values of leakage current on reverse bias indicate the better quality of the junction formed, as discussed previously for the diodes' ideality factor. Moreover, higher shunt resistance is indicative of the low leakage current, as almost zero current is conducted through the diode. Series and shunt resistance of the diodes will be discussed next.

CHRISTIANA NICOLAOU

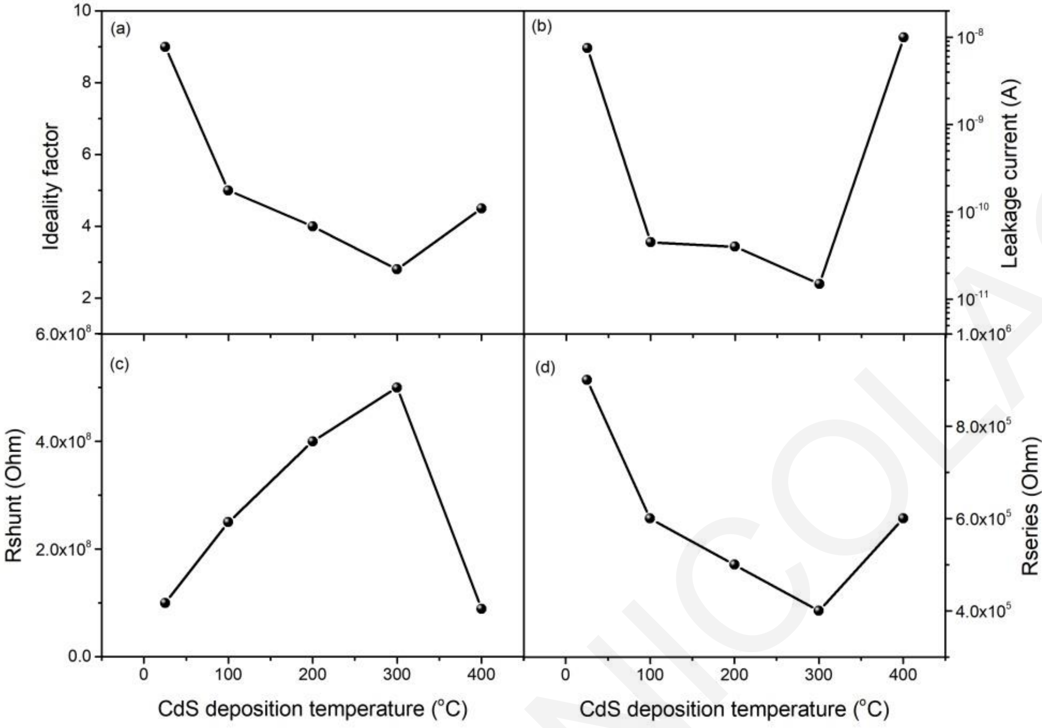

Figure 5.14 (a) Ideality factor, (b) leakage current, (c) shunt and (d) series resistance of the CdS/CIGS/Mo structures as function of CdS deposition temperature, from room temperature up to 400°C. The CdS/CIGS/Mo structures grown at CdS deposition temperature of 200 and 300°C exhibit low values of ideality factor and leakage current, low series and high shunt resistances.

Figure 5.14c and 5.14d displays the series and shunt resistances of the CdS/CIGS/Mo structures as function of CdS deposition temperature, respectively. Diode series and shunt resistances depend on multiple underlying mechanisms and each one contributes by a different weight to the overall macroscopic resistance [256-259]. In this work, the observed trends of series and shunt resistances of the samples are being explained using plausible mechanisms, which emerge from the compositional and structural characterization.

Shunt resistance of CdS/CIGS diode increases as CdS deposition temperature increases from room temperature up to 300°C. However, a decrease of shunt resistance is observed for the sample of which CdS was grown at 400°C (Figure 5.14c). The highest diode shunt resistance is obtained for CdS deposition temperature at 200 and 300°C. The low shunt resistance at 25, 100 and 400°C can be attributed to the increased concentration of defects and non-idealities at the junction which can cause partial shortening of the junction through low resistive paths. The increased concentration of defects can arise by the non-stoichiometric CdS layers, as indicated by S/Cd ratio in Figure 5.11. Sulfur-deficient CdS layers may introduce point defects, like sulfur vacancies, near the junction. In previous

CHRISTIANA NICOLAOU

works, sulfur vacancies have been reported as being the responsible defects which contribute to the low resistivity in sulfur deficient CdS layers [230, 260-262]. Here, it can be assumed that sulfur vacancies could be present near the junction of the diodes with CdS layer grown at room temperature, 100ºC and 400ºC and provide to the current lower resistive paths to pass through, thus the resulting shunt resistance is low. The CdS/CIGS diodes with CdS layer grown at 200 and 300ºC exhibit the highest shunt resistance due to the lower concentration of defects, as CdS layer is nearly stoichiometric for these samples.

Moreover, the low shunt resistance of CdS/CIGS diode with CdS grown at 400ºC can be attributed to the formation of $CuInS_2$ secondary phase as indicated by the XRD patterns (Figure 5.12). The presence of $CuInS_2$ phase indicates the introduction of lattice defects such as Cu vacancies and In_{Cu} antisites [193, 263-265] into CIGS layer, as well as S vacancies and interstitials [266, 267] into CdS layer, because Cu, In and S are being drawn out from CIGS and CdS layers in order to form the $CuInS_2$ phase. This large amount of lattice defects near the junction, arising from the presence of $CuInS_2$ phase, could provide to the diode shunt paths causing the shunt resistance to drop.

Series resistance of CdS/CIGS diode decreases as CdS deposition temperature increases from room temperature up to 300ºC (Figure 5.14d). The lowest diode series resistance is obtained for CdS deposition temperature at 200 and 300ºC. The higher series resistance at low CdS deposition temperatures can be attributed to the low crystallinity of the CIGS and CdS layers, as indicated by the XRD patterns in Figure 5.12, which result to the increased scattering of the carriers on grain boundaries and lattice defects. As the temperature of CdS deposition increases, the crystal quality of the layers improves and the series resistance decreases.

However, the CdS/CIGS diode with CdS grown at 400ºC exhibits high series resistance (Figure 5.14d), despite the enhancement of layers' crystallinity. This observation can be associated with the formation of $CuInS_2$ secondary phase which is observed only for the samples with CdS grown at 400ºC (Figure 5.12). $CuInS_2$ is a ternary chalcopyrite compound with an energy gap of about 1.5eV at room temperature [268, 269]. The electrical properties of $CuInS_2$ strongly depend on the stoichiometry of the compound, that is, excess-sulfur films are generally p-type while sulfur-deficient and indium-rich films are n-type. Resistivity and carrier concentration of $CuInS_2$ are subjected to large variations in respect to the stoichiometry and type of conductivity, with resistivity ranging from 10^{-1} to 10^{2} Ω.cm and carrier concentration from 10^{13} to 10^{19} cm^{-3} [270, 271]. Such high values of resistivity and low values of carrier concentration may contribute to the higher series resistance of the CdS/CIGS diode with CdS grown at 400ºC.

CdS deposition temperature has a major impact on the electrical properties of the CdS/CIGS/Mo diode. Low series and high shunt resistances are obtained for the samples where CdS is grown at 200 and 300ºC. The high shunt resistance corroborates with the low leakage current obtained for those samples (Figure 5.14). In addition, the CdS/CIGS diode grown at CdS deposition

CHRISTIANA NICOLAOU

temperature of 300ºC exhibits the lowest ideality factor, which is close to 2, indicating the better quality of the diode with less non-idealities.

5.2.3 Conclusions

The influence of CdS deposition temperature has been investigated on the properties of CdS/CIGS junction grown by PLD. The best quality CdS/CIGS diodes have been grown at CdS deposition temperatures of 200 and 300ºC, exhibiting low ideality factor, low leakage current, low series and high shunt resistances. This chapter demonstrates that the sequential deposition of CIGS and CdS layers on Mo-coated SLG substrates using PLD results in high-quality CdS/CIGS diodes and puts forward PLD as a novel, alternative deposition method for the fabrication of CIGS solar cells in a simple and fast line production process.

CHRISTIANA NICOLAOU

Chapter 6 – Optimization of the ZnO and ZnO:Al layers

A great interest exists in zinc oxide (ZnO) materials because of their usefulness in a wide range of high technology applications, low cost, resource availability, non-toxicity and very high thermal and chemical stability [272]. ZnO is a direct wide-bandgap semiconductor with an energy bandgap of 3.4eV [273]. The structures shared by the ZnO crystal are wurtzite, zinc blende and rocksalt. At ambient pressure and temperature, ZnO crystallizes in the hexagonal wurtzite structure [274]. The n-type conductivity of the undoped ZnO has been attributed to intrinsic defects such as Zn interstitials, oxygen vacancies, or hydrogen [275-279]. Extrinsic doping of ZnO can be achieved using the elements of group III (Al, In, Ga, Cu, Cd, etc) as dopants which serve as donors in the ZnO lattice. Extrinsic doping of ZnO results to the increase of both n-type conductivity and bandgap, leading to improved electrical and optical properties. It is worth to underline that among all the elements of group III, Al is a cheap, abundant and non-toxic material. Thus Al-doped ZnO (ZnO:Al) films are prominent, low-cost substitutes of indium tin oxide films as transparent conducting films in the photovoltaic thin film applications [280].

The transparent conducting oxide (TCO) thin film materials with high electrical conductivity and high optical transparency are widely used in photovoltaic devices as window layers. Based on these requirements, ZnO:Al transparent conducting film is a suitable TCO which has been commonly used as a window layer for $Cu(In,Ga)Se_2$ thin film solar cells [49, 281, 282]. A bilayer of an intrinsic and Al-doped ZnO layer was found to increase the V_{oc} of the device leading to higher efficiencies [49, 50]. The intrinsic ZnO layer provides, together with the CdS buffer layer, protection of the device from local electrical losses that may originate from inhomogeneities of the CIGS absorber [283]. The exact role of this additional layer, whether it just introduces resistance into short circuits and/or changes the interfacial energetics, is not well understood [283]. The optimization of this interface is, therefore, a critical need.

Almost all the major deposition techniques such as sputtering [284, 285], chemical vapor deposition [286], sol-gel [287], chemical spraying [288], electron plasma sputtering [289], or ion-beam assisted deposition [290, 291] have been utilized for the growth of ZnO films. The highest efficiency CIGS cell to date was fabricated using an intrinsic and Al-doped ZnO layer grown by RF-sputtering [11]. However, the bombardment of high-energy particles onto the CIGS/CdS interface during the sputtering process of the ZnO deposition can lead to the degradation of the junction properties. Therefore, the identification of a low damage deposition process is preferable to avoid degradation of the CIGS absorber layer. High substrate temperatures during the deposition of the TCO can also be a source of damage [292, 293]. For high-efficiency cells the TCO deposition temperature should be lower than 150°C in order to avoid the detrimental interdiffusion across

CHRISTIANA NICOLAOU

CdS/CIGS interface [210]. Consequently, the deposition of the ZnO/ZnO:Al bilayer at low deposition temperature using a less destructive deposition method is desirable. In addition, low deposition temperature enables the fabrication of thin film solar cells on plastic substrates.

PLD can offer the potential of growing high-quality crystalline films at relatively lower substrate temperatures than other techniques, due to the non-equilibrium process occurring during the growth [294, 295]. In addition, it is well known that PLD is the most suitable method to grow high quality oxide thin films [108], and its use in depositing intrinsic [296-299] and Al-doped ZnO films [300-303] has been extensively studied. This chapter reports on the utilization of pulsed laser deposition (PLD) for the deposition of the ZnO:Al, ZnO, CdS and CIGS layers on Mo-coated SLG substrates in one growth sequence. In the previous chapters, the growth of CIGS (Chapter 4) and CdS (Chapter 5) layers has been discussed and the optimum deposition parameters have been defined based on the properties of each layer along with the properties of their adjacent interfaces. This chapter focuses on the investigation of the deposition parameters of ZnO and ZnO:Al films.

Sections 6.1 and 6.2 of this chapter reports on the systematic investigation of the influence of PLD growth parameters on the properties of ZnO films deposited on SLG substrates and on the CdS/CIGS/Mo/SLG structure, respectively. In section 6.1, a comprehensive characterization of structure and morphology has been carried out to understand the impact of the deposition parameters on the properties of ZnO films. In addition, optical measurements of ZnO films have been performed in order to study the optical properties of the films. The optimum PLD growth conditions for ZnO films are identified based on an overall assessment of film characteristics. The results of section 6.1 regarding the deposition of ZnO on SLG substrates have been used to consequently grow optimized ZnO films on top of the CdS/CIGS/Mo/SLG structure. ZnO, CIGS and CdS layers have been deposited on Mo-coated SLG using PLD without interrupting the deposition process. The influence of ZnO deposition temperature on the properties of ZnO/CdS/CIGS/Mo junction has been studied through structural and electrical characterization.

Section 6.3 and 6.4 deals with the investigation of the growth of ZnO:Al films on SLG substrates and on the ZnO/CdS/CIGS/Mo/SLG structure, respectively. In section 6.3, ZnO:Al films have been deposited on SLG substrates using the optimum parameters identified from sections 6.1 and 6.2 regarding the investigation of ZnO films. The structural, optical and electrical properties of ZnO:Al films are presented in section 6.3. In section 6.4, the deposition temperature of ZnO:Al is investigated to grow ZnO:Al films on top of the ZnO/CdS/CIGS/Mo/SLG structure. ZnO:Al, ZnO, CdS and CIGS layers have been deposited on Mo-coated SLG using PLD without interrupting the deposition process. The influence of ZnO:Al deposition temperature on the properties of ZnO:Al/ZnO/CdS/CIGS/Mo junction has been studied through structural and electrical characterization. The fabrication of the PLD-grown ZnO:Al/ZnO/CdS/CIGS/Mo/SLG devices are investigated and studied for the first time herein.

CHRISTIANA NICOLAOU

6.1 ZnO on SLG

6.1.1 Materials and experimental methods

ZnO films were deposited on SLG substrates by PLD using a KrF excimer laser source (λ = 248 nm, $\tau \leq 25$ ns) in a high-vacuum chamber (Figure 6.1a). A polycrystalline ZnO target (*Testbourne, England*) was used for the deposition of ZnO films. The substrate was placed at a fixed distance of 5 cm. The deposition was carried out in the presence of oxygen gas at pressure of 0.25 mbar, after the chamber was evacuated at a base pressure of 4×10^{-6} mbar. The repetition rate and number of pulses were kept constant at 10 Hz and 1500, respectively, for all depositions. Prior to deposition, the substrates were ultrasonically cleaned with a sequence of organic solvents. Section 6.1 is focused on the parametric investigation of laser fluence and deposition temperature of PLD-grown ZnO films.

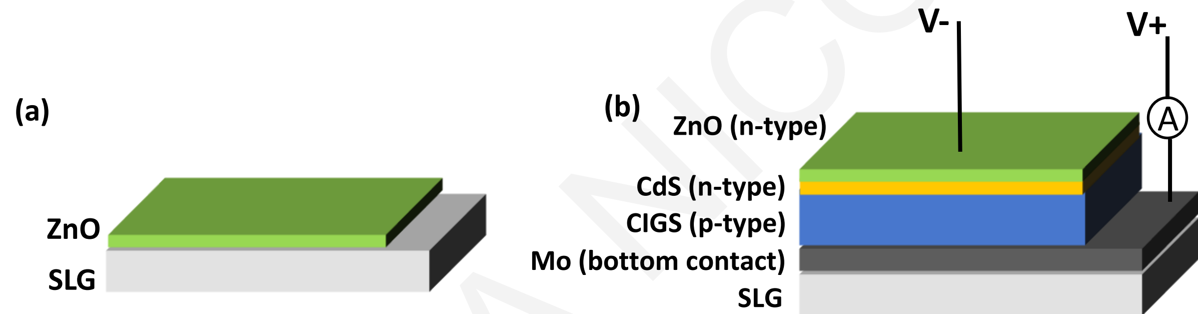

Figure 6.1 Schematic deposition structures: (a) ZnO on SLG and (b) ZnO/CdS/CIGS/Mo/SLG structure fabricated by the sequential deposition of CIGS, CdS and ZnO on Mo-coated SLG.

Structural properties and crystallinity of the films were studied by X-ray diffraction (SmartLab RIGAKU, Cu Kα, λ = 1.5405 Å). The thickness of the films was measured by a stylus profilometer. Topography and surface roughness were probed via atomic force microscopy (AFM, Agilent Technologies). EDS analysis for the stoichiometry of ZnO films was not applicable as the oxygen is not identifiable**.**

6.1.2 Results and discussion

6.1.2.1 Impact of laser fluence

The influence of laser fluence on the growth of ZnO films has been investigated by depositing ZnO on SLG substrates at 300°C using PLD, with laser fluence varying from 1.0 to 1.6 J/cm^2. The structural characteristics and crystallinity of ZnO films have been examined by grazing incidence XRD (GIXRD) with 2θ values ranging between 10° and 90°; the XRD patterns are shown in Figure 6.2a. The peaks of the XRD patterns are identified by the hexagonal ZnO (PDF card 9004178), revealing the polycrystalline nature of the films. No secondary phase is observed on the XRD patterns, indicating the existence of the pure ZnO phase in the films, independently of laser

CHRISTIANA NICOLAOU

fluence. In Figure 6.2b, FWHM and crystallite size are presented as function of fluence. The crystallite size was calculated using the Debye-Scherrer formula for (002) diffraction peak. The crystallinity of the films is high for the films deposited at 1.0, 1.2 and 1.4 J/cm^2 and decreases for the film grown at 1.6 J/cm^2, as shown in Figure 6.2b.

The results of crystallite size calculated from the XRD patterns can be correlated with the change of the films' thickness as the fluence increases, shown in Figure 6.3a. The thickness of the films increases from 155 to 240 nm as the fluences increases from 1.0 to 1.2 J.cm^2. Then, an abrupt decrease of the thickness is observed for the higher fluences of 1.4 and 1.6 J/cm^2. This unexpected decrease of thickness at higher fluences can be attributed to the occurrence of sputtering of the films' surface by the ablated atoms. The kinetic energy of the ablated atoms increases with fluence and a substantial fraction of the particles have a kinetic energy lying in the range where the sputtering yield increases considerably with energy [304-306]. Thus, at fluences of 1.4 and 1.6 J/cm^2, the films are subjected to sputtering of the surface, which counteracts the deposition, therefore the thickness of the films decreases. At fluence 1.6 J/cm^2, the impact of sputtering of the film's surface becomes more significant, and the crystallinity of the film is affected, resulting to a decreased crystallinity compared to the films deposited at lower fluence.

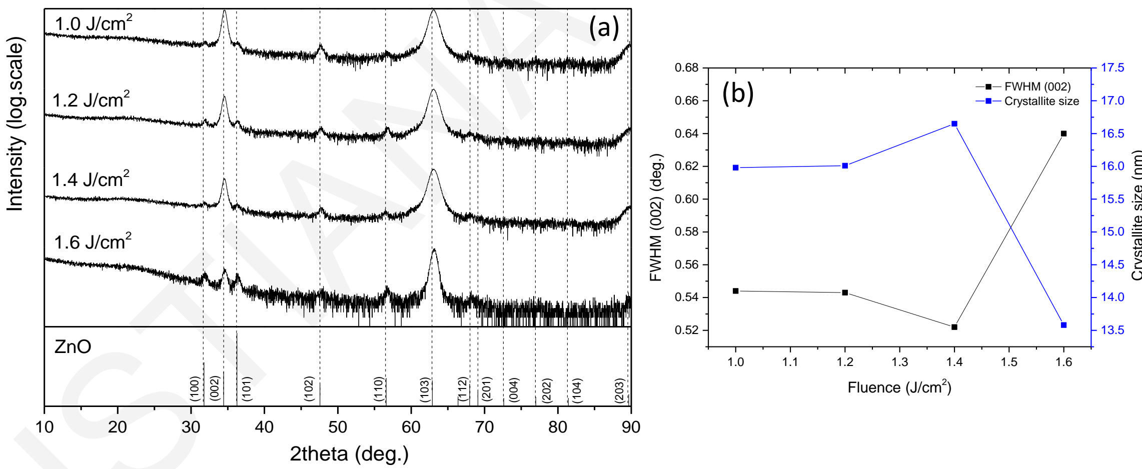

Figure 6.2 (a) XRD patterns and (b) FWHM and crystallite size of ZnO thin films deposited on SLG substrates at fluence of 1.0 to 1.6 J/cm^2. The bottom plot of (a) shows the linear XRD pattern of ZnO hexagonal phase according to PDF card 9004178.

CHRISTIANA NICOLAOU

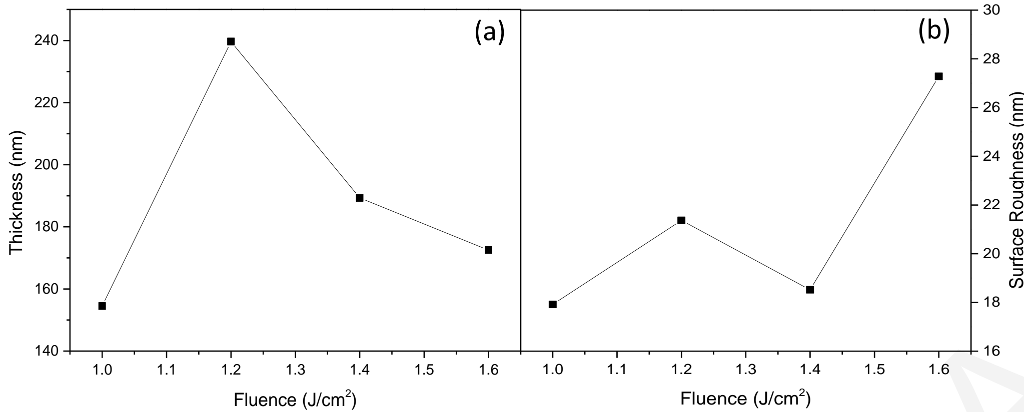

Figure 6.3 (a) Thickness and (b) surface roughness of ZnO thin films deposited on SLG substrates as function of fluence from 1.0 to 1.6 J/cm^2.

The surface roughness of the films as a function of fluence was measured by AFM within an area of 80x80 μm^2 and is presented in Figure 6.3b. Surface roughness slightly increases from 18 to 28 nm with increasing fluence. These low values of the measured roughness indicate the high smoothness of ZnO films obtained by PLD. The highest value of surface roughness obtained for the film deposited at 1.6 J/cm^2 can be correlated with the occurrence of sputtering on the film's surface. As the sputtering of the surface at 1.6J/cm^2 becomes significant, the surface of the film is expected have more irregularities and therefore the surface roughness becomes higher.

6.1.2.2 Impact of deposition temperature

The influence of deposition temperature on the growth of ZnO films has been investigated by depositing ZnO on SLG substrates using PLD, with deposition temperatures varying from 20 to 300°C, at fluence of 1.2 J/cm^2. ZnO films deposited at various deposition temperatures have been examined by grazing incidence XRD (GIXRD) with 2θ values ranging between 10° and 90°; the XRD patterns are shown in Figure 6.4a. The peaks of the XRD patterns are identified by the hexagonal ZnO (PDF card 9004178), revealing the polycrystalline nature of the films. No secondary phase is observed on the XRD patterns indicating the pure ZnO phase of the films, independently of deposition temperature.

The quality of the films is enhanced as the deposition temperature increases due to the higher crystallinity of the films, as shown in Figure 6.4b and 6.4c. The crystallite size was calculated using the Debye-Scherrer formula for (103) diffraction peak. The crystallite size of the films increases as the deposition temperature increases from room temperature up to 200°C and then decreases at 300°C. The decrease of crystallinity at 300°C can be attributed to the formation of oxygen vacancies in the film due to the evaporation of the volatile oxygen atoms from the film's surface during the deposition. As a result, the films grown at 300°C can deviate from the stoichiometry leading to oxygen deficiency and increased structural defects. These defects act as low-energy nucleation

CHRISTIANA NICOLAOU

centers that limit the crystallite growth due to multiple adjacent crystallites growing next to each other [109]. Therefore, the ZnO film grown at 300ºC is composed of smaller crystallites compared to the films grown at lower deposition temperatures. Similar results have been found in studies dealing with the growth of ZnO film using PLD [240, 241].

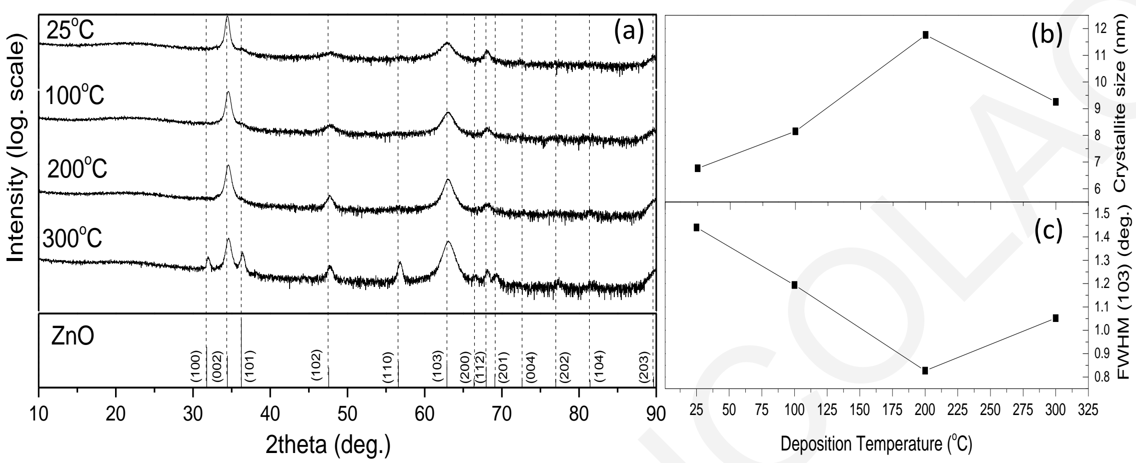

Figure 6.4 (a) XRD patterns, (b) crystallite size and (c) FWHM of ZnO thin films deposited on SLG substrates as function of deposition temperature. The bottom plot of (a) shows the linear XRD pattern of ZnO hexagonal phase according to PDF card 9004178.

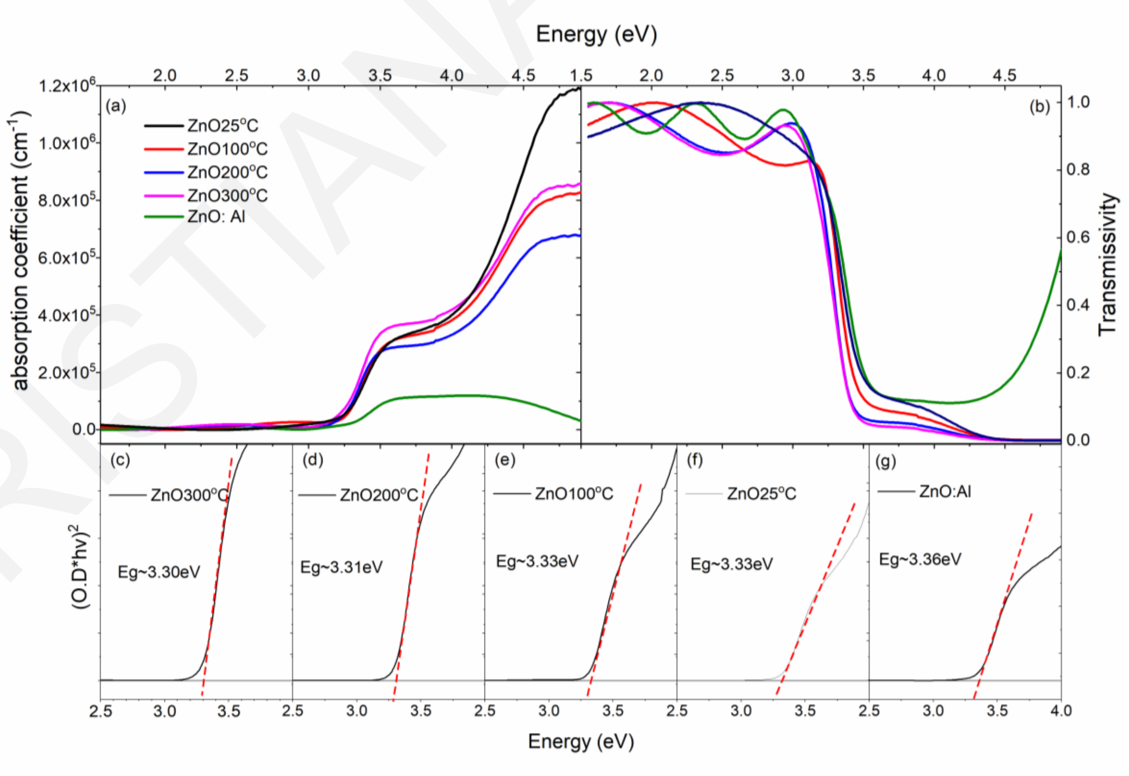

Figure 6.5 Spectral variation of the (a) absorption coefficient and (b) transmissivity of ZnO films

CHRISTIANA NICOLAOU

grown at various substrate temperatures. (c)-(f) Tauc plots of the undoped ZnO films and (g) the doped ZnO:Al film. The estimated energy gap for each film is also shown.

The absorption coefficient and optical transmissivity of undoped ZnO films at room temperature are shown in Figure 6.5. High transparency with transmissivity over than 80% in the visible spectral region is observed in all the films. The bandgap of the ZnO is obtained by the interpolation of the linear part of the spectra to y=0 in the the Tauc plots of the figure i.e. $(O.D.*h\nu)^2 = f(h\nu)$, where O.D. is the optical density. The absorption edge appears to gradually blue shift by as much as 30 meV as PLD temperature drops from 300°C to 25°C. The experimental values are comparable to those reported in the literature [307, 308].

6.1.3 Conclusions

The impact of fluence and deposition temperature on the properties of ZnO films grown by PLD has been investigated through structural, chemical and optical characterization. Polycrystalline films with relatively large crystallites and low roughness without the occurrence of sputtering at the film's surface are obtained at fluence of 1.0 and 1.2 J/cm^2. In addition, the films grown at 200°C present high crystallinity and high transmittance which are the desirable properties for the ZnO layer in the photovoltaic device.

6.2 ZnO on CdS/CIGS/Mo/SLG

6.2.1 Materials and experimental methods

A sequential deposition of CIGS, CdS and ZnO layers on Mo-coated SLG substrates was carried out using PLD with a KrF excimer laser source (λ = 248 nm, $\tau \leq$ 25 ns) in a high-vacuum chamber (Figure 6.1b). Commercially available Mo-coated SLG substrates were purchased (Techinstro, India) and used as is. The thickness of Mo films was 500 nm. The PLD chamber hosts a target carousel which can take up to four targets and the sequential deposition of CIGS, CdS and ZnO was feasible. Polycrystalline targets of ZnO, CdS and $CuIn_{0.7}Ga_{0.3}Se_2$ (Testbourne, England) were used for the deposition of the three layers. Prior to deposition, the chamber was evacuated at a base pressure of $4x10^{-6}$ mbar. The deposition of ZnO was carried out in the presence of oxygen gas at 0.25 mbar. The number of pulses, repetition rate and target to substrate distance were kept constant at 1500, 10 Hz and 5cm respectively, for all ZnO depositions. CIGS and CdS layers were deposited at 300°C and in the presence of argon gas at 0.01mbar. The optimum deposition parameters were used for the deposition of CIGS and CdS layers which are discussed in Chapter 4 and 5, respectively. This section is focused on the parametric investigation of the ZnO deposition temperature for the fabrication of the ZnO/CdS/CIGS/Mo/SLG structure.

An X-ray diffractometer (XRD) (*SmartLab RIGAKU, Cu Kα, λ = 1.5405 Å*) was used to identify the crystal phases present in the ZnO/CdS/CIGS/Mo/SLG multi-layer structures. Current-

CHRISTIANA NICOLAOU

Voltage (IV) measurements were performed at room temperature using a two-probe configuration, as shown in Figure 6.1b. The electrodes of the voltage source/ ammeter were mechanically placed on ZnO and Mo surface, creating an electrical circuit. The ZnO/CIGS/CdS junction was electrically forward and reverse biased with an applied voltage of ±1V. The IV measurements have been performed at room temperature and in ambient atmosphere.

6.2.2 Results and discussion

6.2.2.1 Impact of ZnO deposition temperature

The XRD patterns of ZnO/CdS/CIGS/Mo/SLG structures with different ZnO deposition temperatures have been examined by grazing incidence (GIXRD) with 2θ ranging from 10° to 90° and are presented in Figure 6.6. The fabrication of the ZnO/CdS/CIGS/Mo/SLG structures was conducted by varying the deposition temperature of ZnO from 50 to 300°C while keeping the deposition temperature of CIGS and CdS constant at 300°C. The XRD patterns reveal that the existence of the ZnO and CdS hexagonal phase, the chalcopyrite $CuIn_{0.7}Ga_{0.3}Se_2$ phase and the Mo phase. The identification of Mo phase in the XRD patterns indicates that the grazing incidence angle used was such that the penetration depth of the X-rays was reaching the Mo layer. This is an important fact considering that the XRD scanning must take place through the whole multilayer structure in order to locate any secondary phases that can arise from the interdiffusion of the elements at the interfaces between the layers. Having this in mind, the XRD patterns in Figure 6.6 shows that there is no evidence of secondary phases due to the interdiffusion of the elements between ZnO, CdS and CIGS layers. A secondary phase of $Cu_{2-x}Se$ is present in the CIGS layer which is not a result of the interdiffusion of the elements at the interfaces. The existence of $Cu_{2-x}Se$ in the CIGS layer is thoroughly discussed in Chapter 4.

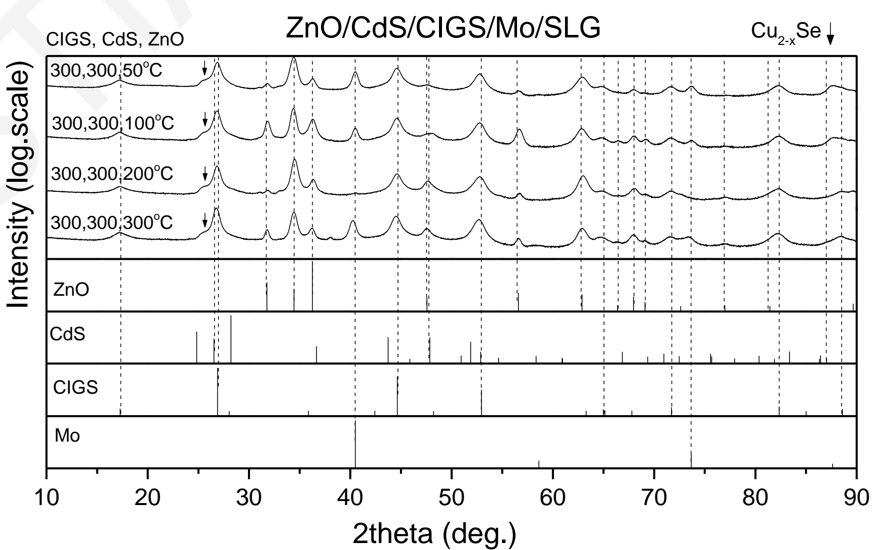

CHRISTIANA NICOLAOU

Figure 6.6 XRD patterns of ZnO/CdS/CIGS/Mo/SLG multi-layer structures with different ZnO deposition temperatures. The bottom plots show the XRD pattern of ZnO hexagonal phase (PDF 9004178), CdS hexagonal phase (JCPDS 96-900-8863), $CuIn_{0.7}Ga_{0.3}Se_2$ (JCPDS 35-1102) and Mo (PDF 9008543). Secondary phase of $Cu_{2-x}Se$ (JCPDS 37-1187) is present in CIGS layer.

The impact of ZnO deposition temperature on the electrical properties of the ZnO/CdS/CIGS/Mo structure has been investigated by performing dark IV measurements using the 2-probe configuration, as shown in Figure 6.1b. The details of the IV measurement are given in section 6.2.1. The results of the IV measurements are presented in Figure 6.7 for the ZnO/CdS/CIGS/Mo structures with different ZnO deposition temperatures. The deposition temperature of ZnO varied from 50 to 300ºC, while the deposition temperature of CIGS and CdS layers was kept constant at 300ºC. As shown in Figure 6.7a-c, the ZnO/CdS/CIGS/Mo structures in which the ZnO layer has been deposited at 300, 200 and 100ºC, respectively, exhibit ohmic behavior. A rectifying diode-like behavior is identified only for the structure in which ZnO layer has been deposited at 50ºC (Figure 6.7d). The ohmic behavior of the ZnO/CdS/CIGS/Mo structures of which ZnO is deposited at high deposition temperatures (100ºC and higher) indicates the presence of low resistive paths that cause shunting between the layers. The shunts between the layers make the layers effectively lose their role in the diode formation leading to the ohmic IV curve. The shortening of the ZnO/CdS/CIGS junction can be attributed to the concentration of defects and non-idealities at the junction. The concentration of these defects and non-idealities increases as the ZnO deposition temperature increases (100ºC and higher) but are not visible from the XRD patterns (Figure 6.6). However, the diode-like behaviour obtained for the ZnO/CdS/CIGS/Mo structure of which ZnO has been deposited at lowest temperature of 50ºC indicates that the concentration of defects and non-idealities at the junction reduce and the quality of the junction is higher, thus the diode-like IV curve is obtained.

CHRISTIANA NICOLAOU

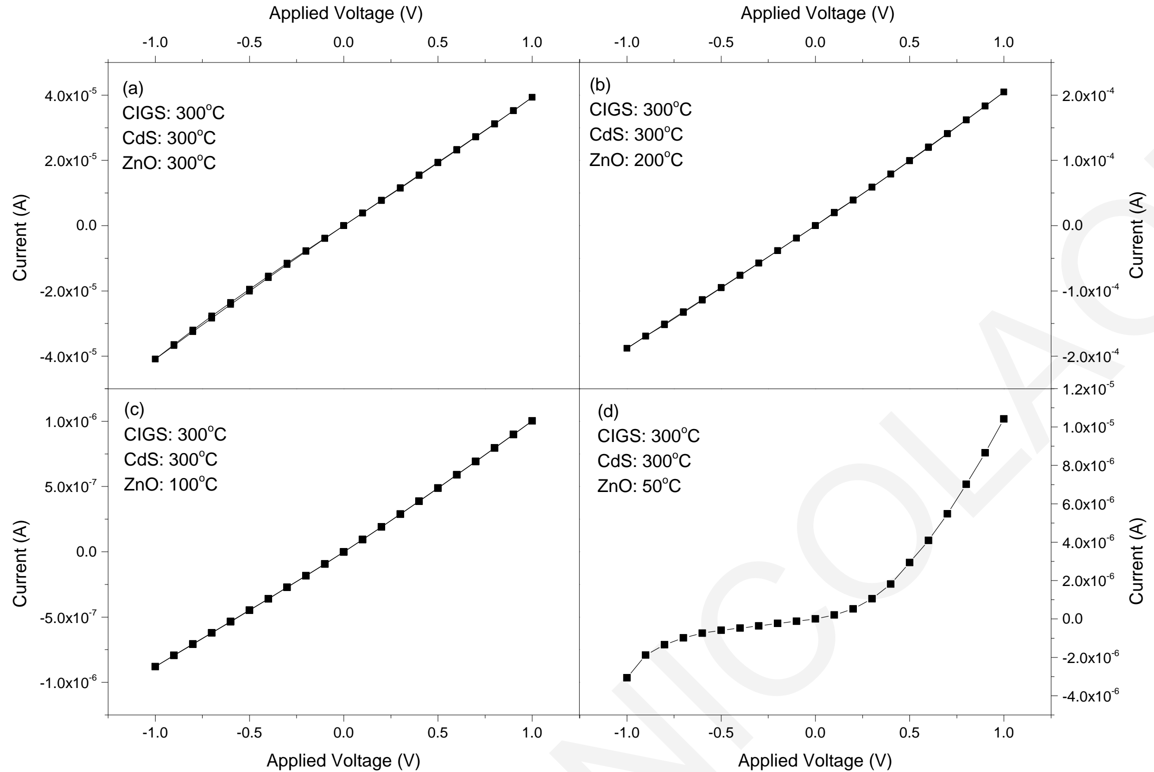

Figure 6.7 IV curves of ZnO/CdS/CIGS/Mo/SLG structures measured by the 2-probe configuration for different deposition temperatures of ZnO layer. CIGS and CdS layers have been deposited at 300ºC and ZnO at (a) 300ºC, (b) 200ºC, (c) 100ºC and (d) 50ºC.

The rectifying performance of a diode in the dark considering the single diode model and the parasitic resistances of the diode can be described by Equation 6.1:

$$I = I_O \left[exp\left(\frac{q(V-IR_s)}{nkT}\right) - 1\right] + \frac{V-IR_s}{R_{sh}} \quad , \qquad \text{(Equation 6.1)}$$

where I is the current through the diode, V is the applied voltage across the diode, I_o is the dark saturation current (or leakage current), n is the ideality factor, T is the temperature in kelvin, q is the electron charge, K is the Boltzmann constant and R_s and R_{sh} are the series resistance and shunt resistance of the diode, respectively.

Ideality factor, leakage current, shunt and series resistance were calculated by the fitting of Equation 6.1 on the experimental data of the IV curve for ZnO/CdS/CIGS/Mo structure shown in Figure 6.7d, using the equivalent circuit calculator by PV Lighthouse [253]. The calculated diode characteristics of ZnO(50ºC)/CdS(300ºC)/CIGS(300ºC)/Mo structure are presented in Table 6.1, along with the diode characteristics of the best performing CdS(300ºC)/CIGS(300ºC)/Mo structure for comparison. The CdS/CIGS/Mo structure is thoroughly discussed in Chapter 5, where the characteristics of the best performing CdS(300ºC)/CIGS(300ºC)/Mo structure are calculated.

CHRISTIANA NICOLAOU

The main difference between ZnO(50ºC)/CdS(300ºC)/CIGS(300ºC)/Mo and CdS(300ºC)/CIGS(300ºC)/Mo structures appears to be in the calculated value of shunt resistance. There is a noticeable reduction of shunt resistance for the ZnO/CdS/CIGS/Mo structure compared to the value obtained for the CdS/CIGS/Mo structure. This result indicates that the addition of ZnO layer on the CdS/CIGS/Mo structure reduces the shunt resistance of the whole device. Shunt resistance depends on multiple underlying mechanisms and each one contributes by a different weight to the overall macroscopic resistance [256, 259]. The approach of calculating the shunt resistance from Equation 6.1 cannot provide insights of the underlying mechanisms causing the shunts. Having this in mind, the reduction of shunt resistance for the ZnO(50ºC)/CdS(300ºC)/CIGS(300ºC)/Mo structure can be attributed to several mechanisms that contribute in different weight. These mechanisms can include defect states at the bandgap, enhanced recombination centers, impurities in the space charge region, pinholes, crystallographic defects, and non-passivated edges at the junction.

Structure	Deposition temperature (ºC)	Ideality factor	Leakage current (A)	Shunt Resistance (Ohm)	Series Resistance (Ohm)
ZnO/CdS/CIGS/Mo/SLG	CIGS: 300 CdS: 300 ZnO: 50	2.7	3×10^{-11}	2.5×10^{5}	1×10^{4}
CdS/CIGS/Mo/SLG	CIGS: 300 CdS: 300	2.8	1.5×10^{-11}	5×10^{8}	4×10^{5}

Table 6.1 Diode characteristics of the best performing ZnO/CdS/CIGS/Mo and CdS/CIGS/Mo structures: ideality factor, leakage current, shunt and series resistance.

6.2.3 Conclusions

The impact of ZnO deposition temperature on the properties of ZnO/CdS/CIGS/Mo/SLG structure grown by PLD has been investigated through structural and electrical characterization. There are no observed secondary phases due to the interdiffusion of the elements between ZnO, CdS and CIGS layers, as the XRD patterns have revealed for the ZnO/CdS/CIGS/Mo/SLG structure having the deposition temperature of ZnO varying from 50 to 300ºC. However, ZnO deposition temperature has a major impact on the electrical properties of the ZnO/CdS/CIGS/Mo diode. A rectifying diode-like behavior is identified only for the structure in which ZnO layer has been deposited at 50ºC, while ohmic behavior is observed for the ZnO/CdS/CIGS/Mo structures of which ZnO is deposited at high deposition temperatures (100ºC and higher). Therefore, the optimum temperature of depositing the ZnO layer on CdS/CIGS/Mo/SLG structure is at 50ºC.

CHRISTIANA NICOLAOU

6.3 ZnO:Al on SLG

6.3.1 Materials and experimental methods

Al-doped ZnO (ZnO:Al) films were deposited on SLG substrates by PLD using a KrF excimer laser source (λ = 248 nm, τ ≤ 25 ns) in a high-vacuum chamber (Figure 6.8a). A polycrystalline ZnO:Al (2 wt% Al doping) target (*Testbourne, England*) was used for the deposition of ZnO:Al films. The substrate was placed at a fixed distance of 5 cm. The deposition was carried out in the presence of oxygen gas at pressure of 0.25 mbar, after the chamber was evacuated at a base pressure of 4×10^{-6} mbar. The repetition rate and number of pulses were kept constant at 10 Hz and 4000, respectively, for all depositions. Prior to deposition, the substrates were ultrasonically cleaned with a sequence of organic solvents. Section 6.3 is focused on the characterization and properties of ZnO:Al film on SLG substrate. The deposition of ZnO:Al was carried out using the optimum parameters identified on the previous sections 6.1 and 6.2 regarding the deposition of ZnO films. Therefore, the fluence and deposition temperature used for the deposition of ZnO:Al films were 1.2J/cm^2 and at room temperature, respectively.

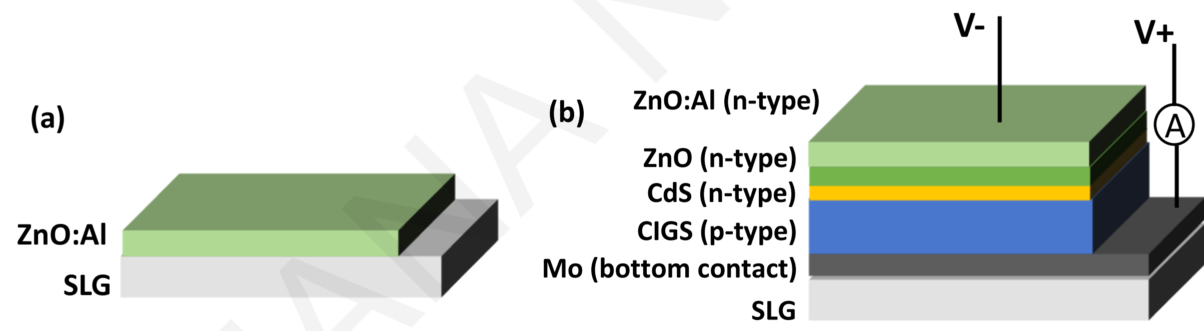

Figure 6.8 Schematic deposition structures: (a) ZnO:Al on SLG and (b) ZnO:Al/ZnO/CdS/CIGS/Mo/SLG structure fabricated by the sequential deposition of CIGS, CdS, ZnO and ZnO:Al on Mo-coated SLG.

Structural properties and crystallinity of ZnO:Al films were studied by X-ray diffraction (SmartLab RIGAKU, Cu Kα, λ = 1.5405 Å). Morphology of the films was determined by scanning electron microscopy (SEM Tescan Vega LSU). The thickness of the films was measured by a stylus profilometer. Topography and surface roughness were probed via atomic force microscopy (AFM, Agilent Technologies). EDS analysis for the stoichiometry of ZnO films was not applicable as the oxygen is not identifiable.

The electrical resistivity ρ, and carrier concentration n, of the films were measured at room temperature using the Van der Pauw method and Hall Effect measurement. Au wires were directly attached on the films' surface using conductive silver paste. A current of 2 μA and a magnetic field of 2 T were applied for the electrical measurements. Hall mobility was calculated by the following equation:

CHRISTIANA NICOLAOU

$$\mu = \frac{1}{\rho n e}. \qquad \text{(Equation 6.2)}$$

6.3.2 Results and discussion

The deposition of ZnO:Al films was carried out at fluence of 1.2 J/cm^2 and at room temperature, based on the optimum deposition parameters obtained from the investigation of ZnO films in sections 6.1 and 6.2. ZnO:Al films deposited on SLG have been examined by grazing incidence XRD (GIXRD) with 2θ values ranging between 10° and 90°; the XRD patterns are shown in Figure 6.9. The peaks of the XRD patterns are identified by the hexagonal ZnO (PDF card 9004178), revealing the polycrystalline nature of the films. No characteristic reflection peaks related to Al or other alumina phases were detected in the X-ray pattern which supports that Al ions were substituted into the Zn sites in the lattice of ZnO crystal.

Comparing the XRD patterns of ZnO:Al and ZnO films, a slight shift of the Bragg angles towards higher values is observed for ZnO:Al films. More specific, the diffraction angle of the (002) peak for ZnO:Al film at 34.495^o is slightly higher compared to 34.412^o of the ZnO film. This result may be due to the substitution of zinc ions by the smaller in size aluminum ions into the hexagonal lattice of ZnO [309] and/or due to the residual stress parallel to the c-axis [310]. The c-axis lattice parameter was calculated from the XRD patterns for ZnO and ZnO:Al films and was found to be 0.5208 and 0.5196 nm, respectively. Since the ionic radius of Zn^{2+} is bigger than that of Al^{3+} (72 and 53 pm, respectively) [311], the length of the c-axis is expected to be shortened when Al atoms substitutes Zn atoms in the crystal. Similar results are reported for the ZnO:Al and ZnO films grown on glass substrates using PLD [303] and other deposition methods [312].

Moreover, the crystallite size of the ZnO and ZnO:Al films was calculated from the (002) diffraction peak using the Debye-Scherrer formula. The crystallite size was found to be 11.35 nm for the ZnO:Al film and 23.67 nm for the ZnO film. Comparing the two values, the calculated crystallite size of ZnO:Al is more than 50% smaller than that of ZnO film. The decrease of the crystallite size of ZnO:Al film can be attributed to the incorporation of Al atoms in the ZnO lattice where some of the Al atoms rather than replacing the Zn atoms in the crystal, are located at interstitial sites or at crystallite boundary regions creating defects. These defects act as nucleation centers which limit the growth of the adjacent crystallites, therefore the crystallite size of ZnO:Al film is smaller. Similar results have been found in the literature for PLD-grown ZnO:Al films [302, 303] or by using other deposition methods [312].

CHRISTIANA NICOLAOU

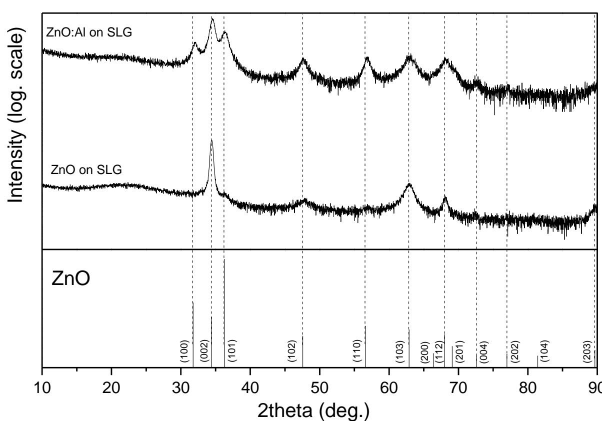

Figure 6.9 XRD patterns of ZnO:Al and ZnO thin films deposited on SLG substrates at fluence of 1.2 J/cm^2 and at room temperature. The bottom plot shows the XRD pattern of ZnO hexagonal phase according to PDF card 9004178.

The PLD deposition parameters for the growth of ZnO and ZnO:Al on SLG along with the thickness, roughness and energy gap of each film are presented in Table 6.2. The surface roughness of the films was measured by AFM within an area of 80x80 μm^2. The low values of the measured roughness indicate the high smoothness of ZnO and ZnO:Al films obtained by PLD. The absorption edge of Al-doped ZnO appears to blue shift by as much as 30 meV compared to the ZnO film deposited at 25°C. The band gap energy of the doped ZnO:Al is calculated at 3.36 eV. The experimental values are comparable to those reported in the literature [313]. The absorption coefficient and optical transmissivity of Al-doped ZnO film at room temperature are shown in Figure 6.5. High transparency with transmissivity over than 80% in the visible spectral region is observed.

Sample	Fluence (J/cm^2)	Deposition temperature (^{o}C)	Pulses	Thickness (nm)	Roughness (nm)	Energy gap (eV)
ZnO on SLG	1.2	25	1500	62	10.4	3.33
ZnO:Al on SLG	1.2	25	4000	182	10.3	3.36

Table 6.2 PLD deposition parameters, thickness, roughness and energy gap of ZnO and ZnO:Al films deposited on SLG substrates.

CHRISTIANA NICOLAOU

The dark electrical resistivity and carrier concentration of ZnO:Al film grown at 25^oC were measured at room temperature using the van der Pauw method and are tabulated in Table 6.3, along with the calculated mobility.

Sample	**Deposition temperature (^oC)**	**Type of conductivity**	**Electrical resistivity (Ohm.cm)**	**Carrier concentration (cm^{-3})**	**Mobility ($cm^2V^{-1}s^{-1}$)**
ZnO:Al on SLG	25	n-type	$2.3x10^{-1}$	$1.1x10^{19}$	2.47

Table 6.3 Planar electrical resistivity, carrier concentration and Hall mobility of ZnO:Al film deposited at 25^oC on SLG substrate.

The ZnO:Al film exhibits n-type conductivity as determined from the Hall measurement. The values of the electrical resistivity, carrier concentration and mobility are within the range of the values reported in the literature for PLD-grown ZnO:Al films on glass substrates. The reported values of electrical resistivity and carrier concentration vary from 10^{-4} to 10^{-1} Ohm.cm and from 10^{18} to 10^{20} cm^{-3}, respectively [301-303, 314, 315]. This wide range of the values found in the literature regarding the resistivity and carrier concentration of PLD-grown ZnO:Al films can be associated with the wide variation of the growth parameters (oxygen pressure, deposition temperature, laser source, etc.) used and the high sensitivity of the growth of ZnO:Al films in relation to the deposition parameters.

6.3.3 Conclusions

The structural, morphological, optical and electrical properties of the PLD-grown ZnO:Al films on SLG substrates have been investigated using the optimum deposition parameters identified by the investigation of ZnO films (sections 6.1 and 6.2). Therefore, the ZnO:Al films were deposited at room temperature and at fluence of 1.2 J/cm^2. The PLD-grown ZnO:Al films have smooth surface, exhibit high transmittance (>80%) in the visible range with wide energy bandgap and low resistivity. The XRD patterns reveal the absence of any secondary phase and indicate the incorporation Al ions in the lattice of ZnO crystal. Based on these results, the PLD-grown ZnO:Al films can be considered as suitable transparent conductive oxide layer for the photovoltaic device.

6.4 ZnO:Al on ZnO/CdS/CIGS/Mo/SLG

6.4.1 Materials and experimental methods

A sequential deposition of CIGS, CdS, ZnO and ZnO:Al layers on Mo-coated SLG substrates was carried out using PLD with a KrF excimer laser source (λ = 248 nm, $\tau \leq$ 25 ns) in a high-vacuum chamber (Figure 6.8b). Commercially available Mo-coated SLG substrates were purchased

CHRISTIANA NICOLAOU

(Techinstro, India) and used as is. The thickness of Mo films was 500 nm. The PLD chamber hosts a target carousel which can take up to four targets and the sequential deposition of CIGS, CdS, ZnO and ZnO:Al was feasible. Polycrystalline targets of ZnO:Al (Al - 2% wt), ZnO, CdS and $CuIn_{0.7}Ga_{0.3}Se_2$ (Testbourne, England) were used for the deposition of the four layers. Prior to deposition, the chamber was evacuated at a base pressure of $4x10^{-6}$ mbar. The deposition of ZnO:Al was carried out in the presence of oxygen gas at 0.25 mbar. The number of pulses, repetition rate and target to substrate distance were kept constant at 4000, 10 Hz and 5cm respectively, for all ZnO:Al depositions. ZnO layer was deposited at 40ºC under oxygen pressure at 0.25 mbar. CIGS and CdS layers were deposited at 300ºC and in the presence of argon gas at 0.01mbar. The optimum deposition parameters were used for the deposition of CIGS, CdS and ZnO layers which are discussed in Chapter 4, 5 and 6.2, respectively. This section is focused on the parametric investigation of the ZnO:Al deposition temperature for the fabrication of the ZnO:Al/ZnO/CdS/CIGS/Mo/SLG structure.

An X-ray diffractiometer (XRD) (*SmartLab RIGAKU, Cu Kα, λ = 1.5405 Å*) was used to identify the crystal phases present in the ZnO:Al/ZnO/CdS/CIGS/Mo/SLG multi-layer structures. The microstructure of the ZnO:Al and ZnO bilayer and interfacial characterization of the CIGS/CdS/ZnO/ZnO:Al structure have been studied using conventional TEM and HRTEM imaging, along with SAED patterns and EDS linescan analysis. Conventional TEM and HRTEM observations were carried out using a JEOL 2011 TEM operating at 200 kV with a point resolution of 0.25 nm and equipped with an EDS detector (EDAX Apollo XLT TEM-SDD).

Current-Voltage (IV) measurements were performed at room temperature using a two-probe configuration, as shown in Figure 6.8b. The electrodes of the voltage source/ ammeter were mechanically placed on ZnO:Al and Mo surface, creating an electrical circuit. The ZnO:Al/ZnO/CIGS/CdS junction was electrically forward and reverse biased with an applied voltage of ±1V. The IV measurements have been performed at room temperature and in ambient atmosphere. The adhesion between the layers and the substrate was investigated using the scotch tape test method by attaching the tape on the surface of the structure and detaching it by applying force manually.

6.4.2 Results and discussion

6.4.2.1 Impact of ZnO:Al deposition temperature

The XRD patterns of ZnO:Al/ZnO/CdS/CIGS/Mo/SLG structures with different ZnO:Al deposition temperatures have been examined by grazing incidence (GIXRD) with 2θ ranging from 10º to 90º. The fabrication of the ZnO:Al/ZnO/CdS/CIGS/Mo/SLG structures was conducted by varying the deposition temperature of ZnO:Al from 40 to 300ºC while keeping the deposition temperature of CIGS and CdS constant at 300ºC and of ZnO at 40ºC. Figures 6.10 and 6.11 present the XRD patterns of the two extremes: ZnO:Al/ZnO/CdS/CIGS/Mo/SLG structure with ZnO:Al layer deposited at 40ºC and ZnO:Al/ZnO/CdS/CIGS/Mo/SLG structure with ZnO:Al layer deposited

CHRISTIANA NICOLAOU

at 300ºC, respectively. The XRD patterns reveal the existence of the ZnO and CdS hexagonal phase, the chalcopyrite $CuIn_{0.7}Ga_{0.3}Se_2$ phase and the Mo phase. Figure 6.10 shows that there is no evidence of secondary phases due to the interdiffusion of the elements between the ZnO, CdS and CIGS layers. A secondary phase of $Cu_{2-x}Se$ is present in the CIGS layer which is not a result of the interdiffusion of the elements at the interfaces. The existence of $Cu_{2-x}Se$ in the CIGS layer is thoroughly discussed in Chapter 4. However, the XRD pattern of the ZnO:Al/ZnO/CdS/CIGS/Mo/SLG structure with ZnO:Al layer deposited at 300ºC (Figure 6.11) shows the presence of $CuInS_2$ secondary phase along with the of Cu_2Se phase in the CIGS layer. Similarly, the $CuInS_2$ secondary phase is identified in the XRD patterns obtained for the ZnO:Al/ZnO/CdS/CIGS/Mo/SLG structures with ZnO:Al layer deposited at 100ºC and 200ºC, which are not presented here. The $CuInS_2$ is a result of the interdiffusion of the elements at the CdS/CIGS interface which takes place while reheating the sample from 40ºC to 100, 200 or 300ºC to proceed from the deposition of ZnO layer to ZnO:Al layer.

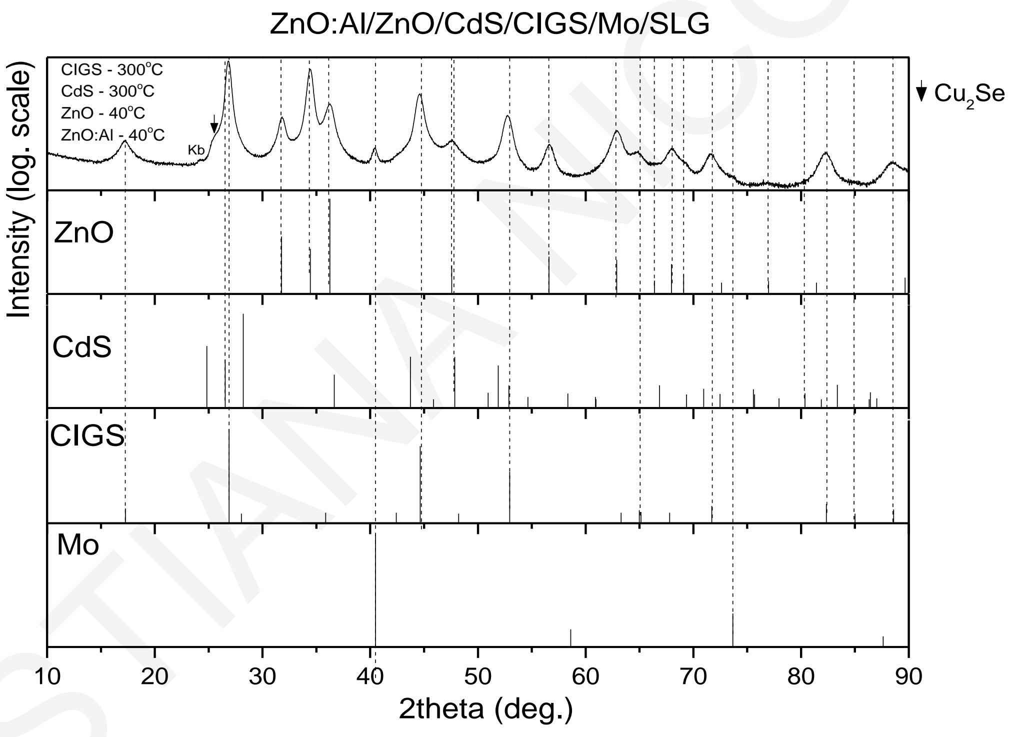

Figure 6.10 XRD pattern of ZnO:Al/ZnO/CdS/CIGS/Mo/SLG multi-layer structure with the ZnO:Al layer deposited at 40ºC. The bottom plots show the XRD pattern of ZnO hexagonal phase (PDF 9004178), CdS hexagonal phase (JCPDS 96-900-8863), $CuIn_{0.7}Ga_{0.3}Se_2$ (JCPDS 35-1102) and Mo (PDF 9008543). Secondary phase of Cu_2Se (JCPDS 04-001-9933) is present in CIGS layer.

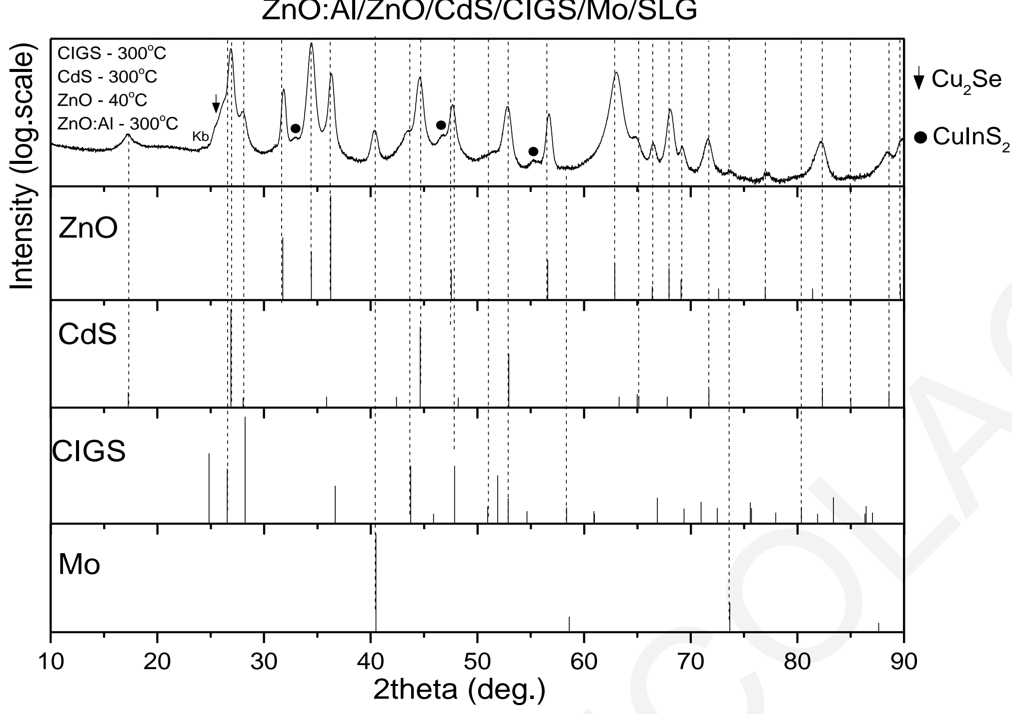

Figure 6.11 XRD pattern of ZnO:Al/ZnO/CdS/CIGS/Mo/SLG multi-layer structure with the ZnO:Al layer deposited at 300°C. The bottom plots show the XRD pattern of ZnO hexagonal phase (PDF 9004178), CdS hexagonal phase (JCPDS 96-900-8863), $CuIn_{0.7}Ga_{0.3}Se_2$ (JCPDS 35-1102) and Mo (PDF 9008543) and secondary phases of $CuInS_2$ (JCPDS 65-1572) and Cu_2Se (JCPDS 04-001-9933).

The impact of ZnO:Al deposition temperature on the electrical properties of the ZnO:Al/ZnO/CdS/CIGS/Mo structure has been investigated by performing dark IV measurements using the 2-probe configuration, as shown in Figure 6.8b. The details of the IV measurement are given in section 6.4.1. The results of the IV measurements are presented in Figure 6.12 for the ZnO:Al/ZnO/CdS/CIGS/Mo structures with different ZnO:Al deposition temperatures. The deposition temperature of ZnO:Al varied from 40 to 300°C, while the deposition temperature of CIGS, CdS and ZnO layers was kept constant at 300, 300 and 40°C, respectively. As shown in Figure 6.12a-c, the ZnO:Al/ZnO/CdS/CIGS/Mo structures in which the ZnO:Al layer has been deposited at 300, 200 and 100°C, respectively, exhibit ohmic behavior. A rectifying diode-like behavior is identified only for the structure in which ZnO:Al layer has been deposited at 40°C (Figure 6.12d).

The ohmic behavior of the ZnO:Al/ZnO/CdS/CIGS/Mo structures of which ZnO:Al is deposited at high deposition temperatures (100°C and higher) indicates the presence of low resistive paths that cause shunts between the layers, leading to the ohmic IV curves. The shortening of the ZnO:Al/ZnO/CdS/CIGS junction can be attributed to defects and non-idealities at the junction. The concentration of these defects and non-idealities is high enough in the samples where the ZnO:Al layer has been deposited at 100, 200 and 300°C to deteriorate the junction, resulting in the ohmic behaviour of these samples. An indication of the defects at the junction is given by the XRD pattern

CHRISTIANA NICOLAOU

in Figure 6.11 in which the formation of $CuInS_2$ secondary phase is identified. The presence of $CuInS_2$ phase indicates the introduction of lattice defects such as Cu vacancies and In_{Cu} antisites [193, 263-265] into CIGS layer, as well as S vacancies and interstitials [266, 267] into CdS layer, because Cu, In and S are being drawn out from CIGS and CdS layers in order to form the $CuInS_2$ phase. This large amount of lattice defects near the junction, arising from the presence of $CuInS_2$ phase, could provide to the diode shunt paths that effectively eradicate the role of each layer in the diode. However, the diode-like behaviour obtained for the ZnO:Al/ZnO/CdS/CIGS/Mo structure of which ZnO:Al has been deposited at the lowest temperature of 40°C corroborates with the XRD pattern in Figure 6.10 in which there is no evidence of secondary phases due to the interdiffusion of the element at the interfaces of the junction. Thus, the concentration of defects and non-idealities at the junction is reduced and the quality of the junction is higher, thus, the diode-like IV curve is obtained.

Figure 6.12 IV curves of ZnO:Al/ZnO/CdS/CIGS/Mo/SLG structures measured by the 2-probe configuration for different deposition temperatures of ZnO:Al layer. CIGS and CdS layers have been deposited at 300°C, ZnO has been deposited at 40°C and ZnO:Al at (a) 300°C, (b) 200°C, (c) 100°C and (d) 40°C.

Studying the dark IV curves of solar cells allows one to determine the diode characteristics of the device which can provide essential insights into the performance parameters and the efficiency of the device. In order to calculate the diode characteristics of the device, the dark IV curve is fitted into a model and the parameters of the model are determined. Here, the single-diode model, which describes the solar cell as a single diode with parasitic resistances, shown in Equation 6.1, is used for

CHRISTIANA NICOLAOU

the calculation of the diode characteristics of the device. Ideality factor, leakage current, shunt and series resistance were calculated by fitting the experimental data of the IV curve for ZnO:Al/ZnO/CdS/CIGS/Mo structure shown in Figure 6.12d on the Equation 6.1, using the equivalent circuit calculator by PV Lighthouse [253]. The calculated diode characteristics of ZnO:Al(40ºC)/ZnO(40ºC)/CdS(300ºC)/CIGS(300ºC)/Mo/SLG device are presented in Table 6.4, along with the diode characteristics of the ZnO:Al/ZnO/CdS/CIGS/Mo/SLG devices reported in the literature for comparison.

ZnO:Al/ZnO/CdS/CIGS/Mo/SLG					
Voltage analysis region	**Ideality factor**	**Leakage current (A)**	**Shunt Resistance (Ohm)**	**Series Resistance (Ohm)**	**Reference**
0.1 V < V < 0.7 V	3.52	1.5×10^{-11}	4.6×10^{6}	1.5×10^{4}	This work
0.2V < V < 0.6 V **0.6 V < V < 0.8 V**	4.06 3.45	1.05×10^{-6} 4.5×10^{-7}	-	-	[316]
0.2V < V < 0.6 V **0.6 V < V < 0.8 V**	4.08 3.44	1.05×10^{-6} 4.5×10^{-7}	2.3×10^{5}	1×10^{1}	[317]
0.2V < V < 0.6 V **0.6 V < V < 0.86 V**	4.884 4.3	6.1×10^{-6} 3.9×10^{-6}	1.22×10^{4} 4.39×10^{4}	-7 0.4	[318]

Table 6.4 Diode characteristics of the ZnO:Al/ZnO/CdS/CIGS/Mo/SLG device and reported values in the literature calculated by dark IV measurements.

The reported values reported of the diode characteristics of the ZnO:Al/ZnO/CdS/CIGS/Mo/SLG devices presented in Table 6.4 have been calculated by fitting the dark IV measurements on the single-diode model using different analysis methods [316-318]. The fabrication of the ZnO:Al/ZnO/CdS/CIGS/Mo/SLG devices, reported in Table 6.4, has been realized by using multiple deposition techniques including sputtering, co-evaporation and CBD. The ZnO:Al/ZnO/CdS/CIGS/Mo/SLG device of this work has been fabricated using PLD as the main deposition technique for the CIGS, CdS, ZnO and ZnO:Al layers. Nevertheless, due to the lack of published works reporting on the diode characteristics of PLD-grown devices, the comparison is presented here and is as close as it can be. The results of ideality factor and shunt resistance of the PLD-grown device are in good agreement with the reported values, however the leakage current and series resistance present large deviation with the literature.

Further analysis of the dark IV data can give insights about the electronic transport mechanisms in the device as well as the recombination mechanisms. This kind of analysis is beyond

CHRISTIANA NICOLAOU

the scope of the current study; however, a literature review is presented here. The temperature dependence of the ideality factor values has been shown to agree with the theoretical expression given for tunnelling enhanced interface recombination mechanism [317]. Moreover, the transport mechanism in ZnO/CdS/Cu(In,Ga)Se_2 device is also reported to be dominated by tunnelling enhanced interface recombination mechanism which is attributed to the presence of Cu-rich and In-poor thin layer possibly formed on the absorber surface [316]. Other studies explain the tunnelling enhanced recombination in the bulk via deep centers in the space charge region or at heterojunction interface [319, 320].

Adhesion test of the ZnO:Al(40°C)/ZnO(40°C)/CdS(300°C)/CIGS(300°C)/Mo/SLG device was performed using the scotch tape method described in 6.4.1. The pictures of the sample, presented in Table 6.5, were taken prior and afterwards the application of scotch tape test. The scotch tape test involved several attempts in order to thoroughly examine the quality of the adhesion between the layers and the SLG substrate.

Sample	**Deposition temperature of the layers (°C)**	**Prior adhesion test**	**After adhesion test**
ZnO:Al/ZnO/CdS/CIGS/Mo/SLG	CIGS – 300 CdS – 300 ZnO – 40 ZnO – 40		

Table 6.5 Pictures taken prior and afterwards the application of the scotch tape test for the ZnO:Al/ZnO/CdS/CIGS/Mo/SLG device with CIGS and CdS layers deposited at 300°C and ZnO and ZnO:Al layers deposited at 40°C.

After the application of the scotch tape adhesion test on ZnO:Al/ZnO/CdS/CIGS/Mo/SLG device, the layers remained intact, as shown in Table 6.5. The pictures show that the sample was stable as no delamination occurred. This result indicates that the adhesion between Mo, CIGS, CdS, ZnO and ZnO:Al layers and SLG substrate is superior for the ZnO:Al/ZnO/CdS/CIGS/Mo/SLG device with CIGS and CdS layers deposited at 300°C and ZnO and ZnO:Al layers deposited at 40°C.

The individual layers of the ZnO:Al/ZnO/CdS/CIGS/Mo/SLG structure with CIGS and CdS layers deposited at 300°C and ZnO and ZnO:Al layers deposited at 40°C, as well as their interfaces were thoroughly studied using advanced electron microscopy (HRTEM, SAED, EDS). In more detail, apart from the Mo/CIGS interface, which is discussed in Chapter 4, the CIGS/CdS and CdS/ZnO interfaces were also investigated. The results from these analyses are depicted in Figure 6.13.

CHRISTIANA NICOLAOU

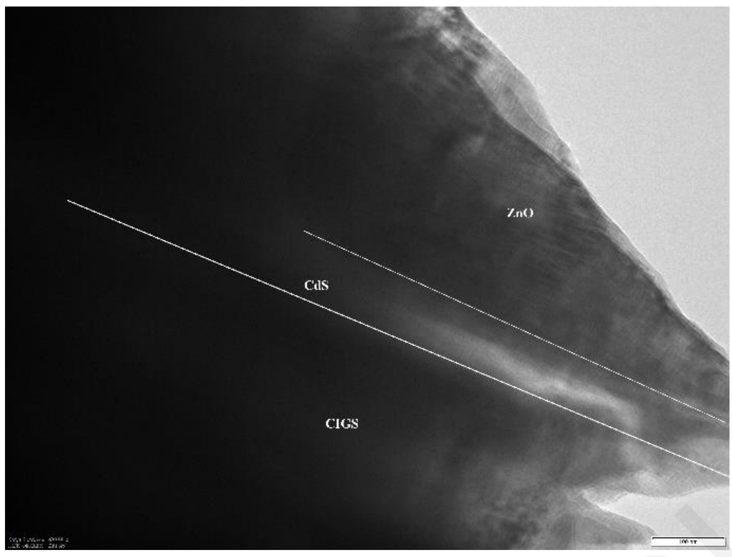

Figure 6.13 Conventional TEM image of the CIGS/CdS and CdS/ZnO interfaces.

The CIGS/CdS interface is generally smooth, taking into account the roughness induced by the columnar morphology of the CIGS film. The CdS layer possesses inferior crystalline quality, as deduced both by HRTEM images and SAED patterns shown in Figure 6.14 a and b, respectively. In more detail, the SAED pattern reveals that the CIGS layer is by far more crystalline than the CdS one, as it comprises of distinct spots, whereas the CdS pattern is formed by nanocrystalline rings. The thickness of the CdS layer, as depicted there, is up to 45 nm and it adopts a highly disordered/amorphous morphology, with only occasional crystallites revealed. The structure and quality of the CIGS/CdS and CdS/ZnO interfaces reveals that the CIGS/CdS interface is generally smoother than the CdS/ZnO one. The ZnO/CdS interface is of good quality, in line with the CIGS/CdS interface, however the ZnO/CdS interface is less sharp compared with the CdS/CIGS one. Average roughness values of these are in the range of 3-5 nm for the CIGS/CdS and 10-15 nm for the CdS/ZnO interface.

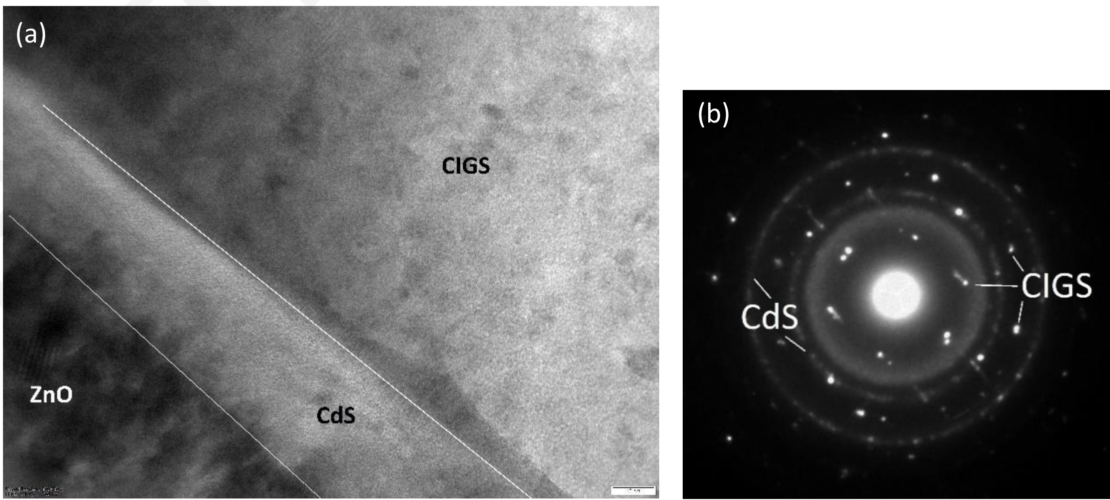

Figure 6.14 (a) HRTEM image of the CIGS/CdS and CdS/ZnO interfaces and (b) common SAED pattern of the CIGS/CdS interfacial area.

CHRISTIANA NICOLAOU

Chemical analysis by EDS line scans in the interfacial regions (Figure 6.15), revealed the simultaneous existence of small quantities of Cu and In inside the CdS layer; potential discrete formation of additional phases has not been confirmed by HRTEM analysis on small crystallites. The only phase found was CdS, either in nanocrystalline morphology (sizes up to 15-20 nm), or in nearly amorphous stage (the latter was confirmed by EDS point analysis). There is also some indication of possible Cd or S atoms diffusion inside CIGS, as EDS electron microscopy results revealed. There is no extended interdiffusion of either Zn or O inside the CdS layer, as EDS point analysis and line scans revealed. These results agree with the XRD pattern of the sample (Figure 6.10), which shows that there is no evidence of secondary phases due to the interdiffusion of the elements between the ZnO, CdS and CIGS layers.

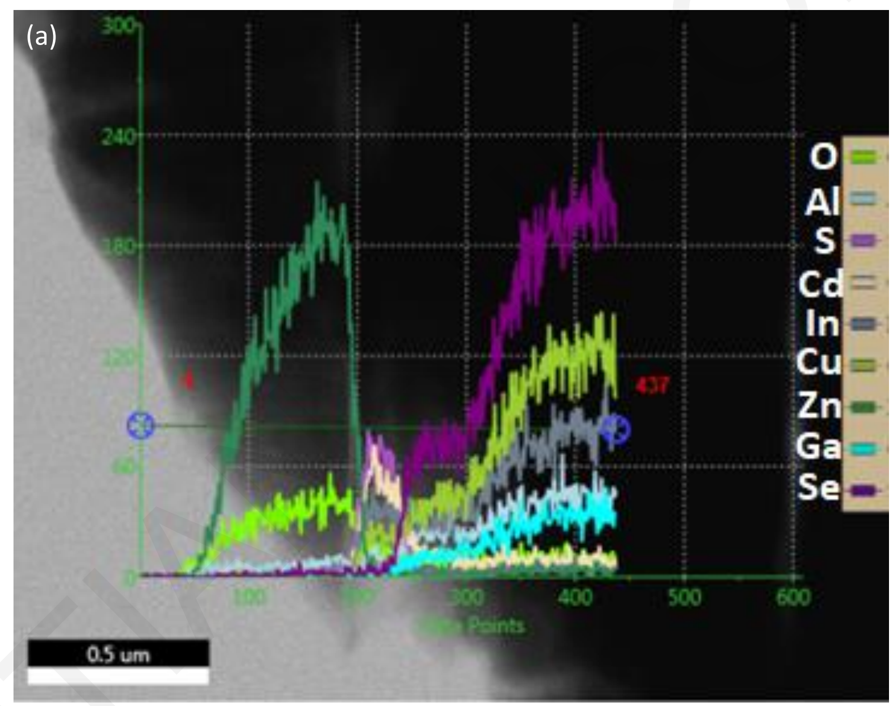

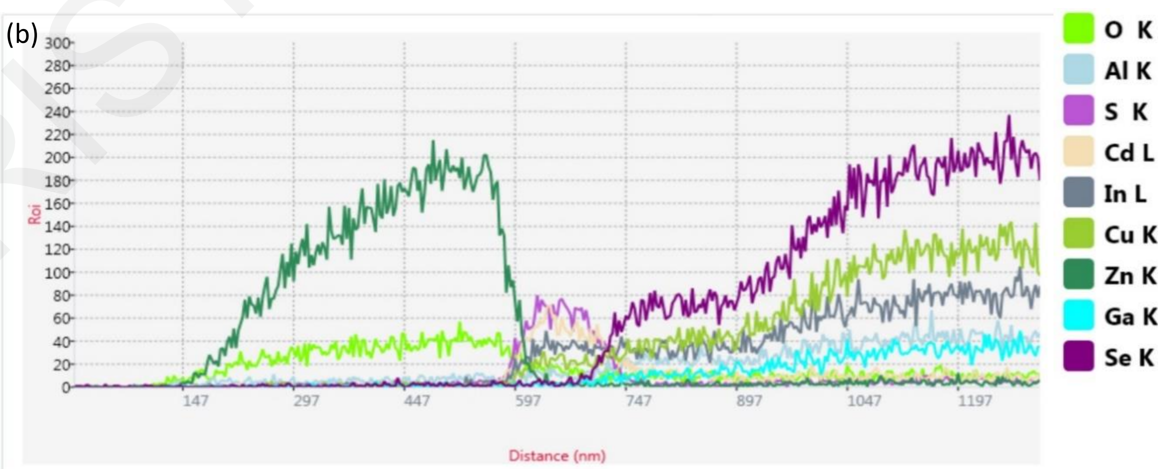

Figure 6.15 EDS linescans of the CIGS/CdS/ZnO/ZnO:Al layers and their interfacial regions: (a) with cross-section SEM image at the background and (b) without cross-section SEM image at the background.

The ZnO:Al – intrinsic ZnO layer exhibits polycrystalline morphology, consisting of numerous crystallites in random orientation, as presented in Figure 6.16. The Al doping was also confirmed by EDS point analysis, in the upper part of the ZnO:Al layer grown on top of the multi-structure.

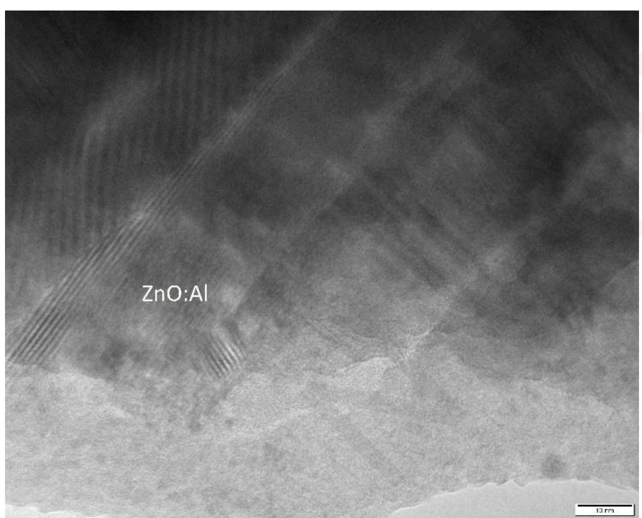

Figure 6.16 The upper area of the ZnO:Al – intrinsic ZnO layer.

6.4.3 Conclusions

The impact of ZnO:Al deposition temperature on the properties of ZnO:Al/ZnO/CdS/CIGS/Mo/SLG structure grown by PLD has been investigated through structural and electrical characterization. ZnO:Al deposition temperature has a major impact on the structural and electrical properties of the ZnO:Al/ZnO/CdS/CIGS/Mo device. A rectifying diode-like behavior is identified only for the device in which ZnO:Al layer has been deposited at 40ºC, while ohmic behavior is observed for the ZnO:Al/ZnO/CdS/CIGS/Mo devices of which ZnO:Al is deposited at high deposition temperatures (100ºC and higher). The diode-like behaviour of ZnO:Al(40ºC)/ZnO/CdS/CIGS/Mo device corroborates with the clear XRD pattern in which there is no evidence of secondary phases due to the interdiffusion of the elements between ZnO:Al, ZnO, CdS and CIGS layers. Moreover, the adhesion test of ZnO:Al(40ºC)/ZnO/CdS/CIGS/Mo device demonstrated the superior adhesion between the layers and the substrate. Thus, the optimum temperature of depositing the ZnO:Al layer on ZnO/CdS/CIGS/Mo/SLG structure is at 40ºC.

The interfacial characterisation of the ZnO:Al/ZnO/CdS/CIGS/Mo/SLG with CIGS and CdS layers deposited at 300ºC and ZnO and ZnO:Al layers deposited at 40ºC, revealing that the

CHRISTIANA NICOLAOU

CIGS/CdS and CdS/ZnO interfaces are generally smooth with the CdS/CIGS interface more abrupt and smoother compared to the ZnO/CdS one. The chemical analysis in the CIGS/CdS interfacial region revealed the existence of small quantities of Cu and In inside the CdS layer, however the HRTEM analysis on small crystallites has confirmed the absence of the potential discrete formation of additional phases. In addition, possible Cd or S atoms diffusion inside CIGS has been indicated by the EDS electron microscopy. Regarding the ZnO/CdS interface, there is no indication of extended inter-diffusion of either Zn or O inside the CdS layer.

CHRISTIANA NICOLAOU

Chapter 7 – Fabrication of CIGS-based solar cells using PLD

Thin-film solar cells based on the chalcopyrite compound $Cu(In,Ga)Se_2$ (CIGS) have shown increased efficiencies through the years with a steeper increase since 2014. Record efficiencies reaching up to 23.35% have been reported by Solar Frontier in 2019 [1].

The CIGS cell consists of several layers of different materials and the cell efficiency is highly affected by each layer, as well as the interaction between them. A variety of methods has been used to prepare each layer of CIGS solar cells. A typical CIGS solar cell with laboratory efficiency over 20% has the following configuration: soda-lime glass as substrate, sputtered Mo as back contact, CIGS as p-type absorber grown by multi-stage co-evaporation or selenisation method, chemical-bath-deposited CdS as n-type buffer layer, sputtered i-ZnO/ZnO:Al bilayer as transparent window, Ni/Al grid, and antireflective MgF_2 coating [2]. Despite the significant progress recorded in CIGS solar cells, several factors related to both device fabrication and cell efficiency hamper their development. The industry norm of using multiple deposition techniques and high processing temperatures (higher than 500°C for the highest efficiency CIGS films) for the different layers in the stack adds time and cost to the fabrication process. Therefore, identifying a single growth method for the fabrication of the functional part of the CIGS cell, which will reduce the fabrication time and cost, is highly desirable.

This chapter demonstrates the utilization of PLD in a novel sequential process for the fabrication of the multi-layer structure described above. The preparation of the functional part of the CIGS solar cell (CIGS/CdS/i-ZnO/ZnO:Al) was carried out by using PLD in one growth sequence and at temperatures lower than 400 °C. While several different growth procedures have been exploited for each constituent layer in developing CIGS solar cells with efficiencies in the range of 14-22%, up to now, no published report exists of using PLD for constructing a CIGS cell in its entirety. Thus, this work constitutes an innovative application of PLD for the fabrication of thin-film CIGS solar cells.

In this chapter, the fabrication of the PLD-grown CIGS solar cells with sequential deposition of CIGS, CdS, ZnO and ZnO:Al layers on Mo-coated SLG substrates is presented. Structural and electrical characterization along with performance analysis of the PLD-grown CIGS solar cells with varying CdS thickness are examined in section 7.1. Moreover, the optimization of the fabrication process has been studied to improve the performance of the PLD-grown CIGS solar cells through the elimination of particulates on the CIGS surface and is discussed in section 7.2 and 7.3.

CHRISTIANA NICOLAOU

7.1 One-step PLD-grown CIGS solar cells

In this section, one step PLD-grown CIGS solar cells have been fabricated using the optimum deposition conditions of each layer based on the results of the previous chapters. In CIGS solar cells, the incorporation of CdS buffer layer between the CIGS absorber and i-ZnO/Al-doped ZnO bilayer holds a key role in the performance of the cell. Numerous published works discuss the beneficial effects of the CdS layer on the properties of CIGS solar cells [21, 45, 75, 210, 217]. Fabrication of thin CdS layers can minimize the light absorption losses in the blue range [44], however for very thin layers, pinholes between the transparent conductive oxide (Al-doped ZnO) and the absorber layer are formed, which create short circuits [8] in the device. Considering the blue absorption losses and the toxicity of Cd, it is crucial to examine the characteristics of CdS layer, especially its thickness. Thus, the performance of PLD-CIGS solar cells has been investigated as function of CdS thickness.

7.1.1 Materials and experimental methods

A sequential deposition of CIGS, CdS, ZnO and ZnO:Al layers on Mo-coated SLG substrates was carried out using PLD with a KrF excimer laser source ($\lambda = 248$ nm, $\tau \leq 25$ ns) in a high-vacuum chamber (Figure 7.1). Commercially available Mo-coated SLG substrates were purchased (Techinstro, India) and used as is. The thickness of Mo films was 500 nm. The PLD chamber hosts a target carousel which can take up to four targets and the sequential deposition of CIGS, CdS, ZnO and ZnO:Al was feasible. Polycrystalline targets of ZnO:Al (Al - 2% wt), ZnO, CdS and $CuIn_{0.7}Ga_{0.3}Se_2$ (Testbourne, England) were used for the deposition of the four layers. Prior to deposition, the chamber was evacuated to a base pressure of $4x10^{-6}$ mbar. The PLD deposition parameters used for each layer were obtained from the results of Chapters 4, 5 and 6 in which the optimum deposition parameters for CIGS, CdS and ZnO/ZnO:Al layers, respectively, were identified. Table 7.1 presents the main deposition parameters for each layer used for the fabrication of the solar cells. The impact of thickness of CdS layer on the performance of the solar cells was investigated by varying the number of pulses as shown in Table 7.1. After the sequential deposition of CIGS, CdS, ZnO and ZnO:Al layers, the fabrication of the devices was completed by the deposition of Al grid on the surface of ZnO:Al layer. Preliminary measurements revealed that the Ni layer, that usually precedes the deposition of Al layer for the fabrication of the grid, had no significant effect on the performance of the devices. Therefore, the Ni layer has been omitted to make the fabrication process of the metallic grid simpler. The deposition of the Al grid was performed through the following steps:

- Attachment of a stainless-steel shadow mask on the top of the multi-layer structure for patterning of the metallic grid
- Deposition of ~1μm of Al using evaporation.

CHRISTIANA NICOLAOU

The design of the pattern for the Al grid has been determined considering the several power-loss mechanisms associated with the metallic grid, aiming for the optimum collection of the photogenerated carriers. The calculations for the optimization of the metallic grid can be found in Appendix A.

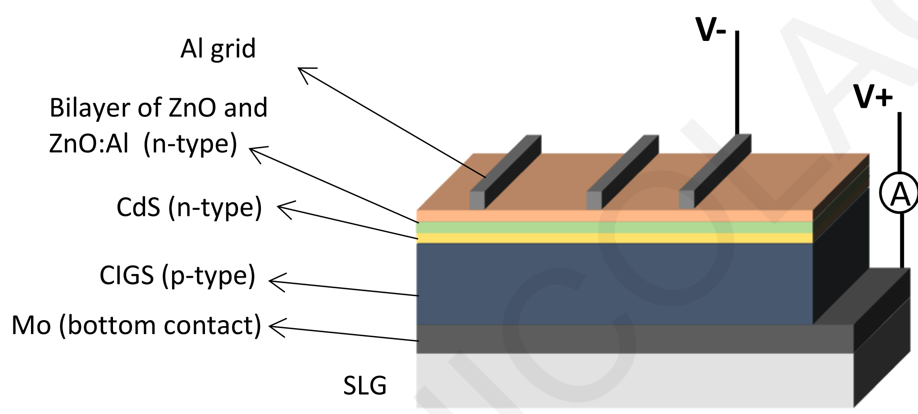

Figure 7.1 The complete multi-layer structure of the CIGS solar cell along with the metallic grid.

Layer	Deposition Temperature (°C)	Fluence (J/cm^2)	Background gas	Pressure (mbar)	Pulses	Thickness (nm)
CIGS	300	1.0	Ar	0.01	15000	~1350
CdS	300	1.1	Ar	0.01	100 - 300	~50-110
ZnO	40	1.2	O_2	0.25	1500	~80
ZnO:Al	40	1.2	O_2	0.25	4000	~200

Table 7.1 PLD deposition parameters for CIGS, CdS, ZnO and ZnO:Al layers for the fabrication of the solar cells.

An X-ray diffractometer (XRD) (SmartLab RIGAKU, Cu Kα, λ = 1.5405 Å) was used to identify the crystal phases present in the ZnO:Al/ZnO/CdS/CIGS/Mo/SLG multi-layer structures. The morphology of the solar cells was determined using scanning electron microscopy (*SEM Tescan Vega LSU*) with the electron accelerating voltage adjusted to 20 kV.

Dark Current-Voltage (IV) measurements were performed at room temperature and in ambient atmosphere using a two-probe configuration, as shown in Figure 7.1. The electrodes of the

CHRISTIANA NICOLAOU

voltage source/ ammeter were mechanically placed on the metallic pad of Al grid and the Mo surface, creating an electrical circuit. The solar cells were electrically forward and reverse biased with an applied voltage varying between -1V and +1V.

Illuminated JV measurements have been performed for the complete solar cell devices under standard conditions (AM1.5G spectrum at light intensity of 1000W/m^2, at 25°C). A two-probe configuration was used with the two probes mechanically placed on the metallic pad of Al grid and the Mo surface, as shown in Figure 7.1.

7.1.2 Results and discussion

The impact of thickness of the CdS layer on the performance of the solar cells was investigated by changing the number of pulses of the CdS layer. Three solar cells were fabricated with different CdS thickness by using 100, 200 and 300 pulses for the deposition of the CdS layer each time. The deposition parameters of the other layers (CIGS, ZnO, ZnO:Al) were identical for the construction of the three solar cells. The pulses of CIGS layer were kept constant at 15000 for all the fabricated devices with varied CdS thickness. The solar cells with varied CdS thickness will be referred as CdS-100, CdS-200 and CdS-300 for the remainder of this chapter, indicating the number of pulses used for the deposition of the CdS layer (e.g., CdS-100 solar cell indicates that the CdS layer was deposited using 100 pulses).

The XRD pattern of the solar cells with varied CdS thickness have been examined by grazing incidence (GIXRD) with 2θ ranging from 10° to 90° and grazing incidence angle fixed at 3°. The XRD pattern of the CdS-300 solar cell is presented in Figure 7.2. The XRD pattern reveals the existence of the ZnO and CdS hexagonal phase, the chalcopyrite $CuIn_{0.7}Ga_{0.3}Se_2$ phase and the Mo phase. The identification of Mo phase in the XRD patterns indicates that the grazing incidence angle used was such that the penetration depth of the X-rays was reaching the Mo layer. This is an important fact, considering that the XRD scanning must take place through the whole multilayer structure in order to locate any secondary phases that can arise from the interdiffusion of the elements at the interfaces between the layers. Having this in mind, the XRD pattern in Figure 7.2 shows that there is no detectable evidence of secondary phases due to the interdiffusion of the elements between ZnO, CdS and CIGS layers. A secondary phase of $Cu_{2-x}Se$ is present in the CIGS layer which is not a result of the interdiffusion of the elements at the interfaces. Similar observations are made in the XRD patterns of the CdS-100 and CdS-200 solar cells which are not shown here.

CHRISTIANA NICOLAOU

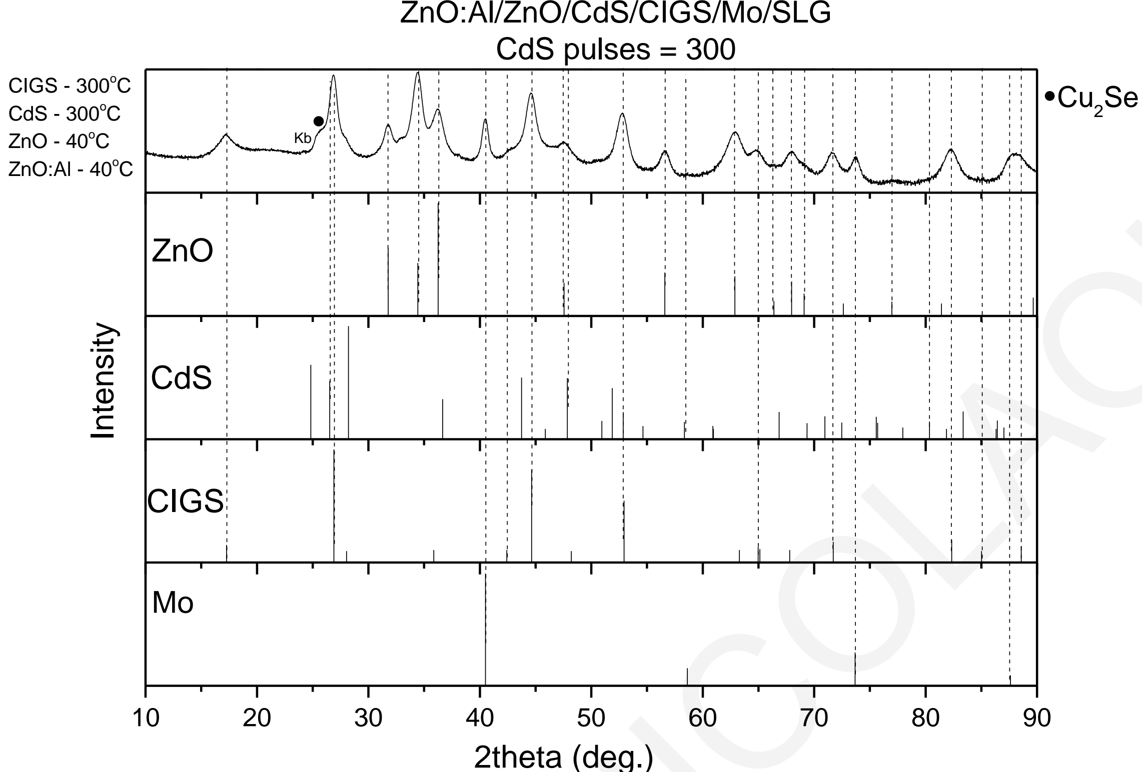

Figure 7.2 XRD pattern of CdS-300 solar cell. The bottom plots show the XRD pattern of ZnO hexagonal phase (PDF 9004178), CdS hexagonal phase (JCPDS 96-900-8863), $CuIn_{0.7}Ga_{0.3}Se_2$ (JCPDS 35-1102) and Mo (PDF 9008543). Secondary phase of Cu_2Se (JCPDS 37-1187) is present in CIGS layer.

Figure 7.3a and b display the SEM images of the surface of CdS-300 solar cell. The surface of ZnO:Al layer and the pattern of the Al grid are shown in Figure 7.3a. The arrows indicate the three components of the metal grid; a central pad, a central busbar and the fingers, all interconnected together. The upper surface of the CdS-300 solar cell in higher magnification is illustrated in Figure 7.3b. The high density and large size of the particulates on the upper surface of the cell is evident. It is speculated that most of these particulates are part of the CIGS layer and protrude through the surface of the cell.

CHRISTIANA NICOLAOU

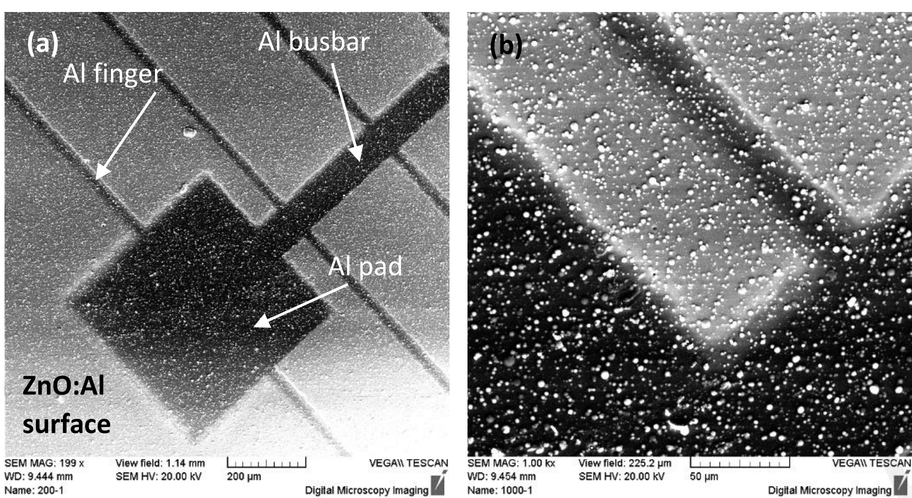

Figure 7.3 SEM image of (a) the upper surface of the CdS-300 solar cell with the arrows indicating the three components of the Al metal grid and (b) the upper surface of the CdS-300 solar cell in higher magnification.

The quality of the solar cell devices has been initially examined by dark IV measurements to identify which devices are suitable for the device performance characterization. A rectifying diode-like behavior is identified only for the CdS-300 as shown in Figure 7.4. The dark IV measurements of the solar cells with smaller thickness of the CdS layer (CdS-100, CdS-200) have resulted in linear IV curves, indicating an ohmic resistance-like behavior. These devices have been rejected since the IV curves didn't show the diode-like behavior, which is prerequisite for a photovoltaic device. Thus, only the CdS-300 solar cell has been characterized in terms of efficiency.

The linear dark IV measurements of CdS-100 and CdS-200 solar cells indicate that the pn-junction is too poor to function as a diode. Based on the SEM images of the cells (Figure 7.3), it is speculated that shunt pathways exist in the stucture of these cells, which are formed by the large and numerous particulates created during the deposition of CIGS layer. These large protruding particulates cannot be homogenously covered by the subsequent depositions of the CdS, intinsic ZnO and Al-doped ZnO. Therefore, pathways connecting the bottom area of the cell (Mo/CIGS) with the upper layers (ZnO/ZnO:Al) are created and the current travels through these low resistive shunts. Thus, the pn junction is bypassed and the ohmic behavior is obtained. This phenomenon is more prevalent for CdS-100 and CdS-200 solar cells in which the CdS thickness is small and insufficient to cover the high roughness surface of the CIGS layer. For CdS-300 solar cells, this phenomenon is partially mitigated as the CdS thickness is large enough to create a functional diode with the high roughness surface of the CIGS layer. However, and as discussed below, shunts continue to exist in the CdS-300 cell, leading to the cell's very low performance. The effect of particulates is discussed in detail in sections 7.2 and 7.3.

CHRISTIANA NICOLAOU

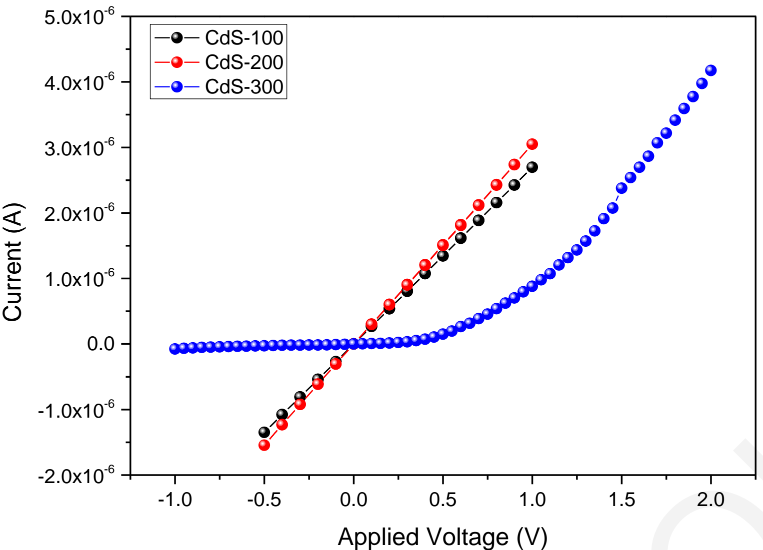

Figure 7.4 2-probe dark IV curves of the CdS-100, CdS-200 and CdS-300 devices based on the SLG/Mo/CIGS/CdS/ZnO/ZnO:Al structure.

Illuminated JV measurement have been conducted on CdS-300 devices and a typical one is shown in Figure 7.5 along with the major electrical parameters of the cell. The fill factor was found to be 0.27 (27%) and the efficiency 0.025%. The very low efficiency of the solar cell can be attributed to significant losses caused by the dissipation of power in the parasitic resistances of the cell. The most common parasitic resistances are series and shunt resistance. Generally, series resistance reduces the fill factor. However, overly high series resistance values may also reduce the short-circuit current [321]. Moreover, series resistance impacts the slope of the JV curve near the open-circuit voltage. As series resistance increases, the JV curve near Voc becomes less steep, indicating a commensurate decrease in the fill factor [322]. Therefore, the very low short-circuit current, the low fill factor and the less steep slope of the JV curve at the open-circuit voltage (Figure 7.5) indicate that the series resistance of the cell is significantly high.

CHRISTIANA NICOLAOU

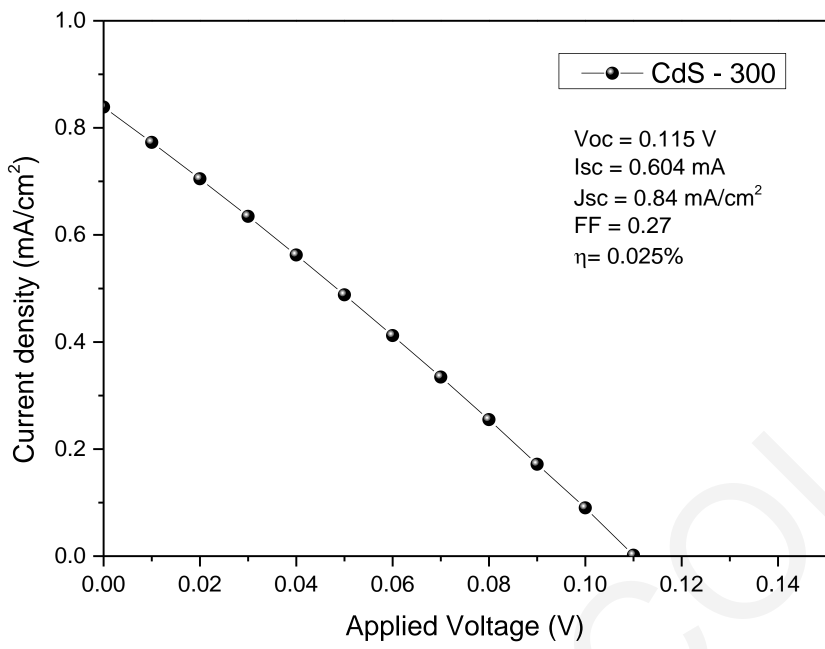

Figure 7.5 Illuminated JV curve and major electrical parameters of a CdS-300 solar cell.

The series resistance of a cell is created as the current flows through the layers and metal contacts of the cell. Thus, the resistances of all the in series-connected layers, the contact resistance at interfaces and the resistance of the metal contacts represent the overall series resistance of the cell [322]. Thus, a part of the excessive high value of the series resistance in the cell derives from the resistance of the individual layers. Further optimization of the individual layers can lead to the reduction of the series resistance, which in turn will improve the performance of the cells. This topic is included as future research work in Chapter 9.

Likewise, substantial power losses are caused by the presence of a shunt resistance. Shunt resistance can arise from imperfections on the device surface and in the bulk as well as from leakage currents across the edge of the cell [323, 324]. Thus, low shunt resistance provides an alternative path for the light generated current and thus, the current flowing through the diode is reduced. As a result, the voltage across the terminals of the solar cell decreases. Low shunt resistance reduces the fill factor and very low values of shunt resistance reduce the open-circuit voltage of the cell [325]. The slope of the JV curve near the short-circuit current point can be used to estimate the shunt resistance of a solar cell: as the shunt resistance decreases, the slope becomes less steep [69]. Thus, the very low open-circuit voltage, the low fill factor and the less steep slope of the JV curve at the short-circuit current (Figure 7.5) indicate that the shunt resistance of the cell is significantly low.

The excessively low shunt resistance of the cell can be attributed to the shunts induced by the presence of the particulates on the surface of the CIGS absorber. The large size and high density of the particulates on the CIGS layers do not allow the homogenous covering of CIGS surface by the

CHRISTIANA NICOLAOU

subsequent layers. Thus, these particulates act as shunts between the top and back contact of the cell, providing low resistive pathways for the light generated current to travel across the cell. Therefore, the pn junction is largely bypassed and the voltage across the cell terminals is reduced. Section 7.2 deals with the elimination of the particulates on CIGS surface by intervening a mask between the target and the substrate during the CIGS deposition. Moreover, the performance of solar cells with low roughness CIGS layers are examined in detail in section 7.3.

In summary, the CIGS solar cells constructed with the optimized conditions based on the work presented in the previous chapters and with varying CdS thickness have resulted to ohmic behaviour or very poor performance. The next section presents the method that has been implemented to improve the performance of the cells, that is eliminating the particulates on the CIGS layer and thus increasing the shunt resistance.

7.2 Elimination of particulates on the CIGS layer

As discussed in section 7.1.2, part of the poor performance of CIGS solar cells can be attributed to the presence of large particulates with diameter up to micron metre on the CIGS surface. The ejection of micron-size particles during the ablation process is a common issue of the conventional PLD method. The high energy density and narrow pulse width of the laser beam, possible inhomogeneities in target density and the high penetration depth of the laser pulse into the target material are usually the reasons that these large particulates are formed [326]. Specifically, during the PLD process, large particles are sputtered from the target surface and having sufficient kinetic energy reach the substrate surface and adhere to it. These large particles produce a shadowing effect which results in an uneven deposition and therefore in an uneven film surface. In addition to the shadowing effects, when a large number of particles is deposited on the substrate, many nucleation seeds are formed and the resulting film is expected to have small crystal grains, many grain boundaries, and high surface roughness [327-329]. Therefore, the presence of these large particulates on the CIGS surface affects the quality of the deposited film through the mechanisms explained above. In addition, a homogeneous coverage of CIGS layer cannot be achieved by the deposition of subsequent layers (CdS, ZnO, Al-doped ZnO) due to the shadowing effect generated by the large protruding particulates of CIGS layer. These effects introduce numerous boundary defects at the interfaces, high carrier recombination rates and low resistive paths between the back and front areas that lead to poor solar cell performance.

Mechanical techniques have been developed to eliminate particulates. These include velocity filters [330], off-axis laser deposition [331], line-of-sight shadow masks [332] and cross-beam techniques [333]. To eliminate the large particulates on the CIGS layer, the shadow mask technique has been employed. The shadow masked pulsed laser deposition (SMPLD) method enables the effective screening of large particles, thereby producing low roughness films [327, 328, 334, 335]. When a mask is placed between the substrate and the target, a shadowed region is created behind the

CHRISTIANA NICOLAOU

mask and between the mask and the substrate (Figure 7.6a). During the deposition, the ablated particles of relatively small size in the plasma plume are more susceptible to change direction due to collisions with gas molecules and eventually enter the shadowed region, where they are able to arrive at the substrate and form a film. However, the large particles preferentially propagate along the normal direction as they are less scattered in the presence of a background gas due to their large mass [189]. Therefore, the large and heavy species of the plume are blocked by the shadow mask, or it is less likely to reach the shadow area. As a result, the presence of large particulates on the deposited film is eliminated and the film's roughness is substantially reduced [108].

Numerous works have used the SMPLD method to produce low roughness films in various material systems using shadow masks of various shapes, sizes and configurations [328, 334-337]. Low roughness films with the elimination of micron-size particulates from the surface have been achieved for Cu_2ZnSnS_4 (CZTS) by Juguang Hu et al. (2018) using the SMPLD method. CZTS is a direct bandgap semiconductor, with high absorption coefficient and is used as an alternative to CIGS absorber for photovoltaic applications. Specifically, Juguang Hu et al. (2018) have demonstrated that the CZTS film prepared by SMPLD were smooth, even and compact, and their surface roughness decreased one order of magnitude compared to the CZTS film prepared with the conventional PLD method. In addition, the efficiency of the CZTS thin film solar cell prepared by SMPLD increased by 1.3% compared to the solar cell with CZTS layer prepared with the conventional PLD method [338]. Here, a cone shaped shadow mask is used for the elimination of particulates during the deposition of the CIGS layer, as shown in Figure 7.6. The apex of the cone is positioned at the center of the plume, pointing at the laser spot on the target. The cone shape essentially offers a tapered masking effect which helps to avoid the bounce-back effect of plume observed when using a flat-plate mask and thereby improving the speed of thin film deposition [338].

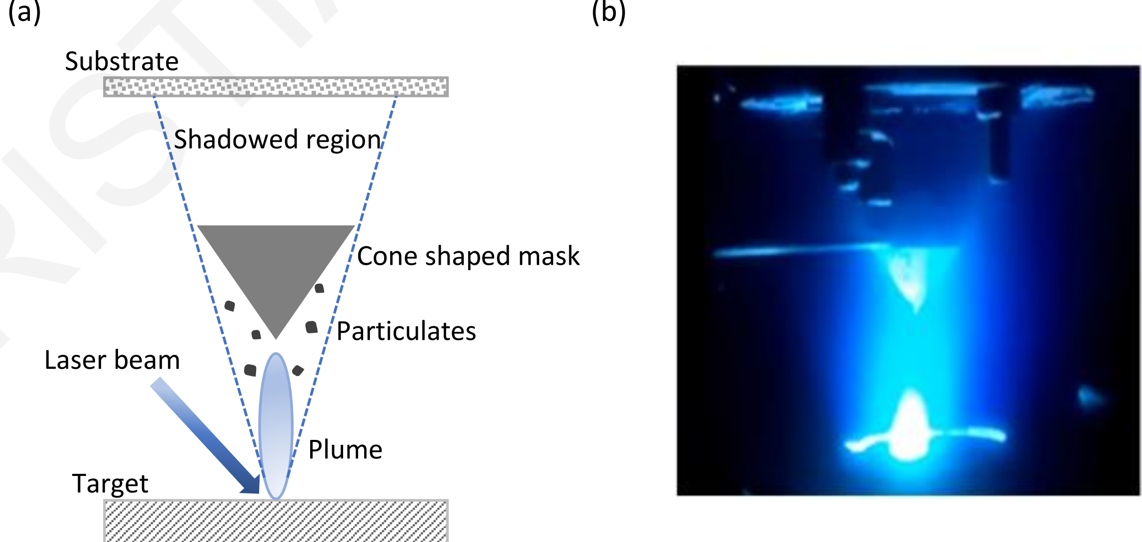

Figure 7.6 (a) Schematic representation of the shadow masked PLD used for the deposition of CIGS

CHRISTIANA NICOLAOU

layer and (b) Photo image of the PLD chamber during the deposition of CIGS layer with the cone shaped mask.

7.2.1 Materials and experimental methods

CIGS films were deposited on soda-lime glass (SLG) substrates by SMPLD using a cone shaped shadow mask placed between the CIGS target and SLG substrate as shown in Figure 7.6. For the remainder of this chapter, the CIGS films deposited with SMPLD will be referred as SMPLD-CIGS and the CIGS films deposited with the conventional PLD will be referred as PLD-CIGS. The deposition process of PLD-CIGS and SMPLD-CIGS films is described in section 4.1.1, with the presence of the cone as the only difference for the deposition of SMPLD-CIGS films. The conical mask was placed at a fixed distance of 2cm from the substrate holder. The bottom diameter and height of the cone was 11 mm and 7.5 mm, respectively[1]. The deposition parameters of PLD-CIGS and SMPLD-CIGS films are obtained from the results of Chapter 4 in which the optimization of the deposition parameters of CIGS films was achieved. As the presence of the cone during the deposition of the SMPLD-CIGS films reduces the overall film thickness, the number of pulses of SMPLD-CIGS films was systematically varied from 15K-90K. The deposition parameters of PLD-CIGS and SMPLD-CIGS films are shown in Table 7.2.

Structure, morphology, chemical composition, thickness, electrical and optical properties of the CIGS films deposited by SMPLD and conventional PLD have been studied using the techniques described in section 4.1.1.

Layer	Deposition Temperature (°C)	Fluence (J/cm^2)	Ar Pressure (mbar)	Pulses (x10^3)	Repetition rate (Hz)	Target-Substrate distance (cm)
PLD-CIGS on SLG	300	1.0	0.01	15	10	4.5
SMPLD-CIGS on SLG	300	1.0	0.01	15-90	10	4.5

Table 7.2 Deposition parameters of CIGS films prepared by the conventional (PLD-CIGS) and shadow masked (SMPLD-CIGS) PLD method.

[1] The dimensions and placement of the conical mask have been determined upon investigation of the shadowing effect of conical masks with different geometrical parameters on the roughness of SMPLD-CIGS films. More details can be found in Appendix B.

CHRISTIANA NICOLAOU

7.2.2 Results and discussion

PLD-CIGS and SMPLD-CIGS films were deposited on SLG substrates to study the size and number of particulates using SEM imaging and analysis. The deposition parameters of PLD-CIGS and SMPLD-CIGS films can be found in Table 7.2. The number of pulses of both films was 15000. Since the SMPLD process involves molecular scattering of ablated atoms with the background gas, the properties of the deposited film (e.g., morphology, stoichiometry, etc.) are strongly dependent on lateral position, that is the distance from the deposition center which coincides with the center of the cone and the shadowed area. Thus, SEM images have been obtained at various distances along a line through the center of the SMPLD-CIGS film which corresponds to the deposition center. The size and number of particulates has been calculated by analysing the SEM images using the ImageJ software.

Figure 7.7a shows the number of particulates as function of particulate area at various lateral distances along a line through the center of the SMPLD-CIGS and at the center of the PLD-CIGS. Regarding the SMPLD-CIGS sample, the number of particulates increases as the distance from the center increases for all particulate sizes. In addition, as the distance from the center increases, larger particulates are observed on the film surface. Particularly, the largest particulate size of the SMPLD-CIGS film identified at the center is ~1μm^2, ~2μm^2 at 0.65 cm and ~4μm^2 at 0.85 cm. The above observations are also illustrated in the SEM images of Figure 7.7b. Since the center of the SMPLD-CIGS films is aligned with the center of the conical mask, it is likely that the center of the film is well shielded against large particulates. Moving away from the center and towards the periphery of the sample, the shielding effect of the shadow mask is reduced. Therefore, there is a higher probability for larger and more particulates to reach the film surface. Comparing the particulates observed on SMPLD-CIGS and PLD-CIGS films, the particulates of SMPLD-CIGS film are substantially reduced in number and size compared to the particulates of PLD-CIGS film (Figure 7.7a).

CHRISTIANA NICOLAOU

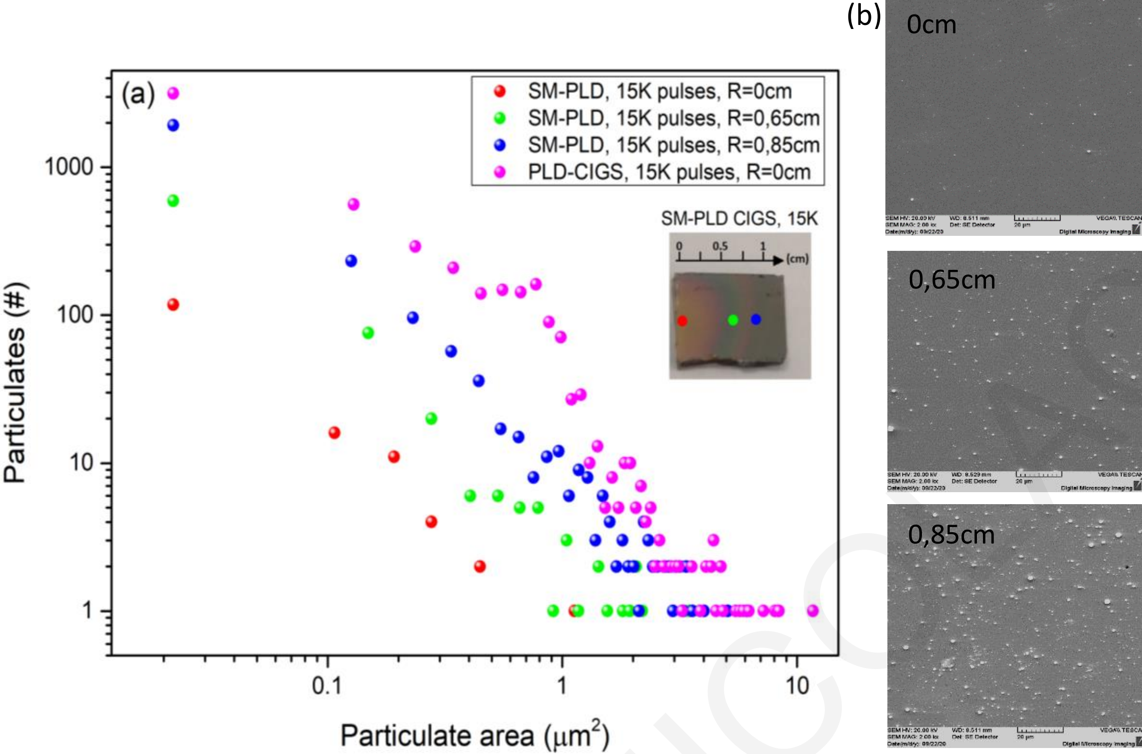

Figure 7.7 (a) Number of particulates as function of particulate area at various lateral distances along a line through the center of the SMPLD-CIGS sample and at the center of the PLD-CIGS, (b) SEM images of SMPLD-CIGS sample at various lateral distances. The number and size of particulates increases along the lateral distance away from the center of SMPLD-CIGS film. The particulates of SMPLD-CIGS film are substantially reduced in number and size compared to the particulates of PLD-CIGS film.

Figure 7.8 shows the compositional ratios of the SMPLD-CIGS film at various lateral distances along a line through the center of the film obtained by EDS measurements. The stoichiometry of the PLD-CIGS film is included in the graph for comparison. The compositional ratios of a stoichiometric transfer from the target to the film are denoted on Figure 7.8 with the dashed lines and are the following: CGI=Cu/(Ga+In)=1, GGI=Ga/(Ga+In)=0.3, IGI=In/(Ga+In)=0.7 and Se/M=Se/(Cu+Ga+In)=1. As the figure shows, the SMPLD-CIGS film exhibits a stoichiometric variation across the surface. Near the center, the film is significantly Cu-deficient and Se-rich, while towards the periphery the Cu content increases towards the stoichiometric value. The SMPLD-CIGS film is slightly In-rich and Ga-poor across the lateral distance. The GGI ratio of the films is ~0.26, which lies within the range of high-efficiency cells [181].

Due to the fact that Cu atoms are the lightest among the atoms ablated from the CIGS target and that Se atoms are slightly heavier than Cu atoms, the increased Se concentrations and reduced Cu concentrations found in the SMPLD-CIGS film was not expected. Specifically, the order of light to heavy elements is Cu (Z=29), Ga (Z=31), Se (Z=34) and In (Z=49). Due to the light mass of Cu atoms, uniform and stoichiometric distribution of Cu atoms on the film was expected, as light ablated

CHRISTIANA NICOLAOU

atoms are scattered more easily by the background gas than heavy ones and their angular distribution is broader [107, 339]. Consequently, light atoms are more likely to arrive in the shadowed region after scattering by molecules of the background gas and be deposited to the substrate. However, the transport efficiency of the atoms in the shadow zone is not solely determined by their atomic masses. The propagation and relative distribution of different atomic species on the substrate is a complex process which involves an interplay of numerous mechanisms and factors, such as the scattering cross section of each atom with the background gas, re-sputtering effects at the substrate surface, kinetic energy of the atoms and other growth mechanisms that influence the growth and stoichiometry of the film.

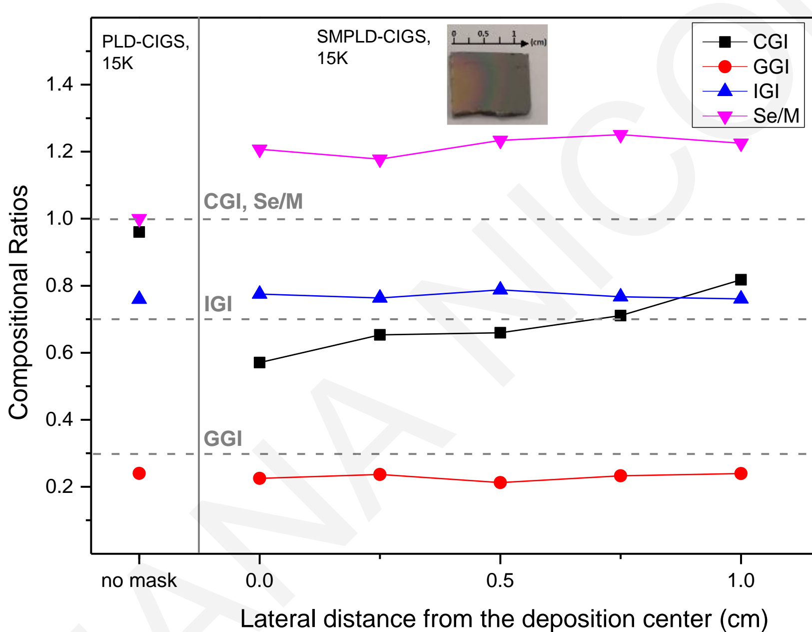

Figure 7.8 Compositional ratios of PLD-CIGS and SMPLD-CIGS film obtained at various lateral distances along a line through the deposition center. Dashed lines indicate the ratios of a stoichiometric film, being CGI=Cu/(Ga+In)=1, GGI=Ga/(Ga+In)=0.3, IGI=In/(Ga+In)=0.7 and Se/M=Se/(Cu+Ga+In)=1. The SMPLD-CIGS film is significantly Cu-deficient and Se-rich across the surface.

SMPLD-CIGS films were systematically deposited on SLG substrates with different numbers of pulses to identify the optimum number of pulses based on the examination of chemical, structural and morphological properties of the films. EDS results of SMPLD-CIGS films at different number of pulses and PLD-CIGS film with 15000 pulses are shown in Figure 7.9. For each film, EDS measurements were obtained at several different positions and the mean compositional ratio was calculated by taking the average value of all positions. As the figure shows, all SMPLD-CIGS films exhibit Cu deficiency and Se excess, except the one deposited at 30000 pulses. In addition, Ga and In concentrations slightly deviate from the stoichiometric values for the SMPLD-CIGS films

CHRISTIANA NICOLAOU

deposited at 15000 and 30000 pulses. Above 30000 pulses, the IGI and GGI ratios are very close to the stoichiometric values.

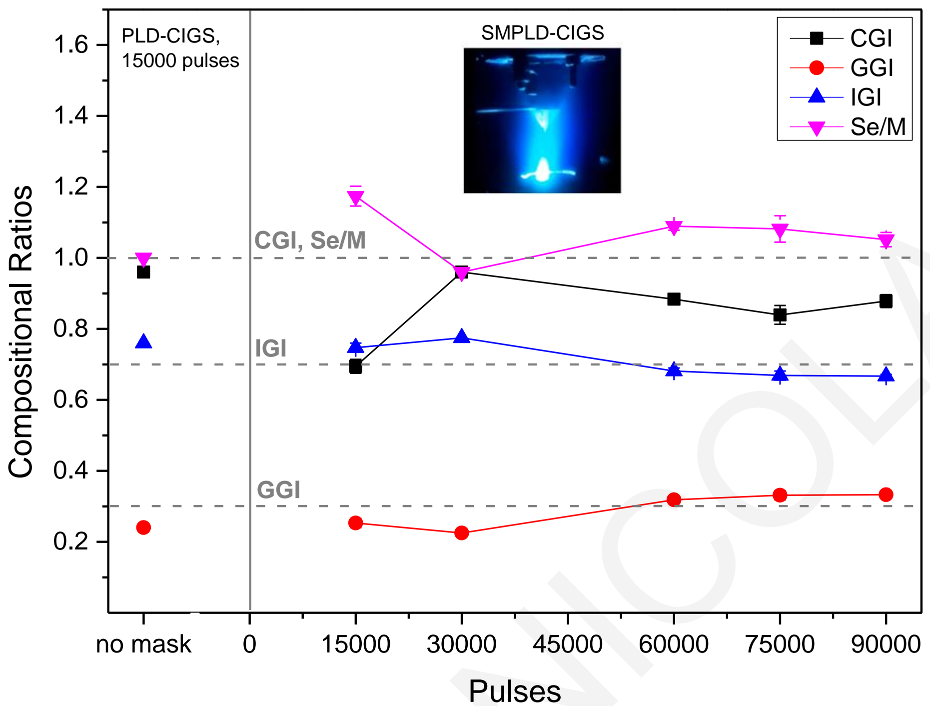

Figure 7.9 Compositional ratios of SMPLD-CIGS films with different number of pulses and PLD-CIGS film with 15000 pulses. Dashed lines indicate the ratios of a stoichiometric film, being CGI=Cu/(Ga+In)=1, GGI=Ga/(Ga+In)=0.3, IGI=In/(Ga+In)=0.7 and Se/M=Se/(Cu+Ga+In)=1.

Grazing incidence XRD (GIXRD) patterns of SMPLD-CIGS films deposited at different number of pulses and the PLD-CIGS film at 15000 pulses, with 2θ ranging between 10° and 90° are shown in Figure 7.10. All films exhibit various diffraction peaks of the $CuIn_{0.7}Ga_{0.3}Se_2$ chalcopyrite phase (JCPDS 35-1102), with (112) peak being the most prominent. The XRD patterns reveal the polycrystalline nature of the films. As discussed in section 4.1.2. of Chapter 4, the (112) texture of CIGS films is beneficial for obtaining good lattice matching with CdS layers [340]. An additional peak at ~25.6° appears on the GIXRD patterns in all deposited films and is attributed to the Cu_2Se secondary phase (JCPDS 37-1187). It is worth mentioning that the minor peak of Cu_2Se phase can only be distinguished when the GIXRD intensity data are presented in a logarithmic scale. The appearance of the Cu_2Se secondary phase in PLD-CIGS films grown at fluence of 1 J/cm^2 and Ar pressure of 0.01 mbar is discussed in section 4.1.2. of Chapter 4. It is likely that similar mechanisms are responsible for the formation of Cu_2Se in the SMPLD-CIGS films since these films are also deposited at fluence of 1 J/cm^2 and Ar pressure of 0.01 mbar.

As the XRD patterns show, the intensity of the diffraction peaks is higher for the SMPLD-CIGS film of 90000 pulses and is comparable to the PLD-CIGS film at 15000 pulses. This can be attributed to two factors: the fact that the SMPLD-CIGS film of 90000 pulses is thicker than the other

CHRISTIANA NICOLAOU

SMPLD-CIGS films and that the longer deposition time allows for more crystallization to occur at 300ºC. A systematic shift of the peaks to higher 2θ values is also observed for the SMPLD-CIGS films which indicates that the CIGS films obtained with the SMPLD method have a crystal structure with smaller lattice parameters. This reduction in lattice parameters is most likely due to changes in stoichiometry and/or strain effects during the deposition of the SMPLD-CIGS films.

The crystallite size for the films was calculated from the peak broadening of the (112) and (220) diffraction peaks using the Scherrer formula. In the case of PLD-CIGS film grown with 15000 pulses, an average grain size of 17.1 nm was calculated. On the other hand, the average crystallite size of the film deposited at 15000 pulses using the SMPLD method was 14.8 nm. This apparent reduction in the average crystallite size is attributed to the smaller thickness of SMPLD-CIGS film. Indeed, for the SMPLD-CIGS film deposited at 90000 pulses, the average grain size was calculated at 16.7 nm, which is closer to the PLD-CIGS film of 15000 pulses. The increase of crystallite size with increase in thickness has also been reported for CIGS films deposited with PLD [341].

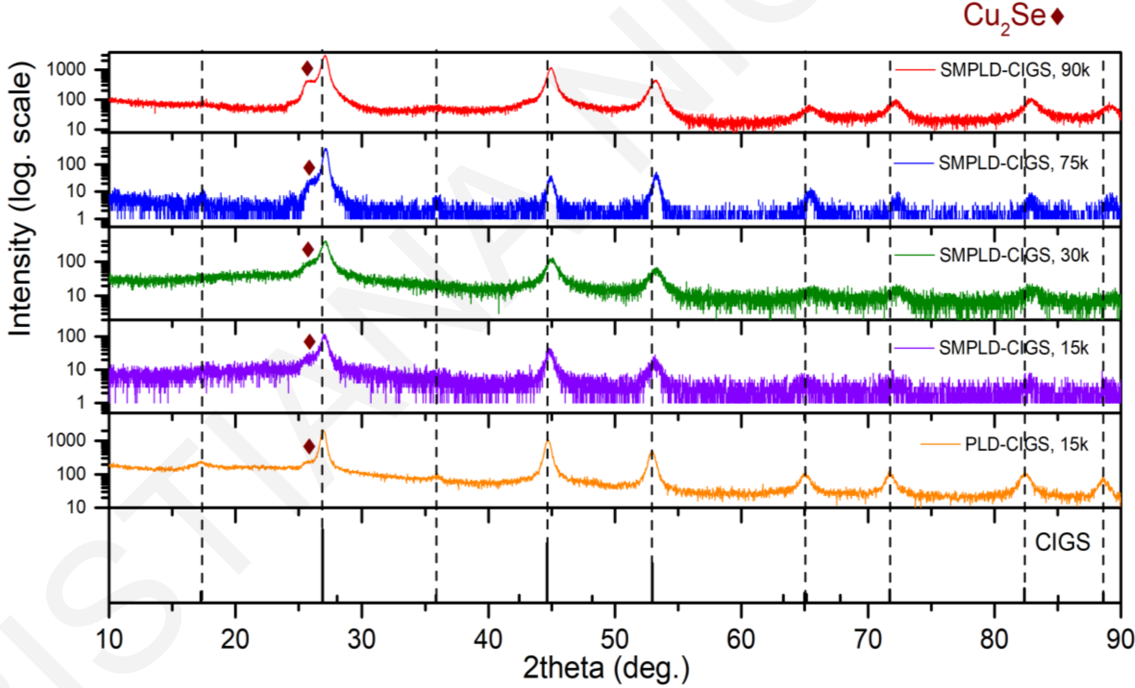

Figure 7.10 XRD patterns of SMPLD-CIGS films deposited on SLG substrates at different pulses and PLD-CIGS deposited at 15000 pulses. The bottom plot shows the XRD pattern of CuIn0.7Ga0.3Se2 according to JCPDS 35-1102. A minor secondary phase of Cu_2Se appears in all films.

The surface roughness of SMPLD-CIGS films as a function of pulses, measured by AFM, is presented in Figure 7.11a. Different areas were scanned for each film and the surface roughness was calculated by averaging the rms roughness of each area. The surface roughness of the PLD-CIGS film deposited at 15000 pulses is also shown in the figure. The surface roughness of SMPLD-CIGS

films slightly increases from ~5 nm to 16 nm as the number of pulses increases from 15000 to 90000. Similar behaviour has been observed in CIGS films deposited on SLG substrates with different pulses, as discussed in Chapter 4. More importantly, the surface roughness of SMPLD-CIGS films is significantly reduced by an order of magnitude compared to that of PLD-CIGS with 15000 pulses. The 3-dimensional images obtained with AFM also demonstrate that SMPLD-CIGS film of 90000 pulses has a smoother surface with fewer and smaller particulates in comparison to PLD-CIGS film (Figure 7.11b).

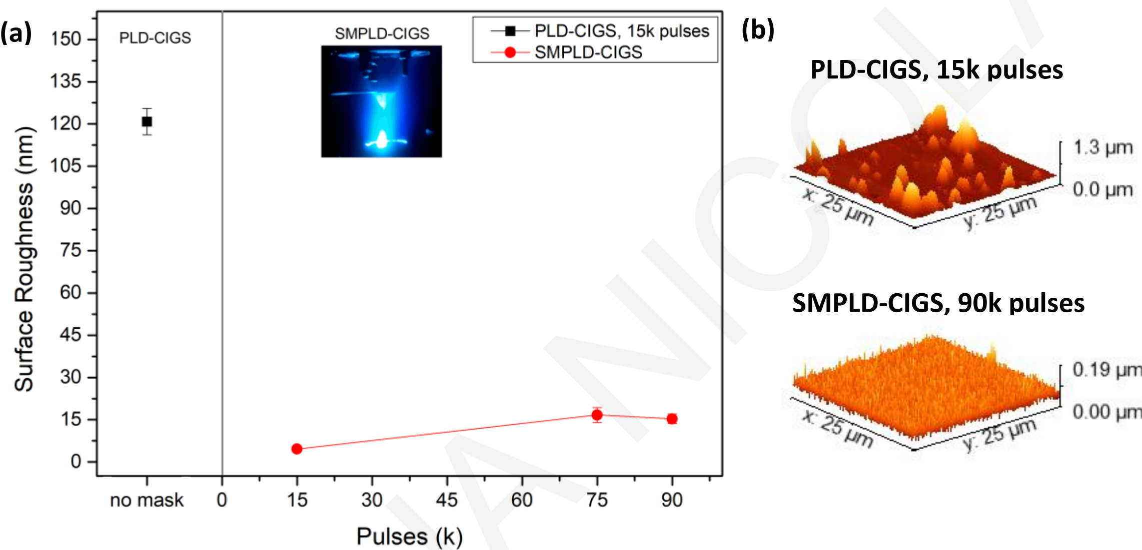

Figure 7.11 (a) Surface roughness of SMPLD-CIGS thin films deposited on SLG substrates with different number of pulses and a PLD-CIGS film with 15000 pulses, (b) 3-D images of PLD-CIGS surface of 15000 pulses and SMPLD-CIGS surface of 90000 pulses. SMPLD-CIGS films have a surface roughness that is one order of magnitude lower than that of PLD-CIGS.

The examination of chemical, structural and morphological characteristics of SMPLD-CIGS films with different number of pulses has not revealed significant differences between the samples. Therefore, the thickness of the films was the determinant factor for selecting the number of pulses for the SMPLD-CIGS layer. Since the CIGS absorber layer should have a minimum thickness of ~1.5μm [2], the SMPLD-CIGS film produced with the highest number of pulses (90000 pulses) has been chosen as the most suitable. With 90000 pulses, SMPLD-CIGS film has a thickness of ~1200 nm, which is close to the thickness of PLD-CIGS film of ~1350 nm. Moreover, the SMPLD-CIGS

[2] In theory, CIGS layer with thickness of 1.5 μm thick absorbs almost the entire incident light (if the energy of photons is greater than the bandgap) due to its superior absorption coefficient of as high as 10^5 cm^{-1} [21]. However, high efficiency solar cells that exhibit efficiencies over 20% require a CIGS layer of about 2μm [55], as there are various limitations that may impact the performance and properties of the CIGS layer.

CHRISTIANA NICOLAOU

film deposited at 90000 pulses exhibits a nearly stoichiometric composition, a structure of crystalline $CuIn_{0.7}Ga_{0.3}Se_2$ chalcopyrite phase with a minor secondary phase of Cu_2Se and a low-roughness surface.

Figure 7.12 shows the compositional ratios of the SMPLD-CIGS film deposited at 90000 pulses at various positions from the center to the corner of the film, obtained by EDS measurements. As the figure shows, the stoichiometric ratios of the elements are constant across the surface of the film. The film is Cu-deficient and Se-rich and the In and Ga compositional ratios are very close to the stoichiometric values throughout the film.

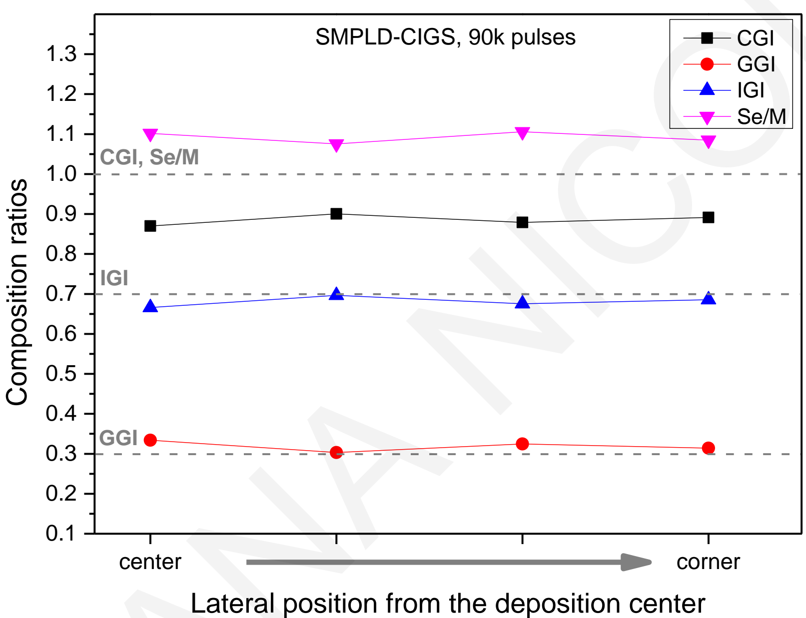

Figure 7.12 Compositional ratios of SMPLD-CIGS film deposited at 90000 pulses obtained at various positions from the center to the corner of the film. Dashed lines indicate the ratios of a stoichiometric film, being CGI=Cu/(Ga+In)=1, GGI=Ga/(Ga+In)=0.3, IGI=In/(Ga+In)=0.7 and Se/M=Se/(Cu+Ga+In)=1.

The surface roughness of SMPLD-CIGS film with 90000 pulses at various areas along a line through the center, measured by AFM, is presented in Figure 7.13. The surface roughness of the film increases from ~16 nm to 25 nm as the distance from the center increases. Since the center of the film is being more effectively shielded against particulates from the cone mask, the center of the film exhibits the lowest roughness and smoothest surface. Moving away from the center and towards the periphery of the sample, the shielding effect of the shadow mask is reduced. Therefore, larger and more particulates are more likely to reach the film surface. As an illustration of the above observations, Figure 7.13 includes the 2-dimensional AFM images of the surface roughness measurements.

CHRISTIANA NICOLAOU

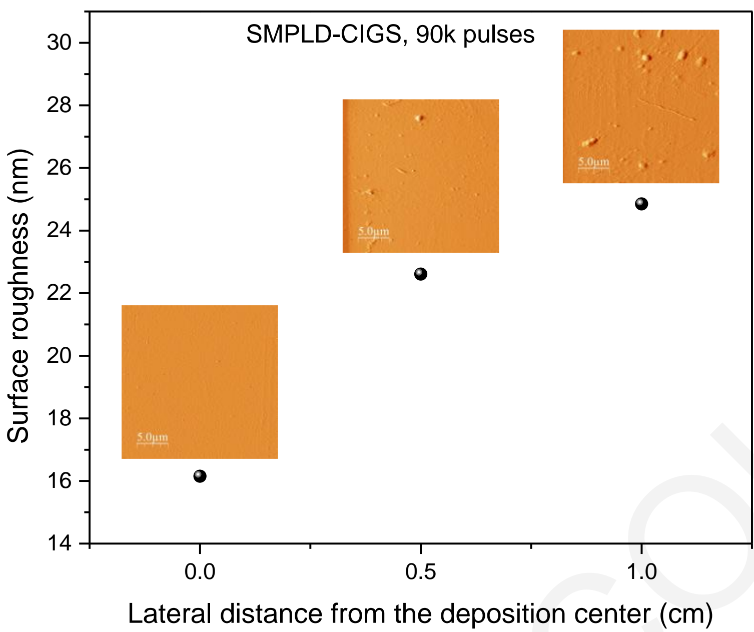

Figure 7.13 (a) Surface roughness of SMPLD-CIGS thin film deposited at 90000 pulses at various lateral distances from the deposition center. Surface roughness increases as the distance from the center increases. This tendency is also illustrated by the 2-D AFM images.

Dark electrical resistivity for SMPLD-CIGS film deposited at 90000 pulses was measured at room temperature by the van der Pauw four-probe technique and was found to be in the order of 10^1 Ω·cm (Table 7.3). In addition, the p-type conductivity of the sample has been confirmed by the Seebeck measurement[3]. The main properties of SMPLD-CIGS film deposited at 90000 pulses are listed in Table 7.3.

Sample	Pulses	Thickness (nm)	Resistivity (Ohm.cm)	N/P type	Energy gap (eV)	Surface roughness (nm)
SMPLD-CIGS on SLG	90k	~1200	1.42 x 10^1	P	~1.14	~21

Table 7.3 Main properties of the SMPLD-CIGS film deposited at 90000 pulses.

[3] More information about the Seebeck measurement can be found in [342].

CHRISTIANA NICOLAOU

7.3 One-step SMPLD-grown CIGS solar cells

In this section, one-step SMPLD-grown CIGS solar cells have been fabricated with low roughness CIGS layers. Smoother CIGS surface without the presence of micron-size particulates is expected to improve the efficiency of the SMPLD-CIGS solar cells due to the elimination of shunts at the pn junction. The performance of SMPLD-CIGS solar cells has also been investigated as function of CdS thickness.

7.3.1 Materials and experimental methods

SMPLD-CIGS solar cells were fabricated with the CIGS layer prepared by the SMPLD method using the cone shaped shadow mask during the deposition. The fabrication of the solar cells was achieved with the sequential deposition of SMPLD-CIGS, CdS, ZnO and ZnO:Al layers on Mo-coated SLG substrates using PLD. The SMPLD-CIGS solar cells were completed by the deposition of an Al grid directly on the surface of ZnO:Al layer. The details of the fabrication process can be found in section 7.1.1. The impact of thickness of CdS layer on the performance of the solar cells was investigated by varying the number of pulses of this layer. Table 7.4 presents the main deposition parameters for each layer used for the fabrication of the SMPLD-CIGS solar cells. Structural, morphological, electrical characterization and performance analysis of the SMPLD-CIGS solar cells have been carried out with the techniques described in section 7.1.1.

Layer	Deposition Temperature (°C)	Fluence (J/cm²)	Background gas	Pressure (mbar)	Pulses	Thickness (nm)
SMPLD-CIGS	300	1.0	Ar	0.01	90k	~1200
CdS	300	1.1	Ar	0.01	300-800	~110-275
ZnO	40	1.2	O_2	0.25	1500	~80
ZnO:Al	40	1.2	O_2	0.25	4000	~200

Table 7.4 PLD deposition parameters for SMPLD-CIGS, CdS, ZnO and ZnO:Al layers for the fabrication of the SMPLD-CIGS solar cells.

7.3.2. Results and discussion

The impact of thickness of the CdS layer on the performance of the SMPLD-CIGS solar cells was investigated by changing the number of pulses of the CdS layer. Three solar cells were fabricated with different CdS thickness by using 300, 600 and 800 pulses for the deposition of the CdS layer each time. The deposition parameters of the other layers (SMPLD-CIGS, ZnO, ZnO:Al) were identical for the construction of the three solar cells. The number of pulses for the deposition of the CIGS layer were kept constant at 90000 for all the fabricated devices with varied CdS

CHRISTIANA NICOLAOU

thickness. The SMPLD-CIGS solar cells with varied CdS thickness will be referred as SMPLD-CIGS/CdS-300, SMPLD-CIGS/CdS-600 and SMPLD-CIGS/CdS-800 for the remainder of this chapter, indicating the number of pulses used for the deposition of the CdS layer (e.g., SMPLD-CIGS/CdS-300 solar cell indicates that the CdS layer was deposited using 300 pulses and the CIGS layer was deposited using the SMPLD method).

SEM images of the upper surface of SMPLD-CIGS/CdS-300 solar cell are displayed in Figure 7.14, with the surface of the ZnO:Al layer and the pattern of the Al grid denoted. It is evident that the particulates have been drastically reduced in size and density (see Figure 7.3 for comparison with the CdS-300 solar cell). As a result of the low roughness of SMPLD-CIGS film, the upper surface of the cell is significantly smoother, which allows the Al metal grid to be uniformly deposited on the ZnO:Al layer.

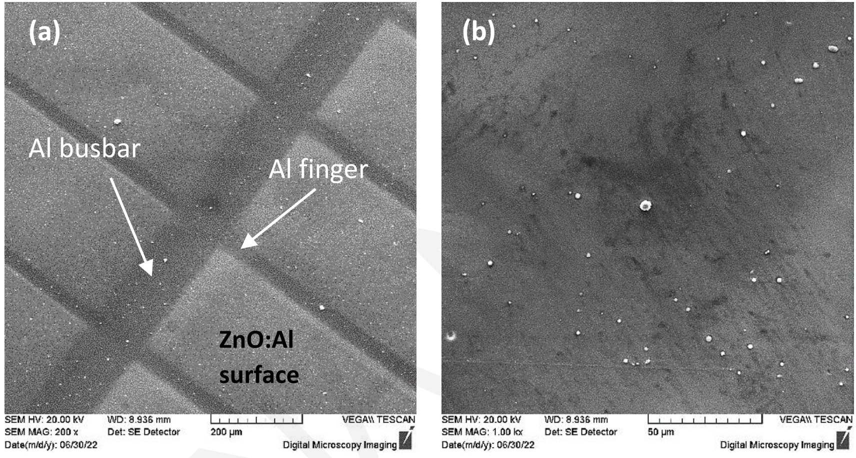

Figure 7.14 SEM image of (a) the upper surface of SMPLD-CIGS/CdS-300 solar cell with the arrows indicating components of the Al metal grid and (b) the upper surface of SMPLD-CIGS/CdS-300 solar cell in higher magnification.

The XRD patterns of the SMPLD-CIGS solar cells with varied CdS thickness have been examined by grazing incidence (GIXRD) with 2θ ranging from 10° to 90° and grazing incidence angle fixed at 3°. The XRD pattern of the SMPLD-CIGS/CdS-300 solar cell is presented in Figure 7.15. The XRD pattern reveals that the existence of the ZnO and CdS hexagonal phase, the chalcopyrite $CuIn_{0.7}Ga_{0.3}Se_2$ phase and the Mo phase. The identification of Mo phase in the XRD patterns indicates that the grazing incidence angle used was such that the penetration depth of the X-rays was reaching the Mo layer. The XRD pattern in Figure 7.15 shows that there is no evidence of secondary phases due to the interdiffusion of the elements between ZnO, CdS and CIGS layers. A secondary phase of $Cu_{2-x}Se$ is present in the CIGS layer, which is not a result of the interdiffusion of the elements at the interfaces. The Al peak comes from the Al metal grid deposited at the top of the cell. Similar conclusions are derived from the XRD patterns of the SMPLD-CIGS/CdS-600 and SMPLD-CIGS/CdS-800 solar cells which are not shown here.

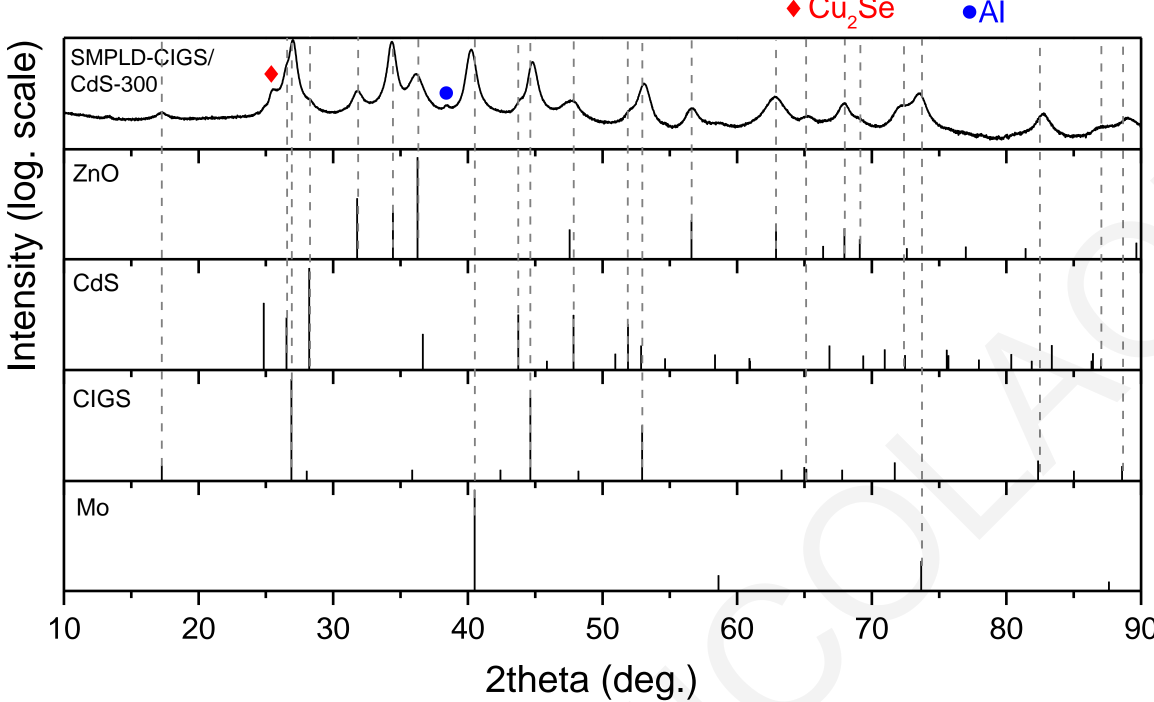

Figure 7.15 XRD pattern of SMPLD-CIGS/CdS-300 solar cell. The bottom plots show the XRD pattern of ZnO hexagonal phase (PDF 9004178), CdS hexagonal phase (JCPDS 96-900-8863), CuIn0.7Ga0.3Se2 (JCPDS 35-1102) and Mo (PDF 9008543). Secondary phase of Cu2Se (JCPDS 37-1187) is present in CIGS layer.

Illuminated JV measurements are shown in Figure 7.16, for the SMPLD-CIGS/CdS-300, SMPLD-CIGS/CdS-600 and SMPLD-CIGS/CdS-800 solar cells. In addition, the light JV curve of the CIGS solar cell with the CIGS layer deposited using conventional PLD method with 15000 pulses and similarly for CdS with 300 pulses is also included in Figure 7.16.

CHRISTIANA NICOLAOU

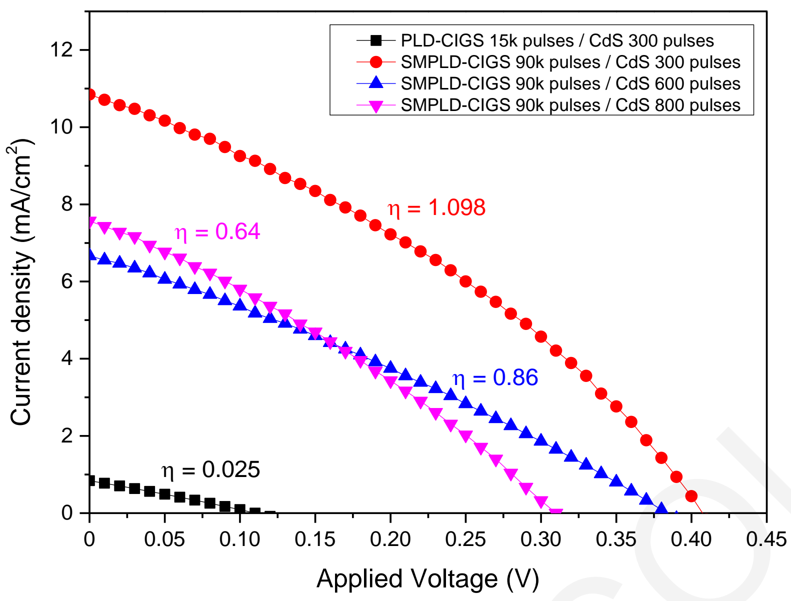

Figure 7.16 Light JV curves of SMPLD-CIGS solar cells with different CdS pulses (SMPLD-CIGS/CdS-300, SMPLD-CIGS/CdS-600, SMPLD-CIGS/CdS-800) and PLD-CIGS solar cell.

Device	V_{oc} (V)	I_{sc} (mA)	J_{sc} (mA/cm^2)	FF (%)	η (%)
PLD-CIGS 15k – CdS 300	0.115	0.604	0.84	27	0.025
SMPLD-CIGS 90k – CdS 300	0.407	7.81	10.85	34.2	1.098
SMPLD-CIGS 90k – CdS 600	0.385	4.88	6.78	29	0.86
SMPLD-CIGS 90k – CdS 800	0.305	5.45	7.57	30.89	0.64

Table 7.5 Electrical parameters of SMPLD-CIGS solar cells with different CdS pulses (SMPLD-CIGS/CdS-300, SMPLD-CIGS/CdS-600, SMPLD-CIGS/CdS-800) and PLD-CIGS solar cell.

The light JV curves of the solar cells demonstrate that SMPLD-CIGS solar cells exhibit significantly higher efficiencies and better electrical parameters compared to the PLD-CIGS solar cell (Figure 7.16). The electrical parameters of SMPLD-CIGS solar cells and PLD-CIGS solar cell are listed in Table 7.5. It is evident that the low roughness of the SMPLD-CIGS layer and thus, the reduction of shunt paths, in the SMPLD-CIGS solar cells lead to better CIGS/CdS junction quality, resulting in higher short-circuit currents, open-circuit voltages and power conversion efficiencies. The highest efficiency (η = 1.098 %) along with the best electrical parameters are obtained for the SMPLD-CIGS solar cell with the lowest CdS thickness, that is the SMPLD-CIGS/CdS-300 solar cell (CdS deposited at 300 pulses, CIGS deposited with the SMPLD technique at 90000 pulses), whereas the efficiency of SMPLD-CIGS/CdS-600 and SMPLD-CIGS/CdS-800 solar cells decreases as the

CHRISTIANA NICOLAOU

CdS thickness increases. Reduction in efficiency with increasing CdS thickness has also been reported in the literature [343-347].

While major improvements in efficiency have been achieved by using the SMPLD technique to grow the CIGS layer, the SMPLD-CIGS solar cells still suffer from markedly high series and low shunt resistances which result in low efficiencies and low values for the electrical parameters (low Jsc, Voc and FF). The low efficiency of the SMPLD-CIGS solar cells can also be attributed to the small thickness of the CIGS absorber layer. It has been shown that a decrease in the thickness of the CIGS absorbing layer less than 1.5 μm leads to a significant decrease in the photocurrent and efficiency [343-349] [4].

The thinner CIGS layer in the SMPLD-CIGS cells leads to reduced absorption and enhanced interface recombination at the back contact. For thin CIGS layers (below 1500 nm), the CIGS/CdS junction and the depletion region are located closer to the back contact. As a result, the interface recombination of the photogenerated carriers at the back contact increases and the collection of these carriers is limited. Thus, while the bulk recombination likely decreases in thin CIGS absorbers, it is counteracted by the increased interface recombination at the back contact [346, 353, 354].

SMPLD-CIGS/CdS-300 solar cell exhibits the highest Jsc among the investigated SMPLD-CIGS solar cells. The high Jsc of SMPLD-CIGS/CdS-300 solar cell can be attributed to the reduced series resistance because of the thinner CdS layer. According to the literature, the device current is limited by a significant series resistance caused by the resistance of bulk CdS, which increases with thickness [355]. Thus, the Jsc of SMPLD-CIGS/CdS-600 and SMPLD-CIGS/CdS-800 cells is lower due to the higher series resistance caused by the thicker CdS layers. Numerous studies have shown that the Jsc of CIGS solar cells decreases with increasing CdS thickness [343, 345-347].

As observed from the JV measurement (Figure 7.16), the Voc decreases as CdS thickness increases, with SMPLD-CIGS/CdS-300 solar cell exhibiting the highest Voc (Table 7.5). This result is consistent with several studies showing that Voc decreases with increasing CdS thickness [343, 345, 347]. Since Voc is affected by recombination effects and shunt mechanisms, the reduction of Voc with increasing CdS thickness can be attributed to increased recombination effects resulting from the expected higher defect density of the thicker CdS layers. Therefore, it is suggested that

[4] In principle, CIGS absorber thickness of 1-1.5 μm is sufficient for complete absorption of photons with energies larger than the absorber's band gap. This minimum thickness value, above which CIGS solar cells demonstrate high performance, has been determined from optical simulations and experimental investigations [348, 350, 351]. However, in highly efficient CIGS solar cells ($n \geq 20\%$), the CIGS absorber thickness is 2-3 μm [e.g., 11, 352]. Studies focused on fabricating ultra-thin CIGS solar cells and investigating their performance as a function of CIGS thickness, have resulted in moderate efficiencies [351].

CHRISTIANA NICOLAOU

SMPLD-CIGS/CdS-600 and SMPLD-CIGS/CdS-800 solar cells exhibit lower Voc due to the higher recombination effects caused by higher defect densities in the thicker CdS layers.

7.4 Conclusions

PLD-grown solar cells have been fabricated through the sequential deposition of CIGS, CdS, ZnO and ZnO:Al layers on Mo-coated SLG substrates using the optimum deposition parameters of each layer based on the results of the previous chapters. The impact of CdS thickness on the performance of the solar cells was investigated and the PLD-grown solar cells with varying CdS thicknesses have resulted to ohmic behavior or very poor performance. One of the primary reasons identified for the poor performance of these solar cells was the low shunt resistance, which was attributed to the shunt paths induced by the presence of micron-size particulates on the surface of the CIGS absorber.

Therefore, to improve the performance of the cells, the SMPLD technique has been employed using a cone shaped shadow mask during the deposition of CIGS layer to eliminate the large particulates on the CIGS layer. SEM images at various lateral distances from the deposition center revealed that the particulates on the SMPLD-CIGS film surface substantially decrease in number and size as the lateral distance increases.

Next, SMPLD-CIGS films were systematically deposited on SLG substrates with different numbers of pulses. Based on the examination of chemical, structural and morphological characteristics, and thickness, the optimum SMPLD-CIGS film was obtained at 90000 pulses. The SMPLD-CIGS film at 90000 pulses exhibits a nearly stoichiometric composition and a structure of crystalline $CuIn_{0.7}Ga_{0.3}Se_2$ chalcopyrite phase with a minor secondary phase of Cu_2Se. Furthermore, a low-roughness surface is obtained with thickness of ~1200 nm. Particularly, the SMPLD-CIGS at 90000 pulses has a surface roughness that is one order of magnitude lower than that of PLD-CIGS. In addition, no significant variations in chemical composition and surface roughness along the lateral distance from the deposition center have been observed.

Finally, one-step SMPLD-grown CIGS solar cells have been fabricated with low roughness CIGS layers using the SMPLD method. The smoother surface of CIGS absorber without the presence of micron-size particulates has significantly improved the efficiency of the SMPLD-CIGS solar cells due to the elimination of shunt paths. The impact of thickness of the CdS layer on the performance of the SMPLD-CIGS solar cells was investigated and the highest efficiency of 1.098% has been obtained for the SMPLD-CIGS solar cell with CdS layer deposited at 300 pulses. Thus, this chapter has demonstrated the fabrication of CIGS solar cells using PLD in one growth sequence for the multi-layer CIGS/CdS/ZnO/Al:ZnO stucture and at temperatures not exceeding 300 °C.

CHRISTIANA NICOLAOU

Chapter 8 – Conclusions

Among the various PV technologies, thin film solar cells have attracted considerable interest due to high potential conversion efficiencies, high radiation resistance, weight reduction, and space savings. More specifically, $Cu(In,Ga)Se_2$ solar cells exhibit steadily increasing efficiencies, especially during the last decade. However, the current fabrication process is time consuming and expensive due to the multiple deposition techniques used to grow the different layers in the stack and the high processing temperatures required. In this PhD thesis, the pulsed laser deposition technique was utilized to simplify the fabrication process through a novel sequential the growth of the multi-layer CIGS/CdS/ZnO/Al:ZnO stucture. A systematic investigation of the individual layers and the interfaces of the adjacent layers has been carried out to optimize the properties of the multi-layer structure and ultimately the PLD-grown solar cells. The main findings of each chapter are described in the following sections.

8.1 Optimization of the CIGS layer on SLG

A systematic investigation of laser fluence, background gas and substrate temperature was performed to understand the influence of these process parameters on various properties of CIGS thin films grown by PLD on soda-lime glass substrates. Secondary PLD deposition parameters, such as number of pulses, repetition rate, distance between target and substrate and the type of substrate, were also investigated. The main results of the parametric investigations for the optimization of CIGS layer on SLG are presented here and more details can be found in Chapter 4, section 4.1.

The results of the systematic investigation of the fluence on the growth of CIGS thin films revealed the existence of a threshold fluence value of 0.8 J/cm^2 above which stoichiometric films $CuIn_{1-x}Ga_xSe_2$ ($x \sim 0.26$) are obtained. Additionally, a minor secondary phase of Cu_2Se appears at fluences equal or higher than 0.8 J/cm^2. Hence, a fluence of 1 J/cm^2 is deduced to be the most appropriate for the growth of CIGS thin films, because stoichiometric films are obtained having an intermediate roughness of ~80 nm. The high deposition rates of PLD allows the fast deposition of stoichiometric CIGS films with a thickness of ~800 nm in only 10 minutes, without the need of selenization after the deposition.

The systematic investigation of the effect of background pressure on the growth of CIGS thin films revealed a threshold Ar pressure of 0.01 mbar in obtaining stoichiometric $CuIn_{1-x}Ga_xSe_2$ films ($x \sim 0.26$). In addition, a minor secondary phase of Cu_2Se appears in all films. Hence, Ar pressure of 0.01 mbar is deduced as the most appropriate for the growth of CIGS thin films, because stoichiometric films can be obtained having an intermediate roughness of ~ 90 nm.

CHRISTIANA NICOLAOU

The systematic investigation of the effect of deposition temperature on the growth of CIGS thin films revealed that high quality films are obtained at higher temperatures. All films are nearly stoichiometric ($CuIn_{1-x}Ga_xSe_2$ with x~0.26) independently of the deposition temperature. As the deposition temperature increases, the $Cu_{2-x}Se$ secondary phase gradually fades, the electrical resistivity slightly increases from ~0.2 to ~0.5 Ohm.cm and the carrier concentration slightly decreases from ~$4x10^{19}$ to ~$7x10^{18}$ cm^{-3}, the hole mobility increases from ~0.8 to ~2 $cm^2V^{-1}s^{-1}$ and the energy gap increases from ~1.16 to ~1.21 eV.

In conclusion, stoichiometric films with a minor $Cu_{2-x}Se$ secondary phase, moderate surface roughness, high absorption coefficient (>10^4 cm^{-1}) and high lifetime of the minority carriers (~50ns) are obtained at deposition temperatures 300 - 500 ºC, fluence of 1 J/cm^2 and Ar pressure of 0.01 mbar.

8.2 Optimization of the CIGS/Mo/SLG multi-layer structure

The impact of deposition temperature of CIGS on Mo-coated SLG substrates has been investigated by fabricating the CIGS/Mo/SLG structures at deposition temperatures of 300, 400 and 500ºC. The main results for the optimization of CIGS layer on Mo/SLG are presented here and more details can be found in Chapter 4, section 4.2.

CIGS layers on Mo/SLG were nearly stoichiometric and independent from the deposition temperature. The XRD patterns of CIGS/Mo/SLG structures were identified by the CIGS chalcopyrite phase, the Mo phase and a weak peak of Cu_2Se secondary phase in CIGS layers. There was no evidence of $MoSe_2$ phase at the interface for none of the deposition temperatures. The adhesion tests of CIGS/Mo/SLG structures revealed that the adhesion between CIGS, Mo and SLG was superior for the samples of which CIGS was grown at 300 and 400ºC. On the contrary, delamination occurred for the samples grown at 500ºC. HRTEM image of CIGS/Mo/SLG structure with the CIGS layer deposited at 300ºC revealed a generally smooth interfacial region between Mo and CIGS, with both layers in columnar growth. There was no indication for a $MoSe_2$ distinct phase formation in CIGS layer, even though a small amount of residual Mo inside the CIGS layer is identified. A small percentage of small $Cu_{2-x}Se$ crystallites were detected by means of HRTEM in the CIGS layer. The linearity of the IV curve of CIGS/Mo/SLG structure with the CIGS layer deposited at 300ºC indicates the formation of an ohmic contact at CIGS/Mo interface.

The overall assessment of compositional, structural, morphological and electrical properties of the investigated CIGS films grown on Mo-coated SLG substrates indicates that the best properties of CIGS layer and the CIGS/Mo interface are obtained at the CIGS deposition temperature of 300ºC.

CHRISTIANA NICOLAOU

8.3 Optimization of the CdS layer on SLG

Polycrystalline CdS thin films have been deposited on bare SLG substrates using PLD under various growth conditions. A systematic investigation of laser fluence and deposition temperature has been performed and the films were examined through structural, chemical, and optical characterization. The main results are presented here, and more details can be found in Chapter 5, section 5.1.

The systematic investigation of the impact of fluence on the properties of CdS films revealed that polycrystalline CdS films with hexagonal lattice without the presence of secondary phase are grown at all fluences. Stoichiometric CdS films with high crystallinity are obtained at fluence of 1.1 J/cm^2.

The systematic investigation of the impact of deposition temperature on the properties of CdS films revealed that polycrystalline and stoichiometric films with relatively large crystallites are obtained at deposition temperatures of 200 – 400°C. The band gap energy of the films is red shifted from 2.55 to 2.49 eV as the substrate temperature increases from 100 to 400°C. The PL lifetimes of the PLD-grown CdS films were estimated to be in the range of ~4 to 6 ns, which are longer compared to CdS films fabricated by other deposition techniques.

In conclusion, highly crystalline, single phase, stoichiometric CdS films are obtained at a fluence of 1.1 J/cm^2 and at deposition temperatures of 200 – 400°C.

8.4 Optimization of the CdS/CIGS/Mo/SLG multi-layer structure

CdS/CIGS heterojunctions have been grown using PLD in a sequential deposition of CIGS and CdS layers on Mo-coated SLG substrates. A parametric investigation of CdS deposition temperature has been conducted for the fabrication of CdS/CIGS/Mo/SLG structures, with CdS deposition temperature varying from 20 to 400°C. The main results are presented here, and more details can be found in Chapter 5, section 5.2.

The CdS films are sulfur-poor and become stoichiometric as the deposition temperature of CdS reaches at 300°C. An abrupt decrease of S/Cd is observed at 400°C, where the CdS films become sulfur-deficient again. In addition, at the CdS deposition temperature of 400°C, a secondary phase of $CuInS_2$ phase is formed at the CdS/CIGS interface, most likely due to the interdiffusion of the elements between CIGS and CdS layer. The cross-section SEM image of the CdS/CIGS/Mo/SLG structure, with CdS layer grown at 300°C, revealed that the Mo and CIGS layers are readily observed, exhibiting sharp interfaces, while the layer of CdS is less clearly resolved.

The dark IV curves for the samples grown at a CdS deposition temperature from room temperature up to 400°C revealed the diode-like behavior of the CdS/CIGS junction. As the deposition temperature of CdS increases from room temperature up to 400°C, the knee voltage of the

CHRISTIANA NICOLAOU

IV curve decreases, indicating a decrease of the spike-like potential barrier at CdS/CIGS interface. Low series and high shunt resistances are obtained for the samples where CdS is grown at 200 and 300ºC. In addition, the CdS/CIGS diode grown at CdS deposition temperature of 300ºC exhibits the lowest ideality factor, which is close to 2, indicating the better quality of the diode with less non-idealities.

In conclusion, the best quality CdS/CIGS diodes have been grown at CdS deposition temperatures of 200 and 300ºC, exhibiting low ideality factor, low leakage current, low series and high shunt resistances.

8.5 Optimization of the ZnO layer on SLG

The impact of fluence and deposition temperature on the properties of ZnO films grown on SLG substrates by PLD has been investigated through structural, chemical, and optical characterization. The main results are presented here, and more details can be found in Chapter 6, section 6.1.

The systematic investigation of the impact of fluence on the properties of ZnO films revealed that polycrystalline ZnO films with hexagonal lattice without the presence of secondary phase are obtained, independently of laser fluence. The crystallinity of the films is high for the films deposited at 1.0, 1.2 and 1.4 J/cm^2 and decreases for the film grown at 1.6 J/cm^2. At fluences of 1.4 and 1.6 J/cm^2, the films are subjected to sputtering of the surface, which is counteracting during the deposition and the thickness of the films decreases. The low values of surface roughness, that are slightly increased from 18 to 28 nm with increasing fluence, indicate the high smoothness of ZnO films obtained by PLD.

The systematic investigation of the impact of deposition temperature on the properties of ZnO films revealed the polycrystalline nature of ZnO films with hexagonal structure and no secondary phase, independently of deposition temperature. The crystallite size of the films increases as the deposition temperature increases from room temperature up to 200ºC and then decreases at 300ºC due to the presence of oxygen vacancies in the film. High transparency with transmissivity over than 80% in the visible spectral region is observed in all ZnO films. The energy gap of the films appears to gradually blue shift by as much as 30 meV as deposition temperature drops from to 300ºC to 25ºC.

In conclusion, polycrystalline ZnO films with relatively large crystallites and low roughness without the occurrence of sputtering at the film's surface are obtained at fluence of 1.0 and 1.2 J/cm^2. In addition, the films grown at 200ºC present high crystallinity and high transmittance which are the desirable properties for the ZnO layer in the photovoltaic device.

CHRISTIANA NICOLAOU

8.6 Optimization of the ZnO/CdS/CIGS/Mo/SLG multi-layer structure

A sequential deposition of CIGS, CdS and ZnO layers on Mo-coated SLG substrates was carried out using PLD for the fabrication of ZnO/CdS/CIGS/Mo/SLG structures. A parametric investigation of ZnO deposition temperature has been conducted for the fabrication of ZnO/CdS/CIGS/Mo/SLG structures, with ZnO deposition temperature varying from 50 to 300ºC. The properties of ZnO/CdS/CIGS/Mo/SLG structure grown by PLD has been investigated through structural and electrical characterization. The main results are presented here, and more details can be found in Chapter 6, section 6.2.

The XRD patterns reveal that the existence of the ZnO and CdS hexagonal phase, the chalcopyrite $CuIn_{0.7}Ga_{0.3}Se_2$ phase and the Mo phase with no evidence of secondary phases due to the interdiffusion of the elements between ZnO, CdS and CIGS layers. The ZnO/CdS/CIGS/Mo structures in which the ZnO layer has been deposited at 300, 200 and 100ºC, respectively, exhibit ohmic behavior. A rectifying diode-like behavior is identified only for the structure in which ZnO layer has been deposited at 50ºC. A noticeable reduction of the calculated shunt resistance is observed for the ZnO/CdS/CIGS/Mo structure compared to the value obtained for the CdS/CIGS/Mo structure. Therefore, the optimum temperature of depositing the ZnO layer on CdS/CIGS/Mo/SLG structure is at 50ºC.

8.7 Optimization of the ZnO:Al layer on SLG

Al-doped ZnO (ZnO:Al) films were deposited on SLG substrates by PLD using a polycrystalline ZnO:Al (2 wt% Al doping) target. The deposition of ZnO:Al was carried out using the optimum parameters identified by the optimization of ZnO films. Therefore, the ZnO:Al films were deposited at room temperature and at fluence of 1.2 J/cm^2. The structural, morphological, optical and electrical properties of the PLD-grown ZnO:Al films on SLG substrates have been investigated and the main results are presented here. More details can be found in Chapter 6, section 6.3.

The XRD pattern reveals the absence of any secondary phase and indicates the incorporation Al ions in the lattice of ZnO crystal. The low value of the measured roughness indicates the high smoothness of ZnO:Al film. The band gap energy of the doped ZnO:Al is calculated at 3.36 eV and to blue shift by as much as 30 meV compared to the ZnO film deposited at 25ºC. In addition, high transparency with transmissivity over than 80% in the visible spectral region is observed for the ZnO:Al films. The n-type conductivity of the ZnO:Al film is verified from the Hall measurement.

CHRISTIANA NICOLAOU

8.8 Optimization of the ZnO:Al/ZnO/CdS/CIGS/Mo/SLG multi-layer structure

A sequential deposition of CIGS, CdS, ZnO and ZnO:Al layers on Mo-coated SLG substrates was carried out using PLD for the fabrication of ZnO:Al/ZnO/CdS/CIGS/Mo/SLG structures. A parametric investigation of ZnO deposition temperature has been conducted for the fabrication of ZnO:Al/ZnO/CdS/CIGS/Mo/SLG structures, with ZnO:Al deposition temperature varying from 40 to 300ºC. The properties of ZnO:Al/ZnO/CdS/CIGS/Mo/SLG structure grown by PLD has been investigated through structural and electrical characterization. The main results are presented here, and more details can be found in Chapter 6, section 6.4.

ZnO:Al deposition temperature has a major impact on the structural and electrical properties of the ZnO:Al/ZnO/CdS/CIGS/Mo device. The XRD patterns reveal the existence of the ZnO and CdS hexagonal phase, the chalcopyrite $CuIn_{0.7}Ga_{0.3}Se_2$ phase and the Mo phase. The $CuInS_2$ secondary phase is identified in the XRD patterns obtained for the ZnO:Al/ZnO/CdS/CIGS/Mo/SLG structures with ZnO:Al layer deposited at 100, 200 and 300ºC. The $CuInS_2$ is a result of the interdiffusion of the elements at the CdS/CIGS interface which takes place while reheating the sample from 40ºC to 100, 200 or 300ºC to proceed from the deposition of ZnO layer to ZnO:Al layer. There is no evidence of secondary phases due to the interdiffusion of the elements between the ZnO, CdS and CIGS layers for the ZnO:Al/ZnO/CdS/CIGS/Mo/SLG structure with ZnO:Al layer deposited at 40ºC.

A rectifying diode-like behavior is identified only for the device in which ZnO:Al layer has been deposited at 40ºC, while ohmic behavior is observed for the ZnO:Al/ZnO/CdS/CIGS/Mo devices of which ZnO:Al is deposited at high deposition temperatures (100ºC and higher). The diode-like behaviour of ZnO:Al(40ºC)/ZnO/CdS/CIGS/Mo device corroborates with the clear XRD pattern in which there is no evidence of secondary phases due to the interdiffusion of the elements between ZnO:Al, ZnO, CdS and CIGS layers.

Moreover, the adhesion test of ZnO:Al(40ºC)/ZnO/CdS/CIGS/Mo device demonstrated the superior adhesion between the layers and the substrate. Thus, the optimum temperature of depositing the ZnO:Al layer on ZnO/CdS/CIGS/Mo/SLG structure is at 40ºC.

The interfacial characterization of the ZnO:Al/ZnO/CdS/CIGS/Mo/SLG with CIGS and CdS layers deposited at 300ºC and ZnO and ZnO:Al layers deposited at 40ºC, revealing that the CIGS/CdS and CdS/ZnO interfaces are generally smooth with the CdS/CIGS interface more abrupt and smoother compared to the ZnO/CdS one. The chemical analysis in the CIGS/CdS interfacial region revealed the existence of small quantities of Cu and In inside the CdS layer, however the HRTEM analysis on small crystallites has confirmed the absence of the potential discrete formation of additional phases. In addition, possible Cd or S atoms diffusion inside CIGS has been indicated.

CHRISTIANA NICOLAOU

Regarding the ZnO/CdS interface, there is no indication of extended inter-diffusion of either Zn or O inside the CdS layer. The ZnO:Al – intrinsic ZnO layer exhibits polycrystalline morphology, consisting of numerous crystallites in random orientation. The Al doping was also confirmed in the upper part of the ZnO:Al layer grown on top of the multi-structure.

8.9 Fabrication and optimization of CIGS-based solar cells

The fabrication of the CIGS solar cells was carried out through a sequential deposition of CIGS, CdS, ZnO and ZnO:Al layers on Mo-coated SLG substrates using PLD. The deposition parameters for each layer were selected from the previous investigations of each layer and the adjacent interfaces. After the sequential deposition of CIGS, CdS, ZnO and ZnO:Al layers, the fabrication of the devices was completed by the deposition of Al grid on the surface of ZnO:Al layer. The impact of thickness of CdS layer on the performance of the PLD-grown CIGS solar cells was investigated through structural, morphological, electrical and performance characterization. Moreover, the optimization of the efficiency of the solar cells was achieved by using the SMPLD technique which involved the application of a cone shaped shadow mask during the deposition of CIGS layer. The main results are presented here, and more details can be found in Chapter 7.

The PLD-grown solar cells with varying CdS thicknesses have resulted to ohmic behaviour or very poor performance. Low shunt resistance was identified as one of the primary reasons for the poor performance of these solar cells due to micron-sized particulates on the surface of the CIGS absorber.

In order to improve the performance of the cells, the SMPLD technique has been utilised to eliminate the large particulates on the CIGS layer by using a cone shaped shadow mask during the CIGS layer deposition. An initial SEM study revealed that the particulates on the SMPLD-CIGS surface substantially decrease in number and size along the distance from the centre of the cone.

Next, SMPLD-CIGS films were systematically deposited on SLG substrates with different numbers of pulses. Chemical, structural, morphological and thickness characterisation revealed that the optimum SMPLD-CIGS film was obtained at 90000 pulses. The SMPLD-CIGS film deposited at 90000 pulses exhibits a nearly stoichiometric composition and a structure of crystalline $CuIn_{0.7}Ga_{0.3}Se_2$ chalcopyrite phase with a minor secondary phase of Cu_2Se. Furthermore, a low-roughness film is obtained with thickness of ~400 nm. Specifically, SMPLD-CIGS deposited at 90000 pulses exhibits a surface roughness that is one order of magnitude lower than PLD-CIGS. In addition, the characterisation along the distance from the centre of the SMPLD-CIGS with 90000 pulses revealed that there are no significant variations in chemical composition and surface roughness. However, variations of thickness and energy gap were observed across the lateral.

Finally, SMPLD-CIGS solar cells have been fabricated with low roughness CIGS layers using the SMPLD method. SMPLD-CIGS solar cells achieved greater efficiencies through the

CHRISTIANA NICOLAOU

elimination of shunts due to the smoother surface of CIGS absorber without micron-sized particles. An investigation of the effect of CdS thickness on the efficiency of the SMPLD-CIGS solar cells showed that the SMPLD-CIGS solar cell with CdS layer deposited at 300 pulses produced the highest efficiency of 1.098%.

This work has demonstrated the innovative fabrication of CIGS solar cells using PLD for the sequential growth of the multi-layer CIGS/CdS/ZnO/Al:ZnO stucture and at temperatures not exceeding 300 °C. Despite the low efficiencies of SMPLD-CIGS solar cells, this PhD thesis lays the foundations and provides the framework for fabricating CIGS solar cells using the PLD technology. The performance of CIGS solar cells can be further optimized in several ways, which will be discussed in Chapter 9 as future work.

CHRISTIANA NICOLAOU

Chapter 9 – Future work

As discussed in Chapter 7, CIGS solar cells constructed with the optimum deposition parameters of each layer based on the results of the previous chapters and with varying CdS thickness have resulted to ohmic behaviour or very poor performance (0.025%). Two primary factors were identified for causing large losses in the devices: the excessively large series resistance and the significantly low shunt resistance. In order to increase the shunt resistance of the devices, the SMPLD technique was utilised to eliminate the large particulates on the CIGS layer and the efficiency of the solar cells increased from 0.025% to 1.098%.

The excessive high values of the series resistance in the cells partly derive from the resistance of the individual layers. Therefore, reduction of the resistance of each layer can lead to the reduction of the device series resistance. For example, investigation of PLD conditions such as oxygen pressure and pulses of deposition can lead to further optimization of ZnO layers with lower series resistance, which in turn will improve the performance of the cells.

Moreover, the performance of the PLD-grown CIGS solar cells can be improved through several approaches and here we propose the following:

- An antireflective (AR) coating is required to reduce reflection losses and thus improve the efficiency of the devices. The most widely used material as AR coating in CIGS solar cells is magnesium fluoride (MgF_2). MgF_2 has two important characteristics: low refractive index and the ability of forming high quality films [356]. The thickness of the AR coating is the key feature that must be optimized to optically enhance the performance of the device. Modelling together with experimental results can be jointly used to investigate the effect of the AR coating thickness to the performance of the cell.
- While SMPLD technique succeeded in producing low roughness CIGS layer without the presence of micron-size particles, obtaining larger thicknesses proved challenging due to the shadowing effect. Thus, producing a CIGS layer with thickness close to the required one (~2μm) while retaining a low surface roughness without the formation of particulates using the PLD method can be achieved through the use of ultrafast lasers. New insights and promising results in obtaining atomically smooth surfaces by using ultrafast lasers with high repetition rates [357, 358] suggest that thicker PLD-grown CIGS layers with low surface roughness might be possible with ultrafast lasers. Ultrafast lasers can be also explored for the deposition of the other layers for further optimization of their properties.
- The elimination of variations across the layers can be achieved with the rotation of the substrate. Rotation of the substrate during the sequential deposition of the CIGS, CdS, ZnO and Al:ZnO layers can produce uniform layers without inhomogeneities. Therefore,

CHRISTIANA NICOLAOU

consistent layering between the films and sharper interfaces in the multi-layer structure can be successfully achieved.

- Reduction of shunt currents at the edges of the photovoltaic devices using the edge isolation process. The edge isolation process involves the electrical isolation of the front contact from the rear contact. This is achieved through the construction of an isolation channel using high repetition rate lasers with short pulse duration for the ablation of all layers down to the substrate [359-361].

CHRISTIANA NICOLAOU

Bibliography

[1] Solar Frontier, Solar Frontier Achieves World Record Thin-Film Solar Cell Efficiency of 23.35%, 2019. http://www.solar-frontier.com/eng/news/2019/0117_press.html. (Accessed June 17 2022).

[2] P. Jackson, D. Hariskos, E. Lotter, S. Paetel, R. Wuerz, R. Menner, W. Wischmann, M. Powalla, New world record efficiency for Cu (In, Ga) Se2 thin-film solar cells beyond 20%, Progress in Photovoltaics: Research and Applications 19(7) (2011) 894-897.

[3] C. Nicolaou, A. Zacharia, G. Itskos, J. Giapintzakis, Influence of process parameters on the properties of pulsed laser deposited CuIn0. 7Ga0. 3Se2 thin films, Solar Energy 174 (2018) 793-802.

[4] C. Nicolaou, A. Zacharia, A. Delimitis, G. Itskos, J. Giapintzakis, Single-step growth of high quality CIGS/CdS heterojunctions using pulsed laser deposition, Applied Surface Science 511 (2020) 145547.

[5] European Commission, Renewable energy directive., no date. https://ec.europa.eu/energy/en/topics/renewable-energy/renewable-energy-directive. (Accessed June 11, 2022).

[6] United Nations Climate Change, What is the Kyoto Protocol?, 2022. https://unfccc.int/kyoto_protocol. (Accessed May 11, 2022).

[7] United Nations Climate Change, The Paris Agreement, no date. https://unfccc.int/process-and-meetings/the-paris-agreement/the-paris-agreement. (Accessed 19 August 2022).

[8] D. Ginley, M.A. Green, R. Collins, Solar energy conversion toward 1 terawatt, Mrs Bulletin 33(04) (2008) 355-364.

[9] W. Shockley, H.J. Queisser, Detailed balance limit of efficiency of p-n junction solar cells, Journal of applied physics 32(3) (1961) 510-519.

[10] SolarFrontier, Solar Frontier Achieves World Record Thin-Film Solar Cell Efficiency of 23.35%. http://www.solar-frontier.com/eng/news/2019/0117_press.html , 2019 (accessed 17 January 2019).

[11] P. Jackson, R. Wuerz, D. Hariskos, E. Lotter, W. Witte, M. Powalla, Effects of heavy alkali elements in Cu (In, Ga) Se2 solar cells with efficiencies up to 22.6%, physica status solidi (RRL)-Rapid Research Letters 10(8) (2016) 583-586.

[12] J. Palm, F. Karg, H. Schneider, K. Kushiya, L. Stolt, A. Tiwari, E. Niemi, M. Beck, C. Eberspacher, P. Wohlfart, White paper for CIGS thin film solar cell technology. https://cigs-pv.net (2015).

[13] U. Rau, A. Jasenek, R. Herberholz, H.-W. Schock, J.-F. Guillemoles, D. Lincot, L. Kronink, The inherent stability of Cu (In, Ga) Se2-based solar cells, Proc. 2nd WCPEC, 1998, pp. 428-433.

CHRISTIANA NICOLAOU

[14] B. Dimmler, H. Schock, Scaling-up of CIS technology for thin-film solar modules, Progress in Photovoltaics: Research and Applications 4(6) (1996) 425-433.
[15] B. Dimmler, E. Gross, D. Hariskos, F. Kessler, E. Lotter, M. Powalla, J. Springer, U. Stein, G. Voorwinden, M. Gaeng, CIGS thin film module technology: towards commercialization, Proceedings of the 2nd World Conference and Exhibition on Photovoltaic Energy Conversion, 1998, pp. 419-423.
[16] H. Ullal, K. Zweibel, B.v. Roedern, 26th IEEE PhotoVolt, Spec. Conf, 1997.
[17] A. Shah, P. Torres, R. Tscharner, N. Wyrsch, H. Keppner, Photovoltaic technology: the case for thin-film solar cells, science 285(5428) (1999) 692-698.
[18] D. Wang, M. Wright, N.K. Elumalai, A. Uddin, Stability of perovskite solar cells, Solar Energy Materials and Solar Cells 147 (2016) 255-275.
[19] S.S. Dipta, A. Uddin, Stability Issues of Perovskite Solar Cells: A Critical Review, Energy Technology 9(11) (2021) 2100560.
[20] J. Guillemoles, The puzzle of Cu (In, Ga) Se2 (CIGS) solar cells stability, Thin Solid Films 403 (2002) 405-409.
[21] H.W. Schock, R. Noufi, CIGS-based solar cells for the next millennium, Progress in Photovoltaics: Research and Applications 8(1) (2000) 151-160.
[22] T. Solar, TSMC Solar Commercial-size Modules (1.09m2) Set CIGS 16.5% Efficiency Record, 2015.
[23] A. Chirilă, D. Guettler, P. Bloesch, S. Nishiwaki, S. Seyrling, S. Buecheler, R. Verma, F. Pianezzi, Y. Romanyuk, G. Bilger, Optimization of composition grading in Cu (In, Ga) Se2 for flexible solar cells and modules, Photovoltaic Specialists Conference (PVSC), 2010 35th IEEE, IEEE, 2010, pp. 000656-000660.
[24] A. Chirilă, S. Buecheler, F. Pianezzi, P. Bloesch, C. Gretener, A.R. Uhl, C. Fella, L. Kranz, J. Perrenoud, S. Seyrling, Highly efficient Cu (In, Ga) Se2 solar cells grown on flexible polymer films, Nature materials 10(11) (2011) 857-861.
[25] J.H. Scofield, A. Duda, D. Albin, B. Ballard, P. Predecki, Sputtered molybdenum bilayer back contact for copper indium diselenide-based polycrystalline thin-film solar cells, Thin solid films 260(1) (1995) 26-31.
[26] E. Moons, T. Engelhard, D. Cahen, Ohmic contacts to p-CuInSe 2 crystals, Journal of Electronic Materials 22(3) (1993) 275-280.
[27] K. Orgassa, H.W. Schock, J. Werner, Alternative back contact materials for thin film Cu (In, Ga) Se2 solar cells, Thin Solid Films 431 (2003) 387-391.
[28] G. Gordillo, M. Grizalez, L. Hernandez, Structural and electrical properties of DC sputtered molybdenum films, Solar energy materials and solar cells 51(3) (1998) 327-337.
[29] M. Martınez, C. Guillén, Effect of rf-sputtered Mo substrate on the microstructure of electrodeposited CuInSe 2 thin films, Surface and Coatings Technology 110(1) (1998) 62-67.

CHRISTIANA NICOLAOU

[30] J. Hedstrom, H. Ohlsen, M. Bodegârd, A. Kylner, L. Stolt, D. Hariskos, M. Ruckh, H.-W. Schock, ZnO/CdS/Cu (In, Ga) Se/sub 2/thin film solar cells with improved performance, Photovoltaic Specialists Conference, 1993., Conference Record of the Twenty Third IEEE, IEEE, 1993, pp. 364-371.
[31] X.H. Tan, S.L. Ye, B. Fan, K. Tang, X. Liu, Effects of Na incorporated at different periods of deposition on Cu (In, Ga) Se 2 films, Applied optics 49(16) (2010) 3071-3074.
[32] S. Raud, M.-A. Nicolet, Study of the CuInSe2/Mo thin film contact stability, Thin Solid Films 201(2) (1991) 361-371.
[33] N. Kohara, S. Nishiwaki, Y. Hashimoto, T. Negami, T. Wada, Electrical properties of the Cu (In, Ga) Se 2/MoSe 2/Mo structure, Solar Energy Materials and Solar Cells 67(1) (2001) 209-215.
[34] K.-J. Hsiao, J.-D. Liu, H.-H. Hsieh, T.-S. Jiang, Electrical impact of MoSe 2 on CIGS thin-film solar cells, Physical Chemistry Chemical Physics 15(41) (2013) 18174-18178.
[35] T. Wada, N. Kohara, S. Nishiwaki, T. Negami, Characterization of the Cu (In, Ga) Se 2/Mo interface in CIGS solar cells, Thin Solid Films 387(1) (2001) 118-122.
[36] K.H. Ong, R. Agileswari, B. Maniscalco, P. Arnou, C.C. Kumar, J.W. Bowers, M.B. Marsadek, Review on substrate and molybdenum back contact in CIGS thin film solar cell, International Journal of Photoenergy 2018 (2018).
[37] W.N. Shafarman, J. Zhu, Effect of substrate temperature and depostion profile on evaporated Cu (InGa) Se 2 films and devices, Thin Solid Films 361 (2000) 473-477.
[38] A.M. Gabor, J.R. Tuttle, D.S. Albin, M.A. Contreras, R. Noufi, A.M. Hermann, High-efficiency CuIn x Ga1− x Se2 solar cells made from (In x, Ga1− x) 2Se3 precursor films, Applied Physics Letters 65(2) (1994) 198-200.
[39] R. Gay, M. Dietrich, C. Fredric, C. Jensen, K. Knapp, D. Tarrant, D. Willett, Efficiency and process improvements in CuInSe2-based modules, Proc. 12th European Photovoltaic Solar Energy Conference, Amsterdam, The Netherlands, 1994, pp. 935-938.
[40] F. Kurdesau, M. Kaelin, V. Zalesski, V. Kovalewsky, In situ resistivity measurements of Cu–In thin films during their selenization, Journal of alloys and compounds 378(1) (2004) 298-301.
[41] B. Keyes, P. Dippo, J. AbuShama, R. Noufi, Cu (In, Ga) Se2 Thin-Film Evolution During Growth-A Photoluminescence Study: Preprint, National Renewable Energy Lab., Golden, CO.(US), 2002.
[42] R. Ortega-Borges, D. Lincot, Mechanism of Chemical Bath Deposition of Cadmium Sulfide Thin Films in the Ammonia-Thiourea System In Situ Kinetic Study and Modelization, Journal of the Electrochemical Society 140(12) (1993) 3464-3473.
[43] G. Hodes, Chemical solution deposition of semiconductor films, CRC press2002.
[44] W. Witte, S. Spiering, D. Hariskos, Substitution of the CdS buffer layer in CIGS thin-film solar cells: Status of current research and record cell efficiencies, Vakuum in Forschung und Praxis 26(1) (2014) 23-27.

CHRISTIANA NICOLAOU

[45] N. Naghavi, D. Abou-Ras, N. Allsop, N. Barreau, S. Bücheler, A. Ennaoui, C.H. Fischer, C. Guillen, D. Hariskos, J. Herrero, Buffer layers and transparent conducting oxides for chalcopyrite Cu (In, Ga)(S, Se) 2 based thin film photovoltaics: present status and current developments, Progress in Photovoltaics: Research and Applications 18(6) (2010) 411-433.
[46] T. Nakada, M. Mizutani, 18% efficiency Cd-free Cu (In, Ga) Se2 thin-film solar cells fabricated using chemical bath deposition (CBD)-ZnS buffer layers, Japanese Journal of Applied Physics 41(2B) (2002) L165.
[47] T. Negami, Y. Hashimoto, S. Nishiwaki, Cu (In, Ga) Se 2 thin-film solar cells with an efficiency of 18%, Solar energy materials and solar cells 67(1) (2001) 331-335.
[48] T. Negami, T. Satoh, Y. Hashimoto, S. Shimakawa, S. Hayashi, M. Muro, H. Inoue, M. Kitagawa, Production technology for CIGS thin film solar cells, Thin Solid Films 403 (2002) 197-203.
[49] M.A. Contreras, B. Egaas, K. Ramanathan, J. Hiltner, A. Swartzlander, F. Hasoon, R. Noufi, Progress toward 20% efficiency in Cu (In, Ga) Se2 polycrystalline thin-film solar cells, Progress in Photovoltaics: Research and applications 7(4) (1999) 311-316.
[50] X. Wu, High-efficiency polycrystalline CdTe thin-film solar cells, Solar energy 77(6) (2004) 803-814.
[51] U. Rau, M. Schmidt, Electronic properties of ZnO/CdS/Cu (In, Ga) Se 2 solar cells—aspects of heterojunction formation, Thin Solid Films 387(1) (2001) 141-146.
[52] G. Rajan, K. Aryal, T. Ashrafee, S. Karki, A.-R. Ibdah, V. Ranjan, R.W. Collins, S. Marsillac, Optimization of anti-reflective coatings for CIGS solar cells via real time spectroscopic ellipsometry, Photovoltaic Specialist Conference (PVSC), 2015 IEEE 42nd, IEEE, 2015, pp. 1-4.
[53] J. van Deelen, C. Frijters, M. Suijlen, M. Barink, Influence of the grid and cell design on the power output of thin film Cu (InGa) Se 2 cells, Thin Solid Films 594 (2015) 225-231.
[54] Y. Li, S. Yang, X. Zhang, X. Xiao, Optimal design of a CIGS module grid, MRS Online Proceedings Library Archive 1315 (2011).
[55] I. Repins, S. Glynn, J. Duenow, T.J. Coutts, W.K. Metzger, M.A. Contreras, Required material properties for high-efficiency CIGS modules, SPIE Solar Energy+ Technology, International Society for Optics and Photonics, 2009, pp. 74090M-74090M-14.
[56] J. Schou, Physical aspects of the pulsed laser deposition technique: The stoichiometric transfer of material from target to film, Applied Surface Science 255(10) (2009) 5191-5198.
[57] D.H. Blank, M. Dekkers, G. Rijnders, Pulsed laser deposition in Twente: from research tool towards industrial deposition, Journal of physics D: applied physics 47(3) (2013) 034006.
[58] B. Li, J. Liu, G. Xu, R. Lu, L. Feng, J. Wu, Development of pulsed laser deposition for CdS/CdTe thin film solar cells, Applied Physics Letters 101(15) (2012) 153903.
[59] H.M. Christen, G. Eres, Recent advances in pulsed-laser deposition of complex oxides, Journal of Physics: Condensed Matter 20(26) (2008) 264005.

CHRISTIANA NICOLAOU

[60] A.-E. Becquerel, Recherches sur les effets de la radiation chimique de la lumiere solaire au moyen des courants electriques, CR Acad. Sci 9(145) (1839) 1.
[61] R.J. Komp, Practical photovoltaics: electricity from solar cells, aatec publications Ann Arbor, MI1995.
[62] R. Hill, M.D. Archer, Clean electricity from photovoltaics, Imperial College Press2001.
[63] B.G. Streetman, S. Banerjee, Solid state electronic devices, 6th ed., Prentice Hall, New Jersey, 2009.
[64] D.A. Neamen, Semiconductor physics and devices: basic principles, 4th ed., McGraw-Hill2012.
[65] K. Gupta, N. Gupta, Recent Advances in Semiconducting Materials and Devices, Advanced Semiconducting Materials and Devices (2016) 531-562.
[66] A. Morales-Acevedo, Solar cells: Research and application perspectives, BoD–Books on Demand2013.
[67] J. Nelson, The physics of solar cells, World Scientific Publishing Co Inc2003.
[68] M. Hädrich, C. Kraft, H. Metzner, U. Reislöhner, C. Löffler, W. Witthuhn, Formation of CdSxTe1–x at the p-n junction of CdS-CdTe solar cells, physica status solidi c 6(5) (2009) 1257-1260.
[69] C.B.Honsberg, S.G.Bowden, Photovoltaics Education Website, 2019. https://www.pveducation.org.
[70] P. Hersch, K. Zweibel, Basic photovoltaic principles and methods, 1982, Solar Energy Research Inst., Golden, CO (USA).
[71] L.L. Kazmerski, Solar photovoltaics R&D at the tipping point: A 2005 technology overview, Journal of electron spectroscopy and related phenomena 150(2-3) (2006) 105-135.
[72] P. Hersch, K. Zweibel, Basic photovoltaic principles and methods, Solar Energy Research Inst., Golden, CO (USA), 1982.
[73] R. Wittmann, Miniaturization Problems in CMOS Technology: Investigation of Doping Profiles and Reliability, Faculty of Electrical Engineering and Information Technology, Technical University of Vienna, 2007.
[74] P. Vivek, N. Muthuselvan, J. Nanadhagopal, Modeling of Solar PV System for DC-DC Converter with improved voltage stability Using Hybrid-Optimization Techniques, International Conference for Phoenixes on Emerging Current Trends in Engineering and Management (PECTEAM 2018), Atlantis Press, 2018, pp. 187-192.
[75] M.-D. Gerngroß, J. Reverey, CIS/CIGS based Thin-film solar cells, Faculty of Engineering University of Kiel (2008).
[76] T. Meyer, Reversible Relaxationsphänomene imelektrischen Transport von Cu (In, Ga) Se2, Universität Oldenburg, 1999.

CHRISTIANA NICOLAOU

[77] H. Sim, J. Lee, S. Cho, E.-S. Cho, S.J. Kwon, A study on the band structure of ZnO/CdS heterojunction for CIGS solar-cell application, JSTS: Journal of Semiconductor Technology and Science 15(2) (2015) 267-275.
[78] M. Gloeckler, J. Sites, Efficiency limitations for wide-band-gap chalcopyrite solar cells, Thin Solid Films 480 (2005) 241-245.
[79] T. Ericson, J.J. Scragg, A. Hultqvist, J.T. Wätjen, P. Szaniawski, T. Törndahl, C. Platzer-Björkman, Zn (O, S) buffer layers and thickness variations of CdS buffer for Cu2ZnSnS4 solar cells, IEEE Journal of Photovoltaics 4(1) (2013) 465-469.
[80] A.O. Pudov, Impact of Secondary Barriers on CuIn1-xGaxSe2 Solar-Cell Operation, Colorado State University, 2005.
[81] J. Pou, F. Lusquiños, R. Comesaña, M. Boutinguiza, Production of biomaterial coatings by laser-assisted processes, Advances in Laser Materials Processing, Elsevier2010, pp. 394-425.
[82] J. Huang, X. Gao, J.L. MacManus-Driscoll, H. Wang, Ferroelectric thin films and nanostructures: current and future, Nanostructures in Ferroelectric Films for Energy Applications, Elsevier2019, pp. 19-39.
[83] J. Schou, Laser Beam-Solid Interactions: Fundamental Aspects, in: Y. Pauleau (Ed.), Materials surface processing by directed energy techniques, Elsevier, Amsterdam 2006.
[84] J. Schou, S. Amoruso, J.G. Lunney, Plume dynamics, in: C.R. Phipps (Ed.), Laser Ablation and its Applications, Springer2007, pp. 67-95.
[85] D.H. Lowndes, Laser ablation and desorption, in: J.C. Miller, R.F. Haglund (Eds.), Experimental Methods in the Physical Sciences, Academic Press New York, 1998.
[86] R. Kelly, A. Miotello, Mechanisms of pulsed laser sputtering, Pulsed laser deposition of thin films (1994) 55-85.
[87] P. Willmott, J. Huber, Pulsed laser vaporization and deposition, Reviews of Modern Physics 72(1) (2000) 315.
[88] R. Eason, Pulsed laser deposition of thin films: applications-led growth of functional materials, John Wiley & Sons2007.
[89] T.E. Itina, J. Hermann, P. Delaporte, M. Sentis, Laser-generated plasma plume expansion: Combined continuous-microscopic modeling, Physical Review E 66(6) (2002) 066406.
[90] D.B. Geohegan, A.A. Puretzky, Dynamics of laser ablation plume penetration through low pressure background gases, Applied Physics Letters 67(2) (1995) 197-199.
[91] S. Amoruso, A. Sambri, X. Wang, Propagation dynamics of a La Mn O 3 laser ablation plume in an oxygen atmosphere, Journal of applied physics 100(1) (2006) 013302.
[92] J. Siegel, G. Epurescu, A. Perea, F.J. Gordillo-Vázquez, J. Gonzalo, C.N. Afonso, Temporally and spectrally resolved imaging of laser-induced plasmas, Optics letters 29(19) (2004) 2228-2230.
[93] D. Geohegan, Diagnostics and characteristics of laser-produced plasmas, Pulsed Laser Deposition of Thin Films (1994).

CHRISTIANA NICOLAOU

[94] J. Schou, Fundamentals of laser-assisted fabrication of inorganic and organic films, in: A.K. Vaseashta, I.N. Mihailescu (Eds.), Functionalized nanoscale materials, devices and systems, Springer Science & Business Media2008.

[95] Y.B. Zel'Dovich, Y.P. Raizer, Physics of shock waves and high-temperature hydrodynamic phenomena, Courier Corporation2002.

[96] S. Anisimov, D. Bäuerle, B. Luk'Yanchuk, Gas dynamics and film profiles in pulsed-laser deposition of materials, Physical Review B 48(16) (1993) 12076.

[97] R.K. Singh, J. Narayan, Pulsed-laser evaporation technique for deposition of thin films: Physics and theoretical model, Physical review B 41(13) (1990) 8843.

[98] S. Amoruso, R. Bruzzese, N. Spinelli, R. Velotta, M. Vitiello, X. Wang, Dynamics of laser-ablated MgB 2 plasma expanding in argon probed by optical emission spectroscopy, Physical Review B 67(22) (2003) 224503.

[99] S. Amoruso, B. Toftmann, J. Schou, Thermalization of a UV laser ablation plume in a background gas: From a directed to a diffusionlike flow, Physical Review E 69(5) (2004) 056403.

[100] H. Le, D. Zeitoun, J. Parisse, M. Sentis, W. Marine, Modeling of gas dynamics for a laser-generated plasma: Propagation into low-pressure gases, Physical Review E 62(3) (2000) 4152.

[101] Y. Nakata, W.K. Kumuduni, T. Okada, M. Maeda, Two-dimensional laser-induced fluorescence imaging of non-emissive species in pulsed-laser deposition process of YBa2Cu3O7−x, Applied physics letters 66(23) (1995) 3206-3208.

[102] S. Amoruso, J. Schou, J.G. Lunney, Influence of the atomic mass of the background gas on laser ablation plume propagation, Applied Physics A 92(4) (2008) 907-911.

[103] S. Amoruso, B. Toftmann, J. Schou, Broadening and attenuation of UV laser ablation plumes in background gases, Applied surface science 248(1-4) (2005) 323-328.

[104] J.S. Horwitz, J.A. Sprague, Film nucleation and film growth in: D.B. Chrisey, G.H. Hubler (Eds.), Pulsed Laser Deposition of Thin Films, John Wiley & Sons, New York, 1994, pp. 229-254.

[105] B. Thestrup, B. Toftmann, J. Schou, B. Doggett, J. Lunney, A comparison of the laser plume from Cu and YBCO studied with ion probes, Applied Surface Science 208 (2003) 33-38.

[106] D.L. Smith, Thin Film Deposition—Principles and Practice, McGraw-Hill, New York, 1994.

[107] J.M. Warrender, M.J. Aziz, Kinetic energy effects on morphology evolution during pulsed laser deposition of metal-on-insulator films, Physical Review B 75(8) (2007) 085433.

[108] D.B. Chrisey, G.K. Hubler, Pulsed laser deposition of thin films, John Wiley & Sons, New York 1994.

[109] M.N. Ashfold, F. Claeyssens, G.M. Fuge, S.J. Henley, Pulsed laser ablation and deposition of thin films, Chemical Society Reviews 33(1) (2004) 23-31.

[110] H.-U. Krebs, M. Weisheit, J. Faupel, E. Süske, T. Scharf, C. Fuhse, M. Störmer, K. Sturm, M. Seibt, H. Kijewski, Pulsed laser deposition (PLD)--a versatile thin film technique, Advances in Solid State Physics (2003) 505-518.

CHRISTIANA NICOLAOU

[111] C.W. Schneider, T. Lippert, Laser ablation and thin film deposition, Laser processing of materials, Springer2010, pp. 89-112.
[112] A.O. Gonzalez-Posada, PHYSICAL PROCESSES IN PULSED LASER DEPOSITION, ETH ZURICH, 2016.
[113] I.V. Tudose, F. Comanescu, P. Pascariu, S. Bucur, L. Rusen, F. Iacomi, E. Koudoumas, M.P. Suchea, Chemical and physical methods for multifunctional nanostructured interface fabrication, Functional Nanostructured Interfaces for Environmental and Biomedical Applications (2019) 15-26.
[114] V. Dinca, M. Suchea, Functional nanostructured interfaces for environmental and biomedical applications, Elsevier2019.
[115] R. Hippler, Fundamentals of Plasma Chemistry, in: B. Bederson, H. Walther (Eds.), Advances in atomic, molecular, and optical physics, Elsevier2000.
[116] J. Musil, J. Vlcek, P. Baroch, Magnetron discharges for thin films plasma processing, Materials Surface Processing by Directed Energy Techniques 1 (2006) 67-110.
[117] A. Kashin, V. Ananikov, A SEM study of nanosized metal films and metal nanoparticles obtained by magnetron sputtering, Russian Chemical Bulletin 60(12) (2011) 2602-2607.
[118] R.J. Martín-Palma, A. Lakhtakia, Vapor-deposition techniques, Engineered Biomimicry, Elsevier Inc.2013, pp. 383-398.
[119] W. Gao, Z. Li, N. Sammes, An introduction to electronic materials for engineers, 2nd ed., World Scientific, River Edge, NJ, USA, 2011.
[120] A. Adeyeye, G. Shimon, Magnetism of Surfaces, Interfaces, and Nanoscale Materials. Handbook of Surface Science, Amsterdam: Elsevier, 2015.
[121] M. Birkholz, Thin Film Analysis by X-Ray Scattering, John Wiley & Sons, Weinheim, 2006.
[122] B.L. Dutrow, C.M. Clark, X-ray Powder Diffraction (XRD), 2022. https://serc.carleton.edu/research_education/geochemsheets/techniques/XRD.html. (Accessed January 25, 2022).
[123] R. Nave, Bragg's Law, no date. http://hyperphysics.phy-astr.gsu.edu/hbase/quantum/bragg.html. (Accessed January 26, 2022).
[124] Rigaku, Grazing Incidence X-Ray Diffraction (GIXRD) Analysis Of Thin Film Material, 2022. https://www.rigaku.com/applications/bytes/xrd/ultima-iv/388427460. (Accessed January 26, 2022).
[125] J. Goldstein, Practical scanning electron microscopy: electron and ion microprobe analysis, Springer Science & Business Media2012.
[126] D. Brabazon, A. Raffer, Advanced characterization techniques for nanostructures, in: W. Ahmed, M.J. Jackson (Eds.), Emerging nanotechnologies for manufacturing, William Andrew Publishing, Boston, 2015, pp. 53-85.
[127] G. McMahon, Analytical instrumentation: a guide to laboratory, portable and miniaturized instruments, John Wiley & Sons2008.

CHRISTIANA NICOLAOU

[128] A. Alyamani, O. Lemine, FE-SEM characterization of some nanomaterial, in: V. Kazmiruk (Ed.), Scanning electron microscopy, InTech, London 2012.
[129] D. Bondeson, Biopolymer-based nanocomposites: Processing and properties, Department of engineering design and materials Norwegian University of Science and Technology, Trondheim, 2007.
[130] J.I. Goldstein, D.E. Newbury, P. Echlin, D.C. Joy, A.D. RomigJr, C.E. Lyman, C. Fiori, E. Lifshin, Scanning Electron Microscopy and X-Ray Microanalysis. A Text for Biologists, Materials Scientists, and Geologists, 2nd ed., Plenum Press, New York, 1992.
[131] K. Havancsák, High-Resolution Scanning Electron Microscopy, no date. http://www.technoorg.hu/news-and-events/articles/high-resolution-scanning-electron-microscopy-1. (Accessed January 22, 2022).
[132] R.D. Holbrook, A.A. Galyean, J.M. Gorham, A. Herzing, J. Pettibone, Overview of nanomaterial characterization and metrology, in: M. Baalousha, J.R. Lead (Eds.), Characterization of Nanomaterials in Complex Environmental and Biological Media, Elsevier, Amsterdam, 2015, pp. 47-87.
[133] V.D. Scott, G. Love, Quantitative Electron Probe Microanalysis, 2nd ed., Ellis Horwood, Chichester, 1994.
[134] S. Yesilkir-Baydar, O.N. Oztel, R. Cakir-Koc, A. Candayan, Evaluation techniques, in: M. Razavi, A. Thakor (Eds.), Nanobiomaterials Science, Development and Evaluation, Woodhead publishing2017, pp. 211-232.
[135] S.K. Sharma, D.S. Verma, L.U. Khan, S. Kumar, S.B. Khan, Handbook of materials characterization, Springer2018.
[136] A. Yacoot, L. Koenders, Aspects of scanning force microscope probes and their effects on dimensional measurement, Journal of Physics D: Applied Physics 41(10) (2008) 103001.
[137] ClipartPanda.com, 53 images Microscope Diagram And Functions, 2020. http://www.clipartpanda.com/categories/microscope-diagram-and-functions.
[138] ip.com, Improved 'Scotch Tape Test' for Adhesion Measurement, 2007. https://priorart.ip.com/IPCOM/000152224.
[139] L. Pauw, A method of measuring specific resistivity and Hall effect of discs of arbitrary shape, Philips Research Reports 13(1) (1958) 1-9.
[140] L.J. van der Pauw, A method of measuring the resistivity and Hall coefficient on lamellae of arbitrary shape, Philips technical review 20 (1958) 220-224.
[141] E.H. Hall, On a new action of the magnet on electric currents, American Journal of Mathematics 2(3) (1879) 287-292.
[142] R. Nave, Hall Effect, no date. http://hyperphysics.phy-astr.gsu.edu/hbase/magnetic/Hall.html.
[143] S. Stricker, The Hall Effect and its Applications, Advances in Electronics and Electron Physics, Elsevier1968, pp. 97-143.

CHRISTIANA NICOLAOU

[144] D. King, B. Hansen, J. Kratochvil, M. Quintana, Dark current-voltage measurements on photovoltaic modules as a diagnostic or manufacturing tool, Conference Record of the Twenty Sixth IEEE Photovoltaic Specialists Conference-1997, IEEE, 1997, pp. 1125-1128.
[145] Y. Javed, K. Ali, K. Akhtar, M.I. Hussain, G. Ahmad, T. Arif, TEM for atomic-scale study: Fundamental, instrumentation, and applications in nanotechnology, in: S.K. Sharma, D.S. Verma, L.U. Khan, S. Kumar, S.B. Khan (Eds.), Handbook of materials characterization, Springer, New York, 2018, pp. 147-216.
[146] D.C. Joy, S. Bradbury, B.J. Ford, transmission electron microscope (TEM), Encyclopedia Britannica, 2019.
[147] J.S. Kim, T. LaGrange, B.W. Reed, M.L. Taheri, M.R. Armstrong, W.E. King, N.D. Browning, G.H. Campbell, Imaging of transient structures using nanosecond in situ TEM, Science 321(5895) (2008) 1472-1475.
[148] E. Betzig, G.H. Patterson, R. Sougrat, O.W. Lindwasser, S. Olenych, J.S. Bonifacino, M.W. Davidson, J. Lippincott-Schwartz, H.F. Hess, Imaging intracellular fluorescent proteins at nanometer resolution, science 313(5793) (2006) 1642-1645.
[149] B. Corain, G. Schmid, N. Toshima, Metal nanoclusters in catalysis and materials science: the issue of size control, Elsevier2011.
[150] Z. Wang, Transmission electron microscopy of shape-controlled nanocrystals and their assemblies, ACS Publications, 2000, pp. 1153-1175.
[151] Wikipedia, Absorption (electromagnetic radiation, no date. https://en.wikipedia.org/wiki/Absorption_(electromagnetic_radiation).
[152] A. Li, EXCITATION OF PHOTOLUMINESCENCE, 2003. https://ned.ipac.caltech.edu/level5/Sept03/Li/Li4.html.
[153] Warwick Department of Physics, Photoluminescence, 2011. https://warwick.ac.uk/fac/sci/physics/current/postgraduate/regs/mpagswarwick/ex5/techniques/optical/pl/].
[154] HORIBA, Time-Resolved Fluorescence Technical Note TRFT-4. Time-resolved emission spectra / decay associated spectra, no date.
[155] A. Krishnan, Interpreting Current-Voltage Curves of Different Materials, 2017. https://www.allaboutcircuits.com/technical-articles/interpreting-current-voltage-curves-of-different-materials.
[156] A. Romeo, M. Terheggen, D. Abou-Ras, D. Bätzner, F.J. Haug, M. Kälin, D. Rudmann, A. Tiwari, Development of thin-film Cu (In, Ga) Se2 and CdTe solar cells, Progress in Photovoltaics: Research and Applications 12(2-3) (2004) 93-111.
[157] F. Kang, J. Ao, G. Sun, Q. He, Y. Sun, Properties of CuInxGa1− xSe2 thin films grown from electrodeposited precursors with different levels of selenium content, Current Applied Physics 10(3) (2010) 886-888.

CHRISTIANA NICOLAOU

[158] M. Marudachalam, R. Birkmire, H. Hichri, J. Schultz, A. Swartzlander, M. Al-Jassim, Phases, morphology, and diffusion in CuIn x Ga 1− x Se 2 thin films, Journal of Applied Physics 82(6) (1997) 2896-2905.

[159] L. Zhang, F.-f. Liu, F.-y. Li, Q. He, B.-z. Li, C.-j. Li, Structural, optical and electrical properties of low-temperature deposition Cu (InxGa1− x) Se2 thin films, Solar Energy Materials and Solar Cells 99 (2012) 356-361.

[160] L. Zhang, Q. He, W.-L. Jiang, F.-F. Liu, C.-J. Li, Y. Sun, Effects of substrate temperature on the structural and electrical properties of Cu (In, Ga) Se2 thin films, Solar Energy Materials and Solar Cells 93(1) (2009) 114-118.

[161] Z. Yu, Y. Yan, S. Li, Y. Zhang, C. Yan, L. Liu, Y. Zhang, Y. Zhao, Significant effect of substrate temperature on the phase structure, optical and electrical properties of RF sputtered CIGS films, Applied Surface Science 264 (2013) 197-201.

[162] J. Liu, D.-M. Zhuang, M.-J. Cao, C.-Y. Wang, M. Xie, X.-L. Li, Preparation and characterization of Cu (In, Ga) Se2 thin films by selenization of Cu0. 8Ga0. 2 and In2Se3 precursor films, International Journal of Photoenergy 2012 (2012).

[163] Y. Yan, S. Li, Y. Ou, Y. Ji, C. Yan, L. Liu, Z. Yu, Y. Zhao, Structure and properties of CIGS films based on one-stage RF-sputtering process at low substrate temperature, Journal of Modern Transportation 22(1) (2014) 37-44.

[164] J. Levoska, S. Leppävuori, F. Wang, O. Kusmartseva, A. Hill, E. Ahmed, R. Tomlinson, R. Pilkington, Pulsed laser ablation deposition of CuInSe2 and CuIn1-x GaxSe2 thin films, Physica Scripta 1994(T54) (1994) 244.

[165] A. Kindyak, V. Kindyak, V. Gremenok, Energy-gap variations in thin laser-deposited Cu (In, Ga) Se2 films, Materials Letters 28(4-6) (1996) 273-275.

[166] Y.H. Jo, B.C. Mohanty, Y.S. Cho, Crystallization and surface segregation in CuIn0. 7Ga0. 3Se2 thin films on Cu foils grown by pulsed laser deposition, Applied Surface Science 256(22) (2010a) 6819-6823.

[167] Y.H. Jo, B.C. Mohanty, Y.S. Cho, Enhanced electrical properties of pulsed laser-deposited CuIn0. 7Ga0. 3Se2 thin films via processing control, Solar Energy 84(12) (2010b) 2213-2218.

[168] M.G. Tsai, H.T. Tung, I.G. Chen, C.C. Chen, Y.F. Wu, X. Qi, Y. Hwu, C.Y. Lin, P.H. Wu, C.W. Cheng, Annealing effect on the properties of Cu (In0. 7Ga0. 3) Se2 thin films grown by femtosecond pulsed laser deposition, Journal of the American Ceramic Society 96(8) (2013) 2419-2423.

[169] T. Klinkert, B. Theys, G. Patriarche, M. Jubault, F. Donsanti, J.-F. Guillemoles, D. Lincot, New insights into the Mo/Cu (In, Ga) Se2 interface in thin film solar cells: Formation and properties of the MoSe2 interfacial layer, The Journal of chemical physics 145(15) (2016) 154702.

[170] R.J. Matson, K.A. Emery, R.E. Bird, Terrestrial solar spectra, solar simulation and solar cell short-circuit current calibration: a review, Solar cells 11(2) (1984) 105-145.

CHRISTIANA NICOLAOU

[171] P. Russell, O. Jamjoum, R. Ahrenkiel, L. Kazmerski, R. Mickelsen, W. Chen, Properties of the Mo-CuInSe2 interface, Applied Physics Letters 40(11) (1982) 995-997.
[172] T. Wada, N. Kohara, S. Nishiwaki, T. Negami, Characterization of the Cu (In, Ga) Se2/Mo interface in CIGS solar cells, Thin Solid Films 387(1-2) (2001) 118-122.
[173] M. Bär, S. Nishiwaki, L. Weinhardt, S. Pookpanratana, W. Shafarman, C. Heske, Electronic level alignment at the deeply buried absorber/Mo interface in chalcopyrite-based thin film solar cells, Applied Physics Letters 93(4) (2008) 042110.
[174] L. Assmann, J. Bernede, A. Drici, C. Amory, E. Halgand, M. Morsli, Study of the Mo thin films and Mo/CIGS interface properties, Applied Surface Science 246(1-3) (2005) 159-166.
[175] D.A. Keszler, J.F. Wager, Novel Materials Development for Polycrystalline Thin-Film Solar Cells: Final Subcontract Report, 26 July 2004--15 June 2008, National Renewable Energy Lab.(NREL), Golden, CO (United States), 2008.
[176] T. Wada, N. Kohara, T.N.T. Negami, M.N.M. Nishitani, Chemical and structural characterization of Cu (In, Ga) Se2/Mo interface in Cu (In, Ga) Se2 solar cells, Japanese Journal of Applied Physics 35(10A) (1996) L1253.
[177] S.N.S. Nishiwaki, N.K.N. Kohara, T.N.T. Negami, T.W.T. Wada, MoSe 2 layer formation at Cu (In, Ga) Se 2/Mo Interfaces in High Efficiency Cu (In1-xGa x) Se 2 Solar Cells, Japanese Journal of Applied Physics 37(1A) (1998) L71.
[178] D. Abou-Ras, G. Kostorz, D. Bremaud, M. Kälin, F. Kurdesau, A. Tiwari, M. Döbeli, Formation and characterisation of MoSe2 for Cu (In, Ga) Se2 based solar cells, Thin Solid Films 480 (2005) 433-438.
[179] P.B. James, M. Lavik, The crystal structure of MoSe2, Acta Crystallographica 16(11) (1963) 1183-1183.
[180] M. Fox, Optical properties of solids, Oxford university press2010.
[181] M. Contreras, K. Ramanathan, J. AbuShama, F. Hasoon, J. Keane, D. Young, B. Egaas, R. Noufi, Diode characteristics in state-of-the-art ZnO, CdS/Cu (In1− xGax Se2 solar cells. Prog. Photovolt. Res. Appl. 2005, 13, 209–216 (2005).
[182] A. Cazzaniga, A. Crovetto, C. Yan, K. Sun, X. Hao, J.R. Estelrich, S. Canulescu, E. Stamate, N. Pryds, O. Hansen, Ultra-thin Cu2ZnSnS4 solar cell by pulsed laser deposition, Solar Energy Materials and Solar Cells 166 (2017) 91-99.
[183] S. Rampino, F. Bissoli, E. Gilioli, F. Pattini, Growth of Cu (In, Ga) Se2 thin films by a novel single-stage route based on pulsed electron deposition, Progress in Photovoltaics: Research and Applications 21(4) (2013) 588-594.
[184] F. Pattini, M. Bronzoni, F. Mezzadri, F. Bissoli, E. Gilioli, S. Rampino, Dynamics of evaporation from CuGaSe2 targets in pulsed electron deposition technique, Journal of Physics D: Applied Physics 46(24) (2013) 245101.
[185] K. Ito, T. Nakazawa, Electrical and optical properties of stannite-type quaternary semiconductor thin films, Japanese Journal of Applied Physics 27(11R) (1988) 2094.

CHRISTIANA NICOLAOU

[186] D.B. Chrisey, G.K. Hubler, Pulsed laser deposition of thin films, Chapter 3, Wiley - Intersience1994a.
[187] D.B. Chrisey, G.K. Hubler, Pulsed laser deposition of thin films, Chapter 5, Wiley - Intersience1994b.
[188] R. Wood, K. Chen, J. Leboeuf, A. Puretzky, D. Geohegan, Dynamics of plume propagation and splitting during pulsed-laser ablation, Physical Review Letters 79(8) (1997) 1571.
[189] H.M. Urbassek, D. Sibold, Gas-phase segregation effects in pulsed laser desorption from binary targets, Physical review letters 70(12) (1993) 1886.
[190] D.B. Chrisey, G.K. Hubler, Pulsed laser deposition of thin films, Chapter 6, Wiley - Intersience1994c.
[191] G. Padam, The properties of chemically deposited Cu2− xSe thin films, Thin Solid Films 150(1) (1987) L89-L92.
[192] A. Voskanyan, P. Inglizyan, S. Lalykin, I. Plyutto, Y.M. Shevchenko, Fiz. Tekh. Poluprovodn, Soviet Physics: Semiconductors 12(11) (1978) 2096.
[193] S. Zhang, S.-H. Wei, A. Zunger, H. Katayama-Yoshida, Defect physics of the CuInSe 2 chalcopyrite semiconductor, Physical Review B 57(16) (1998) 9642.
[194] C.-Y. Hsu, P.-C. Huang, Y.-Y. Chen, D.-C. Wen, Fabrication of a Cu (InGa) Se2 thin film photovoltaic absorber by rapid thermal annealing of CuGa/In precursors coated with a Se layer, International Journal of Photoenergy 2013 (2013).
[195] D.W. Niles, K. Ramanathan, F. Hasoon, R. Noufi, B.J. Tielsch, J.E. Fulghum, Na impurity chemistry in photovoltaic CIGS thin films: Investigation with x-ray photoelectron spectroscopy, Journal of Vacuum Science & Technology A: Vacuum, Surfaces, and Films 15(6) (1997) 3044-3049.
[196] L. Kronik, D. Cahen, H.W. Schock, Effects of sodium on polycrystalline Cu (In, Ga) Se2 and its solar cell performance, Advanced Materials 10(1) (1998) 31-36.
[197] S.-H. Wei, S. Zhang, A. Zunger, Effects of Na on the electrical and structural properties of CuInSe 2, Journal of Applied Physics 85(10) (1999) 7214-7218.
[198] D.W. Niles, M. Al-Jassim, K. Ramanathan, Direct observation of Na and O impurities at grain surfaces of CuInSe 2 thin films, Journal of Vacuum Science & Technology A: Vacuum, Surfaces, and Films 17(1) (1999) 291-296.
[199] M.B. Ård, K. Granath, L. Stolt, Growth of Cu (In, Ga) Se2 thin films by coevaporation using alkaline precursors, Thin Solid Films 361 (2000) 9-16.
[200] D. Rudmann, G. Bilger, M. Kaelin, F.-J. Haug, H. Zogg, A. Tiwari, Effects of NaF coevaporation on structural properties of Cu (In, Ga) Se2 thin films, Thin Solid Films 431 (2003) 37-40.
[201] G. Bauer, R. Brüggemann, S. Tardon, S. Vignoli, R. Kniese, Quasi-Fermi level splitting and identification of recombination losses from room temperature luminescence in Cu (In1− xGax) Se2 thin films versus optical band gap, Thin Solid Films 480 (2005) 410-414.

CHRISTIANA NICOLAOU

[202] S.-C. Chen, D.-H. Hsieh, H. Jiang, Y.-K. Liao, F.-I. Lai, C.-H. Chen, C.W. Luo, J.-Y. Juang, Y.-L. Chueh, K.-H. Wu, Growth and characterization of Cu (In, Ga) Se 2 thin films by nanosecond and femtosecond pulsed laser deposition, Nanoscale research letters 9(1) (2014) 280.
[203] C.-C. Chen, X. Qi, W.-C. Chang, M.-G. Tsai, I.-G. Chen, C.-Y. Lin, P.-H. Wu, K.-P. Chang, The effects of pulse repetition rate on the structural, optical, and electrical properties of CIGS films grown by pulsed laser deposition, Applied Surface Science 351 (2015) 772-778.
[204] C. Sima, O. Toma, Influence of temperature on the CuIn1-xGaxSe2films deposited by picosecond laser ablation, Applied Surface Science 425 (2017) 1028-1032.
[205] S. Theodoropoulou, D. Papadimitriou, A. Mamalis, D. Manolakos, R. Klenk, M.-C. Lux-Steiner, Band-gap energies and strain effects in CuIn1− xGaxS2 based solar cells, Semiconductor science and technology 22(8) (2007) 933.
[206] M. Maiberg, T. Hölscher, E. Jarzembowski, S. Hartnauer, S. Zahedi-Azad, W. Fränzel, R. Scheer, Verification of minority carrier traps in Cu (In, Ga) Se2 and Cu2ZnSnSe4 by means of time-resolved photoluminescence, Thin Solid Films 633 (2017) 208-212.
[207] M. Maiberg, T. Hölscher, S. Zahedi-Azad, W. Fränzel, R. Scheer, Investigation of long lifetimes in Cu (In, Ga) Se2 by time-resolved photoluminescence, Applied Physics Letters 107(12) (2015) 122104.
[208] W. Metzger, I. Repins, M. Romero, P. Dippo, M. Contreras, R. Noufi, D. Levi, Recombination kinetics and stability in polycrystalline Cu (In, Ga) Se2 solar cells, Thin Solid Films 517(7) (2009) 2360-2364.
[209] I. Repins, S. Glynn, J. Duenow, T.J. Coutts, W.K. Metzger, M.A. Contreras, Required material properties for high-efficiency CIGS modules, Thin Film Solar Technology, SPIE, 2009, pp. 156-169.
[210] U.P. Singh, S.P. Patra, Progress in Polycrystalline Thin-Film Cu (In, Ga) Solar Cells, International Journal of Photoenergy 2010 (2010).
[211] C. Ballif, H. Moutinho, F. Hasoon, R. Dhere, M. Al-Jassim, Cross-sectional atomic force microscopy imaging of polycrystalline thin films, Ultramicroscopy 85(2) (2000) 61-71.
[212] A. Reinders, P. Verlinden, W. Van Sark, A. Freundlich, Photovoltaic solar energy: from fundamentals to applications, John Wiley & Sons2017.
[213] S.M. Karazi, I.U. Ahad, K.Y. Benyounis, Laser Micromachining for Transparent Materials, Reference Module in Materials Science and Materials Engineering (2017).
[214] N. Kohara, S. Nishiwaki, Y. Hashimoto, T. Negami, T. Wada, Electrical properties of the cu (in, ga) se2/MoSe2/mo structure, Solar Energy Materials and Solar Cells 67(1-4) (2001) 209-215.
[215] A. Oliva, O. Solıs-Canto, R. Castro-Rodrıguez, P. Quintana, Formation of the band gap energy on CdS thin films growth by two different techniques, Thin solid films 391(1) (2001) 28-35.
[216] J. Wang, M. Isshiki, Wide-bandgap II–VI semiconductors: growth and properties, Springer handbook of electronic and photonic materials (2007) 325-342.

CHRISTIANA NICOLAOU

[217] R. Klenk, Characterisation and modelling of chalcopyrite solar cells, Thin solid films 387(1-2) (2001) 135-140.
[218] A. Chirilă, P. Reinhard, F. Pianezzi, P. Bloesch, A.R. Uhl, C. Fella, L. Kranz, D. Keller, C. Gretener, H. Hagendorfer, Potassium-induced surface modification of Cu (In, Ga) Se 2 thin films for high-efficiency solar cells, Nature materials 12(12) (2013) 1107.
[219] P. Jackson, D. Hariskos, E. Lotter, S. Paetel, R. Wuerz, R. Menner, W. Wischmann, M. Powalla, Prog. Photovolt: Res. App. 19, 894–897 (2011).
[220] I. Repins, M. Contreras, B. Egaas, C. DeHart, J. Scharf, C. Perkins, B. To, R. Noufi, 19.9% efficient Cu (In, Ga) Se2-based thin–film solar cells," Prog. Photovolt: Res. Appl. 16(3) (2008) 235-239.
[221] A. Romeo, R. Gysel, S. Buzzi, D. Abou-Ras, D. Bätzner, D. Rudmann, H. Zogg, A. Tiwari, Properties of CIGS solar cells developed with evaporated II–VI buffer layers, Technical Digest of the 14th International Photovoltaic Science and Engineering Conference, Bangkok, Thailand, 2004.
[222] M. Rusu, T. Glatzel, C.A. Kaufmann, A. Neisser, S. Siebentritt, S. Sadewasser, T. Schedel-Niedrig, M.C. Lux-Steiner, High-efficient ZnO/PVD-CdS/Cu (In, Ga) Se 2 thin film solar cells: formation of the buffer-absorber interface and transport properties, MRS Online Proceedings Library Archive 865 (2005).
[223] D. Abou-Ras, G. Kostorz, A. Romeo, D. Rudmann, A. Tiwari, Structural and chemical investigations of CBD-and PVD-CdS buffer layers and interfaces in Cu (In, Ga) Se2-based thin film solar cells, Thin Solid Films 480 (2005) 118-123.
[224] J. Kessler, M. Ruckh, D. Hariskos, U. Ruhle, R. Menner, H. Schock, Interface engineering between CuInSe/sub 2/and ZnO, Conference Record of the Twenty Third IEEE Photovoltaic Specialists Conference-1993 (Cat. No. 93CH3283-9), IEEE, 1993, pp. 447-452.
[225] T. Negami, T. Aoyagi, T. Satoh, S.-i. Shimakawa, S. Hayashi, Y. Haskimoto, Cd free CIGS solar cells fabricated by dry processes, Conference Record of the Twenty-Ninth IEEE Photovoltaic Specialists Conference, 2002., IEEE, 2002, pp. 656-659.
[226] M.M. Islam, S. Ishizuka, A. Yamada, K. Sakurai, S. Niki, T. Sakurai, K. Akimoto, CIGS solar cell with MBE-grown ZnS buffer layer, Solar energy materials and solar cells 93(6-7) (2009) 970-972.
[227] R. Sáez-Araoz, A. Ennaoui, T. Kropp, E. Veryaeva, T. Niesen, M.C. Lux-Steiner, Use of different Zn precursors for the deposition of Zn (S, O) buffer layers by chemical bath for chalcopyrite based Cd-free thin-film solar cells, physica status solidi (a) 205(10) (2008) 2330-2334.
[228] A. Hultqvist, C. Platzer-Björkman, J. Pettersson, T. Törndahl, M. Edoff, CuGaSe2 solar cells using atomic layer deposited Zn (O, S) and (Zn, Mg) O buffer layers, Thin Solid Films 517(7) (2009) 2305-2308.
[229] A.J. Nelson, C. Schwerdtfeger, S.H. Wei, A. Zunger, D. Rioux, R. Patel, H. Höchst, Theoretical and experimental studies of the ZnSe/CuInSe2 heterojunction band offset, Applied Physics Letters 62(20) (1993) 2557-2559.

CHRISTIANA NICOLAOU

[230] N. Hernandez-Como, V. Martinez-Landeros, I. Mejia, F. Aguirre-Tostado, C. Nascimento, G.d.M. Azevedo, C. Krug, M. Quevedo-Lopez, Defect control in room temperature deposited cadmium sulfide thin films by pulsed laser deposition, Thin Solid Films 550 (2014) 665-668.
[231] X. Tong, D. Jiang, Y. Li, Z. Liu, M. Luo, Femtosecond pulsed laser deposition of CdS thin films onto quartz substrates, physica status solidi (a) 203(8) (2006) 1992-1998.
[232] H. Kwok, J. Zheng, S. Witanachchi, P. Mattocks, L. Shi, Q. Ying, X. Wang, D. Shaw, Growth of highly oriented CdS thin films by laser-evaporation deposition, Applied physics letters 52(13) (1988) 1095-1097.
[233] B. Ullrich, H. Sakai, Y. Segawa, Optoelectronic properties of thin film CdS formed by ultraviolet and infrared pulsed-laser deposition, Thin Solid Films 385(1-2) (2001) 220-224.
[234] X. Tong, D. Jiang, Z. Liu, M. Luo, Y. Li, P. Lu, G. Yang, H. Long, Structural characterization of CdS thin film on quartz formed by femtosecond pulsed laser deposition at high temperature, Thin Solid Films 516(8) (2008) 2003-2008.
[235] X. Tong, D. Jiang, W. Hu, Z. Liu, M. Luo, The comparison between CdS thin films grown on Si (111) substrate and quartz substrate by femtosecond pulsed laser deposition, Applied Physics A 84(1-2) (2006) 143-148.
[236] V. Senthamilselvi, K. Saravanakumar, R. Anandhi, A. Ravichandran, K. Ravichandran, Effect of annealing on the stoichiometry of CdS films deposited by SILAR technique, Optoelectronics and Advanced Materials-Rapid Communications 5(10) (2011) 1072-1077.
[237] K. Tu, J. Mayer, L. Feldman, Thin film science for electrical engineers and materials scientists, Wiley Publ., NY, 1992.
[238] S. Pandya, K. Raval, Investigation of structural, morphological and optical properties of cadmium sulphide (CdS) thin films at different Cd/S concentration deposited by chemical technique, Journal of Materials Science: Materials in Electronics 28(23) (2017) 18031-18039.
[239] S. Yu, L. Ding, C. Xue, L. Chen, W. Zhang, Transparent conducting Sb-doped SnO2 thin films grown by pulsed laser deposition, Journal of Non-Crystalline Solids 358(23) (2012) 3137-3140.
[240] J.-L. Zhao, X.-M. Li, J.-M. Bian, W.-D. Yu, X.-D. Gao, Structural, optical and electrical properties of ZnO films grown by pulsed laser deposition (PLD), Journal of Crystal Growth 276(3-4) (2005) 507-512.
[241] Z. Zhang, F. Zhou, X. Wei, M. Liu, G. Sun, C. Chen, C. Xue, H. Zhuang, B. Man, Effects of oxygen pressures on pulsed laser deposition of ZnO films, Physica E: Low-dimensional Systems and Nanostructures 39(2) (2007) 253-257.
[242] L. Sun, J. He, Y. Chen, F. Yue, P. Yang, J. Chu, Comparative study on Cu2ZnSnS4 thin films deposited by sputtering and pulsed laser deposition from a single quaternary sulfide target, Journal of Crystal Growth 361 (2012) 147-151.

CHRISTIANA NICOLAOU

[243] S. Vanalakar, G. Agawane, S.W. Shin, M. Suryawanshi, K. Gurav, K. Jeon, P. Patil, C. Jeong, J. Kim, J. Kim, A review on pulsed laser deposited CZTS thin films for solar cell applications, Journal of Alloys and Compounds 619 (2015) 109-121.
[244] G. Perna, V. Capozzi, M. Ambrico, V. Augelli, T. Ligonzo, A. Minafra, L. Schiavulli, M. Pallara, Structural and optical characterization of undoped and indium-doped CdS films grown by pulsed laser deposition, Thin Solid Films 453 (2004) 187-194.
[245] J.-C. Orlianges, C. Champeaux, P. Dutheil, A. Catherinot, T.M. Mejean, Structural, electrical and optical properties of carbon-doped CdS thin films prepared by pulsed-laser deposition, Thin Solid Films 519(21) (2011) 7611-7614.
[246] K. Acharya, J. Skuza, R. Lukaszew, C. Liyanage, B. Ullrich, CdS thin films formed on flexible plastic substrates by pulsed-laser deposition, Journal of Physics: Condensed Matter 19(19) (2007) 196221.
[247] M. Arif, Z.R. Khan, V. Gupta, A. Singh, Effect of substrates temperature on structural and optical properties of thermally evaporated CdS nanocrystalline thin films, (2014).
[248] J.K. Cooper, J. Cao, J.Z. Zhang, Exciton dynamics of CdS thin films produced by chemical bath deposition and DC pulse sputtering, ACS applied materials & interfaces 5(15) (2013) 7544-7551.
[249] A. Klein, T. Löher, Y. Tomm, C. Pettenkofer, W. Jaegermann, Band lineup between CdS and ultra high vacuum-cleaved CuInS 2 single crystals, Applied physics letters 70(10) (1997) 1299-1301.
[250] Y. Hashimoto, K. Takeuchi, K. Ito, Band alignment at CdS/CuInS2 heterojunction, Applied physics letters 67(7) (1995) 980-982.
[251] R. Scheer, I. Luck, H. Lewerenz, 12th European Photovoltaic Solar Energy Conference, Amsterdam, 1994.
[252] H. Sim, J. Lee, S. Cho, E.-S. Cho, S.J. Kwon, A study on the band structure of ZnO/CdS heterojunction for CIGS solar-cell application, Journal of Semiconductor Technology and Science 15(2) (2015) 267-275.
[253] PVLighthouse, Equivalent Circuit Calculator. https://www.pvlighthouse.com.au , 2019 (accessed 10 September 2019).
[254] O. Breitenstein, P. Altermatt, K. Ramspeck, A. Schenk, The origin of ideality factors n> 2 of shunts and surfaces in the dark IV curves of Si solar cells, Proceedings of the 21st European photovoltaic solar energy conference, Citeseer, 2006, pp. 625-628.
[255] W. Shockley, W. Read Jr, Statistics of the recombinations of holes and electrons, Physical review 87(5) (1952) 835.
[256] O. Breitenstein, J. Rakotoniaina, M.H. Al Rifai, M. Werner, Shunt types in crystalline silicon solar cells, Progress in Photovoltaics: Research and Applications 12(7) (2004) 529-538.
[257] J.J. Wysocki, Effect of series resistance on photovoltaic solar energy conversion, RCA Rev. 22(1) (1961).

CHRISTIANA NICOLAOU

[258] M. Wolf, Limitations and possibilities for improvement of photovoltaic solar energy converters: Part I: Considerations for earth's surface operation, Proceedings of the IRE 48(7) (1960) 1246-1263.
[259] M. Langenkamp, O. Breitenstein, Classification of shunting mechanisms in crystalline silicon solar cells, Solar energy materials and solar cells 72(1-4) (2002) 433-440.
[260] A. Ashour, N. El-Kadry, S. Mahmoud, On the electrical and optical properties of CdS films thermally deposited by a modified source, Thin solid films 269(1-2) (1995) 117-120.
[261] A. Hasnat, J. Podder, Optical and electrical characteristics of pure CdS thin films for different thickness, Journal of Bangladesh Academy of Sciences 37(1) (2013) 33-41.
[262] C. Santiago Tepantlán, A. Pérez González, I. Valeriano Arreola, Structural, optical and electrical properties of CdS thin films obtained by spray pyrolysis, Revista mexicana de física 54(2) (2008) 112-117.
[263] L.L. Baranowski, P. Zawadzki, S. Lany, E.S. Toberer, A. Zakutayev, A review of defects and disorder in multinary tetrahedrally bonded semiconductors, Semiconductor Science and Technology 31(12) (2016) 123004.
[264] C. Stephan, S. Schorr, M. Tovar, H.-W. Schock, Comprehensive insights into point defect and defect cluster formation in CuInSe 2, Applied Physics Letters 98(9) (2011) 091906.
[265] R. Noufi, R. Axton, C. Herrington, S. Deb, Electronic properties versus composition of thin films of CuInSe2, Applied Physics Letters 45(6) (1984) 668-670.
[266] F. Gemain, I.C. Robin, S. Renet, S. Bernardi, Photoluminescence studies of CdS layers for solar cells, physica status solidi c 9(8-9) (2012) 1740-1743.
[267] J. Aguilar-Hernandez, G. Contreras-Puente, A. Morales-Acevedo, O. Vigil-Galan, F. Cruz-Gandarilla, J. Vidal-Larramendi, A. Escamilla-Esquivel, H. Hernandez-Contreras, M. Hesiquio-Garduno, A. Arias-Carbajal, Photoluminescence and structural properties of cadmium sulphide thin films grown by different techniques, Semiconductor science and technology 18(2) (2002) 111.
[268] J. Jaffe, A. Zunger, Electronic structure of the ternary chalcopyrite semiconductors CuAl S 2, CuGa S 2, CuIn S 2, CuAl Se 2, CuGa Se 2, and CuIn Se 2, Physical Review B 28(10) (1983) 5822.
[269] J. Jaffe, A. Zunger, Anion displacements and the band-gap anomaly in ternary AB C 2 chalcopyrite semiconductors, Physical Review B 27(8) (1983) 5176.
[270] Y. Wu, H. Lin, C. Sun, M. Yang, H. Hwang, On the growth of CuInS2 thin films by three-source evaporation, Thin Solid Films 168(1) (1989) 113-122.
[271] L. Kazmerski, M. Ayyagari, G. Sanborn, CuInS2 thin films: Preparation and properties, Journal of Applied Physics 46(11) (1975) 4865-4869.
[272] W. Lee, R. Dwivedi, C. Hong, H.W. Kim, N. Cho, C. Lee, Enhancement of the electrical properties of Al-doped ZnO films deposited on ZnO-buffered glass substrates by using an ultrathin aluminum underlayer, Journal of materials science 43(3) (2008) 1159-1161.

CHRISTIANA NICOLAOU

[273] S. Adachi, Properties of semiconductor alloys: group-IV, III-V and II-VI semiconductors, John Wiley & Sons2009.
[274] V.A. Coleman, C. Jagadish, Basic properties and applications of ZnO, Zinc oxide bulk, thin films and nanostructures, Elsevier2006, pp. 1-20.
[275] D.C. Look, J.W. Hemsky, J. Sizelove, Residual native shallow donor in ZnO, Physical review letters 82(12) (1999) 2552.
[276] B. Jin, S. Bae, S. Lee, S. Im, Effects of native defects on optical and electrical properties of ZnO prepared by pulsed laser deposition, Materials Science and Engineering: B 71(1-3) (2000) 301-305.
[277] D.M. Hofmann, A. Hofstaetter, F. Leiter, H. Zhou, F. Henecker, B.K. Meyer, S.B. Orlinskii, J. Schmidt, P.G. Baranov, Hydrogen: a relevant shallow donor in zinc oxide, Physical Review Letters 88(4) (2002) 045504.
[278] C.G. Van De Walle, Strategies for Controlling the Conductivity of Wide-Band-Gap Semiconductors, physica status solidi (b) 229(1) (2002) 221-228.
[279] A.R. Hutson, Hall effect studies of doped zinc oxide single crystals, Physical review 108(2) (1957) 222.
[280] M. Caglar, S. Ilican, Y. Caglar, F. Yakuphanoglu, The effects of Al doping on the optical constants of ZnO thin films prepared by spray pyrolysis method, Journal of Materials Science: Materials in Electronics 19(8) (2008) 704-708.
[281] T. Negami, Y. Hashimoto, S. Nishiwaki, Cu (In, Ga) Se2 thin-film solar cells with an efficiency of 18%, Solar Energy Materials and Solar Cells 67(1-4) (2001) 331-335.
[282] A. Shimizu, S. Chaisitsak, T. Sugiyama, A. Yamada, M. Konagai, Zinc-based buffer layer in the Cu (InGa) Se2 thin film solar cells, Thin Solid Films 361 (2000) 193-197.
[283] U. Rau, M. Schmidt, Electronic properties of ZnO/CdS/Cu (In, Ga) Se2 solar cells—aspects of heterojunction formation, Thin Solid Films 387(1-2) (2001) 141-146.
[284] H.T. Bekman, K. Benoist, J. Joppe, Post-deposition annealing of RF-sputtered zinc-oxide films, Applied surface science 70 (1993) 347-350.
[285] A. Banerjee, D. Wolf, J. Yang, S. Guha, High-rate (∼ 50-Å/s) deposition of ZnO films for amorphous silicon alloy solar-cell back-reflector application, Journal of applied physics 70(3) (1991) 1692-1694.
[286] J. Hu, R.G. Gordon, Textured aluminum-doped zinc oxide thin films from atmospheric pressure chemical-vapor deposition, Journal of Applied Physics 71(2) (1992) 880-890.
[287] W. Tang, D. Cameron, Aluminum-doped zinc oxide transparent conductors deposited by the sol-gel process, Thin solid films 238(1) (1994) 83-87.
[288] M.d.l.L. Olvera, A. Maldonado, R. Asomoza, M. Konagai, M. Asomoza, Growth of textured ZnO: In thin films by chemical spray deposition, Thin Solid Films 229(2) (1993) 196-200.
[289] Y. Manabe, T. Mitsuyu, Zinc oxide thin films prepared by the electron-cyclotron-resonance plasma sputtering method, Japanese journal of applied physics 29(2R) (1990) 334.

CHRISTIANA NICOLAOU

[290] L. Bahadur, T.N. Rao, J. Pandey, Extension of the spectral response of sprayed ZnO thin film electrodes induced by nickel and cobalt doping, Semiconductor science and technology 9(3) (1994) 275.
[291] F. Quaranta, A. Valentini, F.R. Rizzi, G. Casamassima, Dual-ion-beam sputter deposition of ZnO films, Journal of Applied Physics 74(1) (1993) 244-248.
[292] M. Ruckh, D. Hariskos, U. Ruhle, H. Schock, R. Menner, B. Dimmler, Applications of ZnO in Cu (In, Ga) Se/sub 2/solar cells, Conference Record of the Twenty Fifth IEEE Photovoltaic Specialists Conference-1996, IEEE, 1996, pp. 825-828.
[293] R. Groenen, J. Linden, H. Van Lierop, D. Schram, A. Kuypers, M. Van De Sanden, An expanding thermal plasma for deposition of surface textured ZnO: Al with focus on thin film solar cell applications, Applied Surface Science 173(1-2) (2001) 40-43.
[294] J. Narayan, P. Tiwari, K. Jagannadham, O. Holland, Formation of epitaxial and textured platinum films on ceramics-(100) MgO single crystals by pulsed laser deposition, Applied physics letters 64(16) (1994) 2093-2095.
[295] R. Ramesh, T. Sands, V. Keramidas, D. Fork, Epitaxial ferroelectric thin films for memory applications, Materials Science and Engineering: B 22(2-3) (1994) 283-289.
[296] A. Taabouche, M. BOUAFIA, C. BENAZZOUZ, T. Kerdja, Y. BOUACHIBA, S. MENAKH, F. HANINI, F. KERMICHE, A. BOUABELLOU, S. Amara, Effect of Substrates on the Properties of ZnO ThinFilms Grown by Pulsed Laser Deposition, Advances in Materials Physics and Chemistry 3 (2013) 209-213.
[297] S.L. King, J.G. Gardeniers, I.W. Boyd, Pulsed-laser deposited ZnO for device applications, Applied surface science 96 (1996) 811-818.
[298] V. Craciun, J. Elders, a.J. Gardeniers, I.W. Boyd, Characteristics of high quality ZnO thin films deposited by pulsed laser deposition, Applied physics letters 65(23) (1994) 2963-2965.
[299] Y. Lu, H. Ni, Z. Mai, Z. Ren, The effects of thermal annealing on ZnO thin films grown by pulsed laser deposition, Journal of Applied Physics 88(1) (2000) 498-502.
[300] F. Shan, Y. Yu, Band gap energy of pure and Al-doped ZnO thin films, Journal of the European Ceramic Society 24(6) (2004) 1869-1872.
[301] K. Matsubara, P. Fons, K. Iwata, A. Yamada, K. Sakurai, H. Tampo, S. Niki, ZnO transparent conducting films deposited by pulsed laser deposition for solar cell applications, Thin Solid Films 431 (2003) 369-372.
[302] R. Shukla, A. Srivastava, A. Srivastava, K. Dubey, Growth of transparent conducting nanocrystalline Al doped ZnO thin films by pulsed laser deposition, Journal of Crystal Growth 294(2) (2006) 427-431.
[303] Y. Liu, J. Lian, Optical and electrical properties of aluminum-doped ZnO thin films grown by pulsed laser deposition, Applied Surface Science 253(7) (2007) 3727-3730.
[304] T.N. Hansen, J.r. Schou, J.G. Lunney, Angle-resolved energy distributions of laser ablated silver ions in vacuum, Applied physics letters 72(15) (1998) 1829-1831.

CHRISTIANA NICOLAOU

[305] H.H. Andersen, H.L. Bay, Sputtering yield measurements, in: R. Behrisch (Ed.), Sputtering by particle bombardment I, Springer, Berlin-Heidelberg, 1981, pp. 145-218.
[306] W. Eckstein, Sputtering yields, in: R. Behrisch, W. Eckstein (Eds.), Sputtering by particle bombardment, Springer, Berlin-Heidelberg, 2007, pp. 33-187.
[307] L. Zhao, J. Lian, Y. Liu, Q. Jiang, Structural and optical properties of ZnO thin films deposited on quartz glass by pulsed laser deposition, Applied surface science 252(24) (2006) 8451-8455.
[308] A. Zawadzka, P. Płóciennik, Y. El Kouari, H. Bougharraf, B. Sahraoui, Linear and nonlinear optical properties of ZnO thin films deposited by pulsed laser deposition, Journal of Luminescence 169 (2016) 483-491.
[309] J.-L. Zhao, X.-M. Li, J.-M. Bian, W.-D. Yu, C.-Y. Zhang, Comparison of structural and photoluminescence properties of ZnO thin films grown by pulsed laser deposition and ultrasonic spray pyrolysis, Thin Solid Films 515(4) (2006) 1763-1766.
[310] V. Gupta, A. Mansingh, Influence of postdeposition annealing on the structural and optical properties of sputtered zinc oxide film, Journal of applied Physics 80(2) (1996) 1063-1073.
[311] K.C. Park, D.Y. Ma, K.H. Kim, The physical properties of Al-doped zinc oxide films prepared by RF magnetron sputtering, Thin solid films 305(1-2) (1997) 201-209.
[312] A.A. Al-Ghamdi, O.A. Al-Hartomy, M. El Okr, A. Nawar, S. El-Gazzar, F. El-Tantawy, F. Yakuphanoglu, Semiconducting properties of Al doped ZnO thin films, Spectrochimica Acta Part A: Molecular and Biomolecular Spectroscopy 131 (2014) 512-517.
[313] J. Mass, P. Bhattacharya, R. Katiyar, Effect of high substrate temperature on Al-doped ZnO thin films grown by pulsed laser deposition, Materials Science and Engineering: B 103(1) (2003) 9-15.
[314] H. Kim, J. Horwitz, S. Qadri, D. Chrisey, Epitaxial growth of Al-doped ZnO thin films grown by pulsed laser deposition, Thin solid films 420 (2002) 107-111.
[315] H. Kim, J. Horwitz, W. Kim, A. Mäkinen, Z. Kafafi, D. Chrisey, Doped ZnO thin films as anode materials for organic light-emitting diodes, Thin solid films 420 (2002) 539-543.
[316] H. Bayhan, A.S. Kavasoğlu, Tunnelling enhanced recombination in polycrystalline CdS/CdTe and CdS/Cu (In, Ga) Se2 heterojunction solar cells, Solid-state electronics 49(6) (2005) 991-996.
[317] H. Bayhan, Study of CdS/Cu (In, Ga) Se2 interface by using n values extracted analytically from experimental data, Solar energy 83(3) (2009) 372-376.
[318] A. Eltayyan, A new method to extract the electrical parameters from dark IV: T experimental data of Cds/Cu (In, Ga) Se2 interface, Int. J. Adv. Res. Phys. Sci.(IJARPS) 2 (2015) 11-20.
[319] U. Rau, A. Jasenek, H. Schock, F. Engelhardt, T. Meyer, Electronic loss mechanisms in chalcopyrite based heterojunction solar cells, Thin Solid Films 361 (2000) 298-302.

CHRISTIANA NICOLAOU

[320] V. Nadenau, U. Rau, A. Jasenek, H. Schock, Electronic properties of CuGaSe 2-based heterojunction solar cells. Part I. Transport analysis, Journal of Applied Physics 87(1) (2000) 584-593.
[321] M. Wolf, H. Rauschenbach, Series resistance effects on solar cell measurements, Advanced energy conversion 3(2) (1963) 455-479.
[322] J.S. Stein, S. McCaslin, C.W. Hansen, W.E. Boyson, C.D. Robinson, Measuring PV system series resistance without full IV curves, 2014 IEEE 40th Photovoltaic Specialist Conference (PVSC), IEEE, 2014, pp. 2032-2036.
[323] K.R. McIntosh, C.B. Honsberg, The influence of edge recombination on a solar cell's IV curve, Proc. 16th PVSEC, Glasgow, 2000, pp. 1651-1654.
[324] T. McMahon, T. Basso, S. Rummel, Cell shunt resistance and photovoltaic module performance, Conference Record of the Twenty Fifth IEEE Photovoltaic Specialists Conference-1996, IEEE, 1996, pp. 1291-1294.
[325] M. Abbott, T. Trupke, H. Hartmann, R. Gupta, O. Breitenstein, Laser isolation of shunted regions in industrial solar cells, Progress in Photovoltaics: Research and Applications 15(7) (2007) 613-620.
[326] D.R. Norton, Pulsed Laser Deposition of Complex Materials: Progress Towards Applications, in: R. Eason (Ed.), Pulsed laser deposition of thin films: applications-led growth of functional materials, John Wiley & Sons2007, p. 1.
[327] V.Y. Fominski, S. Grigoriev, A. Gnedovets, R. Romanov, M. Volosova, Plume propagation and Pt film growth during shadow-masked pulsed laser deposition in a buffer Ar gas, Nuclear Instruments and Methods in Physics Research Section B: Beam Interactions with Materials and Atoms 343 (2015) 52-61.
[328] V.Y. Fominski, S. Grigoriev, A. Gnedovets, R. Romanov, Pulsed laser deposition of composite Mo–Se–Ni–C coatings using standard and shadow mask configuration, Surface and Coatings Technology 206(24) (2012) 5046-5054.
[329] S. Vanalakar, G. Agawane, S. Shin, M. Suryawanshi, K. Gurav, K. Jeon, P. Patil, C. Jeong, J. Kim, J. Kim, A review on pulsed laser deposited CZTS thin films for solar cell applications, Journal of Alloys and Compounds 619 (2015) 109-121.
[330] E. Pechen, A. Varlashkin, S. Krasnosvobodtsev, B. Brunner, K. Renk, Pulsed-laser deposition of smooth high-T c superconducting films using a synchronous velocity filter, Applied physics letters 66(17) (1995) 2292-2294.
[331] B. Holzapfel, B. Roas, L. Schultz, P. Bauer, G. Saemann-Ischenko, Off-axis laser deposition of YBa2Cu3O7− δ thin films, Applied Physics Letters 61(26) (1992) 3178-3180.
[332] Z. Trajanovic, S. Choopun, R. Sharma, T. Venkatesan, Stoichiometry and thickness variation of YBa 2 Cu 3 O 7− x in pulsed laser deposition with a shadow mask, Applied physics letters 70(25) (1997) 3461-3463.

CHRISTIANA NICOLAOU

[333] A. Gorbunoff, Cross-beam PLD: metastable film structures from intersecting plumes, in: R. Eason (Ed.), Pulsed laser deposition of thin films: applications-led growth of functional materials, John Wiley & Sons2007, pp. 131-60.
[334] Z. Zhang, S. Chen, X. Ji, C. Qin, H. Wang, P. Xie, R. Fan, Large-area, low-cost infrared metamaterial fabrication via pulsed laser deposition with metallic mesh as a shadow mask, Plasmonics 11(2) (2016) 373-379.
[335] J. Martín-Sánchez, A. Chahboun, S. Pinto, A.G. Rolo, L. Marques, R. Serna, E. Vieira, M. Ramos, M. Gomes, A shadowed off-axis production of Ge nanoparticles in Ar gas atmosphere by pulsed laser deposition, Applied Physics A 110(3) (2013) 585-590.
[336] S. Grigoriev, V.Y. Fominski, R. Romanov, A. Gnedovets, Tribological properties of gradient Mo–Se–Ni–C thin films obtained by pulsed laser deposition in standard and shadow mask configurations, Thin Solid Films 556 (2014) 35-43.
[337] S. Grigoriev, V.Y. Fominski, R. Romanov, A. Gnedovets, M. Volosova, Shadow masked pulsed laser deposition of WSex films: Experiment and modeling, Applied surface science 282 (2013) 607-614.
[338] J. Hu, H. Xiao, G. Liang, Z. Su, P. Fan, X. Lin, Preparation of low roughness CZTS thin film and solar cell by SMPLD method, Journal of Alloys and Compounds 765 (2018) 888-893.
[339] R. Wood, K.-R. Chen, J. Leboeuf, A. Puretzky, D. Geohegan, Dynamics of plume propagation and splitting during pulsed-laser ablation, Physical Review Letters 79(8) (1997) 1571.
[340] K.I. Nakazawa, Electrical and optical properties of stannite-type quaternary semiconductor thin films, Japanese Journal of Applied Physics 27(11R) (1988) 2094.
[341] P.K. Mishra, Y.K. Gautam, A. Kumar, R.K. Jain, J. Prasad, A. Choudhary, R. Chandra, Thickness dependent structural, optical and electrical properties of CuIn 0.8 Ga 0.2 Se 2 thin films deposited by pulsed laser deposition, AIP Conference Proceedings, American Institute of Physics, 2014, pp. 33-37.
[342] D.M. Rowe, Thermoelectrics handbook: macro to nano, CRC press2018.
[343] A. Benmir, M. Aida, Analytical modeling and simulation of CIGS solar cells, Energy Procedia 36 (2013) 618-627.
[344] H. Heriche, Z. Rouabah, N. Bouarissa, High-efficiency CIGS solar cells with optimization of layers thickness and doping, Optik 127(24) (2016) 11751-11757.
[345] S. Yaşar, S. Kahraman, S. Çetinkaya, Ş. Apaydın, İ. Bilican, İ. Uluer, Numerical thickness optimization study of CIGS based solar cells with wxAMPS, Optik 127(20) (2016) 8827-8835.
[346] Y. Osman, M. Fedawy, M. Abaza, M.H. Aly, Optimized CIGS based solar cell towards an efficient solar cell: impact of layers thickness and doping, Optical and Quantum Electronics 53(5) (2021) 1-16.
[347] P. Chelvanathan, M.I. Hossain, N. Amin, Performance analysis of copper–indium–gallium–diselenide (CIGS) solar cells with various buffer layers by SCAPS, Current Applied Physics 10(3) (2010) S387-S391.

CHRISTIANA NICOLAOU

[348] M. Tivanov, A. Fedotov, L. Astashenok, P. Wegierek, Effect of absorbing layer thickness on efficiency solar cells based on Cu (In, Ga)(S, Se) 2, (2012).
[349] M.W. Bouabdelli, F. Rogti, M. Maache, A. Rabehi, Performance enhancement of CIGS thin-film solar cell, Optik 216 (2020) 164948.
[350] T. Negami, S. Nishiwaki, Y. Hashimoto, N. Kohara, T. Wada, Effect of absorber thickness on performance of Cu (In, Ga) Se2 solar cells, 2nd World Conference and Exhibition on Photovoltaic Solar Energy Conversion, Vienna, Austria, 1998, pp. 1181-1184.
[351] M. Schmid, Review on light management by nanostructures in chalcopyrite solar cells, Semiconductor Science and Technology 32(4) (2017) 043003.
[352] R. Kamada, T. Yagioka, S. Adachi, A. Handa, K.F. Tai, T. Kato, H. Sugimoto, New world record Cu (In, Ga)(Se, S) 2 thin film solar cell efficiency beyond 22%, 2016 IEEE 43rd Photovoltaic Specialists Conference (PVSC), IEEE, 2016, pp. 1287-1291.
[353] M. Schmid, G. Yin, M. Song, S. Duan, B. Heidmann, D. Sancho-Martinez, S. Kämmer, T. Köhler, P. Manley, M.C. Lux-Steiner, Concentrating light in Cu (In, Ga) Se2 solar cells, Journal of Photonics for Energy 7(1) (2017) 018001.
[354] T. AlZoubi, M. Moustafa, Numerical optimization of absorber and CdS buffer layers in CIGS solar cells using SCAPS, Int. J. Smart Grid Clean Energy 8 (2019) 291-298.
[355] T. Eisenbarth, T. Unold, R. Caballero, C.A. Kaufmann, H.-W. Schock, Interpretation of admittance, capacitance-voltage, and current-voltage signatures in Cu (In, Ga) Se 2 thin film solar cells, Journal of Applied Physics 107(3) (2010) 034509.
[356] G. Rajan, K. Aryal, T. Ashrafee, S. Karki, A.-R. Ibdah, V. Ranjan, R.W. Collins, S. Marsillac, Optimization of anti-reflective coatings for CIGS solar cells via real time spectroscopic ellipsometry, 2015 IEEE 42nd Photovoltaic Specialist Conference (PVSC), IEEE, 2015, pp. 1-4.
[357] E.G. Gamaly, A.V. Rode, B. Luther-Davies, Ultrafast ablation with high-pulse-rate lasers. Part I: Theoretical considerations, Journal of applied physics 85(8) (1999) 4213-4221.
[358] A.V. Rode, B. Luther-Davies, E.G. Gamaly, Ultrafast ablation with high-pulse-rate lasers. Part II: Experiments on laser deposition of amorphous carbon films, Journal of Applied Physics 85(8) (1999) 4222-4230.
[359] G. Račiukaitis, P. Gečys, Picosecond-laser structuring of thin films for CIGS solar cells, J. Laser Micro/Nanoengineering 5(1) (2010) 10-15.
[360] P. Gečys, G. Račiukaitis, E. Miltenis, A. Braun, S. Ragnow, Scribing of thin-film solar cells with picosecond laser pulses, Physics Procedia 12 (2011) 141-148.
[361] P. Gečys, G. Račiukaitis, M. Gedvilas, A. Selskis, Laser structuring of thin-film solar cells on polymers, The European Physical Journal-Applied Physics 46(1) (2009).
[362] M.A. Green, Solar cells: operating principles, technology, and system applications, Prentice Hall, USA, 1982.
[363] H. Serreze, Optimizing solar cell performance by simultaneous consideration of grid pattern design and interconnect configuration, 13th IEEE PVSC, 1978 609 (1978).

CHRISTIANA NICOLAOU

[364] C.E. Froberg, Introduction to numerical analysis, Addison-Wesley, Reading, Massachusetts, 1965.
[365] A. Flat, A. Milnes, Optimization of multi-layer front-contact grid patterns for solar cells, Solar Energy 23(4) (1979) 289-299.
[366] R.A. Serway, J.W. Jewett, Principles of physics, 2nd ed., Saunders College Pub. , Fort Worth, Texas, 1998.
[367] H.-K. Kim, K.-K. Kim, S.-J. Park, T.-Y. Seong, I. Adesida, Formation of low resistance nonalloyed Al/Pt ohmic contacts on n-type ZnO epitaxial layer, Journal of applied physics 94(6) (2003) 4225-4227.
[368] H. Sheng, N. Emanetoglu, S. Muthukumar, S. Feng, Y. Lu, Nonalloyed Al ohmic contacts to MgxZn1− xO, Journal of Electronic Materials 31(7) (2002) 811-814.

CHRISTIANA NICOLAOU

Appendix A - Optimization of the pattern of the Al grid

The design of the pattern for the Al grid has been determined considering the several power-loss mechanisms associated with the metallic grid aiming for the optimum collection of the photogenerated carriers. A typical CIGS solar cell is completed with the deposition of Ni/Al grid which consists of 100 nm Ni and several micrometres Al [2]. However, the deposition of the Ni layer was omitted for the simplicity of the fabrication, as it had no effect on the performance of the devices.

The calculations were based on a simple design with symmetric square scheme consisting of three elements: one central pad, one central busbar and the fingers (Figure A.1). All the elements are interconnected. Busbars are areas with relatively larger width, where fingers are finer elements that spread on the cell surface to collect and deliver the carriers to the busbar [362]. The busbar is connected to the central pad which is directly connected with to the external contacts of the circuit.

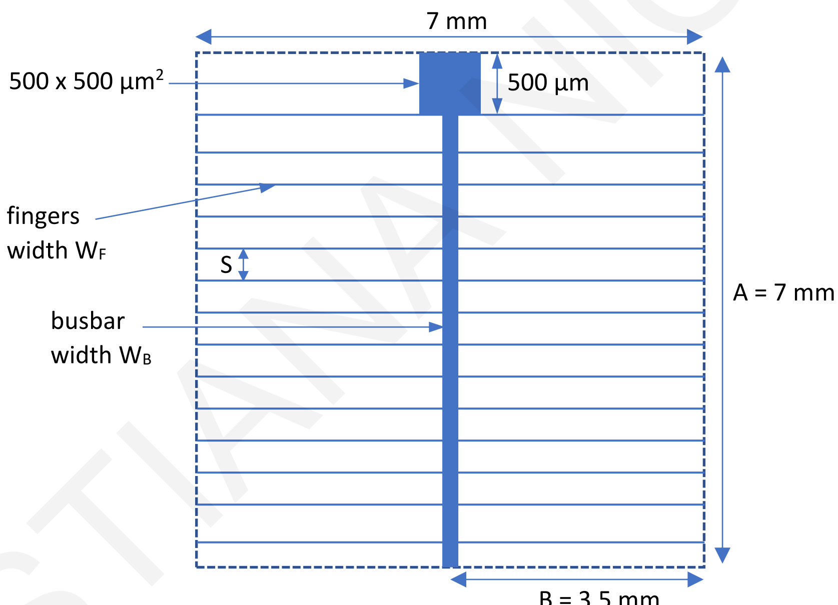

Figure A.1 Schematic representation of the design of the metallic grid illustrating the three components (central pad, central busbar, and fingers) and the parameters A, B, S, W_F and W_B.

The optimization of the design was implemented by taking into account the several mechanisms that hinder the collection of the carriers and contribute to the power losses. These power-loss mechanisms are the following:

- Lateral current flow on the top layer of the cell, that is the ZnO:Al layer
- Shadowing by the busbars and fingers
- Series resistance of the metal lines (fingers and busbar)

CHRISTIANA NICOLAOU

- Contact resistance between the metal lines (fingers and busbar) and the upper surface of the cell (ZnO:Al).

The symmetric scheme of the metallic grid can be broken down into unit cells with dimensions A and B, as shown in Figure A.1. The maximum power output of the unit cell is given by $ABJ_{mp}V_{mp}$, where AB is the area of the unit cell and J_{mp} and V_{mp} are the current density and voltage at the maximum power point, respectively.

The fractional resistive power losses in the fingers and busbars, normalized to the maximum output of the unit cell, are given by the equations A.1 and A.2 [363] respectively:

$$p_{rf} = \frac{1}{m}B^2\rho_{smf}\frac{J_{mp}}{V_{mp}}\frac{S}{W_F}, \qquad \text{Equation A.1}$$

$$p_{rb} = \frac{1}{m}A^2\rho_{smb}\frac{J_{mp}}{V_{mp}}\frac{B}{W_B}, \qquad \text{Equation A.2}$$

where, ρ_{smf} and ρ_{smb} are the sheet resistivities of the contact metals used for the fingers and busbar, W_F and W_B are the width of the fingers and busbar, and S is the pitch of the fingers as indicated in Figure A.1. The value of m is equal to 3 if the respective element has uniform width and equal to 4 if the respective element has linearly tapered width.

The fractional power losses due to shadowing by the fingers and busbar are given by the equations A.3 and A.4, respectively:

$$p_{sf} = \frac{W_F}{S}, \qquad \text{Equation A.3}$$

$$p_{sb} = \frac{W_B}{B}, \qquad \text{Equation A.4.}$$

The fingers are significantly contributing to the contact resistance losses due to their very narrow width and large number, compared to the width of the only one busbar. Therefore, neglecting the contact losses in the busbar, the fractional power loss due to the contact resistance of the fingers is given by equation A.5 as a general approximation:

$$p_{cf} = \rho_{cf}\frac{J_{mp}}{V_{mp}}\frac{S}{W_F}, \qquad \text{Equation A.5}$$

where, ρ_{cf} is the specific contact resistance of the fingers with the upper surface of the cell.

Finally, the loss mechanism related to the lateral current flow on the upper layer of the cell is given in normalized form by equation A.6:

$$p_{ul} = \frac{\rho_{sl}}{12}\frac{J_{mp}}{V_{mp}}S^2, \qquad \text{Equation A.6}$$

where, ρ_{sl} is the sheet resistivity of the upper layer of the cell.

CHRISTIANA NICOLAOU

The total losses related to the busbar are given by the sum of equations A.2 and A.4. The optimum width of the busbar, W_B, can be found by minimising the total losses. Therefore, the optimum W_B is derived by setting the differential of the total losses with respect to W_B equal to zero [363]:

$$W_B = AB\sqrt{\frac{\rho_{smb}}{m}\frac{J_{mp}}{V_{mp}}}, \quad \text{Equation A.7.}$$

A similar approach can be followed to calculate the optimum spacing S and width W_F of the fingers. When the spacing between the fingers is very small ($S \rightarrow 0$), the lateral losses in the upper layers become negligible. Therefore, the total losses related to the fingers are given by the sum of equations A.1, A.3, A.5 and the optimum ratio W_F/S is derived by setting the differential of the total losses with respect to W_F/S equal to zero:

$$\frac{W_F}{S} = B\sqrt{\frac{\rho_{smf} + \rho_{cf}\, m}{mB^2}\frac{J_{mp}}{V_{mp}}}, \quad \text{Equation A.8.}$$

In practice, limitations are placed by the technologies used for the fabrication of the metallic grid, therefore it is not possible to obtain the optimum W_F/S by equation A.8. In this case, the optimum finger design can be achieved by considering the technological limitations for W_F and calculating the optimum value of S corresponding to W_F by a simple iterative process. The optimum value of S can be calculated by successive approximations using equation A.9:

$$S'' = \frac{S'(3p_{sf} - p_{rf} - p_{cf})}{2(p_{sf} + p_{ul})}, \quad \text{Equation A.9.}$$

The starting trial value of S' is calculated by Equation A.8, where W_F is defined by the limitations of the technology used for the fabrication of the grid. The fractional power losses p_{rf}, p_{sf}, p_{cf} and p_{ul} are calculated by equations A.1, A.3, A.5 and A.6, respectively, for the corresponding S'value. The value of $S''$is then calculated by equation A.9 and acts as the new $S'$for the next trial. In each trial, the new fractional power losses p_{rf}, p_{sf}, p_{cf} and p_{ul} are calculated for the corresponding S'value. The iteration process will quickly converge to a constant value corresponding to the optimum value of S for the specific W_F.

Equation A.9 is derived by differentiating the total power losses related to the fingers $p_{rf} + p_{sf} + p_{cf} + p_{ul}$ with respect to S and setting the derivative equal to zero. As a result, a nonlinear equation is obtained for the optimum value of S which minimize the losses. The optimum S is then found by using the Newtonian iteration scheme [364] for finding the roots of a nonlinear equation. It should be noted that the equations described in this appendix are based on certain approximations regarding the magnitude of resistive voltage drop, the direction of current flow and the size of the normalized power losses [365].

CHRISTIANA NICOLAOU

The optimum width of the busbar was calculated by equation A.7 using the values presented in Table A.I. The value of Al resistivity was found in the literature [366] and the Al sheet resistivity was calculated using the thickness t of the grid, as shown in the table. In addition, the J_{mp} and V_{mp} were extracted from the IV curve of the CIGS solar cell with efficiency up to 22.6% [11]. The W_B calculated from equation A.7 is equal to 50 μm and corresponds to the width of the busbar in the unit cell which is the half width of the grid's busbar. Therefore, the optimum width of the busbar for the grid is 100 μm.

The width of the fingers W_F was chosen to be 10 μm and 20 μm, based on the technological limitations (e.g., photolithography). The optimum spacing S for the fingers, corresponding to each W_F, was calculated by equation A.9 through the iteration process described above. Table A.1 shows the values of the individual parameters used for the calculation of the power losses that are involved in equation A.9. The values of the specific contact resistance of Al contact to ZnO:Al [367] and ZnO [368] films was found from the literature and varied from 10^{-4} to 10^{-5} Ohm.cm^2, as shown in the table. However, the value of the specific contact resistance ranging between 10^{-4} to 10^{-5} Ohm.cm^2 had negligible change on the result of the iteration process. The sheet resistance of the upper layer of the cell, that is ZnO:Al, was taken from the VDP measurement performed at room temperature (section 6.3). The optimum spacing S calculated from the iteration process is presented in Table A.1 for the corresponding width of the fingers W_F. The optimum spacing of the fingers S was calculated at 240 μm for W_F at 10 μm and at 304 μm for W_F at 20 μm.

Values of the parameters		**Calculated values, $W_F = 10\ \mu m$**	**Calculated values, $W_F = 20\ \mu m$**
A	7 mm		
B	3.5 mm		
m	3		
t	1 μm		
ρ_{Al}	2.65 x 10^{-6} Ohm.cm [366]		
$\rho_{smf} = \rho_{smb} = \frac{\rho_{Al}}{t}$	2.65 x 10^{-2} Ohm.cm	$W_B = 50\ \mu m$ S = 240 μm	$W_B = 50\ \mu m$ S = 304 μm
J_{mp}	29.4 mA/cm^2 [11]		
V_{mp}	628 mV [11]		
$\rho_{cf} = \rho_{Al\ on\ ZnO:Al}$	**Al on ZnO:** 2.5 x 10^{-5} Ohm.cm^2 [368] **Al on ZnO:Al:** 8 x 10^{-4} Ohm.cm^2 [367]		

CHRISTIANA NICOLAOU

$\rho_{sl} = \rho_{ZnO:Al}$	$9x10^3$ Ohm/□ (measured by VDP, section 6.3)		

Table A.1 Values of the parameters used in the equations for the calculation of the optimum grid features and the optimum calculated features of the unit cell for finger width of 10 μm and 20 μm.

Two designs were used to fabricate the shadow masks, based on the results of the calculation for the optimum grid features. The general design of the shadow masks is presented in Figure A.1 and the optimum features of the patterns are shown in Table A.2. The pad was included in the design so that the performance characterization (illuminated IV) would be feasible using the existing equipment to apply the external contacts.

	W_B (μm)	W_F (μm)	S (mm)
Design 1	100	10	0.25
	W_B (μm)	W_F (μm)	S (mm)
Design 2	100	20	0.3

Table A.2 The optimum features of the designs used for the fabrication of the shadow masks.

CHRISTIANA NICOLAOU

Appendix B – Investigation of the geometrical parameters of the conical shadow masks

In this work, the SMPLD method was applied for the elimination of particulates during the deposition of CIGS layer. The shadow masks were designed to be conical in order to provide a tapered masking effect which helps reduce the bounce-back effect of plume constituents observed when using flat-plate masks [338]. Therefore, various conical shadow masks with different geometrical parameters were tested for the deposition of SMPLD-CIGS films in order to determine the optimized SMPLD configuration based on the surface roughness of these films. The various SMPLD setups are illustrated in Figure B.1.

PLD Setup	1	2	3	4
Cone Type	A	A	B	C
Diameter [mm]	15	15	15	11
Height [mm]	25	25	7.5	7.5
Placement [cm]	1.5	2.0	2.0	2.0

Substrate
P
D
B
C
H
A

Figure B.1 Geometrical parameters and schematic representation of the various conical shadow masks used during the deposition of SMPLD-CIGS films.

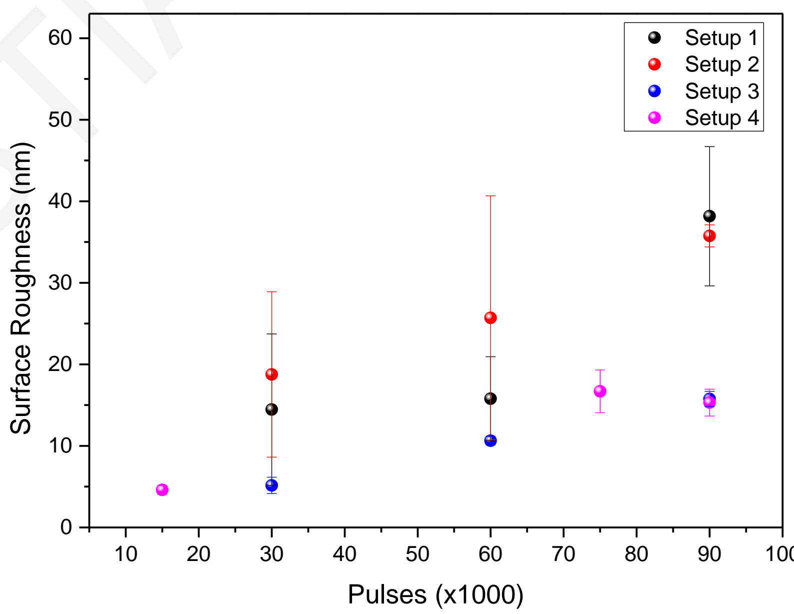

CHRISTIANA NICOLAOU

Figure B.2 Surface roughness of SMPLD-CIGS films with different number of pulses using different SMPLD setups.

SMPLD-CIGS films with different number of pulses were deposited using the four SMPLD setups displayed in Figure B.1. The surface roughness of the films was measured by AFM and is shown in Figure B.2. The roughness of the films increases as the number of pulses increases for the four SMPLD setups and the smoothest SMPLD-CIGS films are obtained with Setup 3 and 4 which correspond to the smaller conical masks. Since Setup 3 and 4 resulted in similar surface roughness, the choice was made according to the thickness of the SMPLD-CIGS layers deposited at 90000 pulses with these two setups. SMPLD-CIGS film deposited at 90000 pulses with Setup 4 was thicker than the corresponding SMPLD-CIGS film of Setup 3. According to these results, Setup 4 was identified as the optimum for the deposition of the CIGS layer. Thus, the diameter, height, and placement of the conical shadow mask were determined at 11 mm, 7.5 mm, and 2 mm, respectively.

CHRISTIANA NICOLAOU